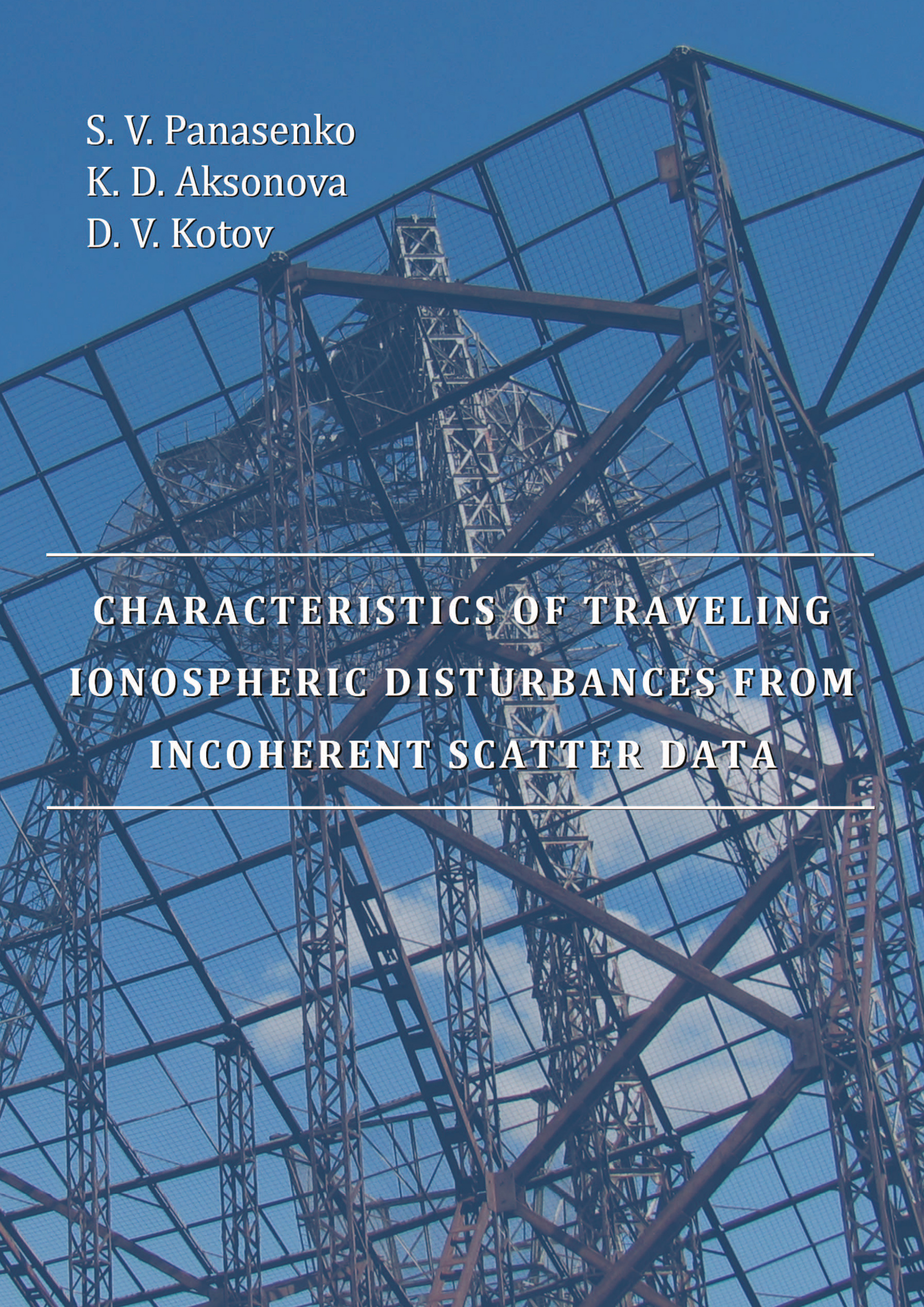

S. V. Panasenko
K. D. Aksonova
D. V. Kotov

CHARACTERISTICS OF TRAVELING IONOSPHERIC DISTURBANCES FROM INCOHERENT SCATTER DATA

S. V. Panasenko, K. D. Aksonova, D. V. Kotov

CHARACTERISTICS OF TRAVELING IONOSPHERIC DISTURBANCES FROM INCOHERENT SCATTER DATA

Dallas, USA
Primedia eLaunch LLC
2021

UDC 550.388.2, 510.535, 551.511.31 *https://doi.org/10.36074/PaAkKo.monograph-2021*
P 21

Recommended for publication by the Academic Council of the Institute of ionosphere (protocol No 4 from 04.06.2021)

Reviewers:

O. V. Shvets Leading Research Scientist of the O. Ya. Usikov Institute for Radiophysics and Electronics of the National Academy of Sciences of Ukraine, Doctor of Sciences in Physics and Mathematics, Senior Researcher.

Yu. P. Sumaruk Leading Researcher of the Department of Geomagnetism, Institute of Geophysics by S.I. Subbotin name of National Academy of Sciences of Ukraine, Doctor of Sciences in Physics and Mathematics, Senior Researcher.

E. V. Rogozhkin Full Professor of National Technical University “Kharkiv Polytechnic Institute”, Doctor of Sciences in Physics and Mathematics, Professor.

***Compilers*:**
Institute of ionosphere (Kharkiv, Ukraine)
61001, Ukraine, Kharkiv, Kyrpychova str. 16

NGO European Scientific Platform (Ukraine)
21037, Ukraine, Vinnytsia, Zodchykh str. 18/81

***Publisher*:**
Primedia eLaunch LLC (USA)
TX 75001, United States, Texas, Dallas

Panasenko S.V.

P 21 Characteristics of traveling ionospheric disturbances from incoherent scatter data : monograph. / S. V. Panasenko, K. D. Aksonova, D. V. Kotov. – Dallas: Primedia eLaunch LLC. – 148 p.

ISBN 978-1-63944-405-2
DOI 10.36074/PaAkKo.monograph-2021

This monograph describes the results of detection of traveling ionospheric disturbances and their parameters estimation based on long-term observations using Kharkiv incoherent scatter radar. For a couple of events, the data of other incoherent scatter radars were employed for comparative analysis. The book reports the results of traveling ionospheric disturbance observations during high energy natural and artificial sources.

The book will be useful for scientific researchers, lecturers, PhD and undergraduate students working and studying in the field of electrical and electronic engineering, space and planetary science, atmospheric science, statistical and nonlinear physics, and geophysics.

UDC 550.388.2, 510.535, 551.511.31

ISBN 978-1-63944-405-2

CONTENTS

PREFACE

The interest in studying the irregular structure of the Earth's ionosphere is based on the continuous using of radio communication in everyday life and the development of outer space. The ionosphere is used by mankind for long-distance radio communication. For the correct application of a definite radio frequency range, one should take into account the features of the ionosphere, its spatial and temporal variability. In addition, each region of the ionosphere is characterized by background ionization processes that depend on the season, day, solar activity, geographical location and geomagnetic activity. The Earth's atmosphere and ionosphere are known to be under the influence of external processes of both natural and artificial origin. Among them, the solar terminator, solar eclipses, magnetic storms, earthquakes, tsunamis, explosions, rocket launches, powerful radio transmission, and other factors play an important role. The main mechanism of energy and momentum transfer from such events in the atmosphere is acoustic-gravity waves (AGWs). In turn, AGWs, which are generated in the lower atmosphere and provide coupling with the upper atmosphere at the heights of the ionosphere, often have manifestations as traveling ionospheric disturbances (TIDs). TIDs can distort radio waves, affect the operation of radars, radio and satellite navigation, worsen the geopositioning accuracy. Studies of the AGW and TID generation and the features of their propagation and damping enable improving the prediction of plasma disturbances and mitigation their effect on the opearation of radio systems having different purposes. That is why the study and monitoring of AGWs and TIDs is a relevant task of radio physics and physics of the atmosphere and geospace. It has not only pure but also great applied importance. Data on variations in the TID characteristics are necessary for in-depth knowledge of the processes occurring in the ionosphere and the mechanisms of interaction between different layers of the atmosphere. The obtained parameters of large-scale and medium-scale TIDs can be used for the development of a model of the irregular ionosphere structure, as well as allow improving the global ionospheric models.

The linkage and coupling between the middle and upper atmosphere are mainly carried out by propagation of atmospheric waves, such as planetary waves, tides, and AGWs. Sources of AGWs are various and often located in the lower and middle atmosphere. During space weather variations, AGWs can be originated by heating areas and temperature gradients resulting from precipitating particle energy deposition. An enhancement of wave activity in the mid-latitude lower ionosphere during a severe magnetic storm has also been reported. Moreover, mesospheric and partially stratospheric ozone depletion occurs due to production of odd nitrogen and hydrogen from NO_x and HO_y as well as changes in prevailing winds. Processes connected with ozone and wind anomalies can effectively generate AGWs and be the tracers of space weather driven effects.

AGWs/TIDs manifest themselves as coupled variations in a number of atmospheric and ionospheric parameters (pressure, neutral and plasma temperatures and velocity, electron density). Experimentally, some of these fluctuations are difficult to associate with wave activity, since they may be contaminated by accompanying aperiodic processes (rapid neutral and/or plasma temperature changes, wind surges). In addition, the fluctuations in one or more parameters of the atmosphere and/or ionosphere caused by AGW/TID propagation can be small enough to be measured by techniques and methods in use. To overcome this problem, the combination of experimental and modeling efforts is needed together with comprehensive analysis of data from as many as possible of ground-based and space-borne facilities capable to operate quasi-simultaneously and detect different wave signatures.

The Institute of ionosphere (Kharkiv, Ukraine) is one of the world's largest scientific centers that conduct research in the fields of near-Earth space physics and solar-terrestrial interactions using the modern, accurate and informative incoherent scatter (IS) technique. The building of the Kharkiv IS radar was started in 1966. The first experimental results were obtained in 1972. The Institute of ionosphere has been conducting experimental and theoretical studies of near-Earth space for more than three cycles of solar activity. The main areas of scientific research in the Institute of ionosphere are the following: experimental study of the ionospheric parameter variations using IS technique in the altitude range of 150 – 100 km; modeling of the geospace parameter variations in quiet helio-geophysical conditions; observations, analysis and interpretation of physical effects of the geospace storms having varying intensity; the study of wave processes of natural and artificial origins in the ionospheric plasma; study of the effects in the atmosphere and ionosphere during partial solar eclipses; development of the Kharkiv IS radar database; development of unique equipment for the near-Earth space research; development of software for geophysical information analysis.

This book describes the results of detection of TIDs and their parameters estimation based on long-term observations using Kharkiv IS radar. For a couple of events, the data of other IS radars such as Millstone Hill and Tromsø UHF radars were employed for comparative analysis.

The first three chapters are devoted to the basic information about the ionospheric processes, space borne and ground-based facilities for wave processes study as well as methods for analysis of data using IS radar and dense GPS networks. These techniques have complementary capabilities and joint data analysis can have the advantage of giving a more complete picture of observed events. The combination of IS and GPS receiver techniques is in this sense an efficient approach for studying threedimensional TID structures, combining the wide observation range and high resolution of IS in the vertical dimension with the same properties of GPS observations in the horizontal one. Chapters 4 and 5 report TID parameters during magnetically quiet and disturbed conditions. The Kharkiv IS data acquired during 2006 – 2018 for days where the nagnetic activity was low were analyzed and both large-scale and medium-scale TIDs were detected. Also TIDs during a number of magnetic disturbances and storms in 2012 and 2016 were detected and characterized. Finally, Chapter 6 addresses TIDs caused by high energy natural and artificial sources and observed during the total solar eclipse on March 20, 2015 and when EISCAT heater facility was operated.

Below, some information about authors is presented.

Sergii V. Panasenko, PhD*,* is Head of Department in the Institute of ionosphere and Associate Professor in National Technical University “Kharkiv Polytechnic Institute”. His current research is focused on development of software for estimating the parameters of wave processes in the ionosphere and detection and analyzing wave disturbances of natural and artificial origin. The ongoing activity is to investigate traveling ionospheric disturbances accompanying high energy natural and artificial effects such as solar terminator, solar eclipse, geospace storm, powerful radio waves, etc. using the experimental data acquiring by Kharkiv incoherent scatter radar facility as well as incoherent scatter radar and dense GPS receiver networks.

Kateryna D. Aksonova is Junior Researcher in Institute of ionosphere. Her research is focused on sources, propagation and damping of acoustic gravity waves and traveling ionospheric disturbances originated by high energy natural processes.

Dmytro V. Kotov, PhD, is Senior Research Scientist in Institute of ionosphere and Associate Professor in National Technical University “Kharkiv Polytechnic Institute”. His activities are associated with investigations of ionosphere – plasmasphere interactions, including those through acoustic-gravity waves, using all available ground based and space born research facilities and physical models; simulations of the ionosphere – plasmasphere system; exploration of space weather effects in the near-Earth space environment.

Sergii V. Panasenko
Kateryna D. Aksonova
Dmytro V. Kotov

ABBREVIATIONS

ACF	Autocorrelation function
ADC	Analog-to-digital converter
AFT	Adaptive Fourier transform
AGW	Acoustic-gravity wave
APC	Absorption in the polar cap
DPS	Digital portable sounder
EISCAT	European incoherent scatter radar
ESR	EISCAT Svalbard radar
GIRO	Global ionospheric radio observatory
GNSS	Global navigation satellite system
GPS	Global positioning system
IGW	Internal gravity wave
IMF	Interplanetary magnetic field
IRI	International reference ionosphere
IS	Incoherent scatter
LSM	Least squares method
LSTID	Large-scale TID
MLT	Mesosphere and lower thermosphere
MST	Mesosphere-stratosphere-troposphere
MSTID	Medium-scale TID
MU	Middle and upper atmosphere
PC	Personal computer
RF	Radio frequency
SID	Sudden ionospheric disturbance
SDR	Software defined radio
ST	Solar terminator
STEC	Slant TEC
TEC	Total electron content
TID	Traveling ionospheric disturbance
UHF	Ultra high frequency
UHR	Upper hybrid resonance
USRP	Universal software radio peripheral
UT	Universal time

CHAPTER 1

BACKGROUND VARIATIONS AND WAVE PROCESSES IN THE IONOSPHERE

This chapter aims at brief description of ionospheric and atmospheric processes. It gives information about ionospheric inhomogeneities and disturbances and reports the traveling ionospheric disturbances are often the ionospheric signatures of acoustic gravity waves. Classification of traveling ionospheric disturbances is provided according to their periods and spatial characteristics. The sources and propagation of waves in the ionosphere are described. Several aspects of coupling between background and wave processes are given and main atmospheric and ionospheric models that will be employed later to evaluate the characteristics of wave processes are described.

1.1. Introduction to ionospheric processes

The ionosphere is a part of the Earth's atmosphere. It is located at altitudes above 50 km and characterized by the presence of free charged particles: electrons and ions. The ionosphere is weakly ionized plasma permeated by the Earth's magnetic field. It is basically formed under the influence of electromagnetic and corpuscular radiation of the Sun [Kamide & Chian, 2007]. The ionosphere was discovered in the early 20th century by two groups of scientists: E. Appleton and M. Barnett from Great Britain, and G. Breit and M. Tuve from the USA. They experimentally established the existence of a region that reflects radio waves and is located at the altitude of about 100 km. This Heaviside-Kennelly region, is known as the E region of the ionosphere at present [Heaviside, 1902; Kennely, 1902].

The ionosphere consists of positive ions (mainly O^+, O_2^+, NO^+, N^+, $N2^+$, He^+ and H^+) and electrons. It is divided into such regions as D, E, F1 and F2 according to the electron density, which experiences the solar cycle, season and day variations and affects the propagation of electromagnetic waves. The main source of ionization during the day is short-wave radiation from the Sun, as well as corpuscular fluxes, galactic rays, and others. Each type of ionized radiation affects only certain areas of altitude. The more the ionizing impact of sunlight is, the more the conductivity and thickness of the ionized layers are and the lower they are located. During the day, their conductivity and thickness is greater, and the height above the ground is less than at night. In summer, the conductivity and thickness of the ionospheric layers is greater, and the height is less than in winter.

Consider briefly the structure of the ionosphere. Figure 1.1 shows typical altitude profiles of the electron density N_e.

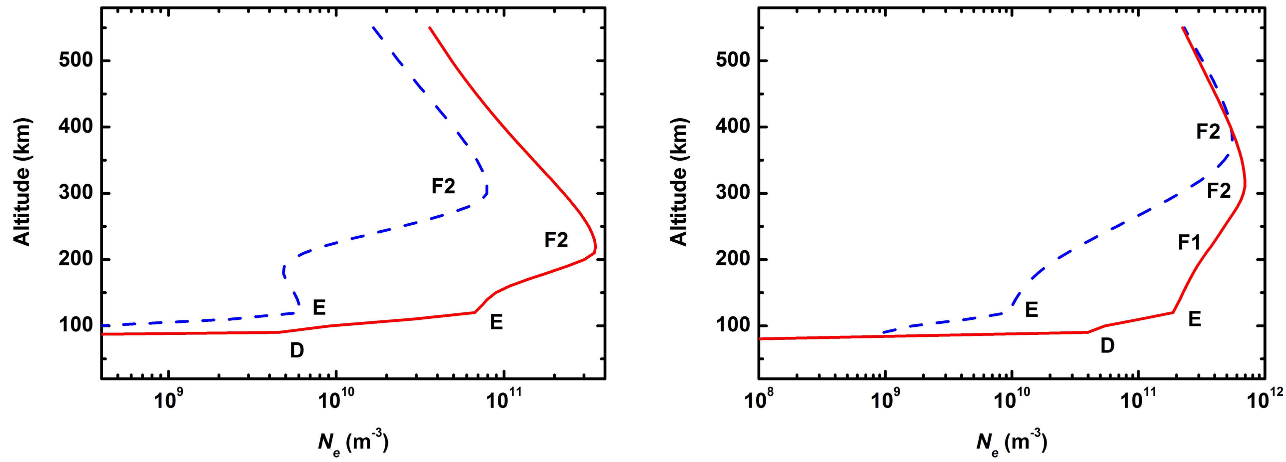

Figure 1.1. Typical altitude profiles of the electron density on December during solar minimum (left) and June during solar maximum (right) for daytime (solid) and nighttime (dash) conditions.

The D region is located at the altitudes of 60 – 80 km and exists during the day only. The main contribution to its ionization is made by extreme ultraviolet (hydrogen Layman-alpha line) and X-ray radiation from the Sun. Also, a definite role is played by additional weak sources of ionization, such as meteorites, cosmic rays, as well as energetic particles precipitated from the magnetosphere. The peak electron density is about 10^8 – 10^9 m^{-3}.

The main source of ionization for the E region (90 – 120 km) is ultraviolet and X-ray radiation. The N_e values increase to about 10^{10} m^{-3} during the daytime, while at night, they decrease to about 10^9 m^{-3} due to the rapid recombination process. The electron density does not drop below these values due to the constant diffusion of charged particles from the upper F region. At altitudes of 100 – 110 km, a thin (0.5 – 1 km thickness) sporadic layer E_s occasionally occurs. It results in reflecting radio waves due to high N_E that is non-typical for the E region.

The ionospheric F region is located above 130 – 140 km. The main peak in the electron density ($N_e \approx 10^{11}$ – 10^{12} m^{-3}) is formed at the altitudes of 250 – 400 km. During the daytime, strong solar ultraviolet radiation acts to produce a "ledge" or "step", which is called the F1 region (150 – 200 km), in the lower part of the F region. The F2 region is significantly expanded vertically starting from about 200 km. During the nighttime, the F1 region disappears and the main F peak moves to higher altitudes of 300 - 400 km.

The main source of ionization of the atmosphere is solar radiation. It is known the solar activity to be changed with a period of 11 years. During the minimum and maximum of such cycle, the ionization has different levels, minimum and maximum, respectively. The operating frequency range of radars that use the effect of reflection of short radio waves from the Earth's ionosphere also depends on this cycle. One of the manifestations of the solar activity is solar flares. They contribute to a sharp increase in ionized radiation and cause sudden ionospheric disturbances. Hard X-ray waves penetrate the D-region, releasing electrons, which leads to the absorption of high-frequency signals (3 – 30 MHz). In [Leonovich et al., 2005], it is described how the electron density in different regions of the atmosphere changes during sudden ionospheric perturbations. The maximum increase in N_e is detected in the D region and in the E-region (about 50 – 200%), and in the F region (from 10 to 30%). When considering a specific phenomenon, namely, the solar flare on September 23, 1998, the authors found the following. About 75% of N_e change is localized at altitudes of 100 – 300 km. As for temperature, a sharp increase occurred during the pulse phase with a subsequent decrease to values much smaller than the initial ones in undisturbed conditions.

In addition to the background electron density profiles, random variations in N_e are also induced. Such variations are due to the moving of inhomogeneities having different scales, which constantly appear and disappear. They are the result of various photochemical, energetic and dynamic processes occurring in the ionosphere. In particular, the formation of so-called ionospheric "holes" that occur during rocket launches and sudden stratospheric warmings is also possible. In this case, the total number of electrons decreases significantly.

Each launch of the rocket creates inhomogeneities and "holes" that lead to the distortion of the radio communication signals. For instance, the impact of space transport systems on the ionosphere based on the launches of Space Shuttle and Energy rockets is reported in [Chekalin & Shatrov, 1991]. The authors concluded that the ejection of the combustion products significantly change the composition of the atmosphere and the ionosphere in a wide range of altitudes.

Sudden stratospheric warming is known to be a sharp increase in stratospheric temperature in the Earth polar and sub-polar regions, which in turn affects the middle latitudes. The response of the ionosphere over Eastern Siberia to the stratospheric warming in January 2009 was studied using satellites and a network of ionosondes [Shpynev et al., 2014]. The change in the height of the ionization peak and the decrease in the critical frequency during the daytime were revealed.

The specific formations such as the main ionospheric trough that is a region of low electron density also exist. The authors [Tumanova et al., 2016] found changes in such parameters of the ionospheric trough as location, depth and width to be depended on the level of geomagnetic activity. The characteristics of the ionosphere also experience the latitude variations. The ionosphere is latitudinally devided into midlatitude, equatorial, auroral and polar ionosphere. The most disturbed regions are the polar latitudes where the strong coupling between the magnetic field and solar wind particles occurs. In addition, there are so-called magnetic anomalies, for instance, the Brazilian anomaly. In this area, the Earth's ionosphere is more affected by charged particle fluxes from the planet's radiation belts. The most regular is the latitudinal ionosphere.

1.2. Motions in the atmosphere and ionosphere

Analysis of a large number of experimental data obtained by different techniques in the 1950 – 70's showed the inadequacy of ideas about the ionosphere as a quiet static near-Earth space region (see, e. g., [Portnyagin & Shpringer, 1978; Kazimirovsky & Kokourov, 1979; Danilov et al., 1987]). The main atmospheric and ionospheric parameters at the ionospheric altitudes, such as temperature and density of neutral and charged particles, viscosity, thermal conductivity, conductivity, etc. were found to experience constant background and random variations. The processes of mass and momentum transfer, i. e. dynamic processes, play an important role in changing these parameters [Gossard & Hooke, 1975; Davies, 1990; Schunk & Nagy, 2009]. The need for their experimental study is due to the lack of knowledge about the spatio-temporal distribution of all energy sources and sinks.

The ionosphere plasma motions up to the altitudes of 400 – 500 km and 600 – 700 km during the daytime and nighttime, respectively, substantially determined by the motions of neutral particles. This is due to the fact that the charged particles are only small species in the atmosphere and are easily influenced by the motions in the atmosphere.

The hydrodymanics of the atmosphere can be theoretically described by Navier - Stokes equation together with the energy and gas equations. The system of equations for the neutral component has the form [Gossard & Hooke, 1975; Bryunelli & Namgaladze, 1988]:

$$\frac{d\vec{V}}{dt} = \vec{F} - \frac{1}{\rho}\nabla p + \frac{\mu}{\rho}\Delta\vec{V} + \frac{\mu}{3\rho}\nabla(\nabla\cdot\vec{V}),$$

$$\frac{d\rho}{dt} + \rho(\nabla\cdot\vec{V}) = 0,$$

$$\rho c_V \frac{dT}{dt} + p(\nabla\cdot\vec{V}) + \mu[\frac{4}{3}(\nabla\cdot\vec{V})^2 - (\nabla\times\vec{V})^2] - \nabla\cdot(\kappa\nabla T) = P - L,$$

$$p = \rho RT.$$

Here $\vec{V}$ is velocity; ρ, p and T are density, pressure and temperature, respectively; t is time, μ and κ are dynamical viscosity and thermal conductivity, respectively; $\vec{F}$ are external forces acting on a unit mass; c_V is the specific heat capacity at constant volume; P and L describe the sources and sinks of energy, respectively; R is universal gas constant.

All motions in the ionosphere can be roughly divided into three types: prevailing wind or general circulation, wave processes and turbulence [Kazimirovsky & Kokourov, 1979; Danilov et al., 1987]. They form a selfconsistent system with both forward and backward connections. Let's consider the mentioned types of movements in more detail.

Prevailing wind. This term refers to the global motion of the ionospheric plasma under constantly existing pressure gradients and experiencing slow, mainly seasonal changes. A theoretical study of the prevailing wind in the mesosphere and lower thermosphere showed that the quasi-geostrophic approximation is valid at these altitudes. The geostrophic wind is known to be the rectilinear motion of the body due to the Coriolis force and the horizontal pressure gradient balancing each other [Kazimirovsky & Kokourov, 1979].

Zonal V_z and meridional V_m wind speeds are described by the relations [Kazimirovsky & Kokourov, 1979; Bryunelli & Namgaladze, 1988]:

$$V_z = -\frac{1}{2\Omega\rho\sin\varphi}\frac{\partial p}{\partial y}, \qquad V_m = \frac{1}{2\Omega\rho\sin\varphi}\frac{\partial p}{\partial x},$$

where Ω is Earth cyclic speed module; φ is latitude; x and y axes are directed to the east and north, respectively.

However, deviations of the prevailing wind from the geostrophic one were revealed, which is apparently associated with the transfer of energy and momentum from the lower atmospheric layers through wave processes [Portnyagin & Solovjova, 2000; Middleton et al., 2002]. The building of a theoretical model of general circulation that properly describes all the observed processes is still far from completion.

Wave processes. This is the quasi-periodic changes in the atmospheric characteristics, in particular, the wind velocity. Due to a decrease in the volumetric density of atmospheric gas with increasing altitude, the amplitude of upward propagating waves increases until the dissipation processes become significant. Therefore, wave processes are the most important mechanism of coupling between different atmospheric layers (see, e. g., [Gossard & Hooke, 1975; Chernogor, 2011]).

Turbulence. It represents small-scale chaotic spatio-temporal changes in the magnitude and direction of wind velocity, as well as density, pressure, temperature and other parameters of atmospheric gas. The main criterion for the occurrence of turbulence is the Reynolds number Re = $(\rho v l)/\mu$, where l and v are respectively characteristic spatial scale and speed (see, e. g., [Kazimirovsky & Kokourov, 1979]). Turbulent motions almost completely disappear above the mesopause region (80 – 100 km), since the positive altitude gradient of temperature and viscosity ensure the stability of this region. Dissipation of turbulent motions is an additional source of heat and largely regulates the rates of various aeronomic processes.

At present, extensive studies of the atmospheric and ionospheric motions have been carried out using both ground-based and space-borne facilities. Certain regularities in the behavior of general circulation and wave processes were found. The dependence of the zonal (east-west direction) and meridional (north-south direction) wind components on the level of solar activity has been revealed [Middleton et al., 2002; Namboothiri et al., 1993, 1994; Pancheva et al., 2003], and long-period (over several decades) trends have been detected that can be associated with global climate change of the Earth [Merzlyakov & Portnyagin, 1999]. The dependence of the wind speed and direction on the level of magnetic activity has been shown [Singer et al., 1994]. On the basis of the obtained experimental data, models of prevailing winds and wave processes in various ionospheric regions (GSWM, TIME-GCM, GEWM, CMAT, etc., see, e. g., [Roble & Ridley, 1994; Portnyagin & Solovjova, 2000; Harris et al., 2002]) were constructed. However, long-term measurements of wind velocity, amplitudes of the main atmospheric tides (diurnal and semidiurnal) and the spectrum of gravitational waves [Jacobi et al., 1999; Manson et al., 1999, 2002; Middleton et al., 2002; Zhang et al., 2003] showed that only partial agreement of experimental and model data occurred. The mentioned models describe well the behavior of a particular type of motion or the processes in a certain time, altitude intervals or latitudinal-longitudinal sector. Therefore, experimental data still remain the only reliable source of our knowledge about the dynamics of the atmosphere and ionosphere.

1.3. Magnetic storms and the ionosphere

Geomagnetic activity makes a significant contribution to the dynamics of the ionosphere. During geomagnetic storms and substorms, the following processes occur: change in the parameters of the ionospheric plasma (in the F region, both increase and decrease of N_e relative to the background level are possible [Medvedev et al., 2017]); effects of the western electrojet [Danilov, 2013]; enhanced impact of thermospheric wind; equatorward motion of the main ionospheric trough [Chernigovskaya et al., 2019]. Such processes, in turn, lead to the absorption of waves in the D region of the high-latitude ionosphere, the drift of the ionospheric plasma in both the horizontal and vertical directions, and the generation or amplification of ionospheric disturbances.

Geomagnetic storms are irregular phenomena. An initial phase of the storm can vary from a few minutes to several hours. Its duration is about 1 – 7 days. Unfortunately, we still do not know clearly the behavior of ionosphere parameters during such phenomena. This is due to the great variety, varying intensity and duration of storms. It is necessary to study the influence of geophysical conditions, as they are the cause of many anomalous phenomena in the ionosphere, which can lead to the distortion or blackout of radio communication.

Indices of geomagnetic activity. Variations in the geomagnetic field are used as one of the main parameters that characterize the geophysical conditions. Some indices quantifying the geomagnetic activity are A_p, K_p, D_{st}, AE.

AE (Auroral Electrojet) index characterizes the detailed structure of magnetic field fluctuations caused by currents in the auroral zone. It is measured in nanoteslas. To calculate it, magnetograms of H-components from observatories evenly located at different longitudes and auroral or subauroral latitudes, are used. Currently, there are 12 such stations between 60° and 70° N latitude.

D_{st} (Disturbance Storm-Time) is an index of magnetic activity obtained by a network of equatorial geomagnetic observatories, which measures the intensity of a globally symmetric equatorial electric current (ring current). When the storm intensity increases, the D_{st} index decreases. Thus, moderate storms are characterized by D_{st} from –50 to –100 nT. For strong storms it equals from –100 to – 200 nT and its value for extreme storms is lower than –200 nT.

K_p is a planetary index that characterizes the global disturbance of the Earth's magnetic field in a three-hour time interval. It is determined at 13 geomagnetic observatories located between 44° and 60° of northern and southern geomagnetic latitudes. It has levels from 0 to 9, each subsequent level of the scale corresponds to variations of 1.6 – 2 times greater than the previous.

A_p is an index, representing the average value of the magnetic field variations corresponding to the definite K_p index. The level of K_p = 4 approximately corresponds to A_p = 30 nT, and the level of K_p = 9 corresponds to A_p > 400 nT.

Table 1.1 shows a magnetic storm classification. It was developed in Space Weather Prediction Center, National Oceanic and Atmospheric Administration (NOAA, USA) and taken from https://www.swpc.noaa.gov/noaa-scales-explanation. Here G index is used to characterize the intensity of the geomagnetic storm through its influence of variations of the Earth's magnetic field on humans, animals, electrical engineering, communications, and navigation. Scales of the G index are from $G1$ to $G5$, i. e. from weak to extreme disturbances of the Earth's magnetic field.

1.4. Inhomogeneities and disturbances in the ionosphere

The ionosphere undergoes changes from external factors that occur both outside our planet and on its surface. Ionospheric heterogeneities are unevenly distributed around the globe. Their intensity and number depends on the geographical region. The most disturbed regions are the polar cap and the equatorial region, while the inhomogeneities are much weaker in the middle latitudes due to the lack of their own sources of perturbations,. They often move from the polar regions to the middle latitudes. Such structures, caused by various processes occurring in the ionosphere, complicate the prediction the radio communication and radio navigation parameters. Radio waves are able to reflect, weaken, distort or even disappear when interacting with different areas of the atmosphere. The inhomogeneities are observed at all heights of the ionosphere, but differ in the mechanism of formation and features of motion.

Table 1.1. NOAA classification for magnetic storms.

Scale	Description	Effect	K_p index
$G5$	Extreme	Widespread voltage control problems and protective system problems can occur; some grid systems may experience complete collapse or blackouts. Transformers may experience damage. Spacecrafts may experience extensive surface charging, problems with orientation. Pipeline currents can reach hundreds of amps, HF (High frequency) radio propagation may be impossible in many areas for a couple of days; satellite navigation may be degraded for days; low-frequency radio navigation can be out for hours; aurora has been seen as low as 40° geom. lat.	9
$G4$	Severe	Possible widespread voltage control problems and some protective systems will mistakenly trip out key assets from the grid. Spacecrafts may experience surface charging and tracking problems; corrections may be needed for orientation problems. Induced pipeline currents affect preventive measures, HF radio propagation sporadic, satellite navigation degraded for hours, low-frequency radio navigation disrupted, and aurora has been seen as low as 45° geom. lat.	8
$G3$	Strong	Voltage corrections may be required, false alarms triggered on some protection devices. Surface charging may occur on satellite components, drag may increase on low-Earth-orbit satellites, and corrections may be needed for orientation problems. Intermittent satellite navigation and low-frequency radio navigation problems may occur, HF radio may be intermittent, and aurora has been seen as low as 50° geom. lat.	7
$G2$	Moderate	High-latitude power systems may experience voltage alarms, long-duration storms may cause transformer damage. Corrective actions to orientation may be required; possible changes in drag affect orbit predictions. HF radio propagation can fade at higher latitudes, and aurora has been seen as low as 55° geom. lat.).	6
$G1$	Minor	Weak power grid fluctuations can occur. Minor impact on satellite operations is possible. Migratory animals are affected at this and higher levels; aurora is visible at high latitudes.	5

Ionospheric disturbances include deviations of ionospheric parameters from their quiet diurnal variation, which have characteristic time scales from tens of minutes to several days and appear at distances of hundreds and thousands of kilometers. The ionosphere is disturbed by many factors, including such as weather fronts, volcanic eruptions, earthquakes, as well as through artificial influences (heating by powerful radio waves, ejections of chemically active substances and explosions).

Large-scale disturbances are of solar origin. They are associated with solar flares, sharp changes in the parameters of the solar wind and interplanetary magnetic field (IMF), and geomagnetic disturbances. The ionospheric disturbances can be classified on the following types [Bryunelli & Namgaladze, 1988].

1. *Sudden ionospheric disturbances (SIDs).* They manifested themselves as an increase in ionization mainly in the D- and E-regions of the illuminated ionosphere during periods of solar flares due to a sharp increase in solar ionizing radiation.

2. *Absorption of radio waves in the polar cap (APC)*. They associated with the penetration of soft cosmic rays ejected from the Sun during periods of powerful chromospheric flares into the lower ionosphere of the polar caps.

3. *Auroral absorption of radio waves* observed in the auroral zone during magnetic storms and associated with the precipitation of charged particles from the magnetosphere into the lower ionosphere.

4. *Disturbances in the F2 region* that develop on a global scale during periods of magnetic disturbances and are characterized by significant changes in the critical frequencies and heights of the F2 layer. According to the sign of the critical frequency deviation, these perturbations are divided into positive and negative. The mechanism for the disturbance formation in the F2 region is complex and cannot be attributed to any one factor. It is associated primarily with the convection of magnetospheric plasma and its effect on the neutral atmosphere.

Traveling ionospheric disturbances (TID) characterized by quasi-periodic (with periods of 0.2 – 3 hours) variations in a number of ionospheric parameters also constitute as a separate type of ionospheric disturbances. They will be described later in detail.

Each of the mentioned types of disturbances is associated with the following channels of energy transfer from the Sun and solar wind:

1) directly from the Sun as streams of ultraviolet and X-ray radiation, as well as high-energy particles;

2) through the magnetosphere along the magnetic field lines as electric fields, energetic and cold plasma fluxes and heat fluxes;

3) through the neutral atmosphere as wind and wave motions and chemical interaction of charged and neutral components of the ionospheric plasma.

The general morphological picture and physical scheme of the development of ionospheric disturbances associated with solar and magnetic storms can be briefly summarized as follows. The ionosphere most quickly reacts as SIDs on a flare of ultraviolet and X-ray radiation from the Sun. With the approach of high-energy solar protons to the Earth, the travel time of which ranges from tens of minutes to several hours, APC develops. Disturbances in the parameters of the solar wind and IMF that reached the Earth a day or several days after the onset of a solar event lead to a rearrangement of magnetospheric convection, the development of a ring current, and the discharge of energetic particles from the magnetosphere, causing a chain of thermospheric-ionospheric phenomena. These include:

1) enhancement of ionization and the corresponding increase in the electron density in the D and E regions of the high-latitude ionosphere;

2) rebuilding of the horizontal distribution of ionospheric plasma in the F2-region due to precipitation of soft particles and plasma transport by magnetospheric convection;

3) heating of the thermosphere due to the dissipation of ionospheric currents and generation of thermospheric winds;

4) generation of SIDs and TIDs, propagating from high latitudes to low latitudes and deforming the altitude profile of electron density;

5) heating of the outer ionosphere due to the dissipation of the ring current and heat transfer downward by thermal conduction, an increase in the temperatures of charged particles and the plasma height scale.

The combined action of these mechanisms causes electron density changes, which are registered as ionospheric effects of geomagnetic storms.

1.5. Wave processes in the atmosphere and ionosphere

According to the time scale, reflecting the period of oscillations, the wave processes in the atmosphere can be divided into three types.

1. *Planetary waves.* Periodic disturbances of atmospheric parameters with a wavelength of the order of the Earth's radius and a period of several days are called planetary waves [Kazimirovsky & Kokourov, 1979; Danilov et al., 1987]. The description of the waves is the following [Bryunelli & Namgaladze, 1988]:

$$\Delta\xi = \sum_{m=1}^{\infty} A_m(\varphi,h,t)\cos[m\lambda + \lambda_0(\varphi,h,t)],$$

where $\Delta\xi$ is variation in atmospheric parameters; m is zonal wavenumber; λ is longitude; h is altitude; A_m и λ_0 are respectively amplitude and phase of zonal harmonic.

The sources of these waves are the interaction of cold and warm atmospheric fronts, cyclones and anticyclones, as well as other large-scale meteorological phenomena. Most of the planetary waves generated in the troposphere, when propagating upward, almost completely attenuate at mesospheric heights, since the prevailing winds existing in this area prevent their penetration. However, some modes on certain days and seasons penetrate into the upper atmosphere, changing its chemical composition, the temperature of the neutral and ionized components.

2. *Tides.* Atmospheric tides are the waves with periods equal to $1/k$ (k = 1, 2, 3, 4) of a solar or lunar day (solar and lunar tides, respectively). The sources of atmospheric tides are the gravitation of air by the Sun and the Moon (gravitational tides), as well as solar radiation (thermal tides). Thermal diurnal (k = 1) and semidiurnal (k = 2) tides, generated due to uneven absorption of solar radiation by ozone, carbon dioxide, and water vapor, as well as uneven heating of the underlying surface, which is a secondary source of heat for the lower atmosphere, have the largest amplitude. At the heights of the D region, the amplitudes of the tides propagating from below are comparable and often exceed the values of the prevailing wind velocities. The interference of various tidal modes and harmonics, as well as their interaction with other waves, can explain complex diurnal variations in wind speed.

3. *Acoustic gravity waves* (AGWs). This term combines acoustic and internal gravity waves (IGWs). AGWs are generated in the troposphere and tectonosphere due to the natural or man-made processes, such as jet currents, thunderstorms, volcanic eruptions, earthquakes, powerful explosions, rocket launches, etc [Chernogor, 2011]. The IGWs are low-frequency, gravity-modified analogs of acoustic waves.

The dispersion relation for AGW in the simplest case (high-altitude stratified, isothermal medium) is [Danilov et al., 1987]:

$$\omega_I^4 - \omega_I^2 c_s^2 \left(k_x^2 + k_z^2 + \frac{1}{4H^2} \right) + \frac{(\gamma - 1) c_s^4}{\gamma^2 H^2} k_x^2 = 0\,, \tag{1.1}$$

where ω_I is intrinsic angular frequency of the wave; c_S is sound speed; k_X and k_Z are horizontal and vertical wave numbers, respectively; $\gamma = c_P/c_V$ is ratio of specific heat capacities; c_P is specific heat capacity at constant pressure; H is scale height.

The principal difference between IGWs and acoustic waves is that the latter have the air oscillations to be purely longitudinal, but IGWs have an additional, transverse, shear component. It arises due to the action of gravity: the heavier compression region tends to lower, and the lighter vacuum region tends to rise. The IGW phase propagates almost vertically, and the movements of particles in the wave occur almost horizontally. Therefore, the energy and the phase of the wave propagate in the same horizontal direction and with the same speed, but in the opposite directions vertically. Numerical calculations performed for a realistic background atmosphere have shown that waves in the range of IGW periods from 15 to 120 minutes with horizontal phase velocities of about 300 to 800 m/s can propagate freely in the thermosphere, attenuating by the factor of e ($e \approx 2.72$) at horizontal distances from 500 to 5000 km respectively. The main mechanism of AGW effect on the F2 region plasma is a "wind drug", i. e., the transmission of momentum of horizontally moving neutral particles to ions, which as a result acquire additional velocity along the magnetic field lines.

A plenty of confirmations exist that the accumulation of energy and its redistribution between different regions of the atmosphere is carried out by AGWs. The dissipation of these waves is an additional source of turbulence at the heights of the mesosphere and lower thermosphere.

1.6. Classification of traveling ionospheric disturbances

The AGW / TID phenomena can be classified as follows [Hunsucker, 1982]:

1. *Large-scale* disturbances. They have periods from 30 min to 3 hours, horizontal wavelengths greater than 1000 km and horizontal phase velocities of 400 – 1000 m/s.

2. *Medium-scale* disturbances. They have periods of 15 – 60 min, horizontal wavelengths of 200 – 1000 km and horizontal phase velocities of 100 – 300 m/s.

3. *Small-scale* disturbances. Such disturbances have periods of several minutes, horizontal wavelengths of 10 – 100 km and horizontal phase velocities of several dozen meters per second.

Large-scale TIDs (LSTIDs) are thought to be mostly originated in the auroral zone and propagate southward during variations of geomagnetic activity [Borries et al., 2009]. But they were also observed over dawn and associated with sunrise terminator source [Song et al., 2013].

Medium-scale TIDs (MSTIDs) propagate southwestward at night and generally equatorward during the daytime [Kotake et al., 2007]. They are mostly induced by local sources located both in the lower and upper atmosphere (see [Tsugawa et al., 2007; Hernández-Pajares et al., 2012]). However, similar wave signatures were also detected during geomagnetic storm [Nishioka et al., 2009].

Small-scale TIDs have seasonal occurrence peak in the summer and often caused by severe convective activity [Georges, 1973].

1.7. Sources of traveling ionospheric disturbances

Here we consider a number of high-energy processes that could cause TIDs.

1.7.1. Solar terminator

A variety of effects associated with the passage of both sunrise and sunset solar terminator (ST) occurs in the Earth's atmosphere. The study of the influence of such a constantly recurring phenomenon as ST on the variations in the Earth's ionosphere is an important task for researchers. A large number of works are devoted to theoretical and experimental studies of ST as a source of AGW and TID generation. It was established, using various methods of ionosphere sounding, that the motion of the terminator causes plasma oscillations, and hence the formation and propagation of ionospheric disturbances [Karpov & Bessarab, 2008; Somsikov, 2011]. The time of wave onsets changes during the year depending on time of ST arrival. Further, we consider the results of some studies in this field. The authors [Edemsky, 2011] using a network of GPS-receivers analyzed the peculiarities of wave generation over Japan and the United States and found the following. The reaction of the ionosphere to the passage of the sunset ST for the United States was different depending on season. In winter, the disturbances are registered about 4 hours after ST passage, while the strongest response is recorded in summer about 4 hours before the ST. As for sunrise ST, increase in wave processes is observed 2 - 3 hours after ST. Also, the Japanese satellite network has found that waves can occur within 1 to 3 hours after sunrise or sunset having duration of 1 to 2 hours and a period of oscillation in the range of 10 to 30 minutes [Afraimovich, 2010a]. Studies of variations with periods of 2 – 20 min in the lower atmosphere and ionosphere in the middle latitudes showed an increase in amplitudes before and after the passage of ST over the observation site [Karpov et al., 2016]. At the same time, the authors attribute a decrease in amplitudes of waves with periods of 3 – 5 minutes to the difference in the frequencies of acoustic waves and IGWs, which occur during the terminator event. In vertical propagation, such waves quickly reach heights of ~ 300 km.

The authors [Afraimovich et al., 2010b] explain the wave processes with periods of 10 – 30 min and duration from 1 to 2 hours, which are generated before the local ST by the movement of ST through the magnetically conjugate region. This is due to the propagation of magneto-hydrodynamic waves. The author [Chernogor, 2012] came to the same conclusions when analyzing quasi-periodic variations of the geomagnetic field near the solstices over Kharkiv, Ukraine from 2002 to 2011. In that paper, the following parameters of quasi-periodic processes were revealed: periods of predominant oscillations were of 10 – 12 min, durations were of 50 – 60 min, advance time of disturbances was 80 – 100 min. Over the territory of Brazil and the United States, the distribution of wave packets during one year of observations (2008) was as follows [Karpov et al., 2016]. As for the United States, the most pronounced effect of sunset ST occurred in winter, where the waves are observed during the daytime after the passage of the sunset terminator, while in summer they exist at night. For evening ST, the conclusions about the generation of disturbances simultaneously with the passage of the terminator at the magnetically conjugate point are confirmed. Over Brazil, the opposite is true: in winter, disturbances are recorded at night; in summer, they are observed during the day.

For studying the large-scale AGWs and LSTIDs in the equatorial ionosphere caused by the passage of the terminator, the researchers [Lizunov & Fedorenko, 2006] used data from the satellite "Atmosphere Explorer-E". The results showed the generation of disturbances with the following parameters: horizontal wavelengths of 1200 – 1600 km, periods of about 50 min, and duration of 4 – 6 periods. The amplitude of variations was greater for the sunrise ST. Thus, the results of research indicate the generation of both medium-scale and large-scale patterns during the ST time.

As shown earlier, the ST is a regular source of disturbances in the atmosphere and ionosphere over a wide range of periods and spatial scales (see, e. g., [Somsikov, 2011]). At least, two altitude regions are known where gradients of temperature, pressure and density of neutral and charged particles are formed during the transition from night to day and vice versa, and waves can be generated [Song et al., 2013]. The first region covers the stratosphere and mesosphere (20 – 90 km), where significant temperature gradients occur during the ST passage due to heating / cooling of ozone and molecular oxygen. The second region is located at altitudes of 150 – 200 km, between the ionospheric layers F1 and F2, where sharp gradients of electron and ion density occur during changes in the intensity of solar radiation. The reason is due to because the rate of photochemical reactions in layer F1 is higher than in layer F2. It is important that the first region can generate only medium-scale AGWs, while the second one is a source of both types of waves.

1.7.2. Solar eclipse

In contrast to the change of day and night, the shading of the ionosphere during a solar eclipse has characteristic features. The parameters of the generated disturbances, in such conditions, depend on the state of space weather, the solar disk coverage and geographical coordinates. Here we consider the influence of a solar eclipse on the example of a event that occurred on March 20, 2015, at various observation sites of the globe.

The authors [Borchevkina et al., 2017], conducting lidar sounding and analyzing TEC, found the following: the eclipse has a significant effect on variations in the parameters of the atmosphere, where AGWs with periods of 2 – 20 min are amplified. In general, the change in spectral characteristics is similar to those during ST. Another study was conducted using incoherent scatter radar and a digital ionosonde for the mid-latitude European region [Chernogor et al., 2019]. The results showed a decrease in the electron density by 18.5% (for an altitude of 190 km) and 16.5% (210 km). The Ne reaction is absent above 240 km. The electron temperature decreased by from 12% to 19.5% at altitudes of 190 – 580 km. The ion temperature is affected weaker. Altitude profiles of the vertical component of the ionospheric plasma velocity were the same as the night ones. Over this region, other authors [Panasenko et al., 2019] found both LSTIDs and MSTIDs, which were caused by AGWs, with periods of 50 –

60 mins. The average horizontal phase velocity is 803 ± 281 m/s and 144 ± 54 m/s, the absolute amplitudes of TEC variations did not exceed 0.4 TECU and 0.17 TECU (for Northern Europe) for large-scale and medium-scale disturbances, respectively. The direction of propagation for both types is north- east. The reaction of the atmosphere to the solar eclipse for the Czech Republic was as follows. The wave activity was observed at altitudes of 150 – 350 km, the TIDs moved northeastwards with a phase velocity of 70 – 100 m/s and a period of about 65 min [Mošna et al., 2018]. Over China, the average LSTID parameters were as follows: periods of 74.8 ± 1.4 min, horizontal phase velocity of 578 ± 23 m/s and horizontal wavelengths of 2691 ± 80 km. A possible source of disturbances is the propagation of AGWs from high to low latitudes. The results were obtained using GPS stations, Doppler RF receivers and ionosondes.

Obviously, the study of the ionosphere composition during such an event as a solar eclipse is an important task of geophysics and radiophysics. Changing the degree of ionization, reducing the critical frequencies and increasing the reflection height lead to a change the velocity of the radio pulse propagation and its absorption in the ionosphere.

1.7.3. Generation of secondary waves

Most of AGWs is thought to originate at the heights of the troposphere. They are associated with convective motion and turbulence. In turn, such small-scale structures can lead to the transfer of energy from smaller waves to large-scale waves propagating above [Kurdyaeva et al., 2018]. The secondary waves are known to be generated due to the dissipation of AGWs at altitudes above 120 km even during quiet conditions and can cause the appearance of large-scale AGWs and LSTIDs at ionospheric altitudes [Vadas & Liu, 2009]. The authors [Vadas & Liu, 2009] estimated the parameters of the secondary disturbances: periods of 80 min, horizontal wavelengths of 2100 – 2200 km and horizontal phase velocities of 480 – 510 m/s. Other researchers, based on the analysis of temperature changes in the upper atmosphere during hurricanes, found that the dissipation of AGWs at the heights of the mesosphere is the movement of air and heating, which in turn generates the propagating secondary AGWs [Kozak & Pylypenko, 2011].

1.7.4. Impact of geomagnetic activity

Magnetic storms are accompanied by complex physical and chemical processes that lead to significant variations in geomagnetic and electric fields, result in magnetospheric and atmospheric disturbances and negatively impact on human life through disruption of telecommunication, radio navigation and radar systems, malfunctions in operation of spacecrafts (see, e. g., [Buonsanto, 1999; Danilov, 2013; Chernogor & Domnin, 2014]). It is important that such variations in space weather, caused by non-stationary processes on the Sun and energy and impulse transfer from the solar wind to the geospace plasma also manifest themselves as changes in the ionospheric characteristics from high to low latitudes [Adeniyi, 1986; Wu et al., 2013; Chernogor & Domnin, 2014] and at heights from lower to the upper ionosphere [Förster, M., & Jakowski, 2000; Sokolov, 2011; Chernogor & Domnin, 2014]. The processes in the atmosphere stimulated by storm are often quasi-periodic and contribute to AGW generation. LSTIDs propagate from the auroral area to the low latitude ionosphere during magnetic disturbances and storms.

Efficiency of AGW / TID generation during gemagnetic storms depends on the number of factors and is determined not only by spatial and temporal distribution of their sources, but also the previous state the atmosphere and ionosphere. Lorentz forcing. Joule heating and particle precipitations are believed to be main mechanisms responsible for AGW / TID generation during variations of auroral electrojets (e.g. [Hocke and Schlegel, 1996]). The contribution from auroral source obviously increases with enhancement in magnetic activity.

1.8. Propagation of AGWs and TIDs

AGWs are known to have a wide range of periods and are also able to propagate from the surface atmosphere to the heights of the ionosphere. Due to the collisions of neutral particles with charged ones, such waves lead to the movement of ionospheric plasma. Their sources are concentrated both in the troposphere (meteorological fronts, mesoscale processes, jet streams) and near the Earth's surface (wind flow of orographic inhomogeneities and thermal movements between the continent and the ocean) [Nerushev, 2014]. The main mechanisms of AGW dissipation in the upper atmosphere are thermal conductivity, molecular viscosity and ion drug. An analysis of such waves was performed [Suslov et al., 2017]. It turned out that they reach heights of more than 80 km, and can spread over long distances due to the waveguide propagation, depending on the source, in the horizontal direction. Therefore, it is important to consider such properties when studying the ionospheric manifestations of AGWs. The authors [Kunitsyn et al., 2015] used a numerical simulation to analyze the generation and propagation of AGWs from various sources, such as earthquakes, explosions, heating and tsunamis. The following was revealed: the length of AGW packets from two to several tens of waves propagating in the horizontal direction with increasing period and wavelengths (periods of 750 – 1500 s, group velocity of 250 – 310 m/s, horizontal wavelengths of 250 – 280 km).

The impact of wind patterns on the propagation of AGWs and TIDs is also manifested differently depending on the region. According to the theory of wind shear, the formation of sporadic E_s layer due to the redistribution of charged particles is considered in [Gershman, 1974]. Moreover, they can be transported due to horizontal wind movements. Such formations shield the transmission of the signal through the F region, which can result in partial or complete radio communication blackout.

Many studies have been performed concerning the penetration of large-scale IGWs to ionospheric heights due to wind patterns [Hocke, & Schlegel, 1996; Fritts & Alexander, 2003]. The authors [Yerohin et al., 2007] found the impact of IGWs on the distribution of ionosphere parameters at altitudes from 200 to 400 km, due to their transfer by wind. An increase in the amplitudes of the waves was detected, as well as the factors that limit the penetration of such waves into the upper atmosphere such as critical layers and layers of vertical reflection were identified. The horizontal wavelengths of IGWs to propagate to ionospheric heights were evaluated. The interaction of IGWs with neutral wind was also established using the incoherent scatter radar, ionosonde and high-frequency (HF) radar [Medvedev et al., 2017]. The authors confirmed that the neutral wind reduces the amplitudes of the IGWs propagating in the wind direction and increases the ones during opposite propagation. The distribution of the detected horizontal velocities corresponds to the hypothesis of wind filtration at altitudes of 90 – 250 km.

The physical mechanism of propagation of AGWs generated in the polar regions to middle latitudes is described in [Smertin & Namgaladze, 1978; Hunsucker, 1982] on the basis of model simulations. It usually takes about 2 – 3 hours. Here we describe it in more detail. For example, over the Antarctic Peninsula during experiments, the authors [Galushko et al., 2016] found a different direction of disturbance propagation depending on the time of day. At first, the northwestward direction (from 00:00 to 05:00 UT) was prevailing. Then, they propagated southeastwards (from 05:00 to 10:00 UT). Finally, they detected a rotation of the propagation direction to be counterclockwise (northeastward – north – northwestward from 11:00 to 20:00 UT). In the study of the nocturnal auroral ionosphere [Borisova et al., 2007] during the period of medium magnetic activity, two directions of propagation, northeastwards and northwestwards, were obtained. Other authors [Tsugawa et al., 2007] have identified the equatorial direction of daytime MSTIDs and their southwestward propagation at night over the territory of Japan and North America.

1.9. Coupling between background and wave processes

Atmospheric waves are known to significantly contribute to the energy and momentum balance of the atmosphere as a whole [Yigit and Medvedev, 2009]. The linkage and coupling between the middle and upper atmosphere is mainly carried out by propagation of planetary waves, tides, and AGWs. The widespread interest in AGW / TID events is inspired by their important impact on ionospheric variability that results in distortion of radio waves propagating through the ionosphere. Such distortion leads to disruptions for applications using Global Navigation Satellite Systems (GNSS) [Hapgood, 2017]. It is important to note that TID-related variability of the ionosphere not only manifests during disturbed space weather conditions [Tsugawa et. al., 2004; Borries et al., 2017] but also under quiet space weather conditions too [Vadas and Nicolls, 2009; Nygren et al., 2015].

TIDs and other variations of ionospheric parameters such as tides, planetary waves, seasonal variations, etc are thought to be coupled processes. Thus, information about the background state of the ionosphere is important for understanding TID features. TIDs are known to be often manifestations of AGWs at ionospheric altitudes [Hines, 1960]. Here we report a number of aspects which concerns the influence of background atmosphere and ionosphere on propagation and damping of wave processes.

The first aspect concerns the influence of the thermosphere temperature on the dissipation and peak propagation altitude of AGWs. The main reason of dissipation of high-frequency IGWs in the thermosphere is kinematic viscosity and thermal diffusivity. A new anelastic AGW dispersion relation was derived to include the damping effects of these background atmospheric characteristics [Vadas and Fritts, 2005]:

$$\omega_l^2(\omega_l^2+i\alpha\nu)^2\left(1+\frac{i\gamma\alpha\nu}{\omega_l^2\,\mathrm{Pr}}\right)-c_s^2(\omega_l+i\alpha\nu)\left(\omega_l+\frac{i\alpha\nu}{\mathrm{Pr}}\right)\left(k_x^2+k_z^2+\frac{1}{4H^2}\right)+\frac{(\gamma-1)c_s^4}{\gamma^2H^2}k_x^2=0, \quad \mathbf{(1.2)}$$

where

$$\alpha=k_x^2+k_z^2-\frac{1}{4H^2}-\frac{ik_z}{H};$$

$\nu = \mu/\rho$ is kinematic viscosity; $\mathrm{Pr} = c_P\mu/\kappa$ is Prandtl number; i is imaginary unit. It is notable that in the limit of the molecular viscosity and thermal diffusivity to tend to zero, the dispersion relation (1.2) goes into (1.1). The dissipation of AGWs does not depend on an integrated viscosity effect, but on the local value of viscosity. If the temperature increases rapidly above 100 km, this causing the viscosity to increase less rapidly with altitude as compared to an isothermal atmosphere and will cause AGW propagation to much higher altitudes before its rapid dissipation. Thus, high solar activity promotes propagation of AGWs generated in the lower atmosphere on the larger ionospheric altitudes.

The second aspect concerns the coupling between amplitudes of TIDs in the electron density with electron density altitude profiles, and magnetic field inclination I and declination D. Medium-scale TIDs in electron density produced by AGWs are shown to be satisfactorily modelled by the following expression [Hooke, 1968]:

$$\Delta N_e=\frac{iu_{||}}{\omega_l}\left(\frac{\partial N_e}{\partial z}\sin I-ik_{||}N_e\right), \quad \mathbf{(1.3)}$$

where ΔN_e is electron density perturbation; $k_{||}$ and $u_{||}$ are respectively the neutral wind velocity and wave number of the AGW parallel to the magnetic field. The wave number along the magnetic field line from (1.3) can be represented as [Koval et. al., 2018]:

$$k_{||} = \sqrt{k_x^2 + k_z^2} \cos\left(\arctan\left(\frac{k_z}{k_x}\right) - I \right) \cos[(\pi - A) \pm D],$$

where A is azimuth of AGW propagation. The amplitude of ΔN_e is:

$$\Delta N_{e0} = \frac{U_{||}}{\omega_I} \sqrt{\left(\frac{\partial N_e}{\partial z}\right)^2 \sin^2 I + k_{||}^2 N_e^2} \,. \qquad \textbf{(1.4)}$$

The equation (1.4) shows that the peak values of ΔN_{e0} attained at the altitudes where the amplitude of neutral wind velocity along magnetic field line $U_{||}$, N_e, and its height gradient are evident. Such conditions usually occur slightly below the F2 peak. During the high solar activity, this peak is located higher than during low or medium solar activity. Therefore, such coupling also promotes the propagations of TIDs to the higher altitudes with enhancement in solar activity.

The third aspect considers the impact of horizontal neutral wind velocity on observational ability to detect AGWs and TIDs. Indeed, the intrinsic wave angular frequency ω in (1.1) and (1.2) can be expressed as:

$$\omega_I = \omega - \vec{k}\vec{u}\,, \qquad \textbf{(1.5)}$$

where ω is observed wave angular frequency; $\vec{k}$ is horizontal wavenumber vector; $\vec{u}$ is neutral wind velocity. AGWs propagate substantially against the wind to penetrate to ionospheric heights (e. g., [Vadas, 2007]). Hence the scalar product in (1.5) is often negative, and enhancement in absolute value of U will result in increase in ω_I. If ω_I is higher or equal to Brunt – Väisälä frequency, AGWs become evanescent at some height range and can tunnel into the greater heights when the vertical scale of evanescence is smaller than the vertical wavelength. The vertical shears of background neutral wind could be often responsible for observing altitude variations in TID amplitudes.

1.10. Atmosphere and ionosphere models

At present, a number of empirical, theoretical and hybrid models that describe the composition of the ionosphere exist. Their main problem remains the limited applicability due to the lack of data sets over some regions and, as a consequence, inaccuracy in forecasting. The information given by such models often is not presented in real time, as they are obtained by analyzing the acquired data and provide only a climatological description of the ionosphere without taking full account of all processes and irregularities occurring at the ionospheric altitudes. Further, we will briefly escribe some of atmospheric and ionospheric models that are employed for evaluation of TID parameters.

NRLMSISE-00 model is an empirical global reference model of the Earth's atmosphere, which calculates the concentrations of He, O, N_2, O_2, Ar, H, N, total mass density and neutral temperature up to the altitude of 1000 km [Picone et al., 2002]. It uses data from rocket and satellite systems, as well as incoherent scatter radars. Experimental data were obtained during magnetically quiet and disturbed conditions (index $K_p < 8$).

IRI (International Reference Ionosphere) model is an international reference model of the ionosphere, a joint project of the Space Research Committee (COSPAR) and the International Radio Communication Union (URSI) [Bilitza, 2005]. For given geographic coordinates, time, date, solar activity index F10.7 and geomagnetic indices, the IRI model provides average monthly values of electron density, electron temperature, ion temperature and ion composition (O^+, H^+, He^+, N^+, NO^+, $O2^+$ and clusters ions) in the altitude range from 50 km to 2000 km. Also, the model builds a vertical total electron content (TEC).

NeQuick model. Empirically, the NeQuick model is close to the IRI, but has a more accurate shape of the electron density profile in the upper ionosphere, at heights much higher than the peak height. By its construction, it is the median, average monthly. As shown by the authors of the model, the calculation of TEC values is better than for IRI, according to observations [Radicella, 2009]. This has led to the model being used to calculate ionospheric delays in the European Galileo GNSS system.

CHAPTER 2

TECHNIQUES AND FACILITIES FOR DETECTION OF WAVE PROCESSES

This chapter aims at description of variety of techniques employed for studying processes in the lower, middle and upper thermosphere. It gives information about space-borne, global navigation satellite system, and optical techniques. Further, specific techniques for lower ionosphere studying are highlighted. Special attention is paid to radio sounding techniques which are widely used all over the world for detection and estimation of ionosphere process parameters. Some radio facilities and their main characteristics are given. The incoherent scatter technique is described in more detail since it is the versatile one for study of the ionosphere at altitude range from about 100 to 1000 km. The characteristics of several incoherent scatter radars are given with special attention to the radar of Institute of ionosphere (Kharkiv, Ukraine).

2.1. Space-borne techniques

A number of space borne techniques are employed for study of wave processes in the atmosphere and ionosphere. Here we describe some latter-day satellites and satellite missions with onboard facilities to acquire geophysical data.

Arase satellite. It was launched in December 2016 and started regular observations in its full operation mode in March 2017 [Miyoshi et al., 2018]. The Plasma Wave Experiment (PWE)/Onboard Frequency Analyzer (OFA) and High Frequency Analyzer (HFA) instruments onboard the Arase satellite routinely measure the frequency spectrum below 20 kHz and that from 10 kHz to 10 MHz, respectively [Kasahara et al., 2018; Kumamoto et al., 2018]. The ambient plasma density can be derived along the satellite orbit from the frequency of the upper hybrid resonance emissions observed by OFA and HFA and the local cyclotron frequency measured by the magnetometer [Matsuoka et al., 2018].

DMSP satellites. DMSP (Defense Meteorological Satellite Program) is a mission of the United States Air Force that currently consist of four satellites (F15 – F18) flying in circular Sun-synchronous, polar orbits at altitudes between 820 and 860 km [Hairston et al., 2018]. The DMSP spacecraft measure several plasma parameters in the topside ionosphere with the special sensor-ion, electron, scintillation package consisting of the following thermal plasma instruments: Langmuir probe, retarding potential analyzer, scintillation monitor, and ion drift meter [Rich, 1994; Heelis and Hanson, 1998; Brace, 1998]. The electron density, and electron and ion temperatures from all F15 – F18 DMSP satellites are usually applied in studies. Only the data points with good quality flags are used.

Swarm satellites. Swarm is a mission of the European Space Agency primarily intended to study the Earth's magnetic field. The mission has a constellation of three satellites named A, B, and C which were deployed into circular near-polar low Earth orbits at the end of 2013. Swarm A and C orbit side-by-side at the same altitude at ~460 km (inclination 87.4°) and Swarm B flies at an altitude of about 530 km (inclination 88°). All the satellites are equipped with identical instruments. This study used Level 1b 2Hz time resolution data from the Langmuir probes [Knudsen et al., 2017]. The high-quality electron density data from all three Swarm satellites are usually used in studies. Other satellite instruments and models indicated that Swarm typically underestimates the electron density by 10 – 15%. Recent validation studies have reported that the Swarm Langmuir probe electron temperatures can be greatly overestimated. Although a calibration of measured electron temperature was proposed [Lomidze et al., 2018], some problems with the data quality remain including unpredictable jumps along the satellite orbits.

2.2. Global navigation satellite system techniques

At present, global satellite navigation systems (GNSS) have become widespread and used. Their main purpose is to determine the location at any point on the Earth's surface using special navigation or geophysical receivers. The operation principle of GNSS is based on measuring the distance from the antenna on the object, which coordinates must be obtained, to the satellites, which position is known with high accuracy. The table of all satellite positions is called an almanac, which must have any satellite receiver before measurements. Usually, the receiver stores the almanac in memory. Each satellite also transmits the entire almanac in its signal. Thus, knowing the distances to several (at least four) satellites of the system and using the geometric transformations, based on the almanac, one can calculate the position of the object in space and the exact time.

The technique of measuring the distance from the satellite to the receiver antenna is based on the certainty of the radio wave speed. To be able to measure the propagation time of the radio signal, each satellite of the navigation system transmits standard time signals as part of its signal, using a atomic clock precisely synchronized with the system time. During the operation of the satellite receiver, its clock is synchronized with the system time and the subsequent reception of signals calculates the delay between the transmission time contained in the signal and the time of signal reception. Having this information, the navigation receiver calculates the coordinates of the antenna. Additional accumulation and processing of this data over a period of time enables calculation such motion parameters as current, maximum or average speed, traveled distance, etc. [Solov'ev, 2000].

Now, a number of GNSS operate, such as GPS (USA), GLONASS (Russia), Beidou (China) and Gallileo (EU). One of the permanent GNSSs is the NAVSTAR GPS (NAVigation Satellites providing Time And Range; Global Positioning

System), often referred as GPS. The system was developed, implemented and operated by the US Department of Defense. The basis of the system are navigation satellites moving around the Earth in 6 circular orbital trajectories (4 satellites each), at an altitude of approximately 20180 m. The satellites transmit signals in the bands: L1 = 1575.42 MHz and L2 = 1227.60 MHz, the latter models also in L5 = 1176.45 MHz. Navigation information can be received by the antenna (usually in line of sight of satellites) and processed using a GPS receiver. Information in C / A code (standard accuracy) transmitted on the frequency L1 is distributed freely, free of charge, without restrictions on use. Military use (accuracy is an order of magnitude higher) is provided by an encrypted P(Y) code. A total of 24 satellites provide 100% system performance anywhere in the world, but cannot always provide a reliable reception and a good calculation of the position. Therefore, to increase the accuracy of the position and the reserve in case of failure, the total number of satellites in orbit is maintained in greater numbers. The maximum possible number of simultaneously operating satellites in the NAVSTAR system is limited to 37 [Solov'ev, 2000; Xu, 2007].

Another important application of GNSS is remote monitoring of ionospheric plasma. In this case, using the transmission of signals at two frequencies, one can get the value of the total electron content (TEC) along the direction from the receiver to the satellite (slant TEC or STEC). The number of GPS receivers has grown significantly over the last two decades. This allowed the formation of dense networks covering the territories of Western and Northern Europe, the United States, Japan and New Zealand (Fig. 2.1). The presence of such networks enables study not only diurnal, but also shorter-period irregular and wave-like variations of TEC, as well as evaluation their characteristics.

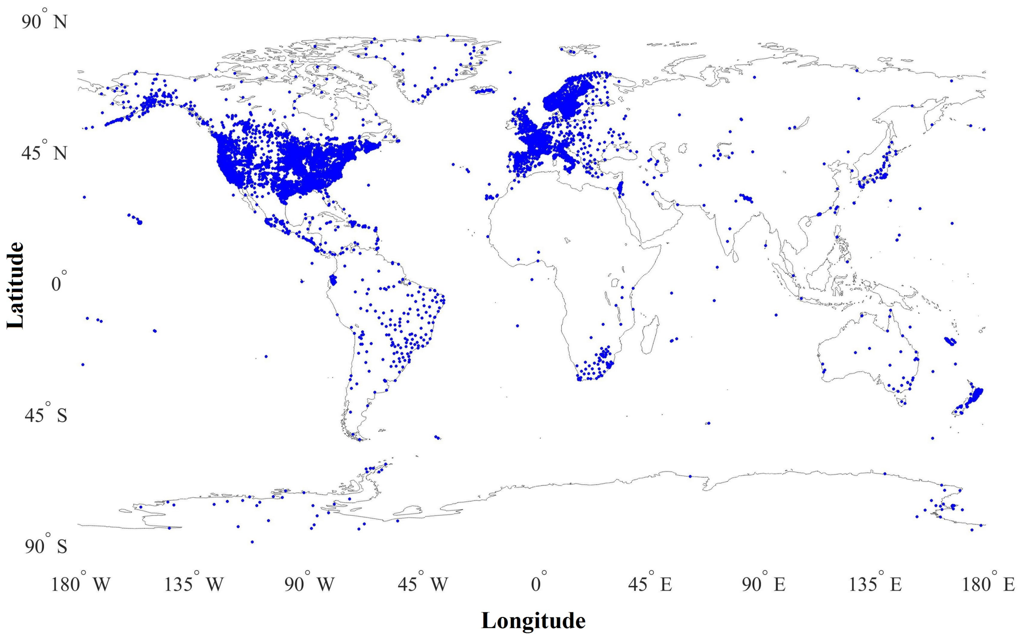

Figure 2.1. Map of GPS receivers producing data for DRAWING TEC database (http://seg-web.nict.go.jp/GPS/DRAWING-TEC/)

Using GPS satellite signals, the STEC value in arbitrary units is calculated using the engineering formula [Mannucci et al., 1999]:

$$\mathrm{STEC} = -\frac{1}{40.308}\frac{f_1^2 f_2^2}{f_1^2 - f_2^2}[(L_1\lambda_1 - L_2\lambda_2) + K + nL], \qquad \textbf{(2.1)}$$

where f_1 and f_2 are operating frequencies; λ_1 and λ_2 are operating wavelengths; L_1 and L_2 are the phase progressions at operating frequencies; K is unknown initial phase value; nL is error in determining the phase path.

The main type of ionospheric data from GNSS technique is global ionospheric maps (GIM) of TEC in the vertical unit area column of the ionosphere [Wilson et al., 1995; Mannucci et al., 1998]. GIM technology is based on the interpolation of TEC measurement data generated at the height of pierce point. The calculations result in global maps of absolute vertical TEC, which enable study the global structure of the ionosphere and large-scale ionospheric processes. The disadvantage of such maps is that the smoothed spatial distribution of TEC and its temporal discontinuity disable conducting research on rapid local processes in the ionosphere.

Let's describe the results of some GPS studies. Based on the use of various GPS techniques, the authors [Yasyukevich et al., 2015] studied the state of the ionosphere during the earthquake on March 11, 2011 over Japan. Intense disturbances of various scales, concentrically diverging from the epicenter, were detected. After the earthquake, the spatial structure of TEC variations moved northwards and existed for almost 2 hours. Three methods were used in the work. The first "distance-time" method is based on the correlation of TEC variations with the onset of ionospheric disturbances and the distance to the source of ionospheric perturbations (earthquake epicenter). The second SADM-GPS method (Statistical Angle-of-arrival and Doppler Method for GPS) is based on the measurement of TEC derivatives by time and space obtained for three specified receiving points. This set of three receivers forms a GPS grid with the minimum required number of elements that allows estimating the speed and propagation direction of ionospheric inhomogeneities. The third method of cluster analysis is used as a technique to combine the objects identified in the initial analysis into groups described by similar parameters. The results showed the following. The method of analysis of "distance-time" diagrams was used to distinguish three modes of earthquake disturbances: fast mode with a speed of 2.2 – 2.6 km/s, medium mode with speeds of 700 - 1000 m/s and slow mode with speeds of 150 – 300 m/s. The SADM GPS method allows distinguishing two modes: large-scale and medium-scale disturbances with an average horizontal velocity of about 635 and 250 m/s, respectively. Both registered types of disturbances propagate radially. The application of cluster analysis methods to the data of the SADM GPS method also allowed detecting the fast mode. The propagation velocities of the observed structures vary from 1.4 to 2.6 km/s, which correspond to the acoustic and fast modes of perturbations detected by the method of analysis of "distance-time" diagrams. Analysis of the appearance of a relatively large number of large-scale wave structures (longer than 500 km and periods greater than 15 min) grouped into clusters showed the presence of a local maximum corresponding to the response of the ionosphere directly to the earthquake.

The presence of large-scale and medium-scale TEC variations formed by the ST movement was proved for the first time using GPS technique over the USA, Japan and Europe [Afraimovich, 2008]. The authors [Afraimovich et al., 2009] investigated the variations of TEC for the period of 1998 – 2008 and reported the morphology of medium-scale wave packets generated by ST. Disturbances were detected to manifest in the form of narrow-band TEC oscillation chains with a duration of about 1 – 2 h, oscillation periods from 15 to 30 min, wavelengths of 100 – 300 km. In winter, medium-scale wave packets were observed mainly 3 hours after the evening ST in the northern hemisphere. During the equinox, medium-scale waves appear after the ST passage almost immediately or with a small lead. In summer, they are registered 2 – 3 hours before the appearance of the evening ST at the observation site.

As a result, the GNSS provide a unique opportunity to obtain the TEC altitude profile in the Earth's ionosphere for different helio- and geophysical conditions. They are available at any time of day and anywhere on the Earth's surface, including oceans and seas, north and south poles.

2.3. Optical techniques

This technique for studying the plasma parameters is based on the atmospheric optical emission under the influence of energetic particles precipitating in the auroral regions during geomagnetic storms. Such emission occurs when electrons in atoms, molecules, and ions fall from excited to lower energy levels. The functions of distribution and density of such particles can be evaluated using measurements of artificial optical emissions at different wavelengths λ (according to different excitation potentials). The following intensive lines and bands are used for research: atomic oxygen emissions λ = 557.7 nm (observed altitudes 85 – 115 km) and λ = 630 nm (120 – 300 km), atmospheric sodium emissions λ = 589.0 – 589.6 nm (80 – 105 km), OH hydroxyl molecule emission (70 – 115 km) and hydrogen emissions at λ = 656.3 nm.

An impact of solar and geomagnetic activities, stratospheric warmings, seismic activity, the propagation of IGWs and TIDs can be traced in the intensity of optical emission. Therefore, this method is effective in studying the physical and chemical properties of the upper atmosphere. Thus, the paper [Shindin et al., 2015] presents the results of the study conducted using the "Sura" heater with interference filters for wavelengths λ = 630 nm (red line) and λ = 557.7 nm (green line). Measurements were performed in the dark under a cloudless sky.

The effective transmission power of the heater ranged from 60 to 100 MW. Moreover, an additional ionization of the ionospheric plasma occurred during such experiments. With a more significant enhancement in transmission power, using such heaters as EISCAT Heater (1200 MW) and HAARP (3600 MW), the formation of additional ionospheric regions occurs [Pedersen et al., 2009]. In [Shiokawa et al., 1999; Otsuka et al., 2002], the authors use wavelengths in the red line of atomic oxygen λ = 630 nm and λ = 777.4 nm and yellow λ = 589.3 nm to receive emission from the night sky over Japan using a Fabry-Perot interferometer. The use of such a device allows evaluating the heating level of the neutral component of the upper atmosphere and the local changes in wind circulation. The results showed the presence of waves of different scale, speed and propagation direction. Two groups of large-scale structures were identified. First structure was observed at altitudes of 96 and 80 km and had horizontal velocity of 160 m/s, horizontal wavelength of 100 km. Second small scale structure had a wavelength of 15 km.

The authors [Afraimovich et al., 2002] studied large-scale TIDs in the mid-latitude ionosphere during a magnetic storm on April 6, 2000 from radiophysical and optical measurements. A good correlation of the data obtained by both methods was noted. The results showed the formation of large-scale waves of a different type with duration of 1 h, a front width of 5000 km and equatorward propagation. The perturbation in the TEC corresponds to an increase in the intensity of emissions in the optical range, demonstrating a time lag at different heights of the ionosphere.

The main disadvantage of this method is the lack of complete information about the composition of neutral particles throughout the atmosphere. Also, the data are available only in the lower layers of the ionosphere, and experiments can be performed only in the dark-time.

2.4. Techniques for the lower ionosphere

At present, a number of direct and indirect techniques are used to study the dynamics of the ionospheric D region and the mesosphere [Kazimirovsky & Kokourov, 1979; Bryunelli & Namgaladze, 1988; Davies, 1990]. Here we give only a brief description of some main techniques for determining the parameters of dynamic processes in this area.

Observation of artificial chemical clouds. Photoluminescent or chemiluminescent traces formed by chemical substances (barium, sodium, etc.) released into the atmosphere are investigated [Kazimirovsky & Kokourov, 1979; Bryunelli & Namgaladze, 1988]. In this case, part of the substance can be ejected in the form of ions, which enables tracing the movement of both neutral and ionized components of the medium. This techniques allows determining the fine structure of dynamic movements, in particular, it provides valuable information on the structure of turbulence at altitudes of 80 – 100 km. Its main disadvantages are the relatively fast diffusive running of the observed trace (within a few minutes) and the limited observation time (clouds are observed from the Earth's surface in the morning or evening hours, when the Sun is below the horizon).

Observation of noctilucent clouds. Specific cloud structures occurring at altitudes of about 80 km are investigated [Kazimirovsky & Kokourov, 1979]. These clouds can be seen at middle and high latitudes. The technique enables determining the parameters of the wind speed vector simultaneously in large latitudinal and longitudinal sectors. However, it has a strong time constraint due to the rarity of such cloud structures.

Tracking the movement of ejected sensors. The technique is based on radar determination of the speed of artificial objects (strips of foil, balloons, etc.) ejected from rockets and moving under the influence of the wind [Kazimirovsky & Kokourov, 1979]. It has a high spatial resolution, since the position of the ejection is tracked experimentally. Its disadvantages include the low maximum observation height (70 – 80 km), as well as limited observation time.

2.5. Remote sensing radio techniques

Remote sensing radio techniques have become widespread for conducting complex studies. This circumstance is associated with the irregular launch and short duration of the flight of geophysical rockets, the lack of flying vehicles at altitudes of 40 – 150 km, as well as the possibility of long-term continuous measurements and the relatively low cost of facilities.

Doppler radio sounding. The technique is based on measuring the Doppler frequency shift of radio signals scattered by large irregularities [Hocking, 1997]. To determine the horizontal components of the wind speed, antennas with narrow radiation patterns (“beams”) oriented at an angle to the vertical and in different horizontal directions are used. This technique enables measuring the vertical component of the velocity using another “beam” oriented to the zenith. However, when determining the horizontal wind speed, it is considered that it has a constant value in the area of the medium with horizontal dimensions of the order of tens of kilometers. In addition, scattering by anisotropic irregularities leads to errors in measuring the horizontal wind speed.

Radio sounding of meteor trails. This technique is based on the scattering of electromagnetic waves by ionized meteor trails [Portnyagin & Shpringer, 1978]. During a lifetime of 10^{-2} – 1 s, the meteor trail moves at a certain distance together with the neutral component of the medium. The speed of movement can be determined experimentally, for example, by measuring the Doppler frequency shift. The main advantage of the technique is the relatively low pulse power (tens of kW) and the relative simplicity of the facility. The technique enables studying dynamic processes in the altitude range of 80 – 100 km. Its disadvantages include the irregularity of the appearance of radio meteors, as well as the lack of information about the reflection height. It is believed that reflections occur at altitudes of 90 – 95 km, where a maximum occurrence of meteor radio echoes takes place.

Partial reflection technique. This technique was proposed by Gardner and Pawsey [Gardner & Pawsey, 1953] and is based on measuring and analyzing the characteristics of radio signals in the medium and high frequency ranges scattered by inhomogeneities of the lower ionosphere (50 – 90 km) [Bryunelli & Namgaladze, 1988]. The main advantage of the technique is the ability to select the reflection (scattering) height, which enables tracing the altitude variation of the wind speed in the lower ionosphere. This technique requires the use of transmitters of high pulse power (tens – hundreds of kilowatts), large antenna systems, highly sensitive receivers, as well as the location of the radar in a place with a low level of external interference.

Oblique reflection of low-frequency radio signals. The technique is based on the registration and analysis of the radio wave characteristics reflected from the lower ionosphere in the frequency range of 30 – 300 kHz [Jacobi et al., 2006]. It is applicable only at night, since during the day radio waves of such range are substantially absorbed in the D-region of the ionosphere. The technique does not allow defining the reflection height. Experiments have shown that the reflection occurs from the lower boundary of the E-region, located at heights of 90 – 95 km.

When dynamic processes in the lower ionosphere and mesosphere are studied, the last two techniques use the method of diversity reception [Hocking, 1997]. Ionospheric irregularities of the D-region, formed due to hydrodynamic turbulence, are modeled in the form of clouds with a different from the background electron density, the horizontal section of which has the shape of an ellipse. Their movement leads to the formation of a complex diffraction pattern of the field near the Earth's surface. The system of spaced receiving antennas registers temporal variations in the parameters of radio signals, which contain information about the parameters of the diffraction pattern moving on the Earth's surface, and hence about the electron density inhomogeneities that generate it, moving at mesospheric heights together with the neutral gas.

Vertical sounding technique. This technique for ionosphere study is based on the receiving radio signals with swinging frequency due to the complete internal reflection of radio waves from the ionosphere [Danilkin, 2008]. Ionograms representing dependencies of time lags on transmitting frequency are analyzed using the international instruction on processing and interpretation of URSI ionograms [Piggott & Rawer, 1972]. This technique can be employed using ionosondes. Such pulse RF sounders allow retrieving the height profiles of the electron density N_e to the height of the main ionization peak. Varieties of the vertical sounding technique are oblique, external, trans-ionospheric and reverse-inclined sounding. For obtaining information about the horizontal distribution of N_e, the size and velocity of inhomogeneities, ionosonde is installed on artificial satellites of the Earth.

Digital ground-based ionosondes are divided into three types. Digisonds are the best in this field, in particular, "DPS-4" [Reinisch et al., 2008]. A distinctive feature is its low power. Due to coherent accumulation, it becomes possible to measure the Doppler frequency shift. Registration of Doppler spectra allows separating signals, which result in measuring a phase difference between the signals that were received on spatially spaced antennas and calculating vertical and azimuthal angles of arrival of radio signals.

This simple technique of ionosphere sounding has certain disadvantages. Namely, observations are made only over the ionosonde. It enables N_e values to F2 peak, as well as using short waves only.

Most Digisonds are integrated into a single global network, the Global Ionospheric Radio Observatory (GIRO, http://giro.uml.edu). Digital ionosondes are installed in more than 80 locations around the globe, with 42 of them providing real-time data [Reinisch & Galkin, 2011]. In [Stepanov et al., 2014], the authors investigated TIDs using four Digisonds located in northeastern Russia. One of the manifestations of such disturbances on ionograms is U - traces that are difficult to detect during magnetically disturbed conditions. The analysis was performed in 2005 during the declining phase of the 23rd solar cycle and in 2011 during the rising phase of 24th solar cycle. The most disturbances (about 85%) turned out to register when $K_p \leq 3$. A sharp increase in U-traces was observed in 2011, compared to 2005, which may be due to this year having more geomagnetically quiet conditions. The average phase velocities of TIDs were about 200 m/s; the periods varied from 50 to 100 min; the horizontal wavelengths were 300 - 400 km.

Incoherent scatter technique. This technique has the most complete diagnostic capabilities in the study of the ionosphere and the ionospheric processes. It enables determining the electron density, ion and electron temperatures, plasma drift velocity, ion composition and other parameters with high accuracy and in a wide altitude range [Evans, 1969]. This technique for studying the Earth's ionosphere was firstly proposed by Prof. William E. Gordon in 1958. It is based on determining the signal power and its correlation functions or spectra. At a given distance, the power of the IS signal is proportional to the electron density in the scattering volume. Observations using the IS technique are carried out using a number of powerful radar facilities. Since the first experiments in the 1960s, the IS technique has improved significantly in technical, theoretical and methodological aspects.

The essence of the IS technique is that a sufficiently powerful (about 1 MW per pulse) radio wave, which length λ_0 significantly exceeds the value of the Debye for the ionospheric plasma D, is scattered by thermal fluctuations in the electron density [Bryunelli & Namgaladze, 1988]. In this case, the spectrum of the scattered signal is described by the expression [Dougherty & Farley, 1963]:

$$S(\theta)=\frac{Nr_e^2}{\Omega_0}\frac{|y_e|^2\sum_n \eta_n \operatorname{Re}(y_{i,n})+\left|\sum_n \mu_n y_{i,n}+j\gamma^2\right|^2 \operatorname{Re}(y_e)}{\left|y_e+\sum_n \mu_n y_{i,n}+j\gamma^2\right|^2}\frac{1}{\pi\theta}. \qquad \textbf{(2.2)}$$

Here r_e is classical electron radius; $\theta = \omega / \Omega_0$, where ω is angular frequency; $y_e(\theta_e) = j[1 - \theta_e G(\theta_e)]$ and $y_i(\theta_i) = j[1 - \theta_i G(\theta_i)]$ are the conductivity functions of electrons and ions, respectively, in the absence of ion-neutral collisions when the angle between the wave vector and the magnetic field is equal to zero;

$$\theta_e = \omega / \Omega_e ; \; \theta_i = \omega / \Omega_i ; \; \Omega_e = \frac{4\pi}{\lambda_0}\sqrt{\frac{2\kappa T_e}{m_e}} ; \quad \Omega_i = \frac{4\pi}{\lambda_0}\sqrt{\frac{2\kappa T_i}{m_e}} ;$$

κ is Boltzman constant; m_e and m_i are electron mass and specific type ion mass, respectively;

$$G(\theta) = j\sqrt{\pi}\exp(-\theta^2) + 2F(\theta) ; \; F(\theta) == \exp(-\theta^2)\int_0^{\theta}\exp(t^2)dt ; \; \gamma = \frac{4\pi D}{\lambda_0} ;$$

D is Debye radius; $\eta_n = N_n / N_e$; N_n is density of n-type ions; $\mu_n = \eta_n \beta$; $\beta = T_e / T_i$.

The frequency Ω_0, to which the angular frequency is normalized, is selected to be equal to one of the frequencies Ω_i in the presence of ions with different masses. For instance, Ω_i corresponding to the ion with the lowest mass, the mass of atomic hydrogen H^+ ion, can be selected as Ω_0.

Using the Wiener – Khinchin transformation, the autocorrelation function (ACF) of the IS signal $R(\tau)$ can be estimated for an arbitrary lag value τ from the spectrum calculated according to expression (2.2):

$$R(\tau) = \int_0^{\infty} S(\theta)\cos(\theta\Omega_0\tau)d\theta . \qquad \textbf{(2.3)}$$

Expressions (2.2) and (2.3) show that the spectrum and ACF of the IS signal depend in a complex way not only on the temperatures of charged particles, but also on the values of the relative concentrations of ions of various types. Thus, the IS technique enables evaluating the characteristics of the ion composition of the ionospheric plasma from the measured spectrum (or ACF) of the IS signal.

2.6. Radars for ionosphere sounding

Here we briefly describe the main characteristics of a number of radars.

2.6.1. Meteor trail radars

These radars typically operate at frequencies between 30 and 40 MHz. The lower limit is due to the interfering influence of reflections from ionospheric irregularities. The upper limit is associated with a decrease in the power of radio signals reflected from meteor trails with an increase in frequency. The pulse power of such radars is 30 – 80 kW. When measuring wind speed, antennas of the "wave channel" type with directivity factors of 15 – 20 are usually used. We will give the main characteristics of some radars located in mid-latitudes.

Radar of the Institute of Experimental Meteorology (Obninsk, Russia, 55°N, 38°E) has a pulsed operating mode [Portnyagin & Shpringer, 1978; Portnyagin et al., 2006]. Its operating frequency is 33.3 MHz; pulse power is 40 kW; pulse repetition rate and duration are 500 Hz and 30 μs, respectively. Four transmitting and four receiving antennas are directed to the north, east, south and west. Almost continuous measurements of wind parameters in the mesosphere have been carried out since 1964.

Radar of the Sheffield University (Department of Physics, University of Sheffild, England, 53°N, 1°W) [Portnyagin & Shpringer, 1978; Middleton et al., 2002]. The operating frequency of the radar is 28.4 MHz. The pulse power is 20 kW, the pulse repetition rate is 500 Hz, and the pulse duration is 20 μs. Using the radar, starting from 1988, almost continuous measurements of the parameters of dynamic processes are carried out. Receiving and transmitting antennas are usually directed to the northwest and northeast, which allows one to study both components (zonal and meridional) of the horizontal wind speed.

Radar of the National University of Radio Electronics (Kharkiv, Ukraine, 50°N, 36°E) [Portnyagin & Shpringer, 1978]. The operating frequency of the radar is 36.9 MHz. The radar operated in a pulsed mode: a pulse power of 100 kW, a pulse repetition rate of 500 Hz, and pulse duration of 10 μs. Measurements have been carried out since the 1960s. Since the late 1990s, studies of the ionosphere using this radar are not carried out.

2.6.2. Radars of oblique reflections of low-frequency radio waves

The radio system used for obtaining a continuous long data array of dynamic process parameters is located at the Collm observatory (Germany, 52°N, 15°E) [Portnyagin & Shpringer, 1978; Jacoby et al., 2006]. The measurements record radio waves reflected from the ionosphere at frequencies of 177, 225 and 270 kHz. They are emitted by three commercial radio stations located at a distance of 170 to 460 km. Reception is carried out on a vertical loop antenna, which provides almost complete suppression of the earth wave. The receiving antennas are located at the vertices of a triangle with a side of 300 m. The measurements have been carried out at night since 1959.

2.6.3. Partial reflection radars

Such radars are located in North America (Poker Flat, 65°N; Saskatoon, 52°N; London, 43°N; Urbana, 40°N; Platteville, 40°N), the Pacific Ocean (Hawaii, 22°N;

Christmas Island, 2°N), Europe (Tromsø, 70°N) and Asia (Wakkanai, 45°N; Yamagawa, 31°N; Wuhan, 30°N). They also are in the southern hemisphere (Davis, 69°S; Rothera, 67°S; Buckland Park, 34°S; Rarotonga, 21°S). The operating frequency of the radars is close to 2 MHz. Receiving antennas are usually located at the vertices of a triangle and are an array of crossed half-wave vibrators. Here we describe the characteristics of several radars.

Radar of the University of Saskatoon (Canada) [Manson et al., 1999, 2002]. Its operating frequency is 2.219 MHz. The radar allows studying dynamic processes at heights of 49 – 142 km with a height resolution of 3 km. Three receiving antennas are located at the vertices of an equilateral triangle with a side of 270 m. The fourth receiving antenna is located at the intersection of the triangle heights. The distance from it to the other three antennas is 156 m. Continuous measurements (data gaps do not exceed several days) using this radar have been carried out since 1979.

The *radar of the University of Adelaide* (Buckland Park, Australia) operates at a frequency of 1.98 MHz [Holdsworth et al., 2001]. Pulse power varies from 25 to 87.5 kW. The receiving antennas are an array of 89 crossed half-wave vibrators located at a distance of 91.4 m from each other and forming a circle with a diameter of 914 m. The radar allows measurements at 25 heights, starting from 50 km in the daytime and at 15 heights starting from 70 km, at night, with a height resolution of 2 km. The observations have been conducted since May 1996.

Radar of Wuhan University (China) was launched at the end of 2000 [Zhang et al., 2004]. Its operating frequency is 2 MHz. The impulse power of the transmission system is 25 kW. Receiving antennas are located at the corners of an equilateral triangle with a side of 185 m. Measurements are carried out at altitudes of 60 – 98 km with an altitude resolution of 2 km.

MF radar of V.N. Karazin Kharkiv National University (Kharkiv, Ukraine). The radar enables study processes in the D-region of the ionosphere using partial reflection technique [Garmash et al., 1999]. The main parameters of the radar are as follows: operating frequency f_0 = 2.2 – 2.3 MHz; pulse repetition rate F_p = 1 – 100 Hz; bandwidth of the radio receiver Δf = 60 kHz; pulse power of the radio transmitter P = 100 kW; antenna gain $G \approx 100$; height resolution Δz = 3 km; the range of the studied altitudes z = 60 – 123 km. The radar operates in two modes.

1. Antenna system I is used to study dynamic processes in the mesosphere and lower thermosphere by the diversity reception method with a small base (110 - 160 m) (Fig. 2.2). The transmitting antenna is a system of four vertical double rhombic antennas and has a cruciform shape (Fig. 2.2,a). Each of the four receiving antennas also consists of Eisenberg antennas and has an angled shape shown in Fig. 2.2,b. The general view of the antenna field is shown in Fig. 2.2,c. The phase centers of the receiving antennas are located at the corners of a square, the side of which is 112 m and the diagonal is 158 m. The phase center of the transmitting antenna is at its center. The pulse repetition rate in these experiments is 24 - 25 Hz.

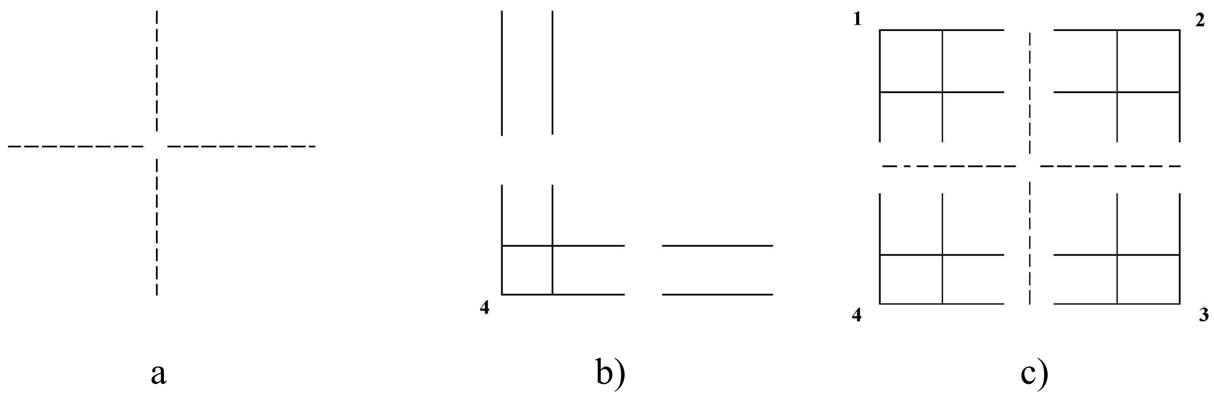

Figure 2.2. Scheme of the receiving and transmitting antenna system I: a – transmitting antenna; b – receiving antenna; c – general view of the antenna field; 1 – 4 are numbers of receiving antennas; solid and dashed lines mark vertical double rhombic Eisenberg antennas.

2. Antenna system II is used to determine the electron density profile in the D-region. The antenna (Fig.2.2, a) is used as a receiving one, and the remaining antenna field (shown by straight lines on Fig. 2.2,c) is used as transmitting antennas.

At the moments of time preceding the transmission of the sounding pulse, several values of the envelopes of the ordinary and extraordinary noise components are recorded, which enables estimating the signal-to-noise ratio for each of the antennas.

2.6.4. SuperDARN HF radars

One more effective ground-based facilities for ionosphere diagnostic are the SuperDARN (Super Dual Auroral Radar Network) radars. It is a system of coherent RF radars located in the auroral regions of the Earth (http://superdarn.jhuapl.edu) [Chisham et al., 2007]. Currently, twenty one radars in the northern hemisphere and eleven radars in the southern hemisphere are operated. The antenna pattern of single radar is phased in 16 azimuthal directions (beams). The beam width in the azimuthal plane is 3.24°. Sounding is carried out at a fixed frequency. Time delay on each beam is about 1 min. The observation sector of each SuperDARN radar is 52°.

The main information retrieving using such facilities is a signal in the form of a coherent echo. At the same time, almost constantly, there is a signal from the back-sloping sounding, which is scattered back. It is used to diagnose medium-scale and large-scale TIDs. In [Oynats et al., 2012], the authors investigated the meteorological effects in the ionosphere using the radar located on Hokkaido, Japan, during tropical cyclones in the Pacific Ocean. The results showed the simultaneous existence of several ionospheric inhomogeneities of different scales. Two main groups of disturbances were identified for September 13, 2008. The first group included inhomogeneities with a period of about 2 h. They had northward propagation direction; the velocity was about 200 m/s. The second group had a period of about 1 h, the northeastward propagation; the velocity was of 100 m/s. On September 24, 2008, in addition to large periods of 1 and 2 hours, shorter-period variations of about 30 minutes were detected. The propagation was northwards; the velocity was of 100 m/s. For September 18, 2009, TIDs with periods of 45 minutes, southeastward propagation, and the velocity of 100 – 200 m/s were detected. In general, the comparison of TID parameters and theoretical estimates of IGW characteristics originated during typhoons and super typhoons showed good consistency. Other authors [Kutelev & Berngardt, 2014] using radar located at the Arti Observatory, Russia, studied ionospheric disturbances during the fall of the Chelyabinsk meteorite. The radial distribution of two inhomogeneities was revealed. The first structure had a velocity of about 500 m/s and a horizontal spatial scale of 150 km; the second structure had the velocity of 220 m/s and the scale of 100 – 150 km. The amplitude was at least 15 %. Such data were confirmed in observations by other SuperDARN facilities and GPS networks.

The main disadvantage of RF radars is the instability of the communication channel due to changes in the ionosphere.

2.6.5. Ionosondes

More than a hundred active ionosondes and vertical sounding stations are operated in the world, located on all continents. Here we briefly describe some of them.

Dynasonde is located near Tromsø (Norway) [Rietveld et al., 2008]. It is one of six digital ionosondes designed and developed at the Laboratory of the Space Environment (Boulder, USA) during 1975 – 1978. For standard sounding, it transmits Gaussian-shaped radio pulses with half-power duration of about 128 μs. The peak power is 10 kW. Two receivers are used with multiplexers at the inputs in such way, that different pairs of six receiving antennas can be connected during the reception of each pulse. The bandwidth of the receiver is 30 kHz.

The transmitting antenna of the Dynasonde was put into operation in 1980 and is a four-mast two-plane logperiodic antenna with a logperiodicity factor τ = 0.92. The gain of this antenna is calculated by the formula: $G(\theta) = 6\cos^{1.5}(\theta)$ dB for frequencies greater than 1 MHz, where θ is the zenith angle of transmission. The receiving antenna is a square array of six long dipoles. The diagonal dimension of the square is 141 m. Each dipole consists of two aluminum tubes having 11 m in length and 15 cm in diameter, located at a height of 2 m above the Earth's surface.

Dynasonde equipment (transmitter, receiver and antenna) has been improved in several stages since its launch in 1980, and software and data processing have been constantly improved. Currently, ionosonde data are presented in real time using more detailed analysis, which has led to a significant improvement in the detail of the results. Since the beginning of 2012, the ionosonde has been operating in a 2-minute mode for more detailed measurements of ionosphere parameters. In 2002, a stand-alone DSND real-time data analysis system was installed. It allows obtaining a greater variety of ionospheric parameters, including altitude profiles of electron density, plasma transport rate, critical frequencies of E- and F-regions, etc. [Rietveld et al., 2008]. Ionosonde data are freely available (http://dynserv.eiscat.uit.no).

The *IPS-42 ionosonde* is located at Academic Vernadsky station (Ukraine) on Galindez Island (65°15' S, 64°15' W) and is a unique research facility developed and manufactured in Australia [Broom, 1984]. The pulse transmitted power is 5 kW; the pulse duration is ~ 40 μs. The frequency range in which the radio sounding is performed is 1.0 – 22.6 MHz. The frequency varies exponentially in the way that the entire sounding range consists of 576 fixed frequencies. The interval of virtual heights is 0 - 800 km. The IPS-42 ionosonde antenna system consists of receiving and transmitting LF and HF antennas. The sounding results are presented in the form of ionograms, showing the virtual heights of the received signals depending on the sounding frequency. Ionogram registration rate is one ionogram every 15 minutes. Ionogram processing is performed according to the standard URSI method.

A *small portable Digisonde Portable Sounder (DPS)* is used in the Millstone Hill Observatory (42°36' N, 71°30' W). It transmits 500-microsecond ("wide") pulses for vertical sounding and 8.5-microsecond ("narrow") pulses for oblique sounding. The use of intra-pulse coding and pulse compression results in a resolution of 67 μs for both signals. The application of the auto-scaling technique for oblique ionograms allows obtaining altitude profiles of electron density using the model of quasi-parabolic layers. A detailed description of this ionosonde is given in [Reinish et al., 1992].

Ionosonde of the radio physical observatory of V. N. Karazin Kharkiv national university consists of a modified broadband radio transmitter "Brig-2", radio receiver IC-R75, synthesizer of direct digital synthesis for the formation of transmitted radio pulses having specific frequency and duration, as well as a microcontroller that performs the digitization of the radio signal and maintains communication with an external personal computer (PC).

Sounding radio pulses having duration of 100 μs, pulse repetition rate of 125 Hz, swinging frequency in the range of 1 – 16 MHz and pulse power of up to 1.5 kW are transmitted by a broadband radio frequency amplifier of the transmitter.

The IC-R75 radio receiver is made according to the superheterodyne scheme with triple frequency conversion. The widest bandwidth is 15 kHz, which is enough to work with radio pulses of the specified duration. The input circuits of the receiver are designed for operating conditions near the transmitters, i.e. have a sufficient dynamic range and overload protection circuits. For remote control of the receiver, it provides a serial interface in the RS232 standard and a communication protocol with an advanced set of commands. The upgrade of the receiver constituted installing additional connectors. The output of the 3rd intermediate frequency amplifier is connected to one of the connectors and then this signal is fed to the amplitude detector in the microcontroller. Through the second connector, a locking pulse is applied to the internal circuits to reduce the pulse interference for the transmission time of the sounding radio pulse (blanking signal). The received high-frequency signal is fed to the antenna input of the receiver through the antenna key, which is also locked at the time of pulse transmission.

The synthesizer is developed on a modern integrated circuit base. It allows synthesizing a signal with a frequency of up to 25 MHz. It has a switching time from frequency to frequency less than 1 μs and is able to generate radio pulses of certain duration. A 24-bit communication bus is used to set the generation frequency and mode of synthesizer operation, through which 24-bit control words are transmitted from the microcontroller. To generate RF radio pulses of the specific duration, the synthesizer also receives a corresponding strobe. The exchange of information between the microcontroller and the external PC is done via a standard USB bus.

The ionosonde uses vertical broadband rhombic Eisenberg antennas to transmit and receive radio waves. The height of the antenna lifting bar is 18 m, and their horizontal size reaches 50 m.

Ionosonde at the Ionospheric observatory, Institute of ionosphere (Ukraine). A portable coherent ionosonde for ionospheric plasma diagnostics was developed at the Institute of Radio Astronomy of the National Academy of Sciences of Ukraine (IRA NAS) [Zalizovski et al., 2018]. The developed facility allows carrying out ionospheric diagnostics in a continuous mode and does not demand considerable financial expenses. During the ionosonde prototype creation, original methods of frequency-angular sounding, multi-position ionosphere Doppler sounding and frequency-time selection, which were previously developed in IRA NAS, were used to expand its diagnostic capabilities.

The main purpose of the developed coherent ionosonde is to measure the frequency response of the ionosphere for calculating the electron density profile. In addition, it allows measuring the vertical velocity component of the area where sounding signal reflects at different frequencies in a wide range of altitudes. The principle of construction of the ionosonde is based on the ideas laid down in the design of similar modern devices, in particular the DPS-4 digisonde, as well as on the use of SDR (Software Defined Radio) technology for ionospheric sounding. The main difference between this facility and the previously developed analogues is the use of a relatively low power communication transmitter. The signal-to-noise ratio at the output of the facility and the altitude resolution sufficient for measurements are provided through the use of long phase-manipulated sounding pulses, their subsequent digital convolution with reference code sequences and Doppler filtering sounding frequency. Signal processing and analysis functions are performed using a PC.

The analog part of the facility is significantly simplified by using standard low-power communication transmitter and program radio (SDR) with a wide bandwidth. The use of such serial instruments has significantly reduced the cost of the created prototype of the ionosonde.

Functionally, the ionosonde consists of a control computer, software radio USRP N200 KIT (Universal Software Radio Peripheral, https://www.ettus.com/product/details/UN200-KIT), antenna switch ZX80-DR230 (https: // ww2.minicircuits.com/pdfs/ZX80-DR230+.pdf) and transceiver ICOM-IC-718 with power supply SP-200-13.5.

The installation is made as follows. In the control PC at each sounding frequency, test pulses are formed, consisting of a sequence of phase-shift keyed sub-pulses ("chirps"). Complementary codes are used to generate sub-pulses, which provide the required height resolution corresponding to the length of one sub-pulse. This encoding improves the signal-to-noise ratio in proportion to the number of sub-pulses ("bit") of the code. In the USRP program radio using a digital-to-analog converter, this sequence is converted into an analog signal, amplified to the desired level on the TX board and, after amplification by the ICOM transceiver, is fed to the transmitting antenna. The signal reflected from the ionosphere is fed to the receiving antenna and from it to the RX receiving board of the USRP device, where it is amplified to the level of the ADC input voltages. After digitization, the received signal enters the PC, which performs the functions of program radio control, signal generation and processing, display and data collection, storage and analysis.

For performing soundings, two antennas are required: receiving and transmitting ones. In practice, antennas of different types with a frequency band of 1.6 – 30 MHz are used. For the transmitting antenna, the allowable input power must be greater than 100 W, and the standing wave ratio in the antenna-feeder path must not exceed 2.5. The parameters of the mode for obtaining the ionogram can vary widely and are selected depending on external conditions and the task.

2.6.6. Incoherent scatter radars

Incoherent scatter (IS) radars operate at high frequencies that significantly exceed the natural frequencies of the ionosphere. Currently, only 8 such type radars are operating in the world. Namely, two observatories are located in Northern Europe (Tromsø, Svalbard) and one each is located in the USA (Millstone Hill), Peru (Jicamarca), Greenland (Sondrestorm), Japan (Kyoto), Russia (Irkutsk) and Ukraine (Kharkiv). Unlike the ionosonde, the IS radar measures the characteristics of the ionosphere not only below the electron density peak, but also above. The radars are unique because they all have different types of construction, use different operating frequencies and are located in different geographical coordinates.

Since the power of the IS signal is many orders of magnitude lower than the power of the sounding signal transmitted into the ionosphere, all operating IS radars use powerful (several megawatts per pulse) sounding signals and antennas with a large effective surface [Evans, 1969]. However, especially high requirements for the energy potential of the IS radar are imposed precisely during measurements in the topside ionosphere. The power of the scattered signal decreases with increasing height in inverse proportion to the square of the transmitted power. An additional significant decrease in the power of the IS signal occurs due to a decrease in the electron density above the ionization peak of the ionosphere. These circumstances limit the possibilities of carrying out measurements above a certain limiting altitude, for which the signal-to-noise ratio becomes less than a value that enables obtaining reliable estimates of plasma parameters.

The length of the radio wave used for sounding the ionosphere is also important. Expression (2.1) shows that the Debye radius increases with a decrease in the electron density and an increase in the electron temperature, which is typical for the outer ionosphere. When λ_0 is insufficiently large, this radius can become comparable to the length of the transmitted radio wave. As a result, when solving the inverse radiophysical problem, it becomes necessary to additionally take into account the electron density as one of the parameters affecting the form of the ACF of the IS signal. This significantly complicates the calculations and reduces the reliability of the obtained estimates of the plasma parameters.

Here we describe some of the radars.

The *EISCAT radar system* is a multi-element facility developed and used mainly for studies of the Earth's ionosphere [Rishbeth & Williams, 1985]. Incoherent scatter radars use two types of transceiver equipment: monostatic and multistatic. Monostatic radars use the same antenna for reception and transmission. Multistatic radars use spaced transmitting and receiving antennas.

The UHF radar, located on the mainland, is a three-static system with antennas located in Kiruna (Sweden), Tromsø (Norway) and Sodankylä (Finland). The antenna in Tromsø is receiving and transmitting, while it is only receiving one in other places. The fourth UHF antenna is located near Longyearbyen (Svalbard archipelago) and is a part of the EISCAT Svalbard radar (ESR). All of these antennas are full-rotation circular paraboloids with a diameter of 32 m. The antenna near Tromsø operates at a frequency of 928 MHz, and the other two mainland antennas operate at a frequency of 1420 MHz. The operating frequency of the ESR antennas is 500 MHz.

In ionospheric studies, the radar near Tromsø is used to irradiate a certain volume of ionospheric plasma with UHF radiation. Some of these radio waves are returned and received by all four antennas. It is possible to measure The parameters of the ionosphere, such as the electron density, ion and electron temperature, are measured.

EISCAT transmitters have been designed to transmit powerful pulses and flexibly change their filling. UHF transmitter running on one klystron transmits a peak power of 2 MW, while one running on two klystrons transmits 5 MW. In transmitters, the frequency can vary by 1 μs. Therefore, this change rate is the main achievement of the EISCAT system, which allows transmitting different pulse sequences during one cycle of transmission. Each of the transmitters can operate on 16 different frequencies. This speed allows transmitting both simple and encoded pulses, including using Barker codes.

The EISCAT system uses supersensitive receivers with very low internal noise. The noise temperature of the system is 40 – 100 K for different radars. Parametric amplifiers are cooled by liquid helium. ADCs operate at a maximum frequency of 500 kHz for one channel, for all channels the frequency is 2 MHz.

Shigaraki Middle and Upper Atmosphere (MU) radar (34.9°N, 136.1°E) is located at Shigaraki MU observatory, Shigaraki, Japan and operated at a frequency of 46.5 MHz [Fukao et al., 1985a,b; Hassenpflug et al., 2008]. It is a fully active phased array system which employs up to four independent beams and realizes sequential sensing toward the magnetic north, east, south and west. Standard incoherent scatter modes are usually used for ionospheric parameter retrieving, in particular, the electron density, drift velocity as well as ion and electron temperatures.

Millstone Hill IS radar facility (42.6° N, 288.5° E) is located in Westford, MA, USA. It consists of zenith-directed 68-m fixed and fully steerable 46-m antennas and transmitters with operating frequency 440 MHz and the peak transmitted power 2.5 MW [Holt et al., 2002]. Electron density is calibrated using UMass Lowell Digisonde or plasma line observations (for new experiments). Data from Millstone Hill IS radar are publicly available through the Madrigal Database (http://madrigal. haystack.mit.edu/madrigal/).

The width of the antenna pattern is approximately 0.44°. Radar is able to measure a number of parameters of the ionosphere, including temperature, ion concentration. Different modes of radar operation are used for observations, which provide different altitude resolutions. Pulse duration of 480 μs or a variable code scheme provides a resolution of 72 km or 4.5 km, respectively. The use of a longer pulse (640 μs) provides a good signal-to-noise ratio, but also a significant spatial convolution, which distorts the detailed picture due to poor altitude resolution.

Kharkiv incoherent scatter radar of Institute of ionosphere (49.6°N, 36.3°E) is located in the north-east of Ukraine. The main radar characteristics, operating modes and software suites for data analysis are described in [Domnin et al., 2014; Bogomaz et al., 2017] as well as presented on the website (http://iion.org.ua).

The radar operated in composite two-frequency radio pulse mode. The first simple pulse has a length of about 650 μs (the carrier frequency f_0 = 158 MHz), providing an altitude resolution of about 100 km, while the second simple one has the pulse length of about 135 μs (the frequency f_1 = (158 + 0.1) MHz) and yields the 20-km altitude resolution. As a result of receiving and processing of the first signal element scattered by the ionosphere, the electron density, the electron and ion temperatures, the vertical component of the plasma velocity, and the ion composition are measured for the altitudes near the peak of the ionospheric F2 layer and in the upper ionosphere (200 – 1000 km). Return signal from the second pulse element allows to determine the altitude profile of the IS signal power at the altitudes h = 100 – 550 km for correction of the altitude electron density profile and estimation of such vertical propagation characteristics of traveling ionospheric disturbances (TIDs) as vertical phase velocity and wavelength.

One of the world's largest antennas is used for transmitting and receiving. A two-mirror parabolic antenna aimed at the zenith has a diameter of 100 m and is made according to the Cassegrain scheme. The width of the pattern is 1°. Effective antenna area is about 3700 m^2. The antenna allows transmitting and receiving radio waves of circular and linear polarization. This is due to the presence of two orthogonal vibrators. The connection between the radio receiving and radio transmitting devices in each of the two channels of the waveguide feeder path is carried out by means of antenna switches of the waveguide-slit type, which are made on gas-filled arresters.

The transmitter consists of two channels of powerful amplifiers that work with external excitation from a common setting device. The pulse power of each channel does not exceed 1.5 MW. To transmit signals with linear or circular polarization, a certain phase shift is established between the signals of the two channels.

The radio receiver is a multi-channel instrument with triple frequency conversion. At its input, a system for selecting the polarization of the receiving signal and low-noise transistor amplifier, which provides sufficient for a meter wavelength sensitivity of the radio receiver (effective noise temperature of the receiver is 120 K, with a noise temperature of 470 – 980 K), are employed.

The bandwidth of the radio low-pass filter is 5.5 – 9.5 kHz. At the output of the radio receiver, for correlation processing, several pairs of quadrature signals obtained by synchronous detection and low-pass filtering is used. To ensure coherence operation of IS radar systems, signals of the heterodyns are formed from the signals of the setting system. It enabled registering Doppler frequency shifts, which are very small relative to the width of the IS signal spectrum, to determine the vertical velocity of the plasma.

A specialized measuring and computing system is used to process the quadrature signals of the receiver at low frequency. It consists of two two-channel correlometers, a four-channel correlometer and several PCs connected by a local area network. Each two-channel correlometer includes a two-processor module, two ten-bit ADCs and a synchronizer. The correlometer allows real-time calculating the complex correlation function of the IS signal, which determines all ionospheric parameters in a wide range of altitudes (200 – 1000 km).

A new hardware and software subsystem for receiving, recording and processing IS signals has been developed. It is designed to operate with signals both on video and intermediate frequency. The practical implementation of the operation mode on the video frequency is simpler, as it does not require refinement of existing radio equipment. The ADC E20-10 module is used for digitization of signals, and appropriate software was created for signal recording and processing.

The method of recording the instantaneous values of the signal directly at the output of the final intermediate frequency amplifier further eliminates the disadvantages inherent to analog circuits. This approach opens the possibility of processing the IS signal at an intermediate frequency in the matched frequency band, taking into account the characteristics of the plasma at different heights. The use of the resulting arrays allows alternative processing options employing high-performance PCs. This can be, in particular, correlation or spectral processing with optimized (for each specific altitude range and state of the ionosphere) parameters.

Kharkiv incoherent scatter radar is the only radar in the world that allows studying the topside ionosphere and its ion composition in mid-latitudes.

CHAPTER 3

METHODS FOR CHARACTERIZATION OF TRAVELING IONOSPHERIC DISTURBANCES

Here we report the different methods aiming at analysis of incoherent scatter data to retrieve absolute and relative variations in IS power and plasma temperatures and estimate the parameters of traveling ionospheric disturbances. The main stages of IS data processing are given starting from filtering data series from noise and interferences, hardware failures and ending by TID propagation parameter estimation. Specific attention was paid to possibility of using temporal dependences of IS power instead those of electron density in many cases. We also consider the method of TID parameter estimation using dense GPS receiver network. GNSS technique is complementary to IS one and enable obtaining more robust information on the horizontal wave properties of the TIDs.

3.1. Filtering of intermittent interferences and hardware failures

The temporal variations in IS signal power are influenced by noises of various nature, irregular interference and instrument failures, which significantly distort the retrieved parameters of the ionospheric plasma. Neglecting of their influence leads to significant errors during this disturbance parameter estimation, as well as to the appearance of false aperiodic and periodic signal variations. Therefore, the problem of reconstructing the time dependences of the IS signal power distorted by interference is relevant.

Radio noise constantly occurs in the propagation channel and is a mixture of receiver noise, as well as space, atmospheric, industrial noise and noise caused by the operation of a large number of radio stations [Chernogor, 2009]. Such noise can often be considered as Gaussian and uncorrelated with the IS signal. The subtraction of the noise power from the noise and IS signal mixture is used.

During the analysis and processing of experimental data, the following types of irregular interference and instrument failures were identified.

1. *A sharp jump in the signal level* occurs when the gain changes or one of the elements of the transmitting-receiving system fails. This “interference” can be modeled as a near-rectangular pulse.

2. *External impulse noise* often occurs during a thunderstorm or is associated with the reception of signals from nearby powerful radio stations. They manifest themselves in the form of a prolonged (about 10 – 60 min) increase in the received signal level.

3. *Coherent reflections* are associated with the reflection of the transmitted signal from spacecraft or fragments of space debris. They represent short-term (less than a minute) bursts or spikes of the received signal power.

For solving the filtration problem, algorithms were developed that were implemented in a computer program. They allow adjusting the signal level and filter out interference based on statistical methods of time series analysis [Anderson & Finn, 2012].

For eliminating a sharp jump in the signal level, it is proposed to determine the average value of the power inside and outside the jump, and then calculate the correction factor k. The correction results are shown in Fig. 3.1,a. This figure shows the time interval corresponding to the failure of one of the transmitters of the Kharkiv IS radar and, consequently, to a decrease in the power of the transmitted radio signal by half (from 1.8 to 0.9 MW).

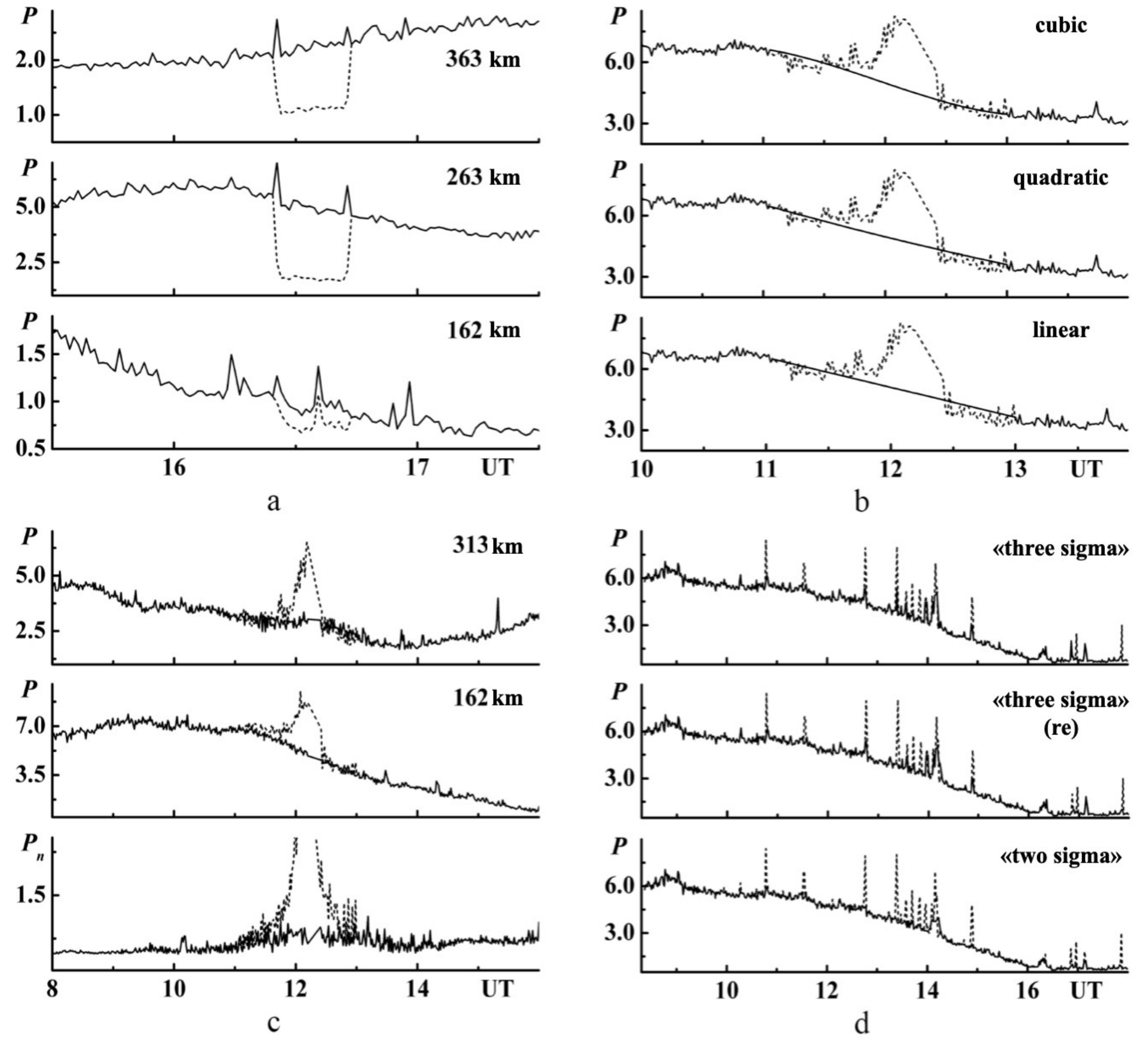

Figure 3.1. Original (dashed line) and filtered (solid line) temporal dependences of the IS signal with noise mixture P and noise P_n: a – elimination of a sharp change in the signal level at different heights; b – cubic, quadratic and linear signal approximation; c – cubic approximation and addition of Gaussian noise; d – filtering coherent reflections using two sigma and three sigma criteria.

Analysis of the data showed that the correction factor in the general case depends on the height (see Fig. 3.1,a). Its values for a number of heights are given in the Table 3.1. The table shows that the value of k initially increases, reaches a maximum at altitudes of 250 – 260 km, and then decreases. This behavior is due to the fact that the Faraday effect prevails in the altitude range of 170 – 400 km, which is known to be in the rotation of the plane of polarization of the radio signal when it passes through a magnetoactive medium (ionospheric plasma), and the noise power noise exceeds the IS signal power at lower and higher altitudes in the evening and at night (the signal-to-noise ratio becomes less than unity).

Table 3.1. Dependence of the correction factor k on the height h for eliminating a sharp change in the signal power level.

h (km)	162	212	263	313	363	413
k	1.28	2.32	2.80	2.40	2.03	1.79

In the presence of powerful impulse noise, the original signal cannot be restored. It was proposed to approximate the corresponding time intervals with polynomials of the first to third degree using the least squares method with the addition of the generated Gaussian noise. The variance of the noise was calculated as the arithmetic mean of the signal variances before the beginning and after the end of the interference. The results of signal correction without adding noise are shown in Fig. 3,1 b, and with its addition are demonstrated in Fig. 3.1, c. The same algorithm can be applied for a signal failure caused by a breakdown of radio devices, a power outage, or other reasons.

For filtering coherent reflections, threshold values were set at the level of $\nu\sigma$, where $\nu > 0$ is a real number, σ is the root-mean-square deviation. In this case, the filtration procedure was repeated several times. Values exceeding the threshold level were replaced either by the arithmetic mean of two adjacent power values, or by the average power value at a given interval. The results of filtering coherent reflections are shown in Fig. 3.1, d. It is demonstrated that when choosing the values of $\nu \geq 3$ it is not possible to filter out some of the rather weak coherent reflections, and when $\nu \leq 2$, distortion of the original signal is possible. Therefore, the choice of the threshold value is based on a specific task.

The influence of interference and instrument failures on the parameters of the IS signal also negatively affects the retrieving the parameters of the geospace plasma (electron density, ion and electron temperature, ion composition, etc.). For eliminating their influence on the data obtained using the Kharkiv IS radar, various filtering algorithms are used, which are described in detail in [Pulyaev et al., 2011]. Filtering is usually performed in the altitude domain, and time intervals where interference or disruptions occur are excluded from following processing. In this case, the main attention is paid to the elimination of coherent reflections [Pulyaev et al., 2011]. This approach is of little use in the analysis of TIDs. To determine their parameters, it is necessary to use classical and modern methods of spectral analysis [Chernogor, 2008], which are suitable only for the analysis of discrete series with a constant time step. In addition, the presence of impulse noise and instrument failures can lead to the appearance of false harmonic components when using various linear and nonlinear transformations.

Therefore, to solve such problems, filtering in the time domain using the algorithms described in this work is necessary. The effectiveness of such combined use is shown in Fig. 3.2. This figure shows the filtered series correspond to the results of theoretical, model and experimental studies of the temporal dependences of the radio noise, as well as the temporal and altitude dependences of the IS signal (see, e.g., [Pulyaev et al., 2011]). On the one hand, the time dependences are relatively smooth, which is necessary to retrieve the regular parameters of the ionospheric plasma, and on the other hand, they experience quasi-periodic variations caused by TIDs of various scales, which are present in the ionosphere.

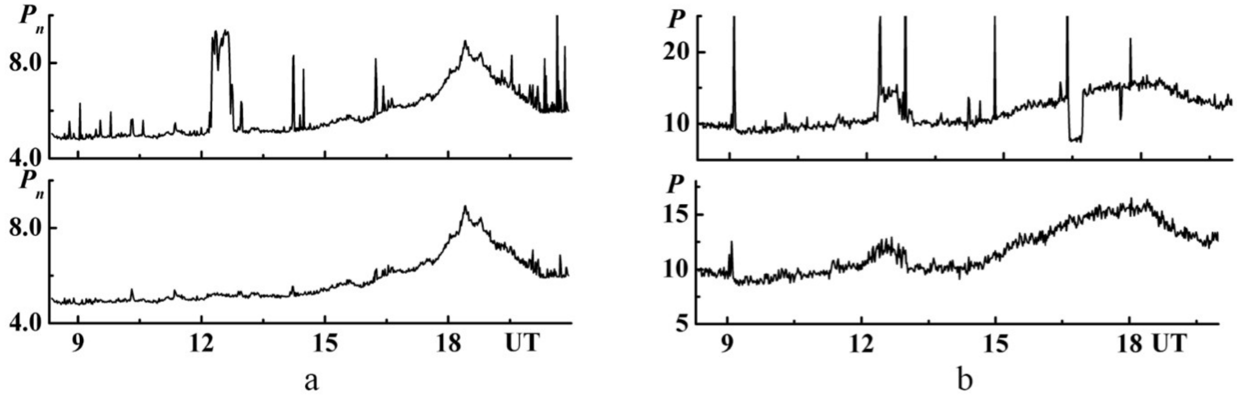

Figure 3.2. Temporal dependences of noise power (a) and IS signal at altitude of 418 km (b) The top panel shows the original dependencies, the bottom one demonstrates filtered signal using the described algorithms.

Summarizing the above, we can make the following conclusion.

1. Based on the analysis of a large array of experimental data, the main types of irregular interference and instrument failures affecting the temporal variations in the power of an IS signal have been identified and classified.

2. Algorithms for eliminating instrument failures, external long-term impulse noise, as well as coherent reflections have been developed on the basis of statistical methods for analyzing time series. A computer program has been implemented that allows filtering power in a semi-automatic mode.

3. A sharp jump in the signal level is shown to be eliminated by introducing a height-dependent correction factor. In the absence of a signal or in the presence of powerful long-term interference, it is necessary to apply a polynomial approximation of the time series. For filtering coherent reflections, threshold values are set at the level of several standard deviations.

4. The results of filtering the IS signal power and the noise power are presented. Preliminary filtering is shown to enable making the received signal suitable for following processing and analysis, in particular, when using classical and modern methods of spectral estimation.

3.2. Estimation of absolute and relative variations

The IS data were initially subjected to pre-filtering in order to remove various interference in accordance with the methodology described in [Panasenko, 2011]. Further, the statistical processing was carried out according to [Burmaka et al., 2005], with minor improvements. In particular, to calculate the trend, we used the approximation of the IS signal power by a polynomial of the third order using the least squares method on a time segment of 120 min with a step of 1 min. This enabled to filtering out the aperiodic variations of the signal more efficiently than by finding the trend using the moving average method, as described in [Burmaka et al., 2005]. However, in this case, there is also a slight decrease in the amplitudes of quasiperiodic processes. Comparison of the results obtained using the presented in [Burmaka et al., 2005] and slightly modified statistical processing are shown in Fig. 3.3 and Fig. 3.4.

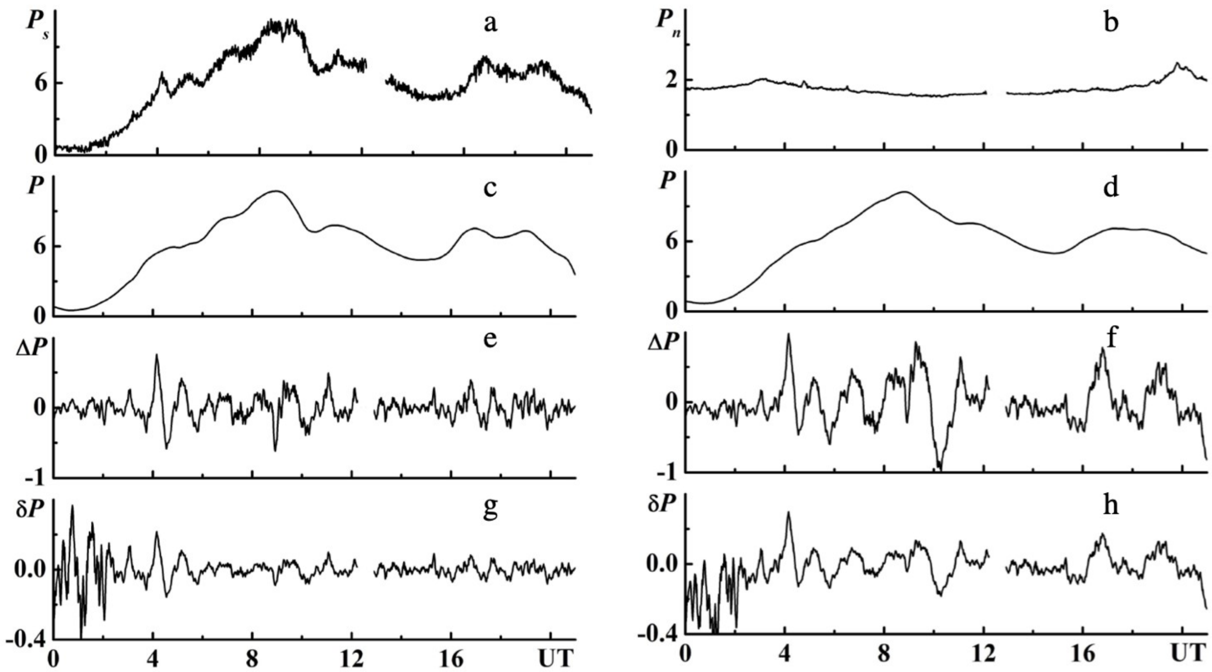

Figure 3.3. Stages of statistical analysis of the IS radar data obtained on August 29, 2012 for an altitude of 255 km: temporal dependences of the IS signal power (a) and noise (b); trends fitted using third-order polynomial approximation (c) and moving average method (d); absolute (e, f) and relative (g, h) variations in the IS signal power, calculated using the trends fitted by approximation by the 3rd order polynomial (e, g) and the moving average method (f, h).

Demonstration of applied stages to obtain the relative variations in IS signal power and electron temperature is shown in Figure 3.5.

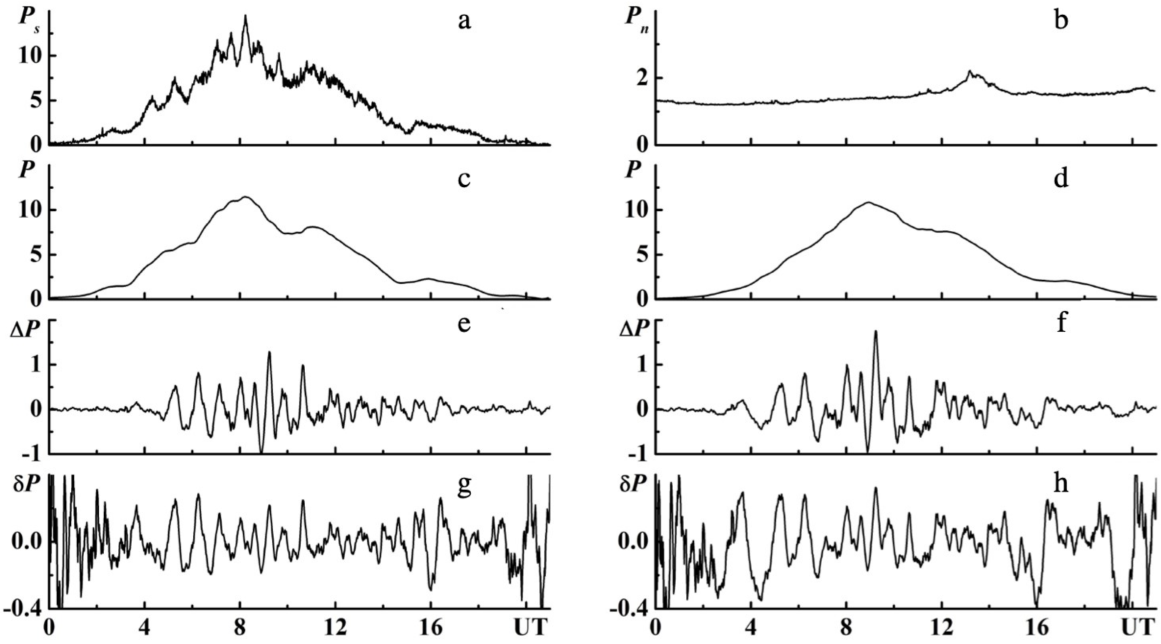

Figure 3.4. Same as in Fig. 3.3., but for November 23, 2012 and an altitude of 225 km

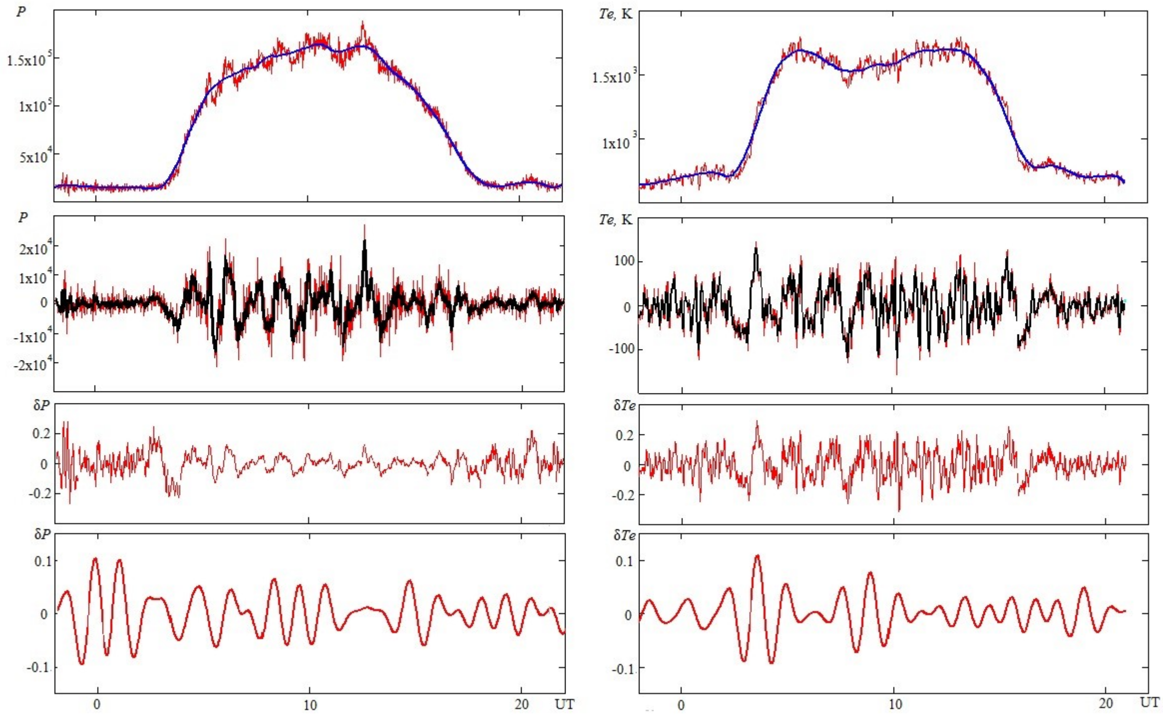

Figure 3.5. Stages of data analysis to obtain TID patterns in the IS power (left) and electron temperature (right). First panel shows original series (red) and trend (blue); second, third and fourth panels present absolute, relative and band-pass filtered variations, respectively.

For identifying wave processes in the ionospheric plasma using data from the Kharkiv IS radar, quasi-periodic variations in the relative power of the IS signal are usually analyzed (see, e. g., [Burmaka et al., 2005; Burmaka & Chernogor, 2012]). In that case, their relative amplitude is assumed to be approximately equal to the relative amplitude of the electron density at a definite altitude, and the effect of quasi-periodic variations in the ion and electron temperatures is negligible.

As is known (see, e.g., [Evans, 1969]), the IS signal power is determined from the following relationship:

$$P = C\frac{N_e}{h^2\left(1+T_e/T_i\right)}, \tag{3.1}$$

where C is constant; h is height of sounded ionospheric region.

The relation (3.1) is valid provided that $4\pi D_e \ll \lambda$, where D_e is the Debye radius for electrons and λ is the radio wavelength. This inequality holds for the Kharkiv IS radar.

Further, the studied value $X = P, N_e, T_e, T_i$ will be represented as

$$X = \overline{X}\left(1+\frac{\Delta X}{\overline{X}}\right) = \overline{X}(1+\delta X), \tag{3.2}$$

where $\overline{X}$ is background variation or trend; ΔX is absolute deviation from $\overline{X}$; $\delta X = \Delta X/\overline{X}$ is relative deviation.

If the temporal dependence of δX is quasi-harmonic, it can be represented as

$$\delta X = \delta_X \cos(\Omega t + \varphi_X), \tag{3.3}$$

where t is time; δ_X and φ_X are relative amplitude and initial phase, respectively, which in the general case can also depend on t.

Substitution of expression (3.2) into (3.1) yields

$$P = C\frac{\overline{N}_e(1-k_T)}{h^2}\frac{(1+\delta N_e)(1+\delta T_i)}{1+k_T\delta T_e+(1-k_T)\delta T_i}, \tag{3.4}$$

where $k_T = \overline{T}_e/(\overline{T}_e+\overline{T}_i)$.

Expression (3.4) shows that, in general case, when wave disturbances in ionospheric parameters occur, the temporal variations of P will not have a quasi-harmonic character due to the presence of a nonlinear dependence in expression (3.1). However, the results of numerous experimental studies indicate that the relative amplitudes of wave disturbances of ionospheric parameters are usually a few percent and do not exceed several tens of percent (see, e. g., [Kirchengast et al., 1995; Hocke & Schlegel, 1996; Hocke et al., 1996]). Therefore, we will first consider the oscillations when $\delta_X \ll 1$. To exclude the denominator of the second fraction in relationship (3.4), we use the Taylor series expansion, limiting to only the first two terms:

$$P = C\frac{\overline{N}_e(1-k_T)}{h^2}(1+\delta N_e)(1+\delta T_i)[1-k_T\delta T_e-(1-k_T)\delta T_i].$$

We represent P in the form (3.2). Then, performing further multiplication, we will leave only the linear terms on the right side of the previous expression. After small transformations, we get the final relationship:

$$\overline{P}(1+\delta P) = C\frac{\overline{N}_e(1-k_T)}{h^2}[1+\delta N_e+k_T(\delta T_i-\delta T_e)],$$

whence it follows that

$$\overline{P} = C\frac{\overline{N}_e(1-k_T)}{h^2} = C\frac{\overline{N}_e}{h^2\left(1+\overline{T}_e/\overline{T}_i\right)}, \tag{3.5}$$

$$\delta P = \delta N_e + k_T(\delta T_i - \delta T_e). \tag{3.6}$$

Expression (3.6) shows that the equality $\delta P = \delta N_e$ is satisfied only when $\delta T_i = \delta T_e$. Taking into account expressions (3.3), this corresponds to the equality of their relative amplitudes ($\delta_{Ti} = \delta_{Te}$) and the initial phases of oscillations ($\varphi_{Ti} = \varphi_{Te}$). Then, the exact equalities $\delta_{Ne} = \delta_P$ and $\varphi_{Ne} = \varphi_P$ hold.

Substituting expressions (3.3) into (3.6), we can obtain the following formula for δ_P:

$$\delta_P = \sqrt{\delta_{Ne}^2 + k_T^2\delta^2 - 2k_T\delta_{Ne}\delta\cos(\varphi_N - \varphi)}, \tag{3.7}$$

where

$$\delta = \sqrt{\delta_{Ti}^2 + \delta_{Te}^2 - 2\delta_{Ti}\delta_{Te}\cos(\varphi_{Ti} - \varphi_{Te})},$$

$$\varphi = \arctan\left(\frac{\delta_{Ti}\sin\varphi_{Ti} - \delta_{Te}\sin\varphi_{Te}}{\delta_{Ti}\cos\varphi_{Ti} - \delta_{Te}\cos\varphi_{Te}}\right).$$

It follows from expression (3.7) that the equality $\delta_{Ne} = \delta_P$ can also be satisfied if

$$\delta_{Ne} = \frac{k_T \delta}{2\cos(\varphi_{Ne} - \varphi)}.$$

The relative systematic error of the δ_{Ne} estimation will be determined as follows:

$$\varepsilon = \frac{\delta_P - \delta_{Ne}}{\delta_{Ne}}$$

which, taking into account (3.6), can be written in the form:

$$\varepsilon = \sqrt{1 + k_T^2 \left(\frac{\delta}{\delta_{Ne}} \right)^2 - 2k_T \left(\frac{\delta}{\delta_{Ne}} \right) \cos(\varphi_{Ne} - \varphi)} - 1. \qquad \textbf{(3.8)}$$

The expression (3.8) demonstrates that both overestimation ($\varepsilon > 0$) and underestimation ($\varepsilon < 0$) of δ_{Ne} occur depending on the relationship between the relative amplitudes and the initial phases of the quasi-harmonic variations of the ionospheric parameters.

If the condition $\delta_X \ll 1$ is not satisfied, then, as mentioned above, the variations of δP will no longer be quasi-harmonic. In this case, we expand the right-hand side of expression (3.4) in a Fourier series and find the relative amplitude of the harmonic component corresponding to the cyclic frequency Ω from the following relation:

$$\delta_P^{Fourier} = \frac{\Delta_P^{Fourier}}{\overline{P}^{Fourier}},$$

where $\Delta_P^{Fourier}$ is harmonic amplitude with relative frequency Ω; $\overline{P}^{Fourier}$ is constant component of the IS signal power. Then the expression for ε will have the form:

$$\varepsilon = \frac{\delta_P^{Fourier} - \delta_{Ne}}{\delta_{Ne}}. \qquad \textbf{(3.9)}$$

It can be shown that when $\delta_X \ll 1$, the equalities $\delta_P^{Fourier} = \delta_P$ and $\overline{P}^{Fourier} = \overline{P}$. Then relation (3.9) is transformed into relation (3.8).

For estimating the ε value for various values of the relative amplitudes and initial phases of oscillations of the ionospheric parameters, a computer simulation was carried out.

Based on the expressions from (3.7) to (3.9), it can be shown that the ε value depends on seven variables, namely:

$$\varepsilon = \varepsilon(k_T, \delta_{Ne}, \varphi_{Ne}, \delta_{Te}, \varphi_{Te}, \delta_{Ti}, \varphi_{Ti}). \qquad \textbf{(3.10)}$$

Since the φ_{Ne} value can always be set by choosing the initial observation time, hereinafter we will assume that $\varphi_{Ne} = 0$. In addition, we will analyze not the errors ε, but their maximum absolute values $\varepsilon_{\max} = |\max(\varepsilon)|$.

The dependence of ε_{max} on δ_{Te} and δ_{Ti} for different values of k_T and δ_{Ne} is shown in Fig. 3.6. Moreover, each value of ε_{max} is the global maximum of the function $|\varepsilon(\varphi_{Te}, \varphi_{Ti})|$ for the constant values of other parameters.

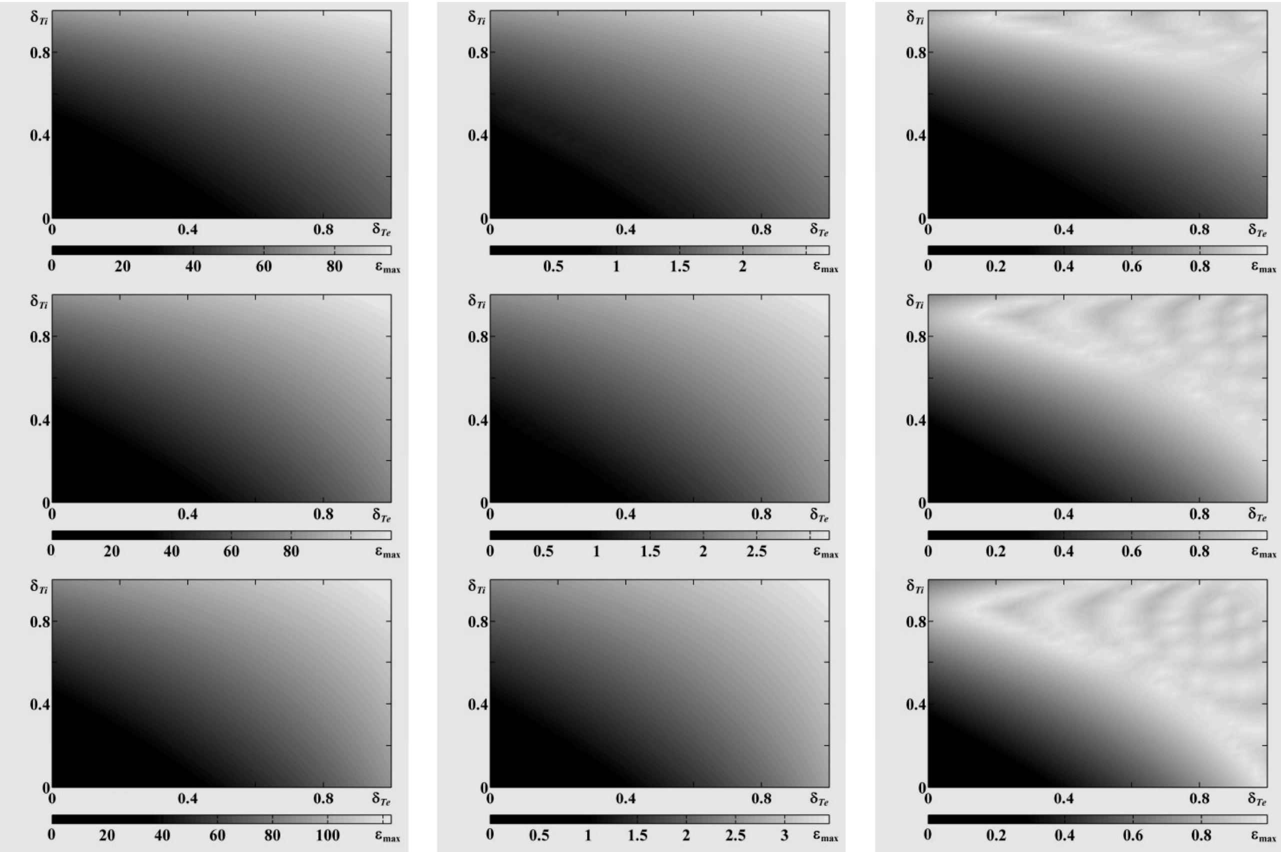

Figure 3.6. Dependence of the maximum systematic relative error ε_{max} on the relative amplitudes of the ion and electron temperature oscillations for k_T = 0.5 (top panel), k_T = 0.67 (middle panel), and k_T = 0.75 (bottom panel) during weak (δ_{Ne} = 0.01, left column), average (δ_{Ne} = 0.3, middle column) and strong (δ_{Ne} = 0.75, right column) quasi-harmonic variations in the electron density.

Fig. 3.6 shows that, as it is expected, the value of ε_{max} significantly increases with an increase in δ_{Te} and δ_{Ti}. In case of strong variations in the electron density for δ_{Te}, $\delta_{Ti} > 0.5 - 0.7$, a pronounced dependence of the ε_{max} values on the ratio between the relative amplitudes of the electron and ion temperatures occurs (see Fig. 1, right column).

It should be noted a significant increase in the relative error with a decrease in δ_{Ne} and its insignificant increase with an increase in k_T coefficient.

Table 3.2 shows the global maxima of the function $\varepsilon_{\max}(\delta_{Te}, \delta_{Ti})$ for a number of k_T and δ_{Ne} values. It can be seen from this table that $\varepsilon_{\max}$ can reach great values (on the order of 1 – 100 or 10^2 – 10^4%) at certain ratios between the ionospheric parameters. At large values of the relative amplitude of the electron density ($\delta_{Ne} \geq 0.75$), the $\varepsilon_{\max}$ value ceases to depend on the relative oscillation amplitudes of the ionospheric parameters, and its value becomes equal to 1 (see Table 3.2).

Table 3.2. Values of $\varepsilon_{\max}$ for various ratios between k_T and δ_{Ne}

k_T \ δ_{Ne}	0.01	0.1	0.3	0.5	0.75	1
0.5	99.42	9.47	2.77	1.41	1.00	0.97
0.67	116.50	11.10	3.26	1.67	1.00	1.00
0.75	126.09	12.02	3.53	1.82	1.00	1.00

Estimation of the systematic error enables obtaining an answer to the question about the possibility and advisability of analyzing temporal variations in the IS signal power to identify fluctuations in the electron density and estimate their relative amplitudes. An important and informative method for such study is computer modeling, which allows analyzing the dependence of this error on ionospheric characteristics and determining the range of its values. It should be taken into account that not all relations between the parameters included in (3.10) can take place in experiments.

For instance, when choosing the values of k_T, we took into account the fact that the temperature ratio T_e/T_i for real ionospheric conditions usually lies within 1 – 3. Therefore, the calculations were carried out for the coefficients k_T = 0.5, 0.67, and 0.75, which correspond to the T_e/T_i ratios, equal to 1, 2 and 3, respectively.

Fig. 3.6 shows that the largest values of $\varepsilon_{\max}$ are reached when $\delta_{Ne} \ll \delta_{Te}$, δ_{Ti}. Such inequalities are practically never occur for the ionosphere, since the heating (cooling) of electrons and ions always leads to expansion (compression) of the ionospheric plasma, which causes significant variations in the electron density.

The characteristics of quasi-harmonic variations in the ionosphere obtained experimentally are presented in [Kirchengast et al., 1995; Hocke & Schlegel, 1996; Hocke et al., 1996].

As for the initial phases of oscillations, as shown in [Kirchengast et al., 1995; Hocke et al., 1996], their average values are 185° (3.23 rad) and 130° (2.27 rad) for δT_e and δT_i, respectively, if we assume, as before, that φ_{Ne} = 0. Thus, quasi-harmonic variations in the electron density, on the one hand, and the ion and electron temperatures, on the other hand, occur almost in anti-phase.

Table 3.3 shows the results for calculations of ε_{max} for a number of observed values of δ_{Ne}, δ_{Te}, and δ_{Ti}. In this case, just as in Fig. 3.6, such values of δ_{Te} and δ_{Ti} were chosen where a global maximum of the absolute relative systematic error was. As can be seen from this table, the maximum systematic error usually does not exceed 0.4 – 0.5, and it significantly decreases to 0.01 – 0.1 with an increase in δ_{Ne},.

Table 3.3. Values of ε_{max} for the observed values of δ_{Ne}, δ_{Te}, and δ_{Ti}. Calculations are performed for k_T = 0.67.

δ_{Ne}	δ_{Te}	δ_{Ti}	φ_{Te}	φ_{Ti}	ε_{max}
0.01	0.01	0.01	3.23	2.27	0.36
0.04					0.07
0.07					0.04
0.1					0.03
0.2					0.01
0.04	0.04	0.02			0.49
0.07					0.27
0.1					0.19
0.2					0.09

Thus, for most observations, it is possible to take the δP values as an estimate of δN_e with an acceptable relative systematic error. However, since the relationship between the ionospheric parameters in each specific experiment is not known in advance, the value of ε in a number of cases can have values significantly larger than those given in Table. 2. Therefore, it is advisable to use such an estimate only when the random errors in determining δ_{Te} and δ_{Ti} are large enough (low values of the signal-to-noise ratio), or the ion and electron temperatures cannot be estimated from experimental data (using the "short" pulse mode to improve the altitude resolution).

Summarizing the above, we can conclude the following. Analysis of quasi periodic variations in the IS signal power in a wide range of altitudes allows detecting TIDs and estimating their parameters. The degree of influence of wave disturbances in the electron density, electron and ion temperature on the level of quasi-harmonic variations in the IS signal power is analyzed at different ratios between ionospheric parameters. A theoretical study and computer simulation were carried out, which enabled estimating the value of the relative systematic error in determining the relative amplitude of the electron density oscillations. It is shown its maximum value usually does not exceed 0.4 – 0.5, and it decreases to 0.01 – 0.1 with an increase in δ_{Ne}.

3.3. Spectral analysis and band-pass filtration methods

The periods of TIDs are detected by spectral analysis based on adaptive Fourier transform [Chernogor, 2008], which is Fourier analysis with a sliding window and a width adjusted to be equal to a fixed number of harmonic periods:

$$A_f(T,\tau)=\sqrt{\frac{2}{\nu T}}\int_{-\infty}^{\infty} s(t)g\left(\frac{t-\tau}{\nu T/2}\right)\exp\left(-i\frac{2\pi}{T}(t-\tau)\right), \quad \textbf{(3.11)}$$

where T is a period, τ is a shift of the window function $g(t)$ in the time domain, ν is the coefficient ($\nu > 0$) equal to the number of harmonic function periods that fall in the $g(t)$ function width and $s(t)$ is an analyzed signal. We set $\nu = 3$ to get the optimum relation between time and period resolutions. The periodogram $|A_f(T,\tau)|$ which are the amplitude density of signal is used further taking the absolute values of function (3.11). The Hamming window was used as $g(t)$, which has the form (see, e. g., [Marple Jr & Carey, 1989]):

$$g(t)=\gamma[0.54+0.46\cos(\pi t)],$$

where $\gamma \approx 1.12$ is normalizing factor.

The energygram is the average power as a function of period (a period density). It is defined as

$$E(T)=\int_{-\infty}^{\infty}|A_f(T,\tau)|^2\,d\tau=\int_{-\infty}^{\infty}S_f(T,\tau)d\tau, \quad \textbf{(3.12)}$$

where $S_f(T,\tau)=|A_f(T,\tau)|^2$ is energy periodogram, and used for estimations of TIDs periods. The local maxima in (3.12) are known to be responsible for the presence of harmonic components with the corresponding periods in the analyzed signal (see [Chernogor, 2008]).

Time series of ionospheric parameters were also passed through a digital band-pass filter with impulse response of the filter determined by the following expression [Chernogor et al., 2015]:

$$h(t)=\frac{2}{T_1}\exp\left(-\frac{t^2}{a^2T_1^2}\right)\mathrm{sinc}\left(2\pi\frac{t}{T_1}\right)-\frac{2}{T_2}\exp\left(-\frac{t^2}{a^2T_2^2}\right)\mathrm{sinc}\left(2\pi\frac{t}{T_2}\right), \quad \textbf{(3.13)}$$

where a is a fitting parameter which was set to 40, T_1 and T_2 are the periods corresponding to the edges of the filter pass-band, and $\mathrm{sinc}(x) = \sin(x)/x$.

Examples of spectral analysis results for data acquired at altitudes of 250 and 1300 km, as well as their 10 – 120 min band-pass filtered variations for altitude ranges 100 – 400 km and 1100 – 1400 km are showed in Fig. 3.7. For the

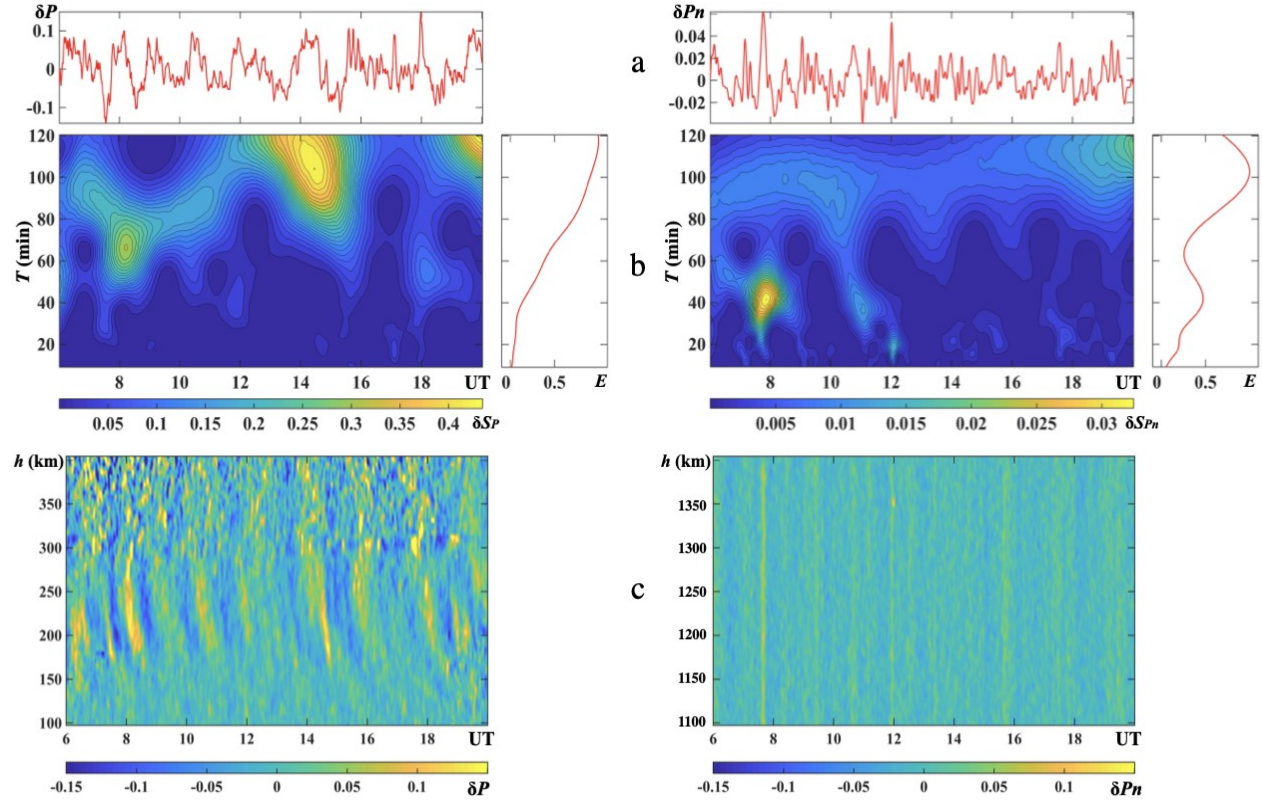

Figure 3.7. The results of processing the observation data on August 31, 2016: the results of spectral analysis, including a – relative variations of IS signal power δP and noise power δP_n; b – energy periodograms δS_P and δS_{Pn} and energygrams E of adaptive Fourier transform; c – the results of band-pass filtering δP and δP_n.

first of these ranges, only the received IS signal power was analyzed. Here $P = P_{sn} - P_n$, where P_{sn} is the received signal, being a mixture of IS signal and noise P_n. For the second range, the signal P_{sn}, which at altitudes of 1100 – 1400 km is identical to the noise signal P_n, is analyzed.

Fig. 3.7 shows that pronounced disturbances with periods of 60 – 80 min and 80 – 120 min are observed near 08:00 and 15:00 UT, respectively. At an altitude of 1300 km no fluctuations with such periods are detected. The values of the noise power spectral density δS_{Pn} turned out to be an order of magnitude less the same values of the spectral IS signal power density δS_P. A significant difference in behavior and the spectra of δP and δP_n (see Fig. 3.7, a) indicates an absence of correlation between IS signal and noise. This is also evidenced by also the altitude-time variations of their relative variations (see Fig. 3.7, b). At the altitudes of 150 – 300 km, wave-like patterns are clearly seen, while in noise variations at altitudes of 1100 – 1400 km such patterns are not observed. It should be noted that prevailing TIDs are visually traced in this figure with curvature of constant phase lines and relative amplitudes depending both from time and from altitude.

3.4. Estimation of propagation characteristics

For determining the TID vertical propagation parameters (vertical phase velocity V_z and wavelength Λ_z), we used cross-correlation analysis. In this case, the value of V_z is estimated using approximation of time lag or advances for oscillations at a number of altitudes relative to fluctuations at a specific altitude (200 km). Then $V_z = dz / d\tau \approx \Delta z / \Delta\tau$, where Δz is a difference between two adjacent altitudes; $\Delta\tau$ is difference between time advances or lags for these altitudes; $\Lambda_z = V_z T$.

Horizontal phase velocity V_h was estimated using the simple anelastic dispersion relation [Gossard & Hooke, 1975]:

$$\omega_I = \frac{k_h \omega_g}{\sqrt{k_z^2 + k_h^2 + 1/(4H^2)}}, \tag{3.14}$$

where $\omega_I = \omega - k_h U_h = 2\pi / T_I$ is intrinsic angular frequency; T_I is intrinsic period; ω is angular frequency of oscillations, observed with IS radar; $k_h = 2\pi/\lambda_h$ and $k_z = 2\pi/\lambda_z$ are horizontal and vertical wave numbers, relatively; λ_z is vertical wavelength; U_h is horizontal wind velocity component directed along V_h; $\omega_g = 2\pi/T_g$, where T_g is the Brunt-Väisälä period; H is the atmosphere density scale height. The T_g and H values were evaluated using the atmospheric parameters from the NRLMSISE-00 model.

Since we have no experimental data about an altitude profile of wind velocity, U_h in (3.14) was set to zero for rough estimation. Then $\omega = \omega_g$ and the horizontal phase velocity is calculated using a simplified expression:

$$V_h = \frac{\omega}{k_h} \simeq \sqrt{\frac{\omega_g^2 - \omega^2}{k_z^2 + 1/4H^2}}. \tag{3.15}$$

The horizontal wavelength $\Lambda_h = V_h T$.

On the basis of theoretical and experimental information about wave processes, we formulated a number of rules for the selection of TIDs. Quasi-periodic variations IS signal power must have a duration of at least two periods and altitude length of at least 40 km; the maximum values of the relative oscillation amplitudes $\delta P_{\max}$ must be at least 0.05 (i.e., 5 %).

3.5. Estimation of wave characteristics using dense GPS networks

Fig. 3.8 shows an example of daily variations of STEC, which was measured by a SCTE GPS receiver located near Lecce in southern Italy, while receiving signals from 26 GPS receivers. As can be seen from Fig. 2, STEC curves have a vertical offset relative to each other, due to the presence of phase uncertainty. Therefore, it is impossible to estimate the exact STEC values using the expression (2.1). For determining it, additional information contained in the source files is used, namely the value of pseudoranges (distances between the receiver and the satellite without taking into account the differences between the clock of the receiver and the satellite) at two frequencies.

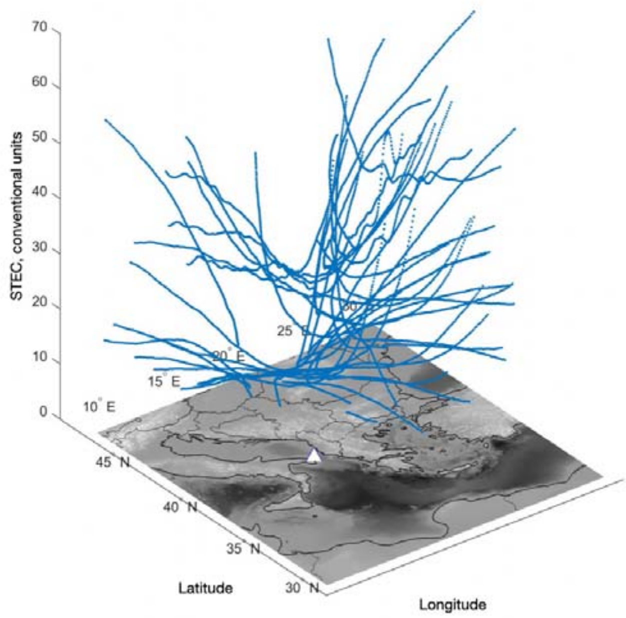

Figure 3.8. Value of the slant total electron content (STEC) for a number of pierce points, measured during the day by a GPS receiver (triangle) when processing signals from 26 satellites

Variations of STEC obtained through pseudoranges are random due to the effect of multipath propagation of radio signals. Since the standard deviation of such random variations is usually several TECUs (1 TECU = 10^{16} m^{-2}), it is necessary to apply further smoothing of the results. However, even after that, the STEC error is not less than 1 TECU [Themens et al., 2013], which does not allow studying wave processes, the amplitude of which is often significantly less than this value.

For the analysis of spatial or temporal TEC variations, a different approach is used using a number of processing methods [Kotake et al., 2007]. The fact is that the absolute values of TEC variations relative to its average value do not depend on K (see Fig. 3.8). In this case, we can use expression (2.1) to determine the STEC (without involving pseudoranges), and estimate and remove slowly changing component (trend) using the least squares method. The value of the theoretical error for estimation of absolute variations of STEC does not exceed 0.01 – 0.02 TECU [Spilker & Parkinson, 1996]. The real error will depend on the accuracy of the trend approximation, as well as the methods of filtering and estimating the parameters of wave disturbances.

3.5.1. Trend estimation

In [Kotake et al., 2007; Otsuka et al., 2013], a method for estimating the trend component for daily STEC changes is reported, which is obtained for each of the receiver-satellite pairs. This method is based on the application of simple moving average in the interval of 60 minutes with a step of 30 s. In order to detect longer periodic oscillations, the averaging interval can be increased to 180 mins.

The results of applying such moving to one of the curves from Fig. 3.8, are shown in Fig. 3.9,a and Fig. 3.9,c. Due to satellite motion, such curves often have an U-shape and this trend approximation is unsatisfactory, especially for an averaging interval of 180 min and during a relatively rapid increase or decrease in function (see Fig. 3.9,a,c). After removing such an approximating curve from the original series, significant non-existent STEC variations will be obtained due to the error of

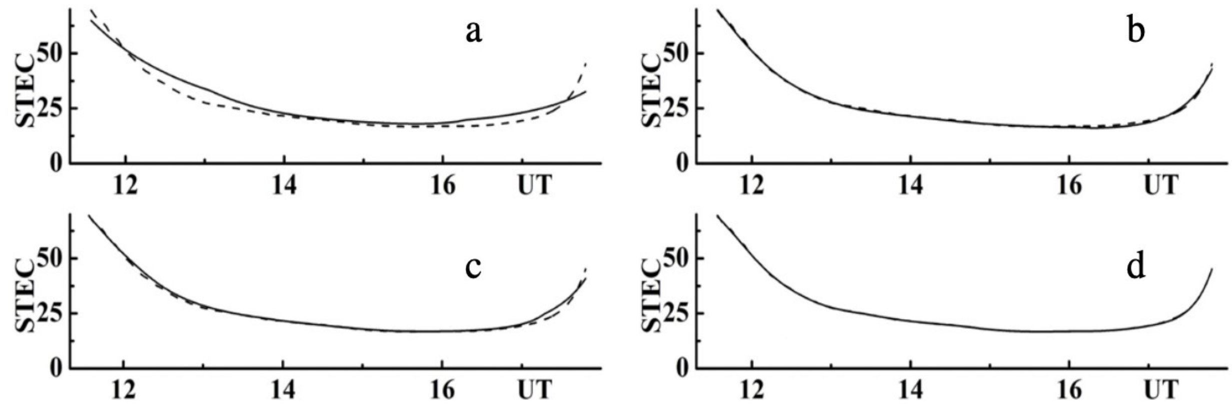

Figure 3.9. Variations of STEC obtained during the day using the receiver – satellite pair (solid curve) and their approximation (dashed curve) using the methods of simple moving average (a, c) and 3rd order least squares (b, d) on at intervals of 180 min (a, b) and 60 min (c, d).

the trend estimate (Fig. 3.10, dashed curves). This will lead, firstly, to incorrect conclusions about the presence of intense wave disturbances, and, secondly, to a significant overestimation of the TID horizontal phase velocity using the cross-correlation analysis.

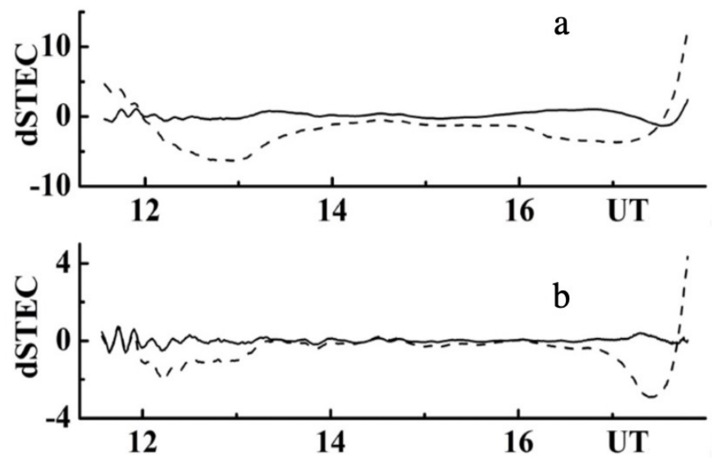

Figure 3.10. Variations of STEC after removal of the trend component (dSTEC), obtained by the methods of simple moving average (dashed line) and 3rd order least squares (solid line) at intervals of 180 min (a) and 60 min (b).

For mitigating the negative impact of the averaging procedure on the estimated values of TID parameters, it was proposed to use the 3rd order least squares method (LSM) at intervals of 60 and 180 min to detect perturbations with different time scales. The advantage of this method is that the approximating curve is a 3rd degree polynomial, which has a maximum, minimum and flexes point. This shape of such curve allows tracking long-term variations of STEC more accurately (Fig. 3.9,b and Fig. 3.9,d) and almost does not lead to additional fluctuations after subtraction of the trend component (Fig. 3.10, solid line). The comparison of solid and dashed curves in Fig. 3.10 shows that they almost coincide at intervals where STEC changes over time slowly (14 – 16 UT) and differ significantly in periods of abrupt changes in STEC (at the ends of the satellite direct visibility interval). It is important that the solid curve in Fig. 3.10, a reasonably reflects wave processes with an amplitude of about 1 TECU, which occurred at 11:30 – 12:30 UT, while they are almost invisible in the variations marked by dashed line. It should be noted that the proposed method of trend removal has proved effective in the detection of wave processes using the Kharkiv IS radar.

3.5.2. Retrieving of traveling ionospheric disturbances

Wave processes with different temporal and spatial scales are known to be constantly present in the Earth's atmosphere. According to the spatial scale, they are divided into acoustic waves, internal gravity waves (IGW), tides and planetary waves. Spectral analysis and band-pass filtering methods are commonly used to detect IGWs and their ionospheric manifestations TIDs (see, e. g., [Panasenko et al., 2018]). The invoking of Fourier transform anticipates the presence of continuous data series, which is often impossible even for current dense GPS networks.

Fig. 3.11,a shows the spatial variations of dTEC over Europe for one time point. They reflect changes in the absolute values of the vertical TEC (VTEC) and are estimated by multiplying dSTEC by the slope factor (slant factor). This factor can be represented in a simplified form as τ_0/τ_1, where τ_0 is the length of the radio signal path between altitudes of 250 and 450 km; τ_2 is the effective thickness of the ionosphere (200 km) [Kotake et al., 2007]. In addition, a preliminary spatial averaging of the signals received over the region having the dimensions 0.75° along the meridian and 0.75°/cos (φ) (φ is a latitude) along the parallel is performed [Otsuka et al., 2013].

As seen from Fig. 3.11,a lack of data ("white spots") occurs even after averaging, when no pierce point of the GPS satellites appeared over some regions at this time. As mentioned above, it is necessary to employ interpolation procedures, as well as band-pass filtering in the temporal and spatial domains to estimate the parameters of the TIDs and obtain the map shown in Fig. 3.11,b.

Interpolation of dTEC values was done in the time domain using 3rd order polynomials selected using LSM. In this case, we used at least 5 points on the left

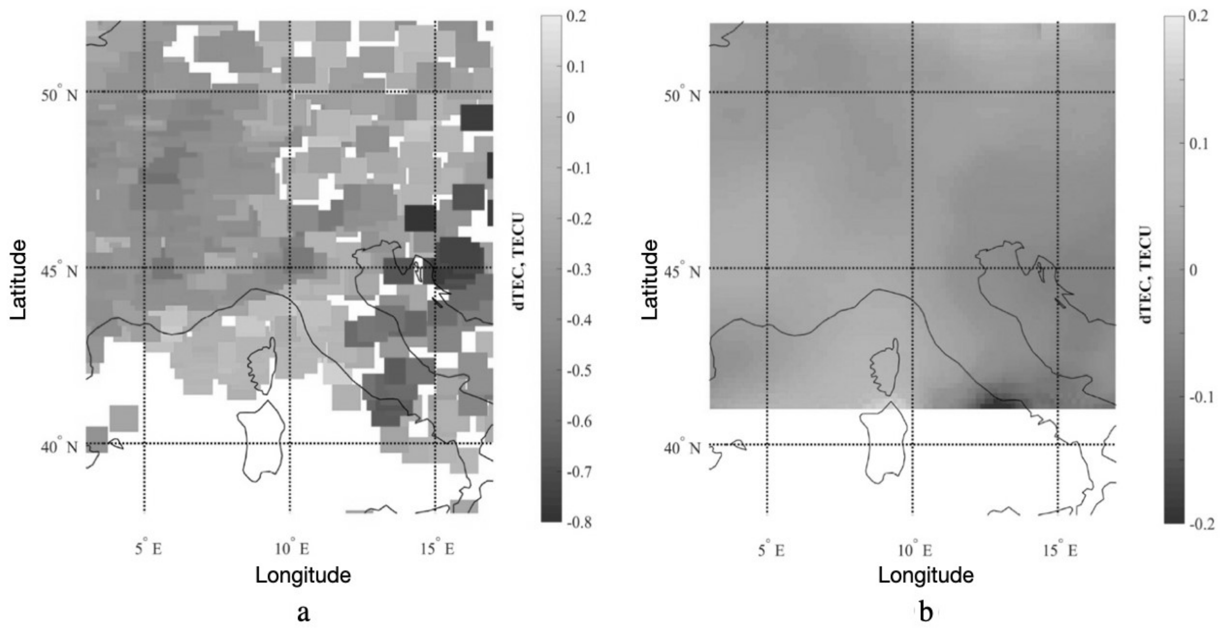

Figure 3.11. Map of VTEC absolute variations over Europe before (a) and after (b) the employing of interpolation procedures, as well as band-pass filtering in time and space domains.

and the same to the right of the interval with the missing data for the correct filling of the gaps. For further analysis, only those time variations were selected where the duration of the interpolated intervals did not exceed 10% of the observation time.

The adaptive Fourier transform was chosen for spectral analysis [Panasenko et al., 2018]. The digital filter described in [Chernogor et al., 2015; Panasenko et al., 2018] was chosen for band-pass filtering in the time domain. Typically, the range of filtered periods included periods of TIDs, which had the largest relative amplitude and were caused by the passage of AGWs during periods of solar terminator and eclipse, geospatial storms and other events.

Two-dimensional filtering in the spatial region was performed to divide TIDs into large-scale TIDs (horizontal wavelength λ > 1000 km) and medium-scale TIDs (λ = 200 – 1000 km). To do this, the dTEC values associated with the pierce points inside the circles with radii of 200 and 1000 km, respectively, were averaged.

Fig. 3.12 presents the spatial variations of the VTEC, which have different temporal and spatial scales. The figure shows that the spatial interference of TIDs, having a wide range of periods does not allow determining the predominant direction of their distribution (Fig. 3.12,a). The use of band-pass filtering in the time domain only also does not work, because TIDs with similar periods can have significantly different spatial scales and directions of propagation (Fig. 3.12,b). The selection of large-scale TIDs separately showed that they spread along the north-south line (Fig. 3.12,c). These results are in good agreement with the accepted ideas about large-scale TIDs, which usually propagate from high to low latitudes and are caused by variations in the auroral electrojet and precipitations of high-energy particles in the auroral region. This leads to heating of the neutral component and generation of AGWs [Hocke & Schlegel, 1996]. Finally, the propagation direction of medium-scale TIDs cannot be determined from Fig. 3.12,d. This is due to the fact that they usually propagate in different directions from local sources located in the lower atmosphere [Hernández-Pajares et al., 2012]. Some authors also observed such disturbances during periods of geospace storms [Nishioka et al, 2009].

Thus, we described improved and developed methods for detecting and estimating the parameters of TIDs having different periods and horizontal wavelengths, using dense GPS networks. The main results are as follows.

1. To remove long-term variations of STEC for each of the receiver-satellite pairs, it is proposed to use the 3rd order least squares method instead of the simple moving average method. This improvement will significantly decrease the errors in estimating the parameters of wave processes, especially at time intervals where the STEC values undergo significant changes.

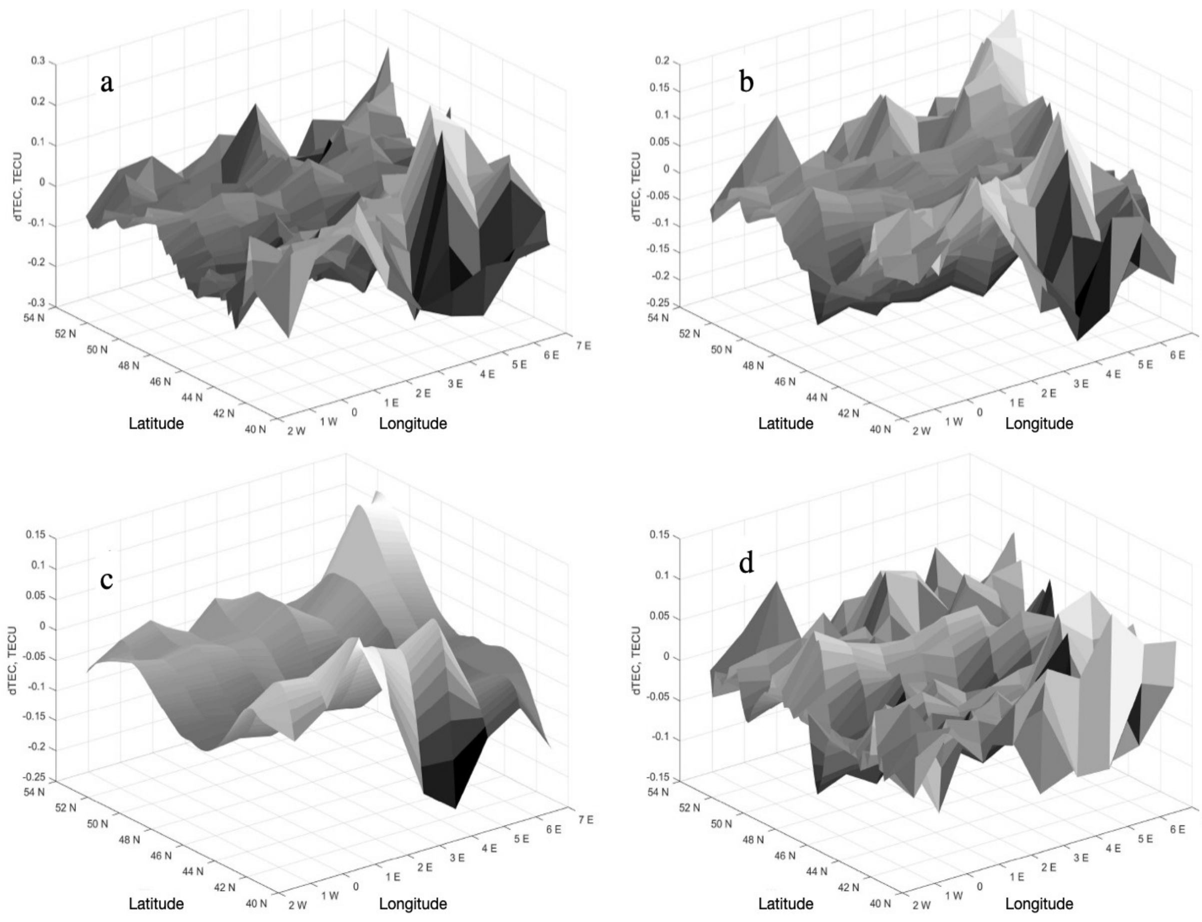

Figure 3.12. Spatial distribution of VTEC absolute variations o after a number of successive stages of band-pass filtration: in the range of periods 5 – 120 min (a) and 40 – 80 min (b); in the range of horizontal wavelengths from 1000 km (c) and 200 – 1000 km (d).

2. The need for interpolation of dTEC time variations is shown to eliminate data gaps, as well as to enable employing spectral analysis and band-pass filtering.

3. For separation TIDs on medium- and large-scale ones, it is proposed to perform two-dimensional filtering of results in the spatial region with averaging of data related to pierce points inside circles with radii of 200 and 1000 km. It is shown that this technique allows determining more accurately the vectors of the wave horizontal phase velocity, which often have not only different absolute values, but also different directions for medium-scale and large-scale disturbances with similar periods.

CHAPTER 4

TRAVELING IONOSPHERIC DISTURBANCES UNDER MAGNETICALLY QUIET CONDITIONS

A number of processes are known to occur both on the Earth's surface and on the Sun, which are responsible for the generation of AGWs and TIDs. At the same time, there are constant difficulties in identifying the sources of disturbances in specific cases. Therefore, to find the ionosphere response to the specific sources, an analysis of the experimental data obtained under similar conditions, when some potential sources of generation and distribution channels are absent, or their role is minimized, is necessary to do.

This chapter aims at identifying and evaluating the parameters of TIDs observed by incoherent scatter radars in periods close to solstices and equinoxes from 2006 to 2018, during low solar activity under quiet or weakly disturbed geomagnetic conditions. Also, we analyzed the possible sources of generation of the detected wave processes. In addition, a wave response on the solar eclipse of March 20, 2015 is reported further, in Chapter 6.

4.1. Solar and magnetic activity

The state of solar activity was estimated using the index F10.7. The level of geomagnetic activity was evaluated using the indices A_p and K_p, (planetary) and A and K (high latitude) (Table 4.1). The high-latitude indices given in the table were obtained from Geophysical Observatory “College” (geographical coordinates: 64.9 N, 148.0 W).

Table 4.1. State of space weather

Data	$F_{10.7}$	A_p	K_p	A	K
30.03.2006	84	4	1 1 0 0 1 2 2 2	2	2 0 0 0 0 0 2 1
17.12.2008	69	5	2 2 1 0 1 2 1 1	6	1 1 2 1 3 3 0 0
14.12.2009	79	4	0 3 2 2 0 1 0 0	4	0 2 2 3 0 0 0 0
24.03.2010	84	3	0 0 0 0 2 2 0 2	4	0 0 0 0 3 3 0 0
23.06.2010	74	4	1 1 1 1 1 1 2 1	3	1 1 1 2 2 1 0 0
24.09.2016	85	5	1 0 1 1 1 1 2 2	2	1 0 0 1 0 0 1 1
21.06.2018	82	3	1 1 1 1 1 0 1 0	2	1 1 1 1 0 0 1 0
19.09.2018	71	4	1 3 2 1 0 1 0 0	4	1 3 2 0 0 0 0 0

Taking into account the values of high-latitude indices in the selection of measurement data for further analysis is due to the fact that sometimes planetary indices incorrectly reflect the increase in geomagnetic activity (which can lead to generation and propagation of AGWs and TIDs) at high latitudes, because they are calculated as average values of mid-latitude and high-latitude indices.

Table 4.1 shows that during the observation periods the Sun remained quiet. Since $K \leq 3$, $K_p \leq 3$, $A \leq 10$ and $A_p \leq 10$, we can claim that the study was performed in magnetically quiet or weakly disturbed conditions.

4.2. The results of spectral analysis

Using the developed IS radar data processing algorithms described in Chapter 3, the search and evaluation of TID parameters were performed in the altitude range of 100 – 400 km.

To identify the predominant TIDs, a spectral analysis of the time variations of the IS signal power was performed within the specified altitude interval with a step of 25 km. The presence of localized in the temporal and periodic regions increases in the values of energy spectral density δ_{SP} at a number of heights was interpreted as a possible manifestation of TIDs.

Fig. 4.1 and 4.2 present the results of spectral analysis for a fixed altitude of 200 km. Each panel on the left shows the energy spectrograms. The panels on the right demonstrate the corresponding energygrams, which are an integral of the spectrogram over time and constitutes the average power as a function of period. The vertical axis is the period in minutes; the horizontal axis is in UT.

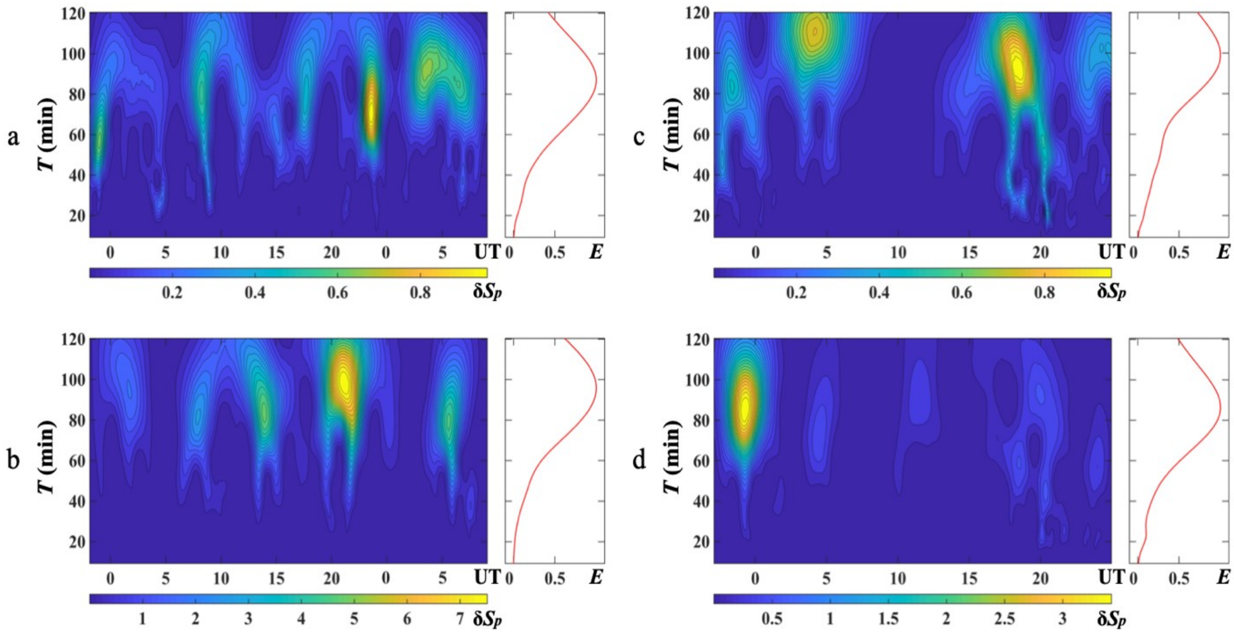

Figure 4.1. Results of spectral analysis performed for temporal variations of IS signal power for (a) December 17–18, 2008, (b) December 14–15, 2009, (c) June 23, 2010 and (d) June 21, 2018 using Kharkiv data at the height of 200 km.

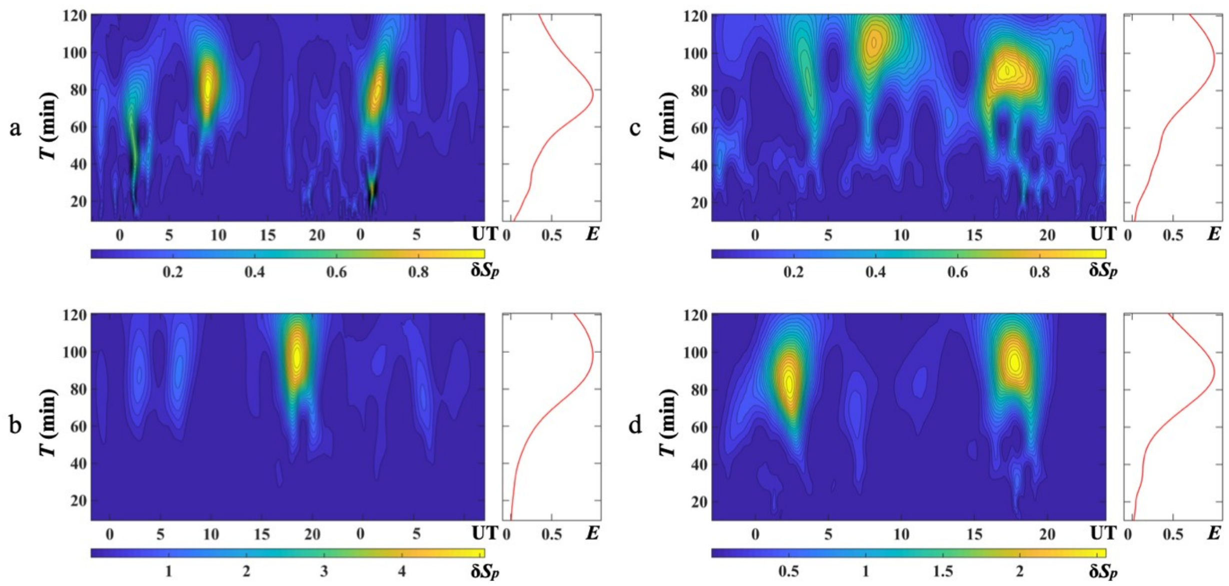

Figure 4.2. Same as Fig. 4.1 but for (a) March 30–31, 2006, (b) March 24-25, 2010, (c) September 24, 2016 and (d) September 19, 2018.

Since the planned observations of the processes in the ionosphere in most cases lasted 1–2 days, we investigated and analyzed the data from 24 to 40 hours of continuous operation of the IS radar. Fig. 4.1 and Fig. 4.2 show that oscillations that were in the range of periods of 60 – 120 min had the greatest energy in all seasons. Near the winter solstices, these fluctuations were observed in the following time intervals: 22:00 – 01:00 (with a period of approximately 60 min), 07:00 – 10:00 (80 min), 16:00 – 20:00 UT (80 min) for December 17, 2008; 22:00 – 00:00 (70 min), 02:00 – 09:00 UT (90 min) for December 18, 2008; 00:00 – 04:00 (95 min), 06:00 – 10:00 (80 min), 13:00 –16:00 (85 min), 20:00 – 23:00 UT (100 min) for December 14, 2009; 04:00 – 07:00 UT (75 min) for December 15, 2009 (Fig. 4.1) (hereinafter, if the first time value is greater than the second, it refers to the previous day). In periods near the summer solstices, fluctuations were detected in the following time intervals: 22:00 – 01:00 (85 min), 02:00 – 08:00 (110 min), 16:00 – 20:00 UT (90 min) for June 23, 2010; 22:00 – 02:00 (85 min), 04:00 – 05:00 (75 min), 10:00 – 13:00 (90 min), 17:00 – 22:00 UT (95 min) for June 21, 2018 (Fig. 4.1).

Near the vernal equinoxes, TIDs took place during 00:00 – 04:00 (60 min), 07:00 – 10:00 UT (80 min) for March 30, 2006; 00:00 – 04:00 UT (75 min) for March 31, 2006; 03:00 – 07:00 (two fluctuations with periods of about 75 min), 06:00 – 20:00 UT (95 min) for March 24., 2010; 06:00 – 08:00 UT (75 min) for March 25, 2010 (Fig. 4.2). In periods near the autumn equinoxes, oscillations were found in the following time intervals 02:00 – 05:00 (80 min), 06:00 – 10:00 (110 min), 16:00 – 20:00 UT (90 min) for September 24, 2016; 01:00 – 04:00 (85 min), 06:00 – 08:00 (70 min), 10:00 – 12:00 (85 min), 16:00 – 20:00 UT (95 min) for September 19, 2018 (Fig. 4.2).

As shown from the results of spectral analysis, wave processes took place throughout the all-time interval of observations. Some disturbances recorded in the morning and evening can be associated with the movement of local ST, as they were manifested both before and after its passage. It should be noted that fluctuations with greater intensity were more often observed in the evening. Disturbances detected during the day require more detailed study of generation sources.

4.3. Evaluation of TID parameters

Based on the most probable periods of TIDs, the appropriate subrange was chosen for further bandpass filtration in the range of 60 – 120 min, which corresponds to large-scale structures. Also, we selected two more subranges of periods for TID search, such as 30 – 60 min (MSTIDs and LSTIDs) and 15 – 30 min (MSTIDs). To reduce the effect of incomplete removal of long-term oscillations, the initial temporal dependences of the received signal were again subjected to the procedure of trend removal and normalization to it before performing band-pass filtering in these intervals. The trend was determined at intervals of 90 and 45 min, respectively.

Figures 4.3 – 4.6 presented band-pass filtered quasi-periodic variations in IS signal power in three period sub-ranges.

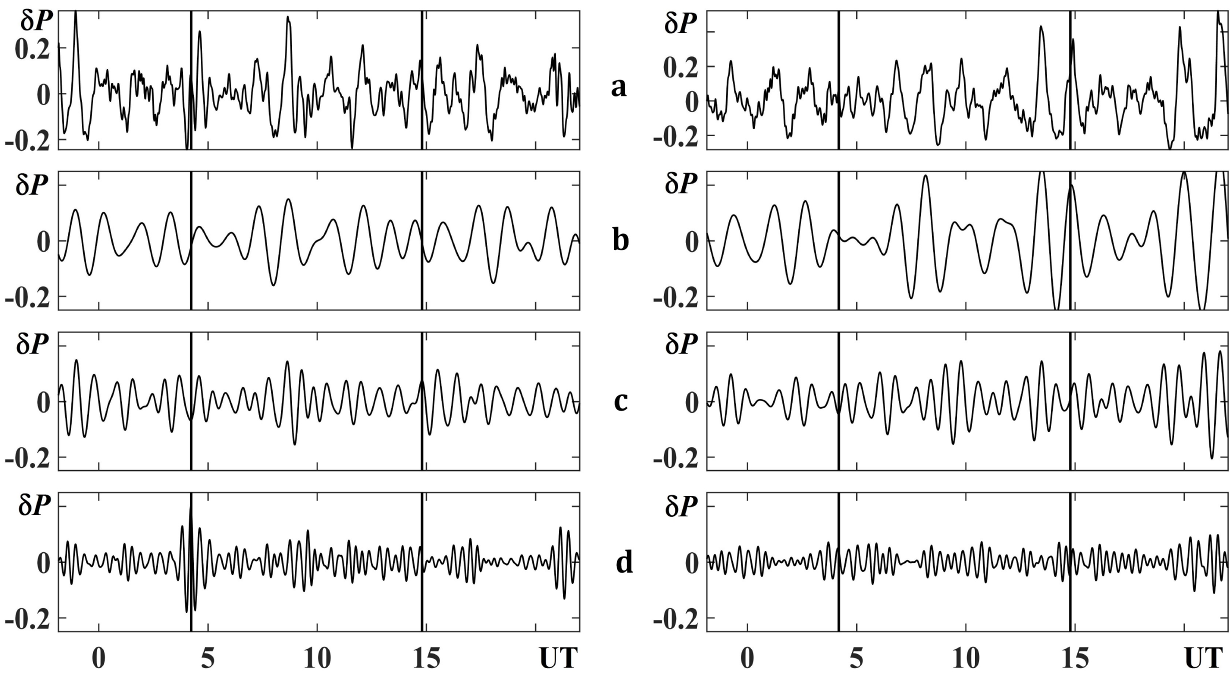

Figure 4.3. Temporal variations of relative fluctuations of IS signal power δP near winter solstice in the period ranges of 10 – 120 min (a), 60 –120 min(b), 30 – 60 min (c), and 15 – 30 min at the altitude of 200 km for December 17, 2008 (left) and December 14, 2019 (right). Solid lines mark sunrise and sunset STs at this altitude.

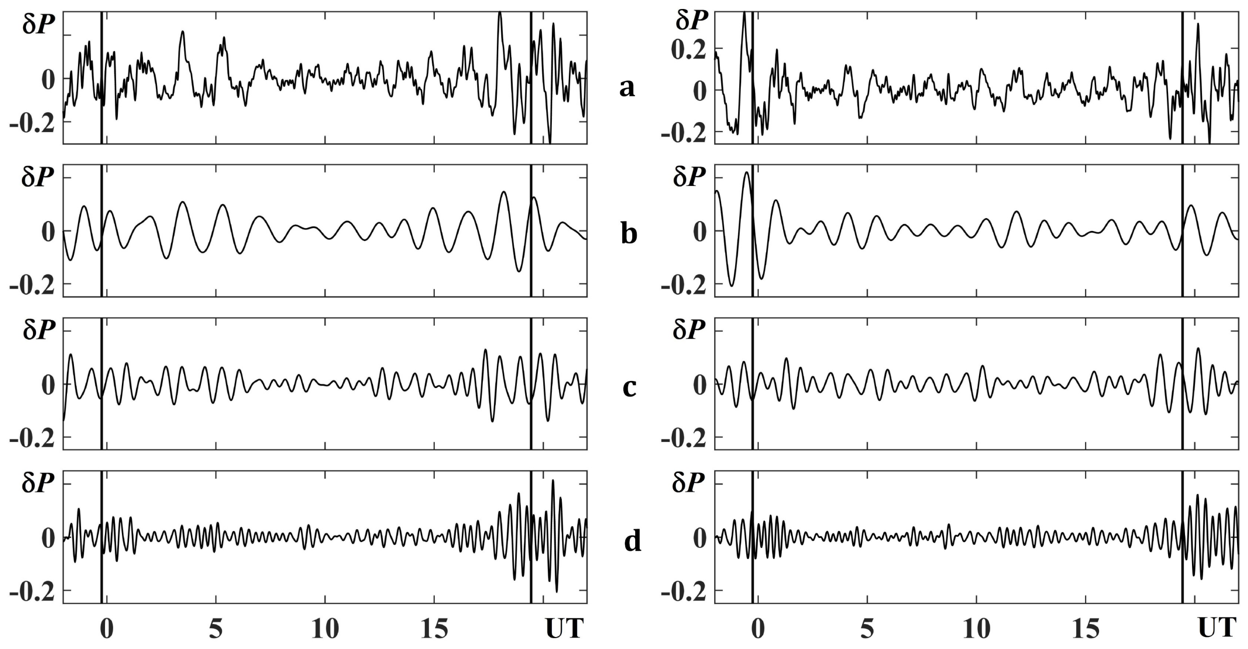

Figure 4.4. Same as Figure 4.3 but near summer solstice for June 23, 2010 (left) and June 21, 2018 Iright).

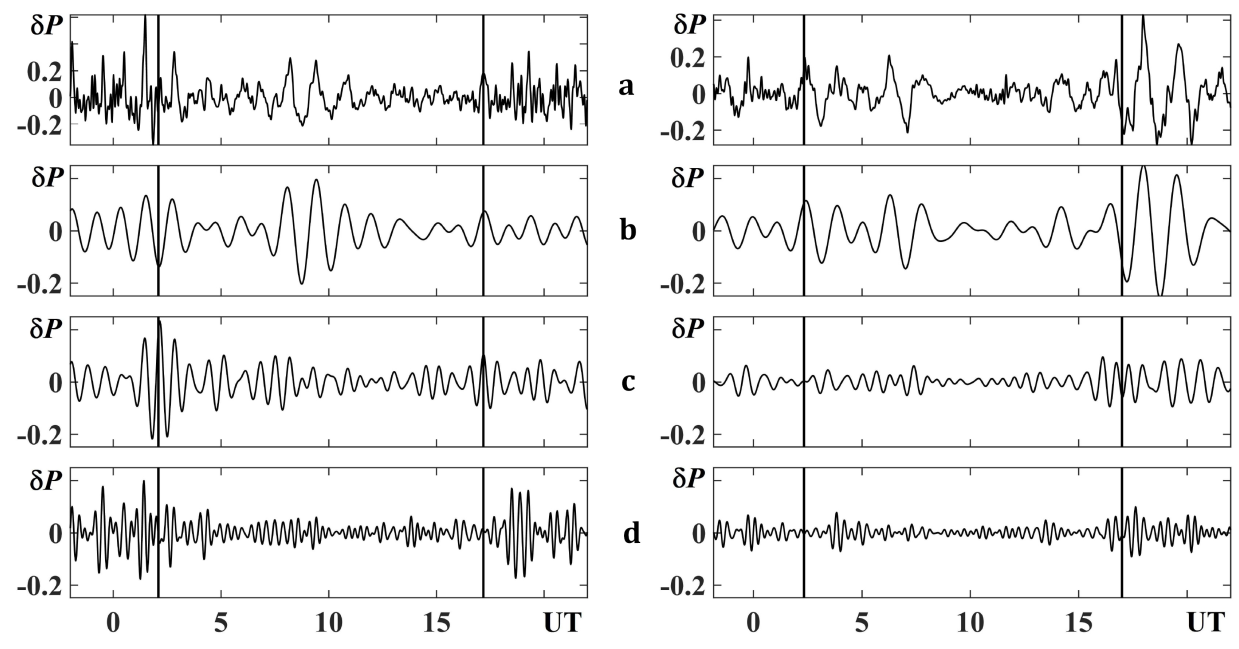

Figure 4.5. Same as Figure 4.3 but near vernal equinox for March 30, 2006 (left) and March 24, 2010 (right).

Figures 4.7 – 4.10 show the altitude-time dependences of the band-pass filtered IS signal power variations for the three bands. For comparative analysis of energy characteristics, all panels in the figures have the same altitude and amplitude scales.

The results of spectral analysis and band-pass filtration indicate the presence of quasi-periodic variations with the studied periods of 60 – 120, 30 –

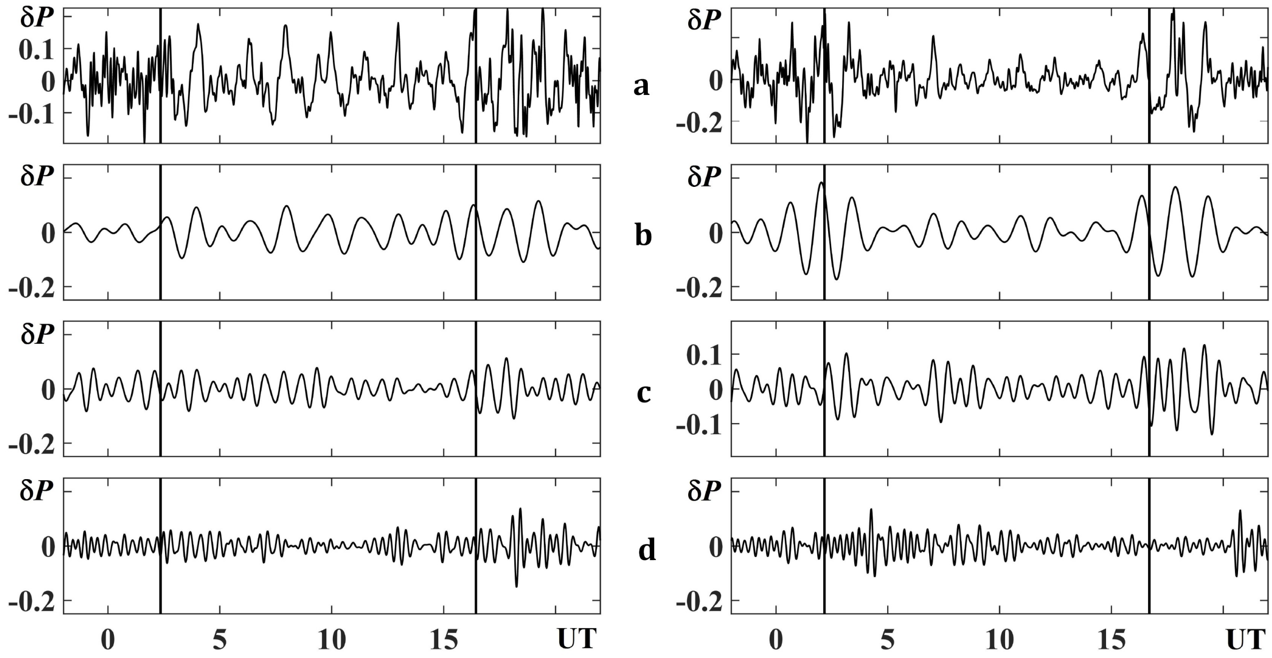

Figure 4.6. Same as Figure 4.3 but near autumn equinox for September 24, 2016 (left) and September 19, 2018 (right).

60 and 15 – 30 min in all seasons. The following features are revealed. Wave processes with periods of 60 – 120 min are present during the whole time of observations in the winter (Fig. 4.3), as well as on 24.09.2016 (Fig. 4.6). In all other seasons, such LSTIDs took place only near the passage of the morning and evening ST. The duration of individual wave processes ranged from 3 to 9 hours. The relative amplitudes of the TIDs in this range of periods were greater than the amplitudes of the disturbances in the other ranges considered. The maximum values of the relative amplitudes of the IS signal power were detected during the winter solstices. TIDs with periods of 30 – 60 min were also observed throughout the day near the winter solstices and autumn equinoxes. In other seasons, they took place near the terminators. The duration of individual TIDs ranged from 2 to 11 hours.

Regarding the range of 15 – 30 min, such TIDs were always detected but on 30.03.2006. They were recorded throughout the day near the winter solstices, and 24.09.2016, while in other periods they took place only near the time of passage evening ST, and 19.09.2018. The duration of individual oscillations was from 2 to 5 hours.

As shown in the figures, we calculated and analyzed the parameters of individual TIDs (total – 59 events) that took place on 17.12.2008 and 14.12.2009 (Fig. 4.3), 23.06.2010 and 21.06.2018 (Fig. 4.4), 30.03.2006 and 24.03.2010 (Fig. 4.5), 24.09.2016 and 19.09.2018 (Fig. 4.6). Using cross-correlation analysis of experimental data, the altitude ranges at which TIDs are present were determined; TIDs periods were specified, $h_{\max}$ heights were found, at which relative amplitudes reached maximum values (and these values themselves),

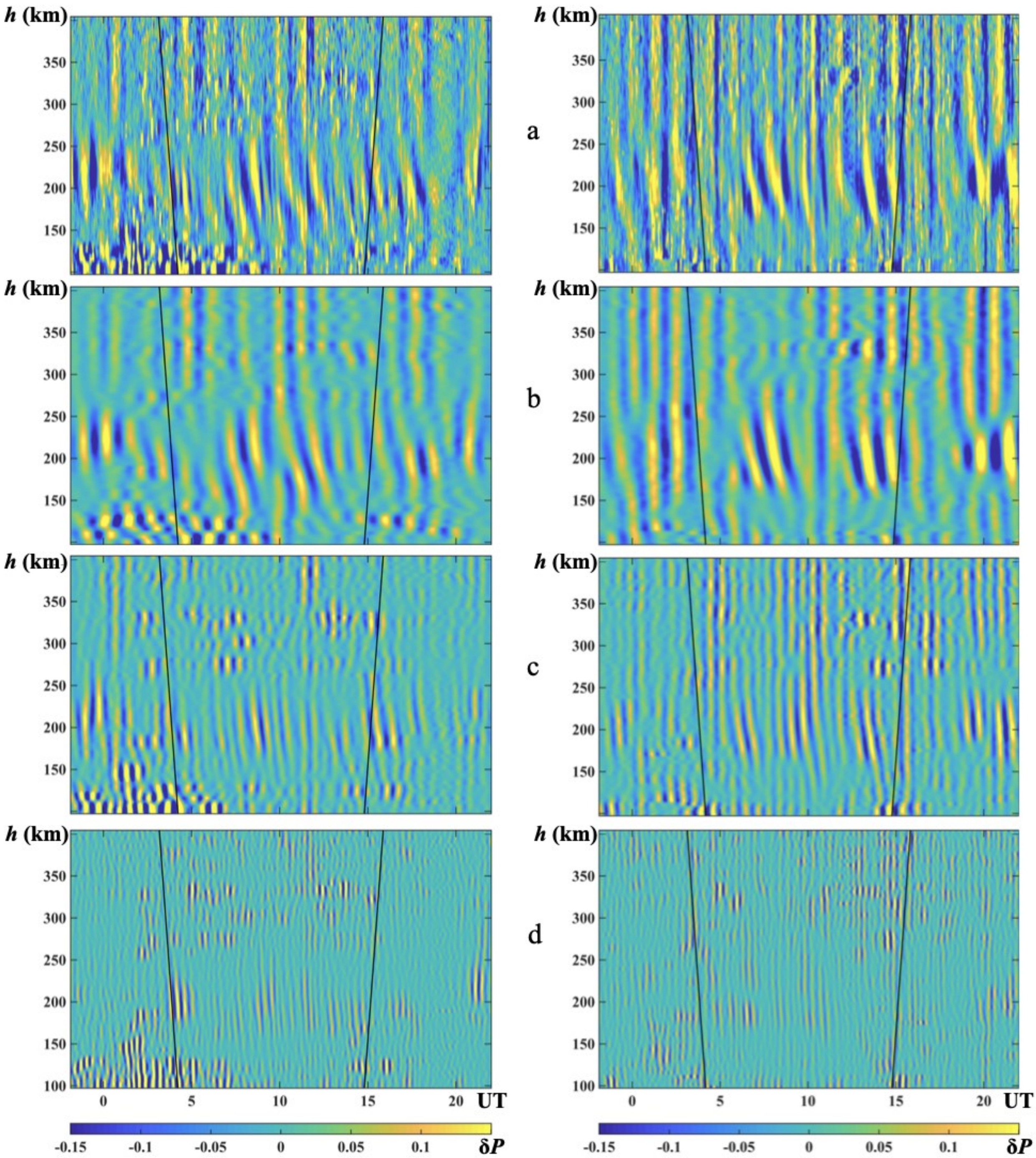

Figure 4.5. Altitude time dependence of (a) 10 – 120 min, (b) 60 – 120 min, (c) 30 – 60 min and (d) 15 – 30 min band-pass filtered relative variations of IS signal power for December 17, 2008 (left column) and December 14, 2009 (right column). Solid lines mark sunrise and sunset STs at analyzed altitude.

vertical V_z and horizontal V_h components of the phase velocities and wavelengths Λ_z and Λ_h were estimated. The values of the estimated parameters for each season are given in Tables 4.2, 4.3, 4.4, and 4.5. Further, we describe the parameters of wave processes observed in different sub-bands of periods in more detail.

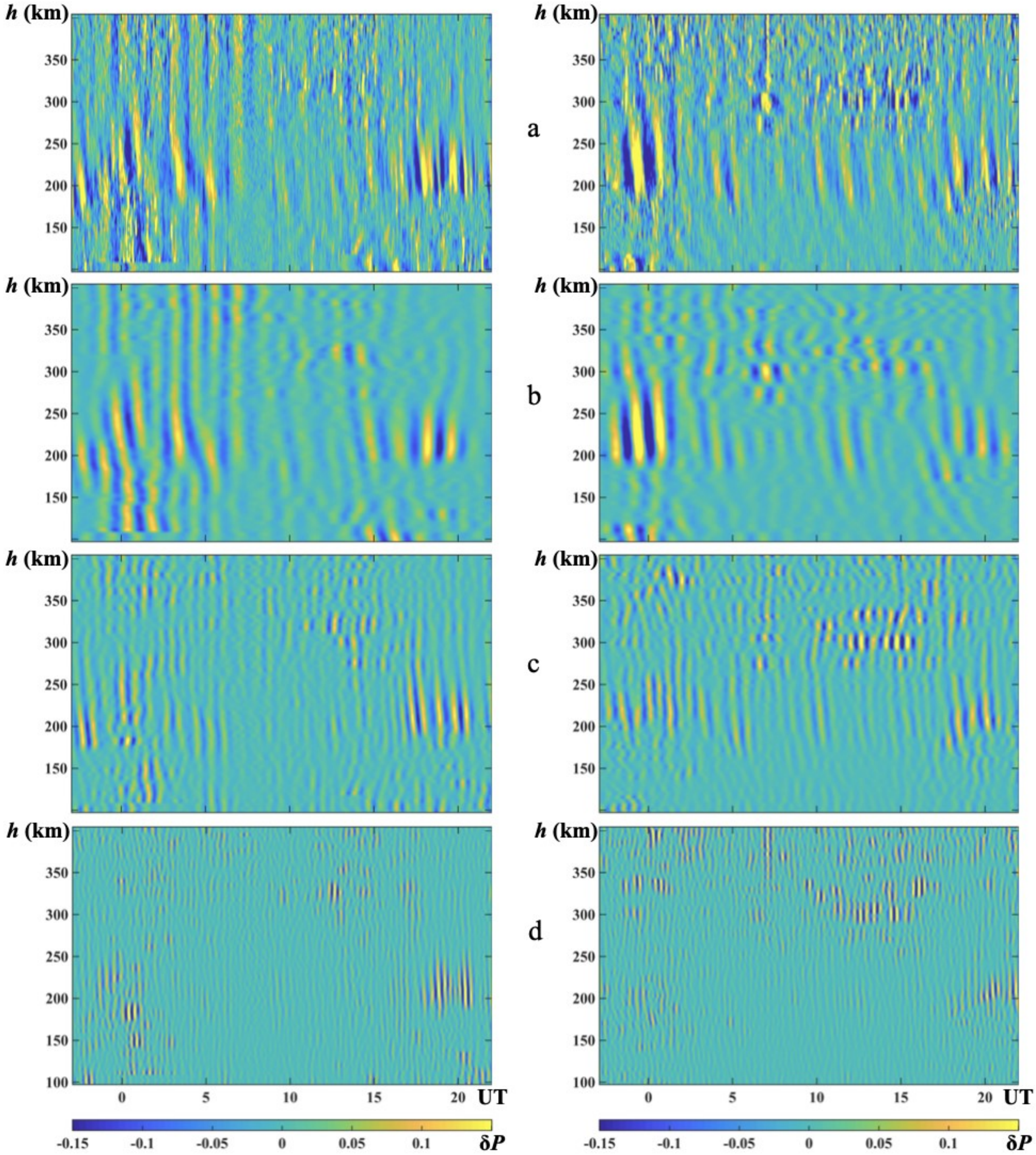

Figure 4.6. Same as Fig. 4.5 but for June 23, 2010 (left column) and June 21, 2018 (right column).

4.3.1. TIDs with periods of 60 – 120 min

Such wave processes were observed in the following altitude ranges: 150 – 260 km in winter, 170 – 280 km in spring, 180 – 280 km in summer and 170 – 300 km in autumn. The values of δP_{max} varied from 0.14 to 0.3 in winter, from 0.07 to 0.3 during the summer solstice, from 0.16 to 0.27 during the spring equinox, and from 0.09 to 0.24 in the autumn. The main periods of TIDs were equal to 70 – 94 min.

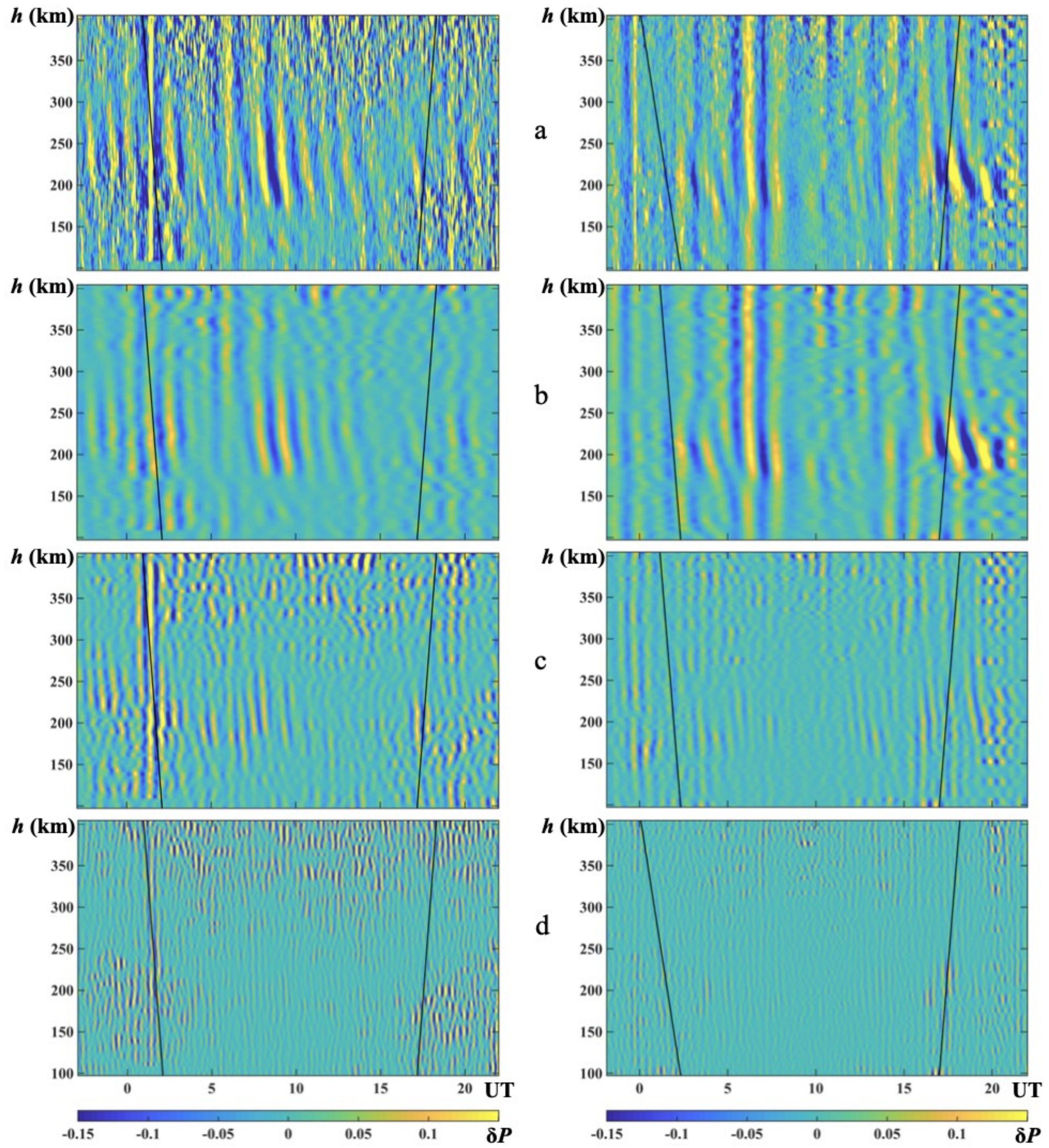

Figure 4.7. Same as Fig. 4.5 but for 30 – 31 March 2006 (left column) and 24 – 25 March 2010 (right column).

4.3.2. TIDs with periods of 30 – 60 min

Such wave processes were observed in the altitude ranges from 160 to 260 km for all seasons. But for autumn measurements, the upper observation altitude reached 300 km. The values of δP_{max} varied from 0.07 to 0.23; the lowest values of maximum amplitudes were recorded on June 23, 2010 and March 24, 2010; the largest were in winter. The main periods of TIDs were equal to 36 – 51 mins.

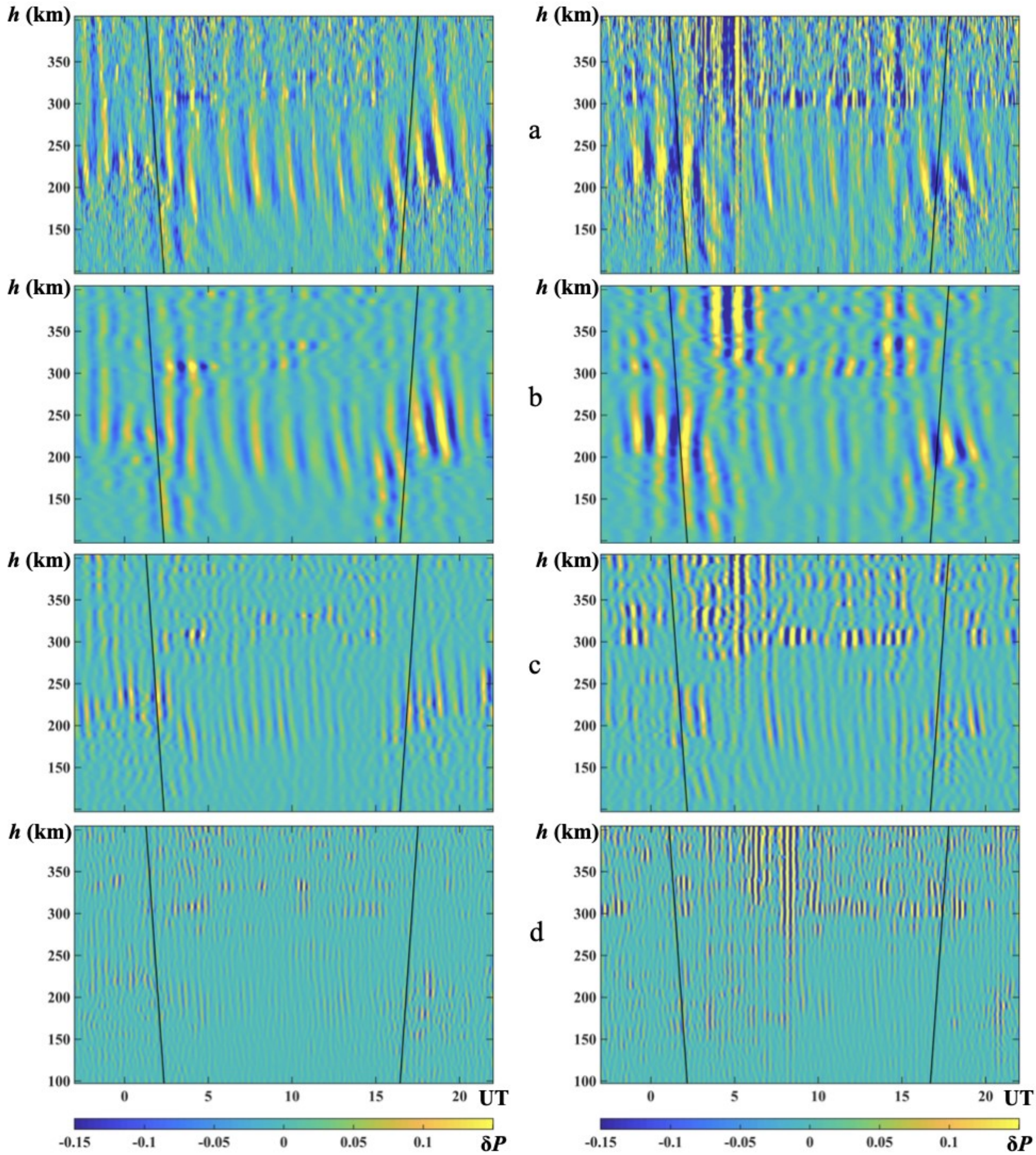

Figure 4.8. Same as Fig. 4.5 but for 24 September 2016 (left column) and 19 September 2018 (right column).

4.3.3. TIDs with periods of 15 – 30 min

Such wave processes were observed in the altitude ranges from 180 – 220 km in winter, 170 – 250 km in spring, 180 – 250 km in summer and 170 – 250 km in autumn. The values of δP_{max} varied from 0.09 to 0.22. The lowest values of the maximum amplitudes were recorded on 24.09.2016. The main periods of TIDs were usually equal to 19 – 25 min. In general, such processes were observed near

Table 4.2. TID parameters during the winter solstice. Hereinafter, horizontal lines separate the sub-bands; the symbols ↓ and ↑ denote TIDs, for which V_z was directed down and up, respectively; TIDs, which cannot be caused by the propagation of AGWs, is given in bold.

Da	Time, UT	Height, km	T, min	h_{max} km	δP_{max}	V_z, m/s	V_h, м/s	Λ_z, km	Λ_h, km	
14.12.2009	22:00–04:00	150÷260	86	216	0.14	65	600	340	3100	↓
	06:00–10:00	150÷260	78	198	0.22	25	210	120	970	↓
	11:00–17:00	160÷250	80	198	0.27	45	360	210	1700	↓
	19:00–24:00	180÷240	89	198	0.31	110	990	560	5300	↓
	04:00–08:00	160÷230	39	179	0.14	30	180	100	500	↓
	08:00–11:00	160÷250	42	207	0.15	75	320	190	800	↓
	11:00–15:00	160÷250	44	180	0.18	35	170	100	450	↓
	18:00–20:00	180÷250	39	212	0.17	70	290	170	700	↓
	20:00–22:00	170÷250	43	193	0.2	90	420	240	1100	↓
	02:00–07:00	160÷210	21	184	0.15	170	370	200	450	↓
	07:00–12:00	160÷210	22	179	0.09	150	340	190	450	↓
	19:00–22:00	**180÷220**	**22**	**193**	**0.15**	**370**	**860**	**490**	**1100**	↑
17.12.2008	22:00–05:00	180÷250	78	221	0.21	110	910	510	4200	↓
	06:00–15:00	180÷250	76	216	0.16	40	300	300	1400	↓
	15:00–22:00	170÷230	82	189	0.15	35	330	180	1600	↓
	22:00–03:00	**190÷240**	**45**	**221**	**0.17**	**650**	**3100**	**1800**	**8400**	↑
	07:00–12:00	160÷250	39	202	0.15	65	260	150	600	↓
	14:00–18:00	160÷270	46	184	0.17	40	200	110	550	↓
	03:00–06:00	160÷240	24	193	0.23	120	320	170	450	↓
	08:00–10:00	180÷240	23	202	0.11	90	220	130	300	↓
	15:00–18:00	180÷220	20	188	0.11	190	420	230	500	↓
	20:00–22:00	**200÷250**	**24**	**216**	**0.18**	**270**	**670**	**390**	**950**	↑

the time of the evening ST. It should be noted that in winter, the characteristics of some TIDs observed at adjacent intervals were quite close, for example during 02:00 – 07:00 UT and 07:00 – 12:00 UT for 14.12.2009, as well as 03:00 – 06:00 UT and 08:00 – 10:00 UT for 17.12.2009 (see Table 4.2). This may indicate the existence of a single wave process over a long period of time (about 7 – 8 hours), the relative amplitude of which undergoes significant time variations, possibly due to modulation by oscillations with larger periods or the effect of changes in the propagation medium.

4.3.4. Oscillations which are not associated with predominant TIDs

Some quasi-periodic variations did not fall under the above TIDs selection criteria. For example, processes that are visually traceable in the interval of periods 15 – 30 min: for 23.06.2010 from 22:00 to 02:00 UT at altitudes from 170 to 250 km (Fig. 4.4); for 24.03.2010 from 22:00 to 05:00 UT at altitudes from

Table 4.3. TID parameters during the summer solstice.

Da	Time, UT	Height, km	T, min	h_{max} km	δP_{max}	V_z, m/s	V_h, m/s	Λ_z, km	Λ_h, km	
23.06.2010	23:00–06:00	210÷280	80	248	0.14	70	550	320	2600	↓
	15:00–21:00	**190÷260**	**87**	**216**	**0.16**	**380**	**3400**	**2000**	**18000**	↑
	03:00–07:00	170÷230	49	207	0.08	110	560	320	1600	↓
	17:00–21:00	180÷270	39	216	0.17	140	590	330	1400	↓
	18:00–21:00	180÷250	21	207	0.22	170	370	210	470	↓
21.06.2018	22:00–02:00	190÷270	77	225	0.29	90	760	430	3500	↓
	10:00–14:00	180÷260	78	198	0.07	40	330	190	1500	↓
	19:00–22:00	200÷260	88	207	0.11	380	3500	2000	18200	↓
	17:00–22:00	210÷250	40	221	0.11	80	360	200	820	↓
	22:00–00:00	180÷220	25	207	0.11	570	1500	860	2300	↓
	18:00–23:00	180÷230	22	207	0.17	140	310	180	400	↓

Table 4.4. TID parameters during the spring equinox.

Da	Time, UT	Height, km	T, min	h_{max} km	δP_{max}	V_z, m/s	V_h, m/s	Λ_z, km	Λ_h, km	
24.03.2010	01:00–09:00	170÷250	84	198	0.16	80	660	390	3300	↓
	16:00–22:00	180÷250	92	207	0.27	20	230	140	1300	↓
	01:00–07:00	160÷200	36	179	0.08	80	300	170	650	↓
	15:00–18:00	160÷250	37	202	0.07	100	360	220	800	↓
	16:00–19:00	170÷250	22	216	0.11	170	370	220	500	↓
30.03.2006	22:00–04:00	170÷280	70	221	0.22	90	610	360	2600	↓
	07:00–14:00	170÷280	78	202	0.2	40	310	180	1400	↓
	00:00–04:00	**170÷220**	**49**	**207**	**0.23**	**230**	**1100**	**660**	**3400**	↑
	04:00–10:00	170÷260	40	188	0.12	50	190	110	460	↓

150 to 220 km (Fig. 4.5); 19.09.2018 from 21:00 to 04:00 UT at altitudes from 150 to 220 km and from 20:00 to 22:00 UT at altitudes from 170 to 200 km (Fig. 4.6). Also processes in intervals from 30 to 60 mins: for 21.06.2018 from 22:00 to 03:00 UT at altitudes of 200 – 260 km (Fig. 4.4) and for 30.03.2006 a number of processes from14:00 to 22:00 UT at altitudes of 150 – 250 km (Fig. 4.5) do not meet the selection criteria described in Chapter 3. Such variations occupy less than 40 km of altitude or have relative amplitude of less than 0.05. Some of these events may be due to the random nature of the signal or to incompletely filtered reflections or impulse noise.

4.3.5. Statistical characteristics of AGW and TID parameters

Estimations given in the Tables 4.2 – 4.5 showed that in most cases the assumption that TIDs are caused by the passage of AGWs (so-called AGWs/TIDs)

Table 4.5. TID parameters during the autumn equinox.

Data	Time, UT	Height, km	T, min	h_{max} km	δP_{max}	V_z, m/s	V_h, m/s	Λ_z, km	Λ_h, km	
24.09.2016	**02:00–05:00**	**170÷270**	**84**	**230**	**0.12**	**180**	**1500**	**890**	**7400**	↑
	05:00–14:00	170÷270	94	202	0.09	30	280	170	1600	↓
	15:00–22:00	200÷300	86	234	0.24	40	350	220	1800	↓
	02:00–14:00	170÷260	89	230	0.12	90	750	470	4000	↓
	00:00–03:00	220÷260	38	234	0.17	100	380	240	870	↓
	03:00–14:00	170÷280	41	188	0.08	60	240	140	580	↓
	15:00–19:00	190÷260	51	225	0.15	110	540	330	1600	↓
	22:00–02:00	200÷250	22	225	0.13	170	380	230	500	↓
	02:00–05:00	170÷230	22	198	0.08	70	170	100	220	↓
	11:00–14:00	180÷230	22	198	0.07	70	150	90	200	↓
	16:00–20:00	180÷240	23	207	0.15	70	150	90	210	
19.09.2018	**22:00–04:00**	**180÷280**	**86**	**225**	**0.26**	**170**	**1500**	**890**	**7800**	↑
	15:00–20:00	190÷250	86	207	0.21	40	310	190	1600	↓
	02:00–04:00	190÷250	46	193	0.12	70	370	200	1000	↓
	06:00–12:00	170÷250	40	193	0.11	50	210	130	510	↓
	16:00–20:00	180÷240	50	198	0.14	60	300	180	890	↓
	03:00–05:00	150÷210	19	170	0.13	3400	7400	3900	8400	↓
	09:00–11:00	170÷220	24	198	0.09	80	190	120	280	↓

is most likely true. It is because the calculated parameters of disturbances were in good agreement with the theoretically and experimentally obtained information about AGWs, which observed at ionospheric altitudes. In particular, the values of the horizontal phase velocity V_h of one of the most important criteria for the presenceof AGWs were estimated, which cannot exceed the speed of sound V_s for waves in a neutral atmosphere. The value of V_s significantly depends on the altitude: V_s. = 250 – 300 m/s in the lower and middle atmosphere, while it can reach 650 – 900 m/s at thermospheric altitudes. Taking into account the possible influence of horizontal wind speeds on the estimated V_h speeds, we took for AGWs/TIDs disturbances V_h < 1000 m/s (shown in Tables 4.2 – 4.5 in normal font). It turned out that all AGWs/TIDs had a vertical phase velocity directed from top to bottom. This indicates the sources of AGWs, located below the investigated area of altitudes, and agrees well with the known results of theoretical and experimental studies.

Also, seven processes that do not correspond to the disturbances that can be caused by AGWs (shown in Tables 4.2 – 4.5 in bold) were identified. For them, the direction of propagation of V_z is upwards. It is worth noting that they observed during nighttime only for all seasons. This indirectly indicates that the detected TIDs were most likely caused by electromagnetic forces. This kind of night disturbances was experimentally detected in [Otsuka et. al., 2004, 2013]), where the reason for their generation is described.

Table 4.6 shows the distribution of AGWs/TIDs by sub-bands, as well as statistical characteristics of their parameters. The table shows that the number of registered LSTIDs is quite large (22 events) and only by 5 disturbances less than the number of MSTIDs (27 events). The obtained results do not confirm the conclusions that LSTIDs are mainly observed during increased magnetic activity.

Table 4.6. Statistical characteristics of TID parameters caused by AGWs. Here $\overline{X}$ ($X = T$, $\delta P_{\max}$, V_z, V_h, Λ_z, Λ_h) is the average value; Δ_X is the standard deviation.

T, min	Type of TIDs (number)	$\overline{T} \pm \Delta_T$, min	$\overline{\delta P}_{\max} \pm \Delta_{\delta P\max}$	$\overline{V}_z \pm \Delta_{Vz}$, m/s	$\overline{V}_h \pm \Delta_{Vh}$, m/s	$\overline{\Lambda}_z \pm \Delta_{\Lambda z}$, km	$\overline{\Lambda}_h \pm \Delta_{\Lambda h}$, km
60 – 120	LS (17)	82±6	0.20±0.07	60±30	470±230	280±130	2300±1200
30 – 60	LS (5)	45±4	0.14±0.04	110±20	500±90	270±50	1400±270
	MS (14)	41±4	0.13±0.04	60±20	270±70	160±40	660±150
15 – 30	MS (13)	22±1	0.13±0.05	130±40	290±90	170±50	400±130

The processes that led to the generation of LSTIDs and MSTIDs require more detailed discussion. It should be noted, however, that we do not have full confidence that all are presented in Table 4.6 TIDs are manifestations of AGWs, as there are no simultaneous measurements of variations in the parameters of the neutral atmosphere at the studied altitudes over Eastern Europe.

4.4. Disturbances in ion and electron temperatures

Detection of TIDs in variations of plasma temperatures was performed for the dates specified in Table 4.1. To do this, the inverse IS problem was solved in order to obtain variations in ion T_i and electron T_e temperatures in the altitude range of 200 – 400 km. The data were processed as described in Chapter 3. The trend was calculated at 180 and 90 min intervals. Then, the relative ion and electron temperature changes were band-pass filtered in the following ranges of 5 – 125 min and 5 – 65 min, for the respective intervals, with subsequent narrowing to 60 – 120 min and 30 – 60 min, respectively.

4.4.1. Spectral analysis of ion and electron temperatures

Fig. 4.9 and Fig. 4.10 show the altitude-time dependences of variations in ion and electron temperatures in the period range of 60 – 120 min (upper panel of each block) and 30 – 60 min (lower panel of each block). Here, the trend was calculated over an interval of 180 min, followed by filtration in the range of 5 – 125 min. Based on the results, we highlight next features.

1. Oscillations with the highest energy had the following periods. For the winter solstice, the periods were of 60 – 100 min throughout the entire interval.

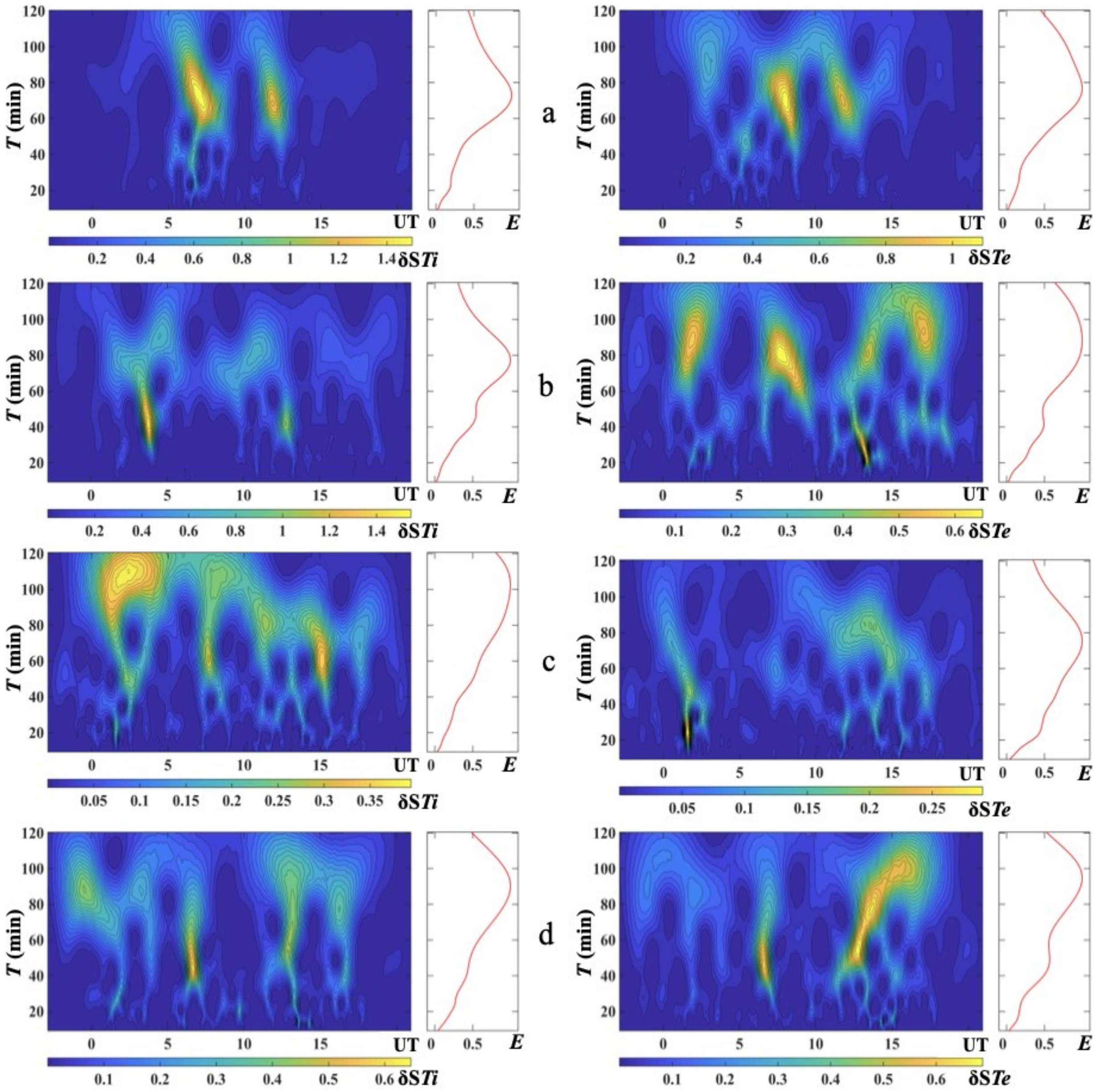

Figure 4.9. Results of spectral analysis performed for temporal variations of ion (left column) and electron (right column) temperature for (a) December 17, 2008, (b) December 14, 2009, (c) June 23, 2010 and (d) June 21, 2018 using Kharkiv data at the height of 275 km.

For the vernal equinox, they were equal to 95 min for T_e, and about 40 min and 70 min for T_i. For the summer solstice, they were 40 – 100 min throughout the day. Finally, for the autumnal equinox they were near 80 min after the passage of the morning ST for both temperatures.

2. The values of δS_{Te} and δS_{Ti} did not exceed 1, while their maxima were recorded on December 14, 2009 and September 24, 2016.

3. In general, the results of spectral analysis show a similar period-time localization of oscillations in all considered variations.

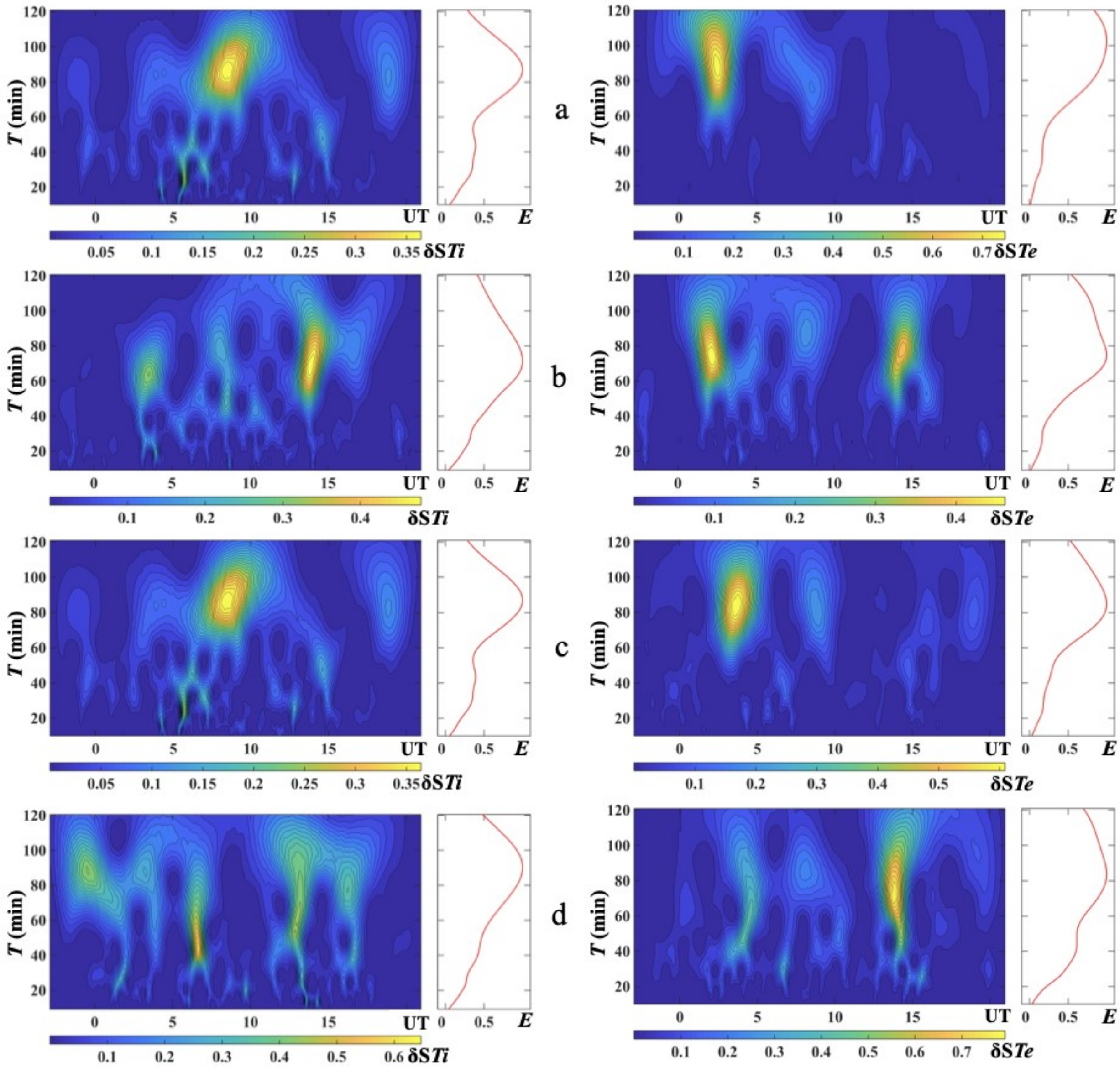

Figure 4.10. Same as Fig.4.9, but for (a) March 30, 2006, (b) March 24, 2010, (c) September 24, 2016 and (d) September 19, 2018.

4.4.2. Prevailing traveling ionospheric disturbances

For isolating TIDs with different parameters localized at different heights, additional band-pass filtering of the data was carried out. Based on the results shown in Fig. 4.8 and Fig. 4.9, another period range of 5 – 65 min was selected with the removal of the trend in the interval of 90 min. Next, filtration was performed in a narrower range of 60 – 120 min and 30 – 60 min, for the corresponding intervals.

Figures 4.11 – 4.18 show the altitude-time dependences of variations in the ion and electron temperatures band-pass filtered in the range of 60 – 120 min. Based on the results obtained, we highlight the observed features.

1. During the winter solstice, quasi-periodic processes were clearly observed throughout the altitude-time interval. Their amplitudes took the largest values.

2. Variations in ion temperatures are more intense than those in electron temperatures, except on December 17, 2008.

3. Visual analysis of the data showed an increase in relative amplitudes with an altitude of up to about 300 km, with a subsequent decrease.

4. The relative amplitudes of variations were 0.03 – 0.26 and 0.03 – 0.21 for the ion and electron temperatures, respectively.

5. The duration of TIDs in ion and electron temperatures did not exceed 2 – 5 periods.

We determined the time intervals and altitude ranges where TIDs were present, and oscillation periods. The maximum values of relative amplitudes $\delta T_{\max}$ for the ranges 60 – 120 min and 30 – 60 min were found. The results are given in Table 4.7 (for solstices) and 4.8 (for equinoxes). As can be seen from the tables, the maximum values of relative amplitudes for the ion and electron temperatures are recorded in the altitude range h_{Te} = 229 – 348 km and h_{Ti} = 220 – 367 km. Some observed disturbances, such as 14.12.2009 (two processes from 08:00 to 20:00 UT for both temperatures), 17.12.2008 (from 05:00 to 15:00 UT for ion temperature), propagating in a similar range of altitudes with similar periods, but at different times, should be referred as a single process.

The sources of the wave processes described above can be meteorological processes, solar terminator passage, as well as variations of the jet stream in the auroral zone. The results obtained are in good agreement with the results obtained by us for other observation periods.

4.4.3. TID manifestations in different ionospheric parameters

Some of the results obtained for ion and electron temperatures are in good agreement with the disturbances in the IS signal power. We compare them below.

December 17, 2008. Disturbances were detected in all considered parameters of the ionosphere (Fig. 4.5 and 4.11) throughout the day from 5 to 15 UT with similar periods of 76 min (δP), 75 min (δT_i) and 70 min (δT_e), as well as the maximum values of amplitudes in the range of 0.14 – 0.16.

December 14, 2009. Fluctuations are present in the time interval 06:00 – 11:00 UT with periods of 78 min and 75 min and the corresponding values of the maximum values of relative amplitudes δP_{max} = 0.22 and $\delta T_{e\,max}$ = 0.11.

June 23, 2010. TIDs that occurred from 14 to 20 UT in δP variations (Fig. 4.6) were detected from 10 to 15 UT in ion and electron temperatures (Fig. 4.13), with corresponding periods of 87, 39 min and 76 – 77, 39 – 40 min. Moreover, the values of the relative amplitudes of oscillations in power are greater by 65%.

Table 4.7. TIDs parameters during the winter and summer solstice.

Data	Parameter	Time, UT	Height, km	T, min	h_{max}, km	δT_{max}
17.12.2008	T_e	05:00÷15:00	250÷330	70	298	0.14
		03:00÷07:00	250÷320	40	293	0.16
		10:00÷16:00	300÷370	37	344	0.26
	T_i	05:00÷10:00	240÷350	74	275	0.15
		10:00÷15:00	260÷330	75	302	0.16
14.12.2009	T_e	00:00÷05:00	220÷300	81	229	0.12
		06:00÷11:00	240÷300	75	289	0.11
		10:00÷14:00	280÷370	84	325	0.16
		16:00÷20:00	240÷350	87	289	0.13
	T_i	08:00÷14:00	250÷300	74	293	0.13
		16:00÷20:00	260÷300	74	293	0.09
		12:00÷15:00	250÷300	33	270	0.2
23.06.2010	T_e	09:00÷16:00	270÷350	76	312	0.12
		01:00÷04:00	240÷300	39	266	0.08
		07:00÷15:00	260÷340	40	298	0.11
	T_i	09:00÷15:00	260÷350	77	312	0.14
		11:00÷15:00	260÷340	40	298	0.11
21.06.2018	T_e	00:00÷10:00	260÷340	79	302	0.09
		11:00÷18:00	260÷370	82	312	0.12
		00:00÷08:00	250÷350	41	280	0.15
		12:00÷20:00	280÷390	39	348	0.24
	T_i	00:00÷10:00	250÷300	80	270	0.08
		00:00÷04:00	250÷330	45	280	0.1
		05:00÷08:00	240÷300	39	266	0.14
		11:00÷18:00	250÷380	36	362	0.21

June 21, 2018. Oscillations from 10 to 15 UT were registered in variations of IS signal power and electron temperature with periods of 78 and 82 min, relative amplitudes of 0.07 and 0.12, respectively.

March 30, 2006. Disturbances were recorded in all parameters after passing the morning terminator from approximately 07 to 14 UT (Figs. 4.7 and 4.15). The calculated periods were 78 min, 87 min and 81 min, the maximum amplitudes were 0.2 (at the altitude of 202 km), 0.07 (234 km) and 0.08 (220 km) for δP, δT_e and δT_i, respectively.

March 24, 2010. TIDs were detected in variations of IS signal power and electron temperature in similar time intervals approximately 00:00 – 09:00 UT. The periods and values of the maximum amplitudes differ significantly, namely 84 min and 75 min and 0.15 and 0.09 for δP and δT_e, respectively.

Table 4.8. TID parameters during the spring and autumn equinoxes.

Data	Parameter	Time, UT	Height, km	T, min	h_{max}, km	δT_{max}
30.03.2006	T_e	00:00÷04:00	230÷310	85	257	0.11
		05:00÷11:00	190÷310	87	234	0.07
		11:00÷14:00	290÷370	79	335	0.06
		03:00÷06:00	240÷310	37	298	0.05
		07:00÷12:00	290÷370	41	344	0.08
		11:00÷16:00	260÷310	37	284	0.07
	T_i	07:00÷15:00	200÷280	81	220	0.08
		09:00÷15:00	290÷380	85	348	0.13
		03:00÷07:00	260÷310	40	289	0.1
		12:00÷15:00	250÷310	39	270	0.12
24.03.2010	T_e	00:00÷10:00	240÷330	76	293	0.09
		12:00÷17:00	260÷330	76	302	0.1
		00:00÷09:00	260÷320	31	284	0.06
		11:00÷17:00	280÷350	40	307	0.09
	T_i	12:00÷17:00	240÷330	80	293	0.09
		11:00÷16:00	260÷350	42	330	0.17
24.09.2016	T_e	01:00÷06:00	250÷350	84	289	0.1
		07:00÷12:00	260÷350	76	307	0.11
		12:00÷17:00	280÷350	41	312	0.09
	T_i	06:00÷14:00	260÷350	81	293	0.12
		03:00÷10:00	260÷330	39	284	0.1
		11:00÷16:00	260÷310	43	275	0.08
19.09.2018	T_e	00:00÷18:00	240÷390	81	321	0.19
		07:00÷12:00	250÷370	40	321	0.15
	T_i	22:00÷05:00	240÷350	74	289	0.12
		07:00÷18:00	260÷390	75	367	0.15
		22:00÷00:00	260÷350	40	335	0.1
		04:00÷15:00	260÷330	43	321	0.14

September 24, 2016. Fluctuations in the time interval from 01:00 to 06:00 UT were detected with the same periods of 84 min and similar intensity. The maximum amplitudes varied about 0.12 for the two parameters of the ionosphere δP (Fig. 4.8) and δT_e. (Fig. 4.17) Also, disturbances from 05:00 to 14:00 UT were found in all analyzed parameters, with the smallest values of the period and amplitude detected in the electron temperature.

September 19, 2018. TIDs with a period of 40 min occurred in δP and δT_e variations during 06:00 – 12:00 UT. The relative amplitudes reached 0.15, while a similar process was observed in δT_i variations, but with a period of 43 min.

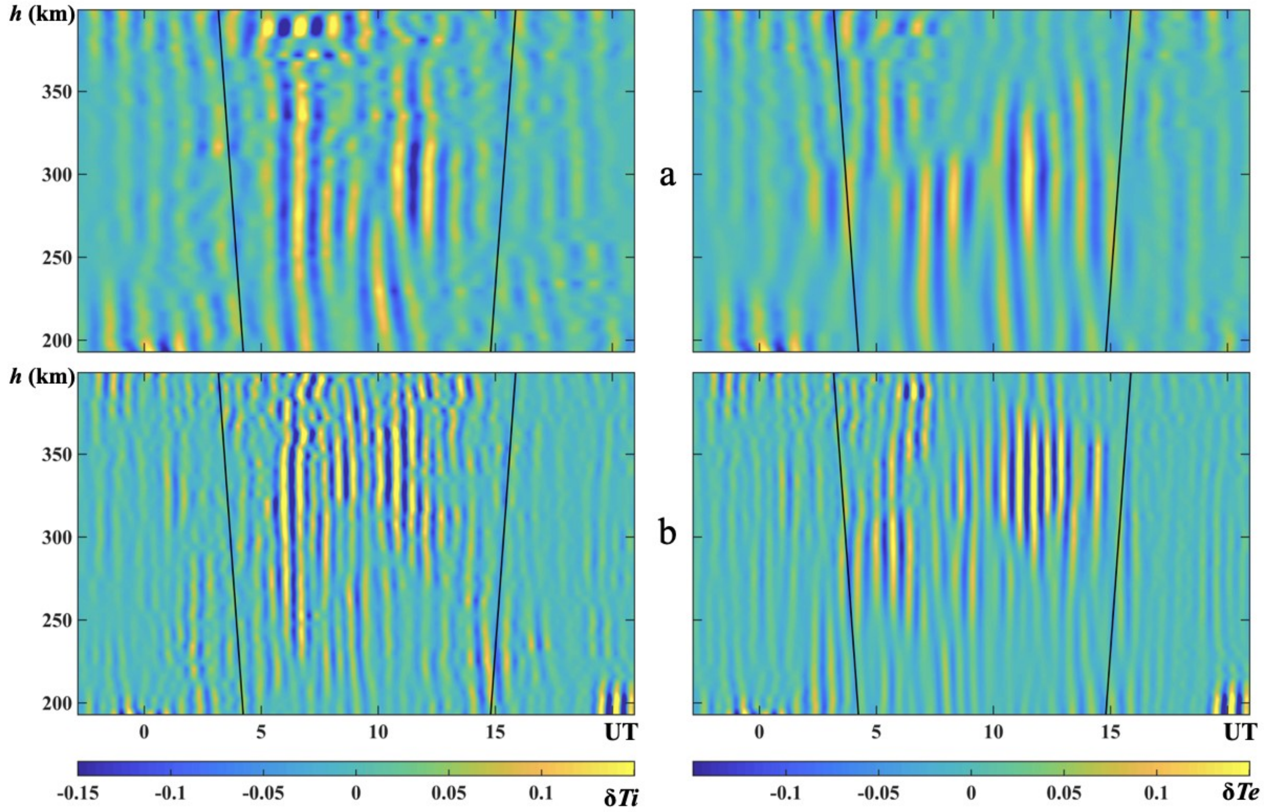

Figure 4.11. Altitude time dependences of 60 – 120 min (top panel) and 30 – 60 min (bottom panel) band-pass filtered relative variations in ion (a) and electron (b) temperatures for December 17, 2008.

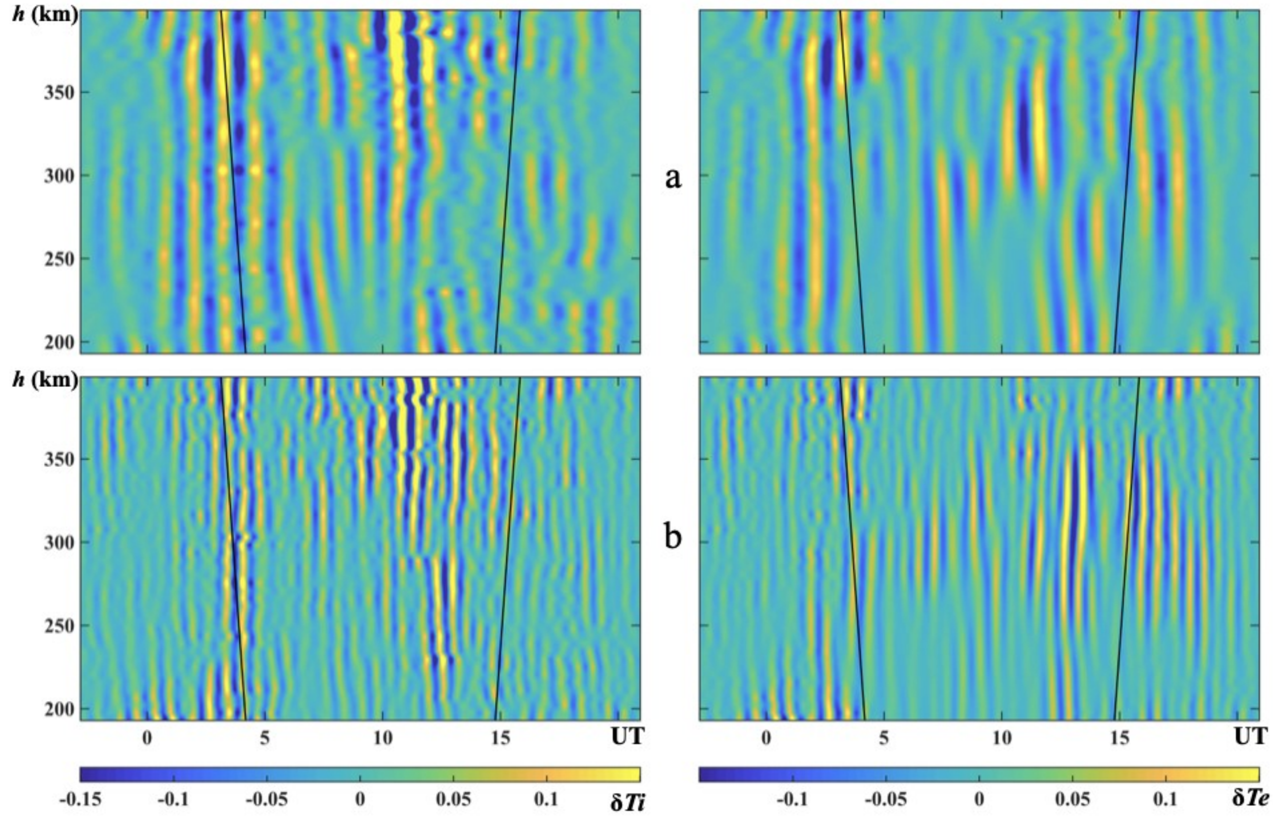

Figure 4.12. Same as Fig. 4.11 but for December 14, 2009.

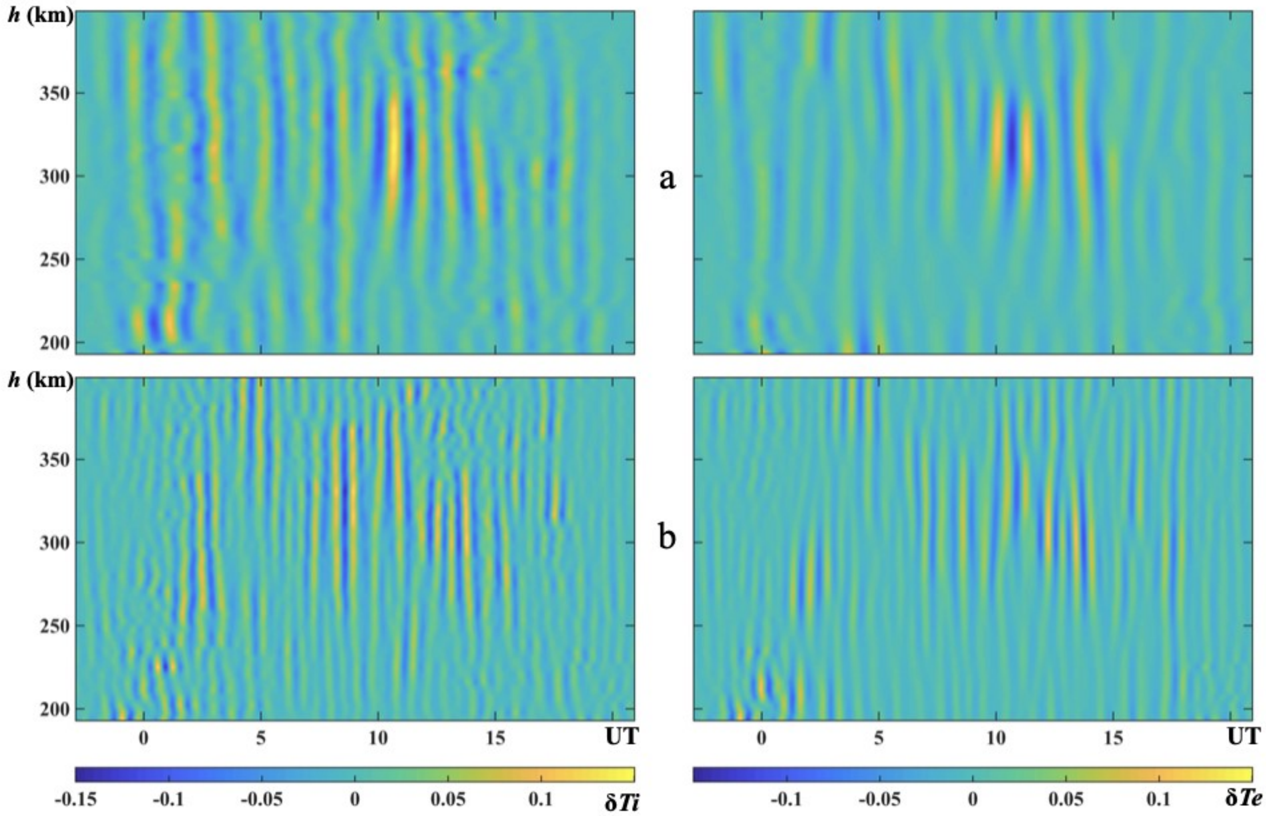

Figure 4.13. Same as Fig. 4.11 but for June 23, 2010.

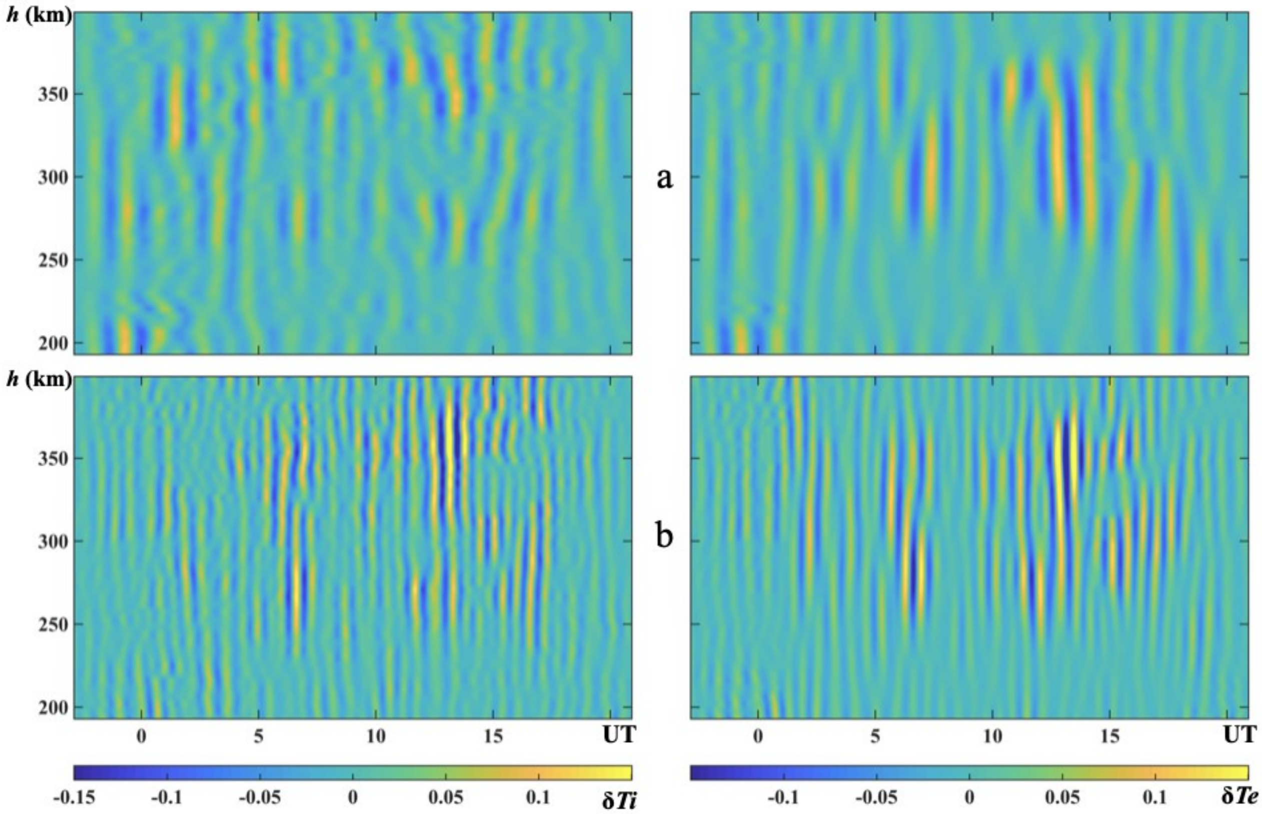

Figure 4.14. Same as Fig. 4.11 but for June 21, 2018.

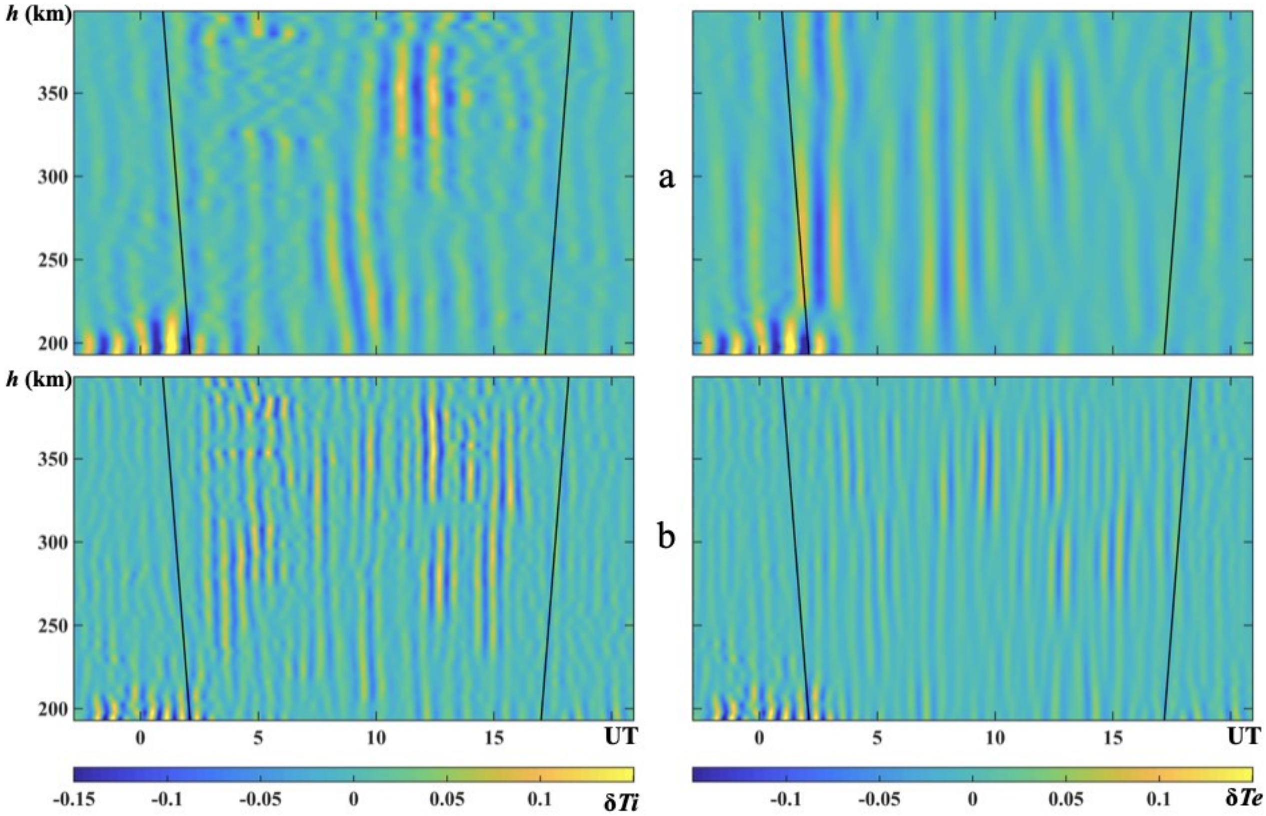

Figure 4.15. Same as Fig. 4.11 but for March 30, 2006.

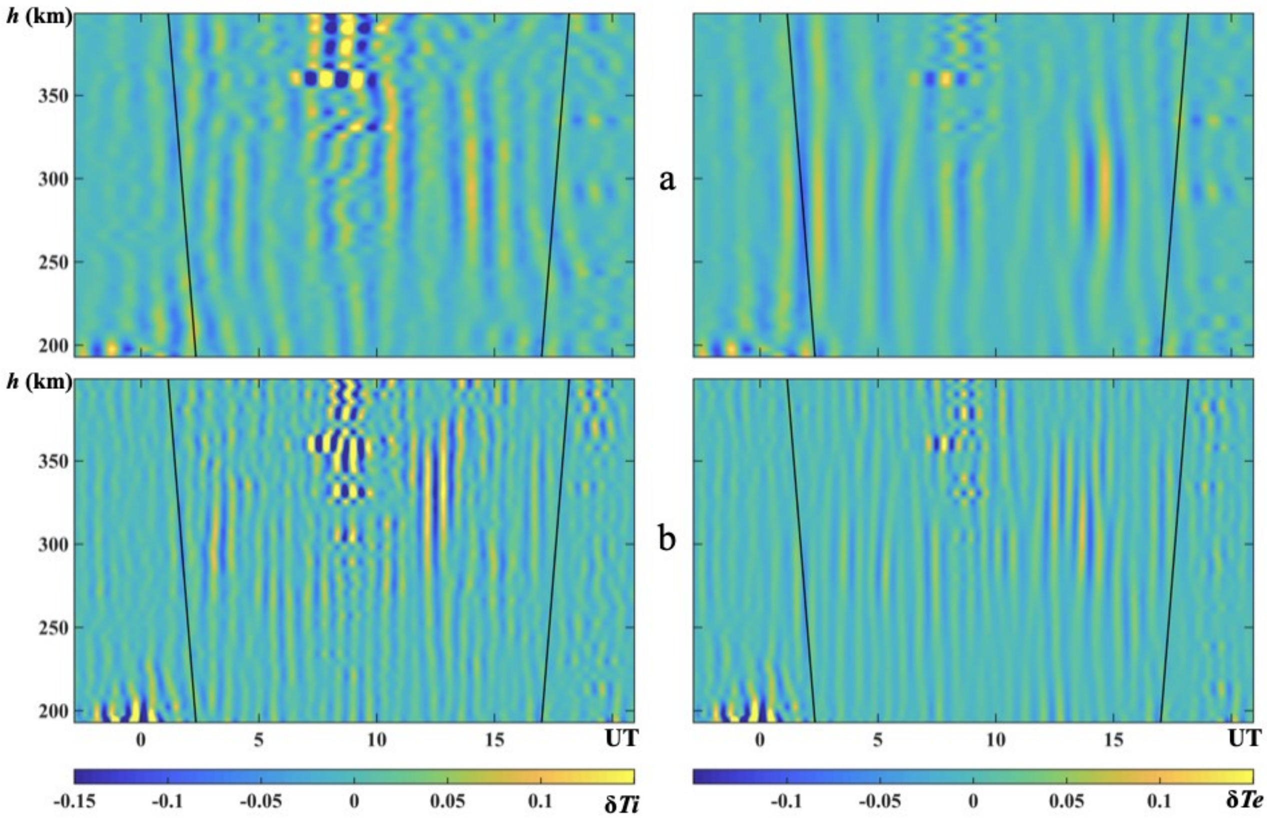

Figure 4.16. Same as Fig. 4.11 but for March 24, 2016.

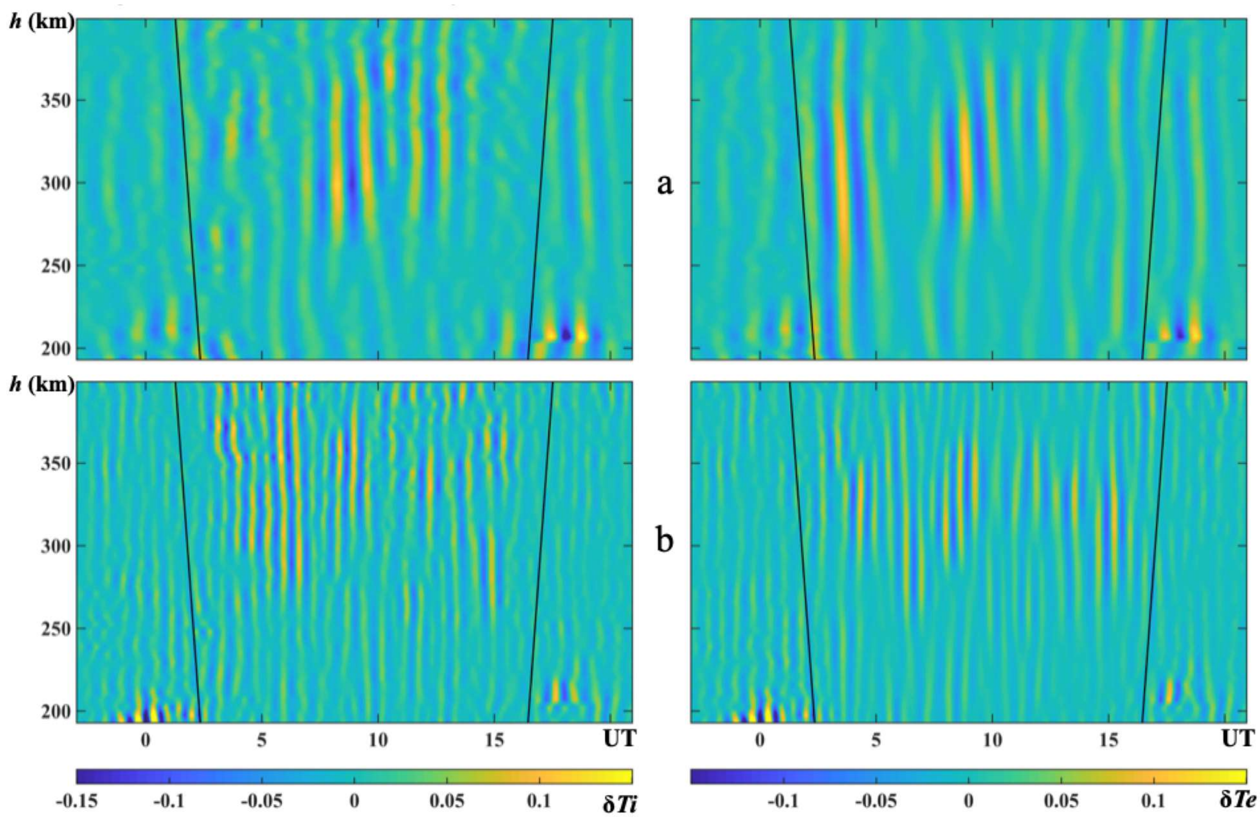

Figure 4.17. Same as Fig. 4.11 but for September 24, 2016.

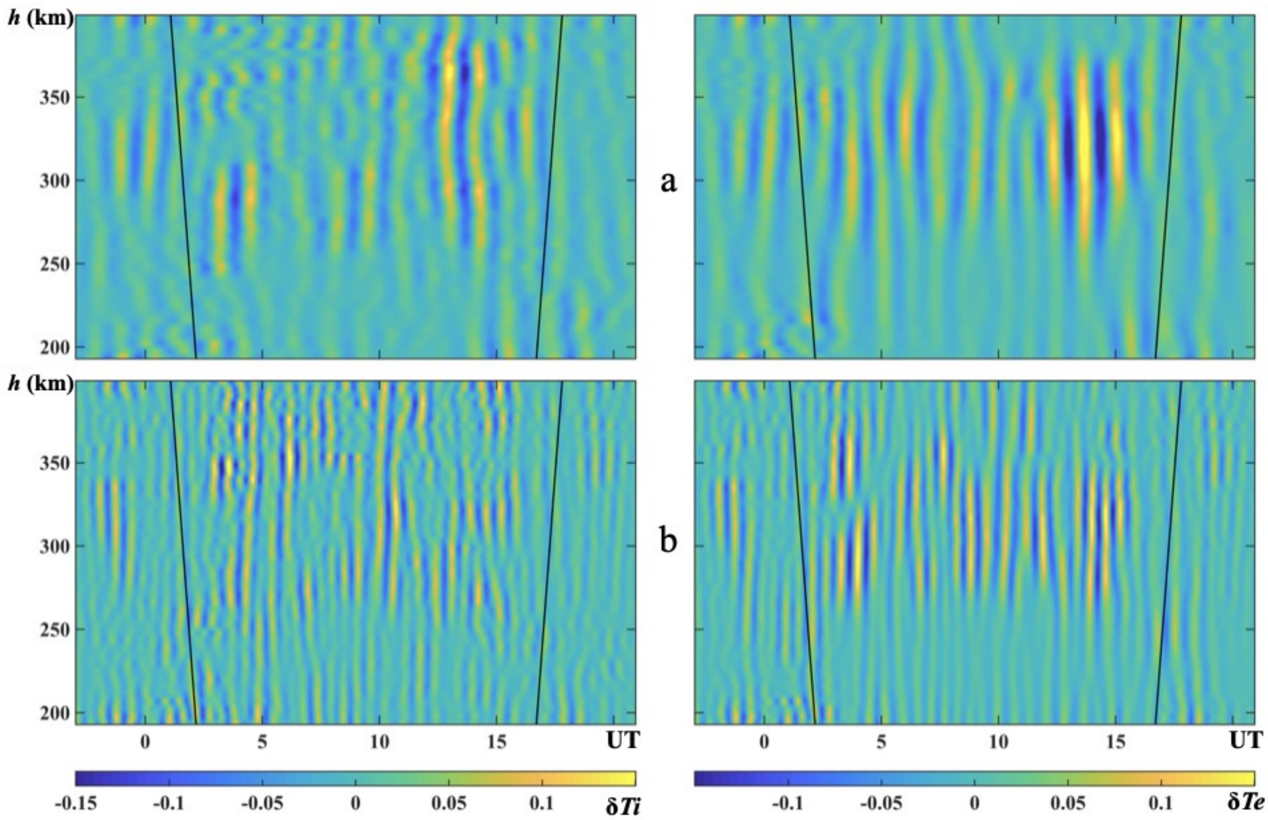

Figure 4.18. Same as Fig. 4.11 but for September 19, 2018.

In general, the obtained results of the calculated parameters of TIDs in different variations do not always agree, which is due to the modes of operation of the IS radar. A pulse with a length of 663 μs is used to find the ion and electron temperatures. It leads to errors in detecting temperature parameters due to insufficient resolution about 100 km, while for a pulse of 135 μs used to find variations in IS signal power, the resolution is about 20 km. Also, AGWs and TIDs are better expressed in one parameter. For example, in it was shown [Vlasov et al., 2011] that TIDs are more often manifested in variations of the plasma drift velocity.

Summarizing the above, the main conclusions of observations of traveling ionospheric disturbances under magnetically quiet conditions are the following.

1. Studies performed near characteristic geophysical periods revealed traveling ionospheric perturbations in a wide range of periods of 5 – 125 min, with relative amplitudes reaching 5 – 30% of background values in variations of IS signal power as well as ion and electron temperatures.

2. Spectral analysis showed that the disturbances with periods of 60 – 120 min had the greatest energy. Additionally, the data were band-pass filtered in the sub-bands of the periods 15 – 30 min and 30 – 60 min. The presence of quasi-periodic processes is demonstrated in all considered intervals for δP and from 30 to 120 min for δT_e and δT_i in all seasons.

3. For the relative variations of the IS signal power, it was found that in 83% of cases (49 events), the detected TIDs are most likely manifestations of AGWs that propagate from lower altitudes. Both large-scale and medium-scale disturbances were detected for all seasons. It is shown that the number of detected LSTIDs (22 events) was not much less than the number of observed MSTIDs (27 events). It was demonstrated that the largest number of TIDs and the maximum values of their relative amplitudes were observed near the winter solstice. It is shown that in 17% of cases (10 events) the detected ionospheric disturbances were not caused by the propagation of AGWs.

4. We calculated and evaluated the parameters of AGWs/TIDs for δP. It is shown that the average values of LSTID parameters in the sub-bands of 30 – 60 min (average oscillation period is 45 min) and 60 – 120 min (average oscillation period is 82 min), respectively, were as follows: maximum relative amplitude of IS signal variations is 0.14 and 0.20; vertical phase velocity is 100 m/s and 60 m/s; horizontal phase velocity is 500 m/s and 470 m/s; vertical wavelength is 290 km and 280 km; horizontal wavelength is 1400 and 2300 km. The average values of these parameters for medium-scale AGWs/TIDs in the sub-bands 15 – 30 min (average oscillation period is 22 min) and 30 – 60 min (average oscillation period is 41 min) were 0.13 and 0.13, respectively (maximum relative amplitude of variations); 130 and 60 m/s (vertical phase velocity); 290 and 270 m/s (horizontal phase velocity); 170 and 160 km (vertical wavelength); 400 and 660 km (horizontal wavelength).

5. The maximum values of relative amplitudes for δT_e and δT_i were in the intervals 0.03 – 0.26 and 0.03 – 0.21, respectively. Disturbances were observed at altitudes from 190 to 390 km, their duration did not exceed 2 – 5 periods. The obtained results for ion and electron temperatures are in good agreement with the variations detected in the IS signal power.

CHAPTER 5

TRAVELING IONOSPHERIC DISTURBANCES DURING MAGNETIC DISTURBANCES AND STORMS

This chapter aims at results of wave process analysis for geomagnetic disturbance and storm periods during 2012 and 2016. We report the altitude-time dependences of relative variations in IS signal power, ion and electron and ion temperatures. The parameters of traveling ionospheric disturbances are calculated for these periods.

5.1. Information about magnetic disturbances and storms

The following observations were obtained during magnetic storms that occurred in 2012 and 2016. The values of such indices as $F_{10.7}$, K_p, D_{st}, describing the state of solar and geomagnetic activity, are listed in Table 5.1. The table shows that the analyzed periods are characterized by different levels of solar activity from 77 to 143. The K_p index reached the values of 5 – 6. The periods of November 15, 2012 and August 31, 2016 (italicized in the Table 5.1) were included as magnetically quiet reference days, where $K_p \leq 3$ and $A_p \leq 8$.

Table 5.1. Space weather state

Data	$F_{10.7}$	A_p	K_p	D_{st}, nT	
				max	min
13.11.2012	143	15	4 3 2 3 3 4 3 3	4	–29
14.11.2012	139	33	6 6 5 4 4 2 1 1	–35	–108
15.11.2012	*138*	*5*	*1 1 0 1 0 0 1 1*	*–22*	*–40*
17.03.2016	92	21	5 5 3 4 2 3 3 3	–23	–52
22.06.2016	78	14	1 1 1 2 2 3 5 4	14	–10
31.08.2016	*99*	*8*	*2 2 1 1 2 1 3 3*	*7*	*–19*
01.09.2016	97	36	4 4 5 4 4 3 5 6	–12	–59
02.09.2016	96	39	6 6 3 3 5 4 3 5	–20	–58
03.09.2016	100	40	4 6 5 4 4 4 4 5	–23	–50

5.1.1. Storm in November, 2012

The geomagnetic storm occurred against the background of moderate solar activity (in the period from November 11 to 17, the values of the $F_{10.7}$ index were in the range of 135 – 146). The storm was caused by coronal mass emissions on November 9 and 10, 2012, which were directed towards the Earth. The maximum values of the geomagnetic activity indices were as follows $K_{p\,\max}$= 6, $D_{st\,\min}$ = -108 nT and $AE_{\max}$ = 1009 nT. According to the generally accepted classifications, the storm on November 13 – 14, 2012 is the moderate storm [Vadas & Liu, 2009].

5.1.2. Storms in March and June, 2016

Geomagnetic storms occurred against the background of low solar activity (the values of the index $F_{10.7}$ were 92 and 78 for March 17 and June 22, 2016, respectively). The maximum values of the geomagnetic activity indices were as follows: $K_{p\,\max}$ = 5, $D_{st\,\min}$ = –52 nT та –10 nT та $AE_{\max}$ ≈ 750 and 1200 nT. According to the classifications, storms on March 17 and June 22, 2016 are the weak storms.

5.1.3. Storm in September, 2016

The geomagnetic storm occurred against the background of low solar activity (the values of the $F_{10.7}$ index varied slightly, ranging from 96 to 100). At the same time, on August 31, 2016, three weak X-ray flares were detected (the highest flare was C2.2). On August 31, 2016, the index of geomagnetic activity K_p did not exceed 3, and $A_p \le 8$, which allowed considering this day as magnetically quiet. The maximum values of the geomagnetic activity indices were as follows: $D_{st\,\min}$ = –59 nT and $AE_{\max}$ > 1500 nT. According to the classifications, the storm on September 1 – 3, 2016 is the moderate storm.

5.2. Results of spectral analysis

Due to the great variety of sources, wave processes can exist in the ionosphere in a wide range of periods. However, studies often concern only the most energetic TIDs, as they significantly contribute to the coupling of different atmospheric and ionospheric regions. Using the developed IS radar data processing algorithms described in Chapter 3, the detection of TIDs and evaluation of their parameters were performed in the altitude range of 100 – 400 km. For identifying the predominant TIDs, a spectral analysis of time variations in the IS signal power, as well as ion and electron temperatures (200 – 400 km) was performed within the specified altitude range with a step of 25 km. The presence of localized in the time and frequency ranges of δS_p values at a number of heights was interpreted as a possible manifestation of TIDs.

5.2.1. Analysis of IS power variations for November 13 – 15, 2012

We studied wave processes in the range of periods 10 – 120 min [Barabash et. al., 2017]. The results of the analysis of time variations of the IS signal power are shown in Fig. 5.1. Each panel represents the periodograms on the left, and the corresponding energy dependences, that are integrals of spectrograms in the time and reflects the energy distribution density over the period, on the right. The vertical axis is the period in mins, the horizontal axis is the time in UT.

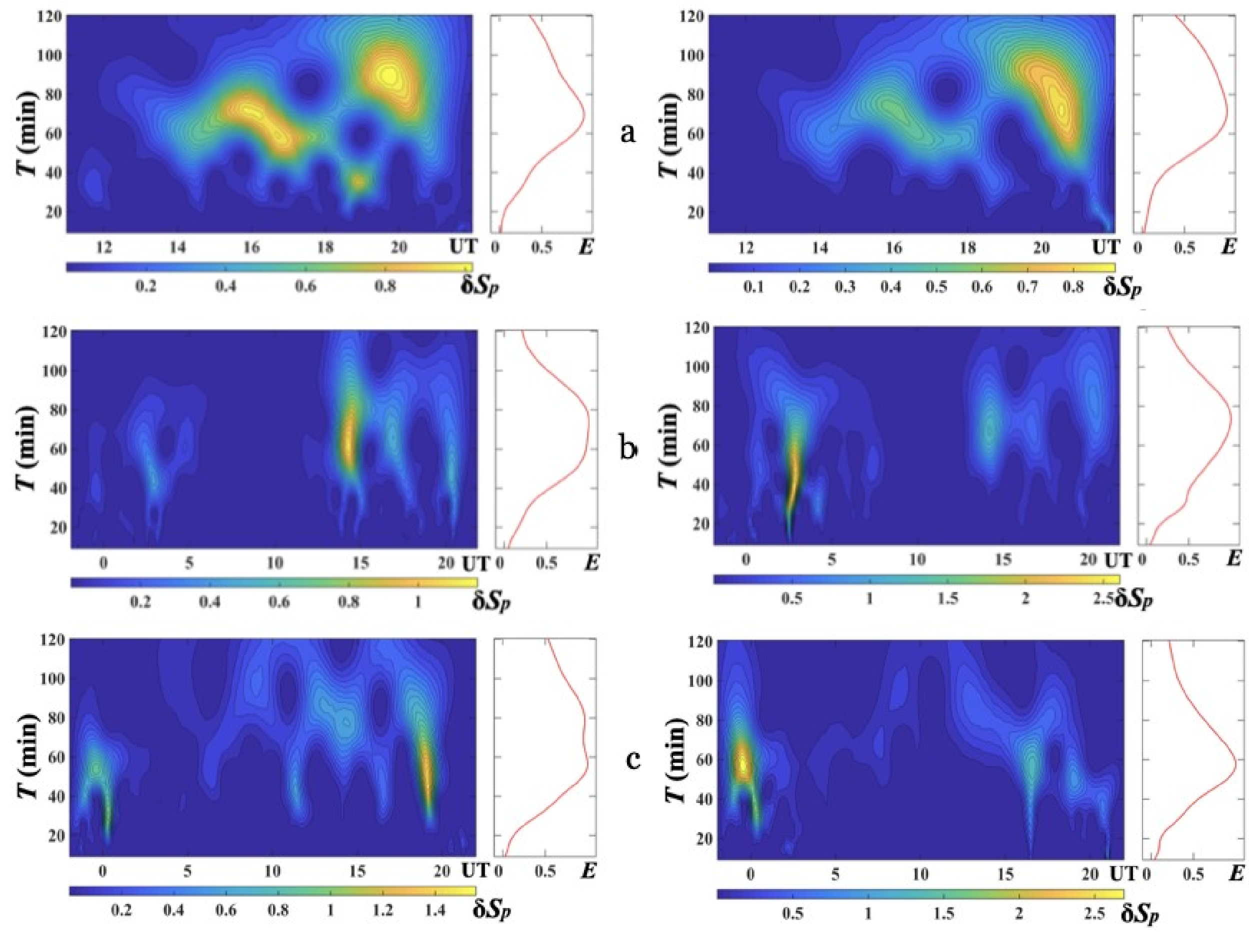

Figure 5.1. Results of spectral analysis performed for temporal variations of IS signal power for November 13 (a), 14 (b) and 15 (c), 2012 using Kharkiv data at the height of 225 km (left panel) and 250 km (right panel).

Fig. 5.1 shows that wave processes with different periods were observed in IS power variations for all days of observations. Thus, on 13 November 2012 waves with a period of 60 – 90 min occurred in the time interval of 14 – 21 UT (Fig. 5.1,a). On November 14, 2012, two types of wave disturbances were observed. The first one had a predominant period of about 50 mins and occurred in the morning, in the interval of 2 – 5 UT. The second one with a period of about 70 mins was observed in the evening, from 14 to 21 UT (Fig. 5.1,b). On November 15, 2012, a number of wave processes were observed in a wide range of periods of 30 – 90 min throughout the day (Fig. 5.1,c). It should be noted that the values of relative amplitudes δP are higher for an altitude of 225 km, except for November 13, where these values are higher at 200 km.

Detected wave processes can be caused by a geospace storm, as well as other natural high-energy sources. The fact that the wave activity enhanced on the morning and evening hours indicates the solar terminator as the most probable additional source of their generation.

5.2.2. Analysis of IS power and temperature variations for March and June, 2016

Figs. 5.2 and 5.3 illustrate periodograms for relative variations of ionospheric parameters obtained using Kharkiv and Millstone Hill radars at fixed altitudes of 280 km for spring and 260 km for summer. We studied the TIDs with periods from 16 to 120 min which correspond to AGW-period range. The lower limit is defined as double time rate of Millstone Hill ISR data. The choice of the upper boundary was made to avoid the data contamination by long period variations including those caused by tidal harmonics.

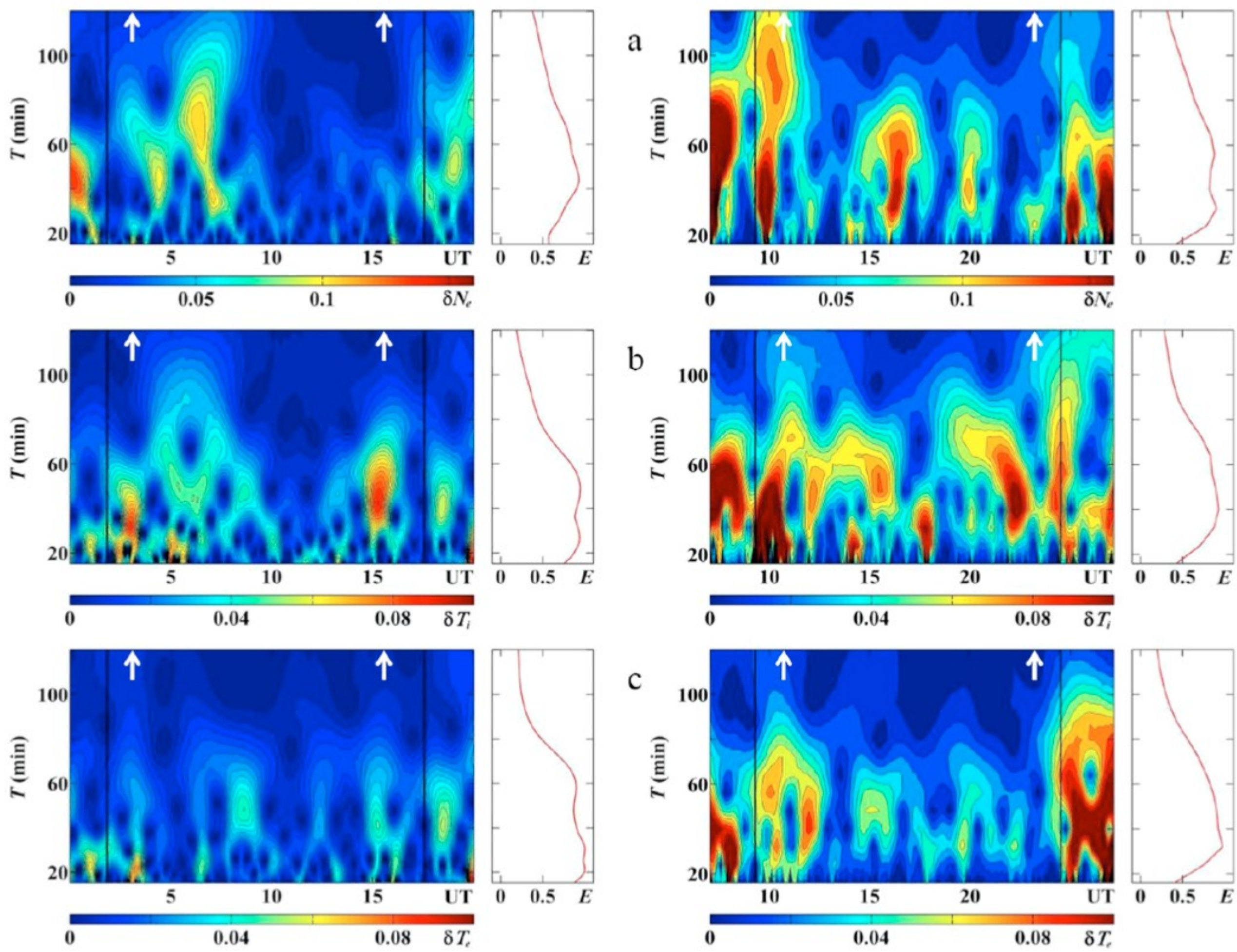

Figure 5.2. Results of spectral analysis performed for temporal variations of (a) electron density, (b) ion temperature and (c) electron temperature using (left column) Kharkiv and (right column) Millstone Hill data at the height of 280 km for March 17, 2016.

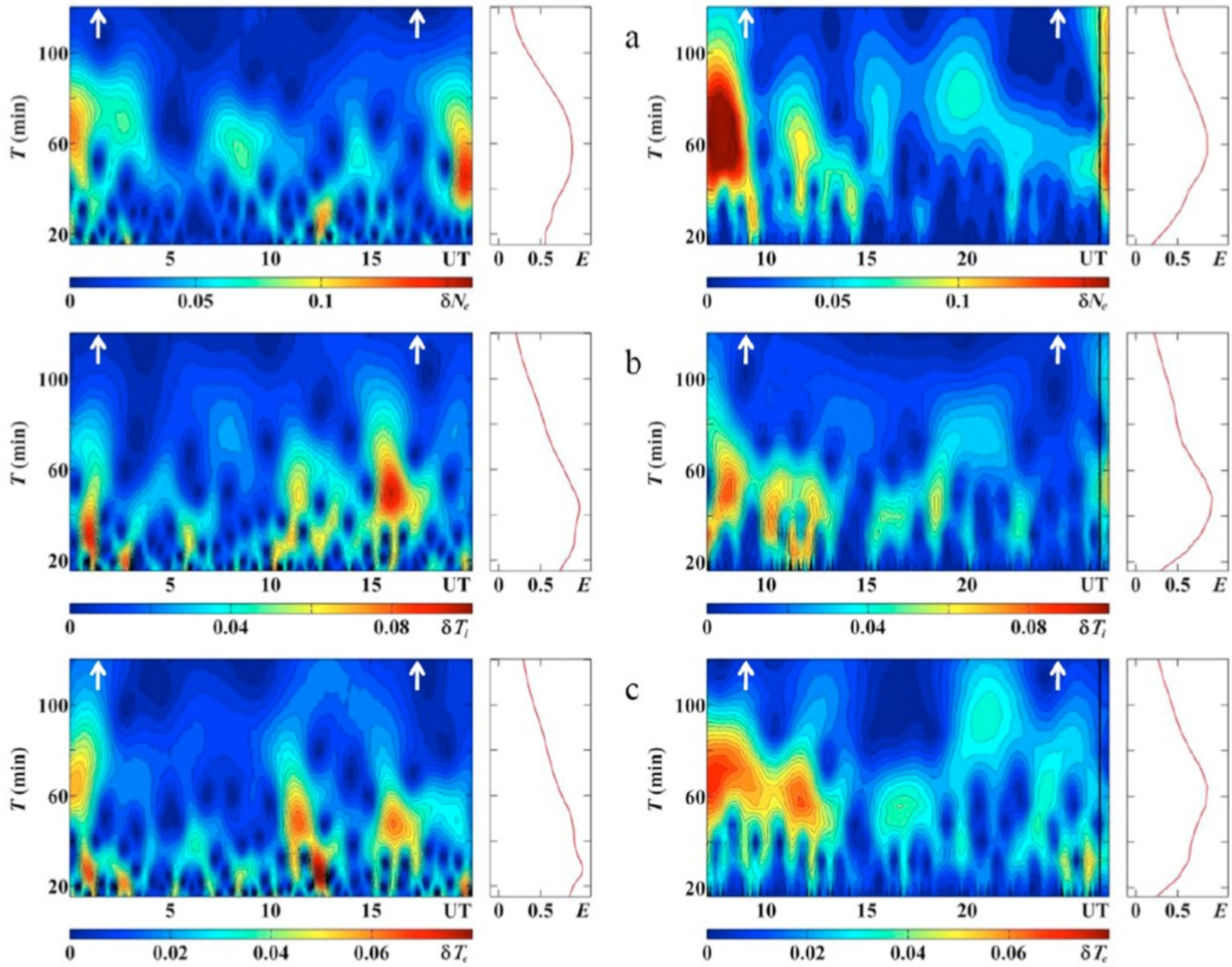

Fig. 5.3. Same as Fig. 5.2 but at the altitude of 280 km for June 22, 2016.

As shown in Fig. 5.2, strong quasi-periodic variations were observed during equinox measurements over both Kharkiv and Millstone Hill. Usually they are strongest near the sunrise and sunset terminators, but on this day TIDs amplitudes in electron density and ion temperature over Kharkiv were not very strong near the solar terminator (see Fig. 5.2,a and 5.2,c). The predominant periods of variations in electron density were close to 45 min for Kharkiv. At the same time, the energygrams (shown to the right of each panel in Fig. 5.2) of both temperature time series exhibit the local maximum near 50 min together with additional maxima, one for ion temperature close to 25 min and two for electron temperature corresponding to the periods of about 20 and 30 min. Two peak periods in electron density over Millstone Hill are close to about 30 and 60 min, whereas prevailing oscillations in temperatures cover a wide range of periods extending from 30 to 70 min without sharp maxima at energygrams.

The behavior of temporal variations during summer solstice period was similar to described above for equinox conditions (see Fig. 5.3). The spectral components of variability in the same ionospheric parameters obtained with two different ISRs have nearly similar relative amplitudes in T_e and T_i, and higher amplitude for TIDs in N_e for Millstone Hill. The maximum amplitudes in N_e and T_e over Kharkiv as well as in N_e over Millstone Hill are nearly the same as those obtained from the springtime campaign, but amplitudes in both ion and electron temperatures over Millstone Hill became smaller. The prevailing oscillations in N_e over both sites have periods falling within a range of 40 – 80 min. The energygrams produced from temperatures over Kharkiv have two peaks near 30 and 45 – 50 min, but second maximum for T_i is weak. Notably, the major peaks in $E(T)$ dependences for temperatures over Millstone Hill correspond to the periods shifted relative to one another. The oscillations in T_e have longer period (about 60 min) than in T_i (about 50 min).

The time intervals with pronounced oscillations are often very similar for different ionospheric parameters during both campaigns, indicating that observed variations did not appear randomly but are apparently caused by a passage of the TIDs. The maximum amplitudes in observed parameters both occur at same times and periods and are shifted related each other. Some discrepancies may be also due to the presence of aperiodic processes and the errors in ionospheric parameter retrieval [Panasenko et al., 2018].

5.2.3. Analysis of IS power and temperature variations for September 1 – 3, 2016

In order to exclude the effects of ST, the parameters of TIDs were estimated only for the daytime from 06 to 18 UT. We studied wave processes in the range of periods of 10 – 120 mins. The trend was determined at an interval of 180 min with a step of 1 min. Then, obtained after subtracting the trend and normalizing the relative variations of the analyzed variations to it, δP, δT_i and δT_e, were subjected to band-pass filtration in a wide range of periods from 5 to 125 min. Here we describe the characteristics of TIDs during this magnetic storm.

Examples of the spectral analysis results at altitudes of 275 km are presented in Figs. 5.4 and 5.5. Periodograms and energygrams often show close localization of oscillations in the period and time domains that occurred in variations of the IS signal and ionosphere parameters on a specific day, although a number of differences was spotted. On the magnetically quiet day of August 31, 2016, two pronounced quasi-periodic processes with T of approximately 80 and 100 min were observed in δP variations near 6:00 UT and 15:00 UT, respectively.

The same two oscillations were detected in ion and electron temperatures. The first oscillation was near 08:00 UT ($T \approx 80$ min and $T \approx 60$ min for δT_i and δT_e, respectively), and the second oscillation had the same period and time of existence as that in variations of IS signal power. During September 1, 2016, two predominant wave processes were also detected in the variations of δP and δT_i. The first of them had a period of $T \approx 80$ min in IS power variations and $T \approx 90$ min in ion temperature variations and was observed between 08:00 – 10:00 UT for both parameters. For the second oscillation, which was present from 12:00 to

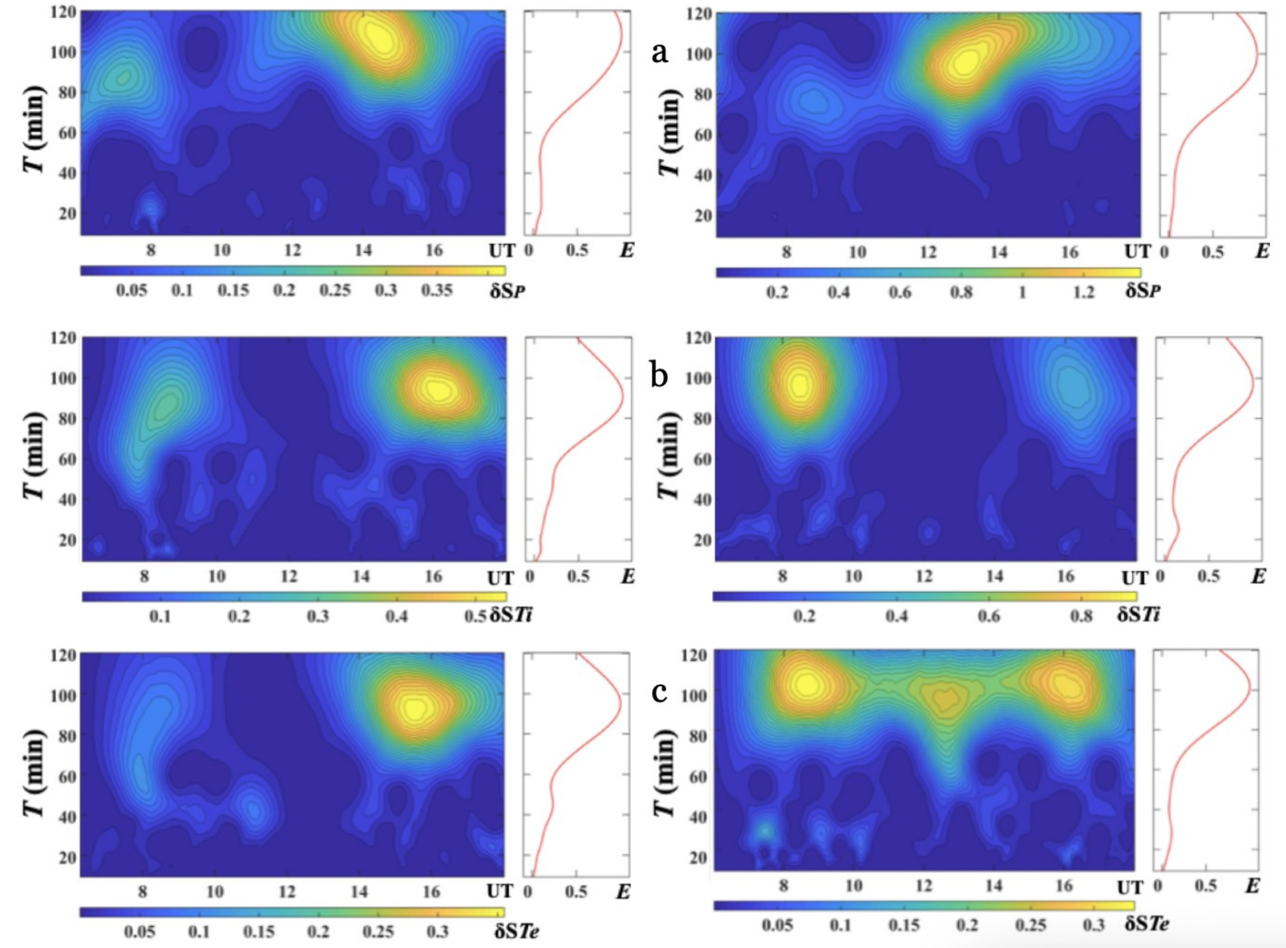

Figure 5.4. Results of spectral analysis performed for temporal variations of IS signal power (a), ion (b) and electron (c) temperature for August 31 (left column) and September 1 (right column), 2016 using Kharkiv IS data at the altitude of 275 km.

15:00 UT and from 15:00 to 18:00 UT in variations of δP and δT_i, respectively, $T \approx 100$ min. Interestingly, on this day, the relative variations of T_e were quasi-harmonic with $T \approx 100$ min during almost the entire observation interval, but their intensity was approximately twice less than the intensity of the first wave process in δT_i. In the afternoon of September 2, 2016, δP variations revealed three fluctuations near 07:00 UT, 13:00 UT and 18:00 UT with periods of approximately 110, 80 and 70 min, respectively. Two oscillations were revealed in ion and electron temperatures: from 07:00 to 10:00 UT ($T \approx 80$ min) and from 14:00 to 17:00 UT ($T \approx 90$ min) in δT_i, as well as from 06:00 to 08:00 UT ($T \approx 60$ min) and from 13: 00 to 17:00UT ($T \approx 100$ min) in variations of δT_e. Finally, on September 3, 2016, in the relative variations of the IS signal power, three oscillations were detected near 06:00 UT, 09:00 UT and 17:00 UT with periods close to 80, 60 and 70 min, respectively. On the same day, in the variations of δT_i and δT_e, two quasi-harmonic processes were observed with the following characteristics: periods of 70 and 110 min (from 06:00 to 10:00 UT), 70 and 90 min,

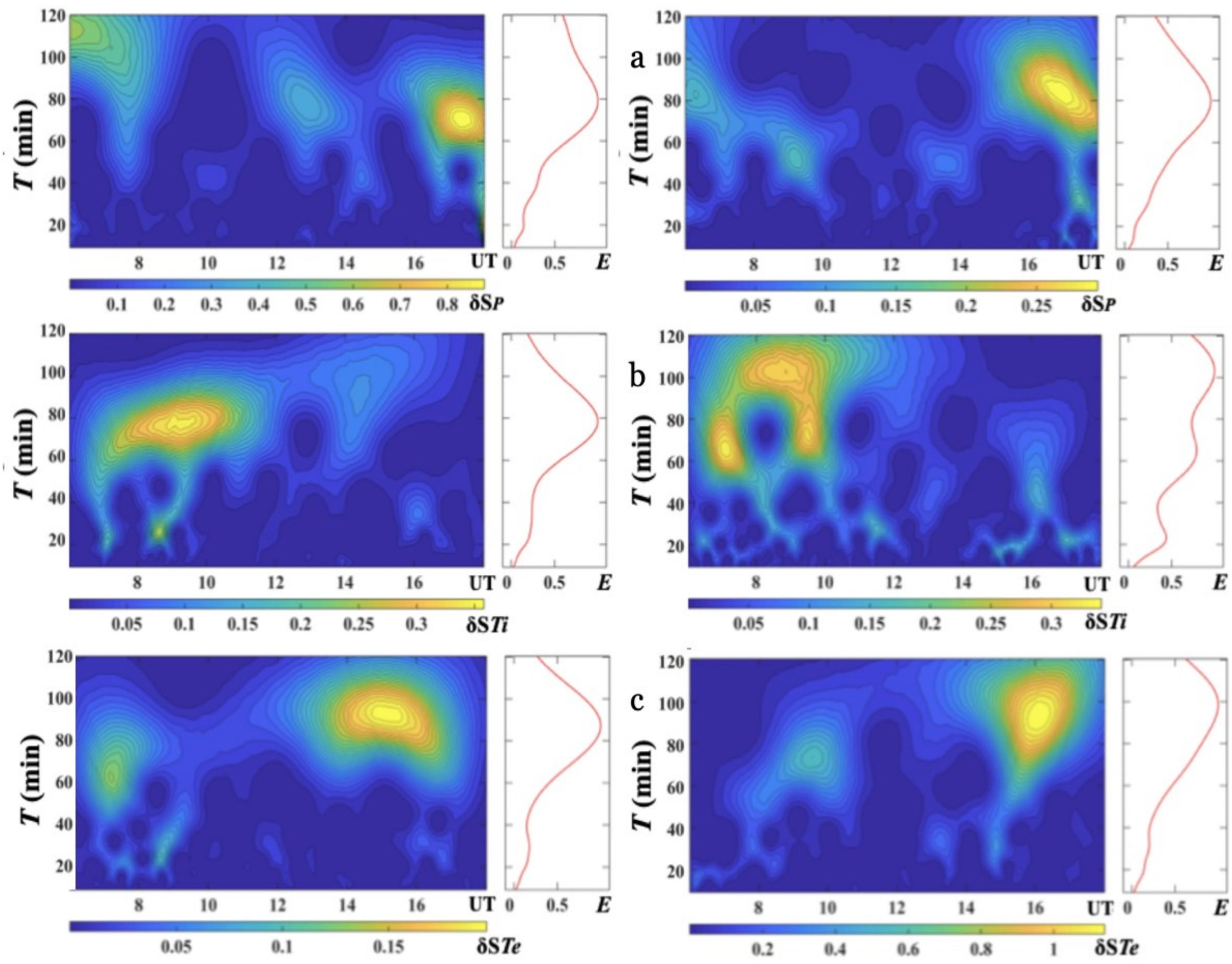

Figure 5.5. Same as Fig. 5.4 but for September 2 (left column) and 3 (right column), 2016.

presence time of 08:00 – 12:00 UT and 13:00 – 17:00 UT., Periodograms show that the intensity of oscillations in all analyzed parameters during the geospace storm was usually higher than on the quiet day, except for the above described variations of δT_e for September 1, and δT_i for September 2, 2016 (see Figs. 5.4, 5.5).

5.3. Estimation of TID parameters

Based on the main periods of TIDs, the appropriate range was selected for further band-pass filtering in a narrower range. The figures below show the altitude-time dependences of the filtered variations of the IS signal power as well as ion and electron temperatures. For δP, the altitude range from 100 to 400 km is considered. The available altitude range for estimating variations in ion and electron temperatures is from 200 to 400 km. The results of cross-correlation analysis of the relative variations of the IS power, as well as the amplitude of these oscillations are presented.

According to experimental data, the altitude ranges at which TIDs are present were determined, the TIDs periods were specified; the $h_{\max}$ heights at which relative amplitudes reached maximum values (and these values themselves) were found; the vertical V_z, Λ_z and horizontal V_h, Λ_h components of phase velocity and wavelength were estimated.

5.3.1. Parameters of predominant TIDs for March and June 2016

Figs. 5.6 and 5.7 present TIDs in relative variations of ionospheric pa- rameters in altitude-time domain. During the vernal equinox, the relative amplitudes over Kharkiv are usually 0.03 – 0.15 of background electron density, and in plasma temperatures do not exceed 0.1. These amplitudes are notably higher over Millstone Hill, by a factor of about 3 in N_e (reaching up to 0.3 – 0.35) and by a factor of 2 in plasma temperatures (reaching 0.1 – 0.15). TIDs are amplified near local solar terminators, although they are also observed throughout the day at both locations (see Fig. 5.6).

The overall wave activity estimated through the occurrence rate of TIDs and the maximum values of their relative amplitudes appears to be weaker during summer solstice, especially over Millstone Hill. The values of relative amplitudes over Kharkiv are 0.08 – 0.15 and 0.03 – 0.08 of background electron density and plasma temperatures, respectively. These values are similar for Millstone Hill (see Fig. 5.7).

Compared with equinox conditions, relative TID amplitudes over Kharkiv are essentially unchanged, whereas those over Millstone Hill are significantly decreased. The solstice TIDs over Millstone Hill are mainly observed around solar terminator periods, similarly to equinox. We note that during summer solstice the ionosphere over Kharkiv is sunlit all the time at heights over 260 km. Appearance of increased TID activity around 00:00 UT and 20:00 UT in Kharkiv data is consistent with times of sunrise and sunset at lower altitudes and ground level, supporting suggestions that solar terminator AGW are generated not in-situ but in the lower atmosphere, and propagate to the F–region where they can be observed by different instruments.

For both observational periods, most of the constant phase lines substantially curve toward increasing time at lower altitudes. Such slopes are easier detected over Millstone Hill due to better height resolution. Millstone Hill data were obtained with alternating code mode that yields 4.5 km range resolution, while Kharkiv ISR operated in unmodulated pulse mode with resolution of about 100 km. In addition, results in Figs. 5.6 and 5.7 span relatively long time range (20 h) that makes it difficult to visually detect the line slopes. Fig. 5.8,a presents one of the TID events occurring after sunrise terminators to demonstrate an oblique pattern in altitude-time behavior. The tilt of constant phase lines indicates the downward phase progression, and therefore the vertical phase velocity of TIDs to be directed downward. It confirms the interpretation of TIDs in terms of manifestation of AGWs propagating from below,

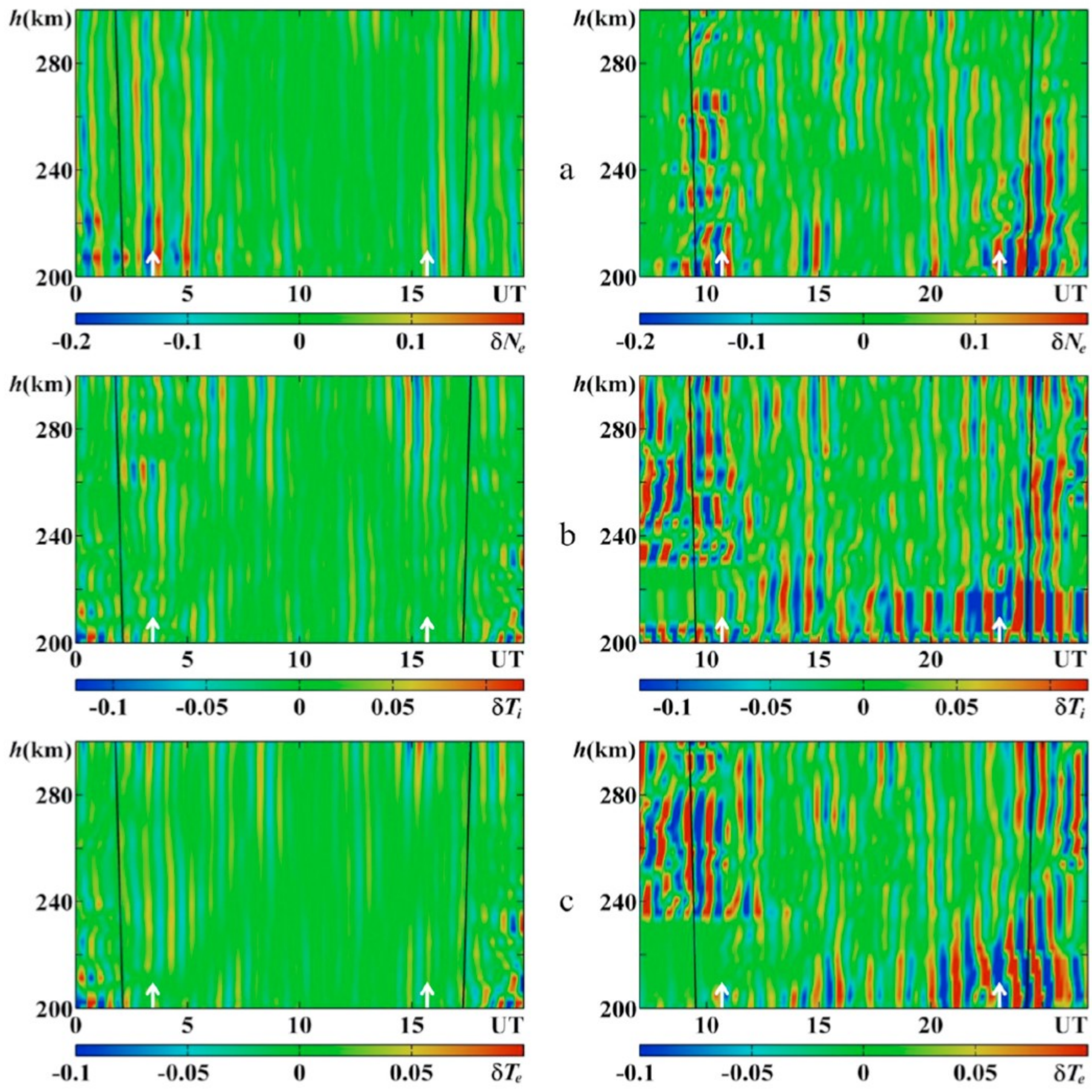

Figure 5.6. Altitude time dependence of 40 – 80 min bandpass filtered relative variations of (a) electron density, (b) ion temperature and (c) electron temperature for March 17, 2016 from (left column) Kharkiv and (right column) Millstone Hill radar data.

since the vertical component of AGW group velocity is well known to be opposite to the phase velocity. Duration of TID events over each radar site usually varies from 2 to 5 periods.

We also analyzed phase relationships between quasi-periodic oscillations of N_e, T_i and T_e in time and altitude intervals where TIDs are well defined for all ionospheric parameters under study. Fig. 5.8,b shows that the phase differences between any two parameters for the same TID depend on height and are different for Kharkiv and Millstone Hill sites. In addition, both phase advance and lag occur for plasma temperatures with respect to N_e. Throughout this paper we

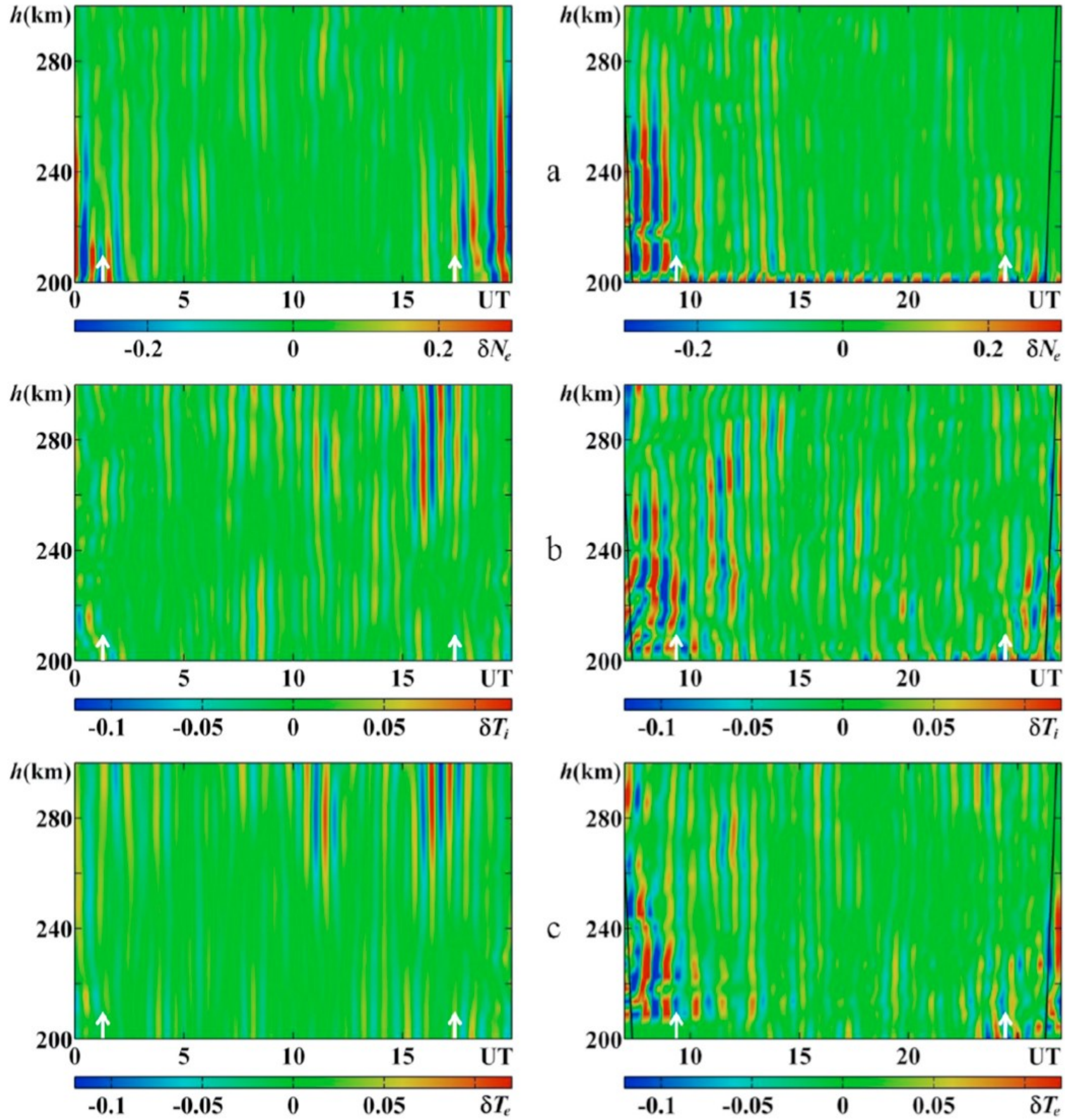

Figure 5.7. Same as Fig. 5.5 but for June 22, 2016.

use terms as phase advance and lag of first ionospheric parameter with respect to the second one if local maximum in the quasi-periodic variations of first parameter occurs earlier or later, respectively, over an analyzed time interval. Similar behavior in variations of ionospheric parameters is also observed during the summer solstice (not shown).

Fig. 5.8,b clearly demonstrates that the variations in N_e, T_i and T_e have unequal but close main periods which slightly vary with time. Because of this, we use cross-correlation analysis to estimate the values of phase differences $\Delta\varphi$ using average period of 60 min.

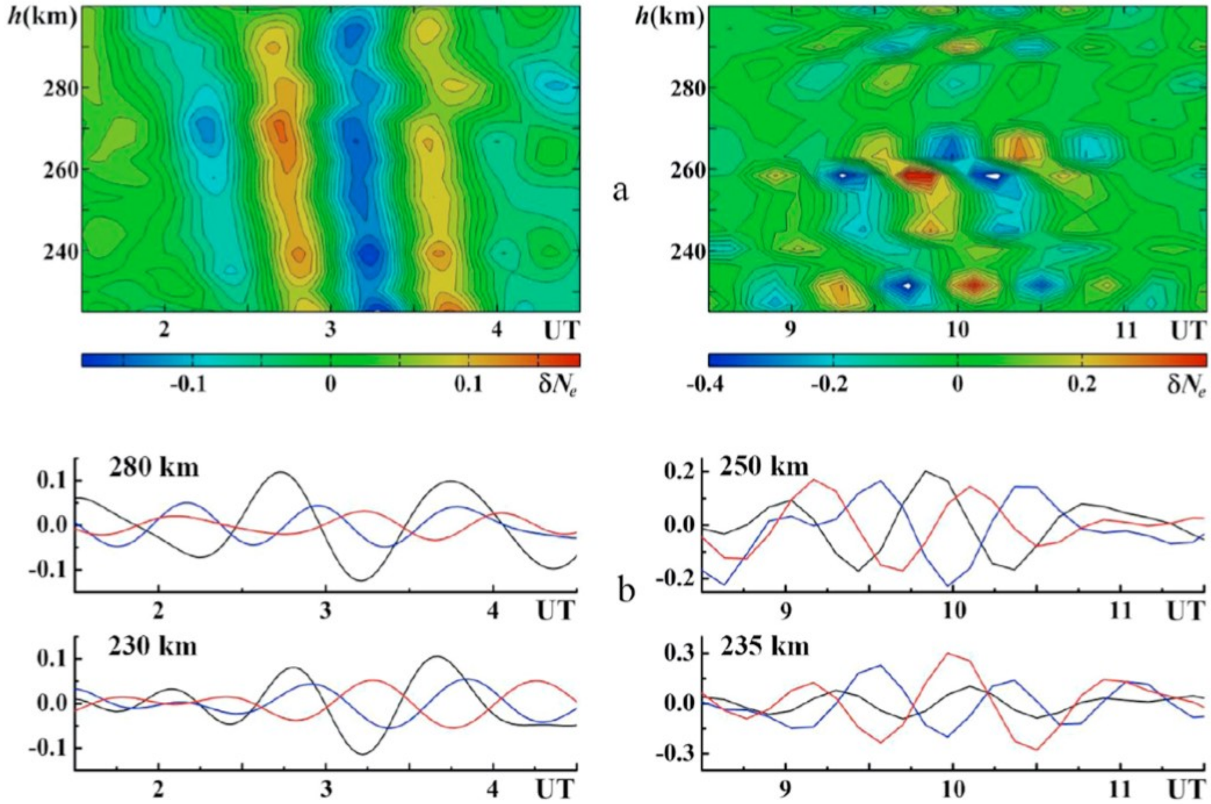

Figure 5.8. Relative variations of ionospheric parameters near sunrise terminator filtered in the band 40 – 80 min for March 17, 2016 from (left column) Kharkiv and (right column) Millstone Hill radar data: (a) altitude time dependence of electron density, (b) time dependence of δN_e (black), δT_i (blue) and δT_e (red) at altitudes of 230 and 280 km for Kharkiv, 235 and 250 km for Millstone Hill.

Table 5.2 provides estimated phase advances and lags between all observed ionospheric parameters for Kharkiv and Millstone Hill data during equinox and solstice conditions.

Table 5.2. Phase relationships between ionospheric parameters from cross-correlation analysis. The positive (negative) sign indicates phase advance (lag) with respect to N_e.

Site	Data	Height, km	$\varphi_{Ti} - \varphi_{Ne}$	$\varphi_{Te} - \varphi_{Ne}$	$\varphi_{Ti} - \varphi_{Te}$
Kharkiv	17.03.2016	230	−48	144	168
		280	−66	210	84
	22.03.2016	220	78	−12	100
		260	48	−48	96
Millstone Hill	17.03.2016	235	−96	48	−144
		250	144	−96	−120
	22.03.2016	235	−144	0	−144
		260	144	96	48

We define two fluctuations as being nearly in phase, quarter- phase, and antiphase if the absolute value of $\Delta\varphi$ varies from 0 to 60 deg, from 60 to 120 deg, and from 120 to 180 deg, respectively. The fluctuations in T_i are nearly in phase with N_e and nearly in antiphase with T_e at both altitudes over Kharkiv during vernal equinox. For the same season, $\varphi_{Ti} - \varphi_{Ne}$ is changed from 96 deg (nearly in quarter-phase) at 235 km to 144 deg (nearly in antiphase) at 250 km over Millstone Hill showing the height dependence. Such dependence is also visible for $\varphi_{Te} - \varphi_{Ne}$ when these parameters fluctuate nearly in phase at 235 km and nearly in quarter-phase at 250 km. Near the summer solstice, T_e and N_e are nearly in phase, whereas T_i and T_e are nearly in quarter-phase over Kharkiv. The strong height variations in $\Delta\varphi$ are observed over Millstone Hill during this period, especially between T_i and T_e, which fluctuate near in antiphase at 235 km and near in phase at 260 km (see Table 5.2). It should be noted that the time resolution of Millstone Hill data does not allow exact phase determination and can result in errors in estimation of phase differences.

The absolute variations in N_e, T_i and T_e in the period range of 40 – 80 min are displayed in Figs. 5.9 and 5.10. These dependencies provide insight into TID morphology regardless of diurnal variations in ionospheric parameters. Near the solar terminators (03 – 05 UT and 16 – 18 UT for Kharkiv), TID amplitudes reach (2 – 3)*10^{10}m^{-3} and vary slightly with height. But for the time interval 07 – 15 UT, significant decrease in N_e amplitudes is observed at altitudes of 240 – 280 km (see Fig. 5.9). In a whole, the absolute amplitudes of TIDs in N_e over Millstone Hill are lower than over Kharkiv by a factor of 2. Such TIDs are almost always present at heights of 200 – 300 km from 12:00 to 18:00 UT and don't exhibit enhanced amplitudes near terminators. The TIDs in plasma temperatures with the greatest absolute amplitudes are mainly observed near solar terminators both over Kharkiv and Millstone Hill (see Fig. 5.9,b and c). These amplitudes reach 70 K and demonstrate strong height variability. They are decreased in the height range of 230 – 260 km during 05:00 – 20:00 UT over Kharkiv, like those for TIDs in N_e.

For summer solstice, TID absolute amplitudes in all studied ionospheric parameters are greater over Kharkiv than over Millstone Hill by a factor of 1.5 – 3 for different TIDs (see Fig. 5.10). Their values over Kharkiv are close to those observed during vernal equinox. We detect the increase in TID absolute amplitudes in ion and electron temperatures over Kharkiv in the height range of 240 – 300 km. Such amplitudes over Millstone Hill usually do not exceed 1.5*10^{10} m^{-3} and 40 K in electron density and plasma temperatures, respectively.

To summarize, TIDs with periods of 40 – 80 min are observed during two joint observational campaigns over both Kharkiv and Millstone Hill locations and over a wide range of heights. Their characteristics, such as absolute and relative amplitudes, time of appearance, durations and phase differences show strong height and seasonal variability. Such variability can be partially related to different levels of geomagnetic activity during the days of joint observations. In some cases, TIDs are most pronounced only in one or two ionospheric parameters.

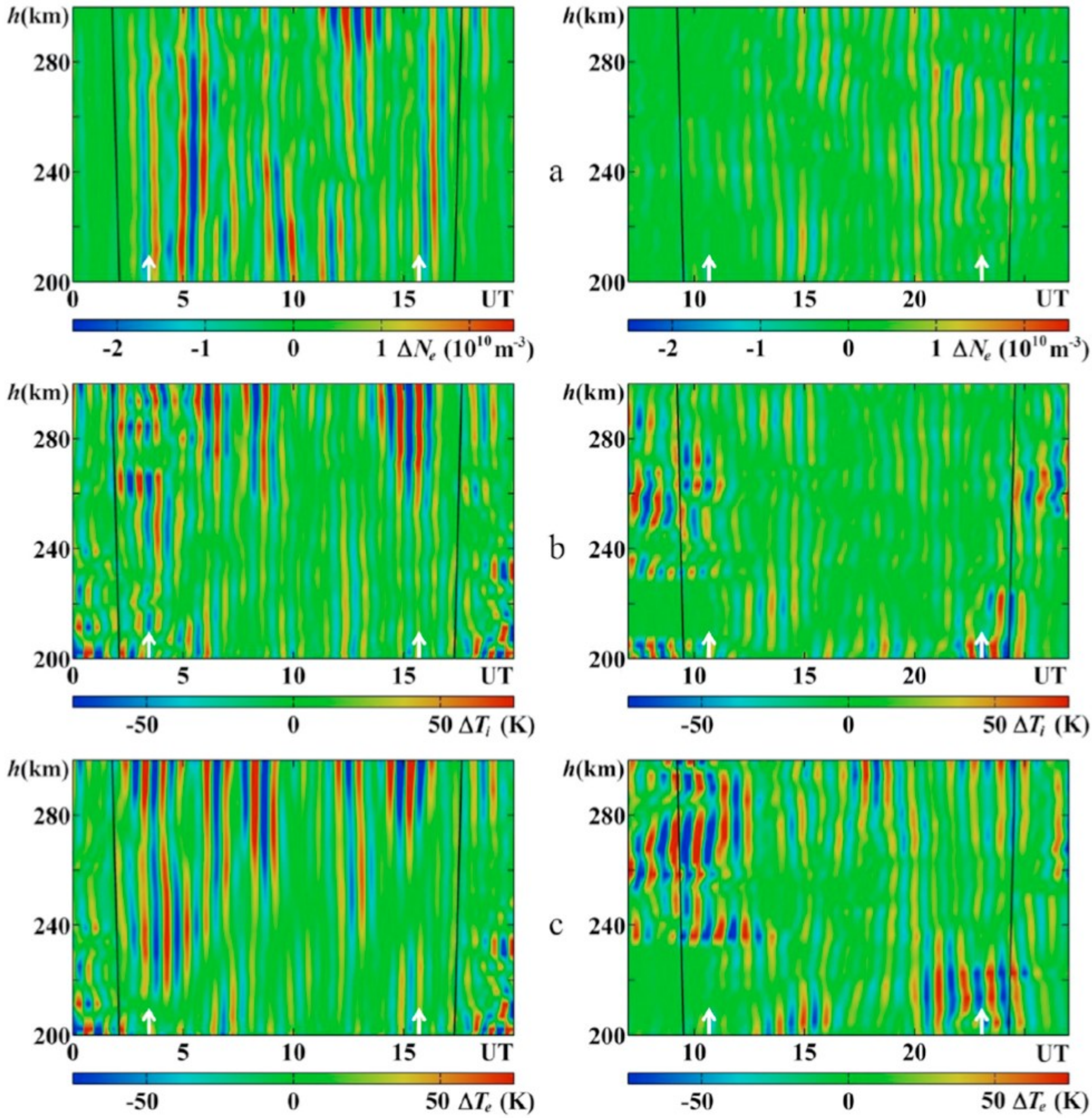

Figure 5.9. Altitude time variations of 40 – 80 min band-pass filtered absolute values of (a) electron density, (b) ion temperature and (c) electron temperature for March 17, 2016 from (left column) Kharkiv and (right column) Millstone Hill radar data.

It is interesting to note that relative amplitudes are substantially greater over Millstone Hill, whereas absolute amplitudes are higher over Kharkiv.

TIDs in ISRs data (Figs. 5.9 and 5.10) are present continuously in both March and June experiments and do not show pronounced changes after the bursts of 40 –80 min wave activity in electric currents. Although our study of two observational cases is clearly not sufficient to draw firm conclusions, it suggests that auroral processes are not the likely driver of the observed TIDs. These results

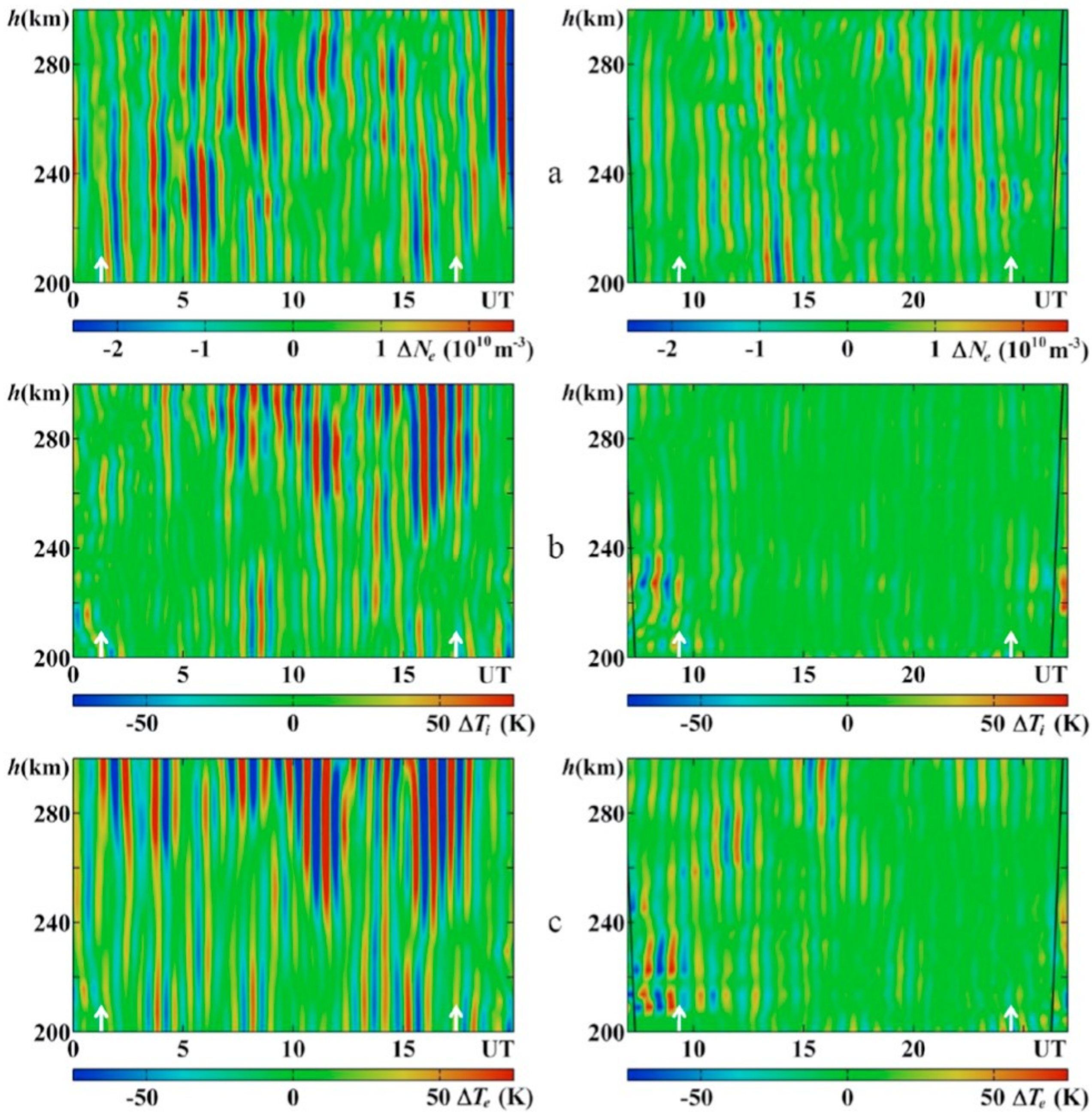

Figure 5.10. Same as Fig. 5.9 but for June 22, 2016.

are consistent with earlier studies [MacDougall & Jayachandran, 2011; Vlasov et al., 2011; Kozlovsky et al., 2013; Nygren et al., 2015], who did not find a correlation between geomagnetic activity and the observed TIDs. However, other authors [Frissell et al., 2014] detected relationship between MSTIDs and auroral electrojet variations. Statistical analysis of characteristics of TIDs observed over Kharkiv and Millstone Hill needs to be done to have reliable conclusion about TID generation during auroral electrojet variations.

Our results demonstrated that relative amplitudes of the majority of TIDs tend to be smaller with height increase (see Figs. 5.6 and 5.7). Such smooth decrease in amplitudes is caused by kinematic viscosity and thermal diffusivity [Vadas, 2007; Vadas & Nicolls, 2009]. Abrupt decrease in absolute amplitudes (up to dissappearence of TIDs) occurred in the 240 – 280 km height range in some cases as mentioned above (see, e.g., Fig. 5.9). It could be explained by the features of AGW propagation in the presence of vertical gradient of background neutral wind velocity. Indeed, the intrinsic wave angular frequency ω_I can be expressed as: $\omega_I = \omega - kU$, where ω is observed wave angular frequency, k is horizontal wave- number vector and U is vector of neutral wind velocity (see Chapter 3). AGWs propagate substantially against the wind to penetrate to ionospheric heights (e. g., [Vadas, 2007]). Hence the scalar product is often negative, and enhancement in absolute value of U will result in increase in ω_I. If ω_I is higher or equal to Brunt–Väisälä frequency, AGWs become evanescent at some height range and can tunnel into the greater heights when the vertical scale of evanescence is smaller than the vertical wavelength. The vertical shears of background neutral wind could be responsible for observing altitude variations in TID amplitudes over Kharkiv and Millstone Hill sites.

In some cases, AGW/TID signatures in this study are detected not simultaneously in all analyzed ionospheric parameters. The authors [Vlasov et al., 2011] reported that TID behavior is better manifested in V_i than in other data. Moreover, they also showed that the numbers of observed events in N_e, T_i and T_e time series is not the same, in consistency with our observations. Following [Vlasov et al., 2011], we suggest that AGW/TID signatures in some parameter are occasionally masked by other ionospheric processes. Another reason for such differences is a short-time enhancement in radio noise, affecting the result accuracy. Thus, the main criteria of AGW/TID existence are the coverage of wide height range by oscillations in all or some measured ionospheric parameters together with their height phase progression.

The phase differences between TID parameters are poorly known at present. To our knowledge, only small number of publications devoted to study of phase relationships (see, e.g. [Hocke & Schlegel, 1996]). These authors presented the results concerning high latitude ionosphere using EISCAT data. They obtained average phase profiles and distributions of phase differences for 45 AGW events. The antiphase fluctuations of N_e and T_e are shown to be often present and near in phase ones for T_i and T_e are usually observed at heights below 250 km. We detected different values of $\Delta\varphi$ for these pairs of parameters from near in phase to near in antiphase fluctuations for two sites, at different heights and for equinox and solstice conditions (see Table 5.2). Such discrepancies can be associated with several reasons. The phase relationships are likely to be different at middle and high latitudes as well as dependent on altitude, season, solar and magnetic activity, etc. At present, the data volume collected during our joint ISR measurements is not enough to make conclusions about average phase behavior at mid-latitudes. Further analysis of IS data acquired for different conditions will be able to establish TID features in a number of ionospheric parameters.

Although we observed decrease in wave activity during summer solstice conditions both for Kharkiv and Millstone Hill, the amount of data obtained during two joint observational campaigns is insufficient to discuss seasonal variation of TID characteristics. To describe seasonal features, we plan to conduct systematic long-term observations of wave processes in the ionosphere using all facilities situated in Kharkiv and Millstone Hill observatories. Such observations can reveal longitudinal variability in TID characteristics, provide a better understanding of the mechanisms of TID generation and propagation, and improve regional and global ionospheric models. Future cooperative efforts in radar facility improvement and experimental data processing are expected to increase accuracy and precision of obtained results and enable estimates of characteristics even for weak ionospheric disturbances generated by natural or artificial sources.

5.3.2. Parameters of predominant TIDs for September 1 – 3, 2016

As shown in Figs. 5.4 and 5.5, the periods of predominant TIDs were usually in the range of 60 – 120 minutes. This range was chosen for further band-pass filtration. Figs. 5.11 – 5.13 demonstrate the altitude-time dependences of the band-pass filtered variations in the IS signal power and plasma temperatures. This figure shows that the wave processes cover altitudes from 150 to 400 km and have selected periods and time localization, which were described above (see subsection 5.3.3).

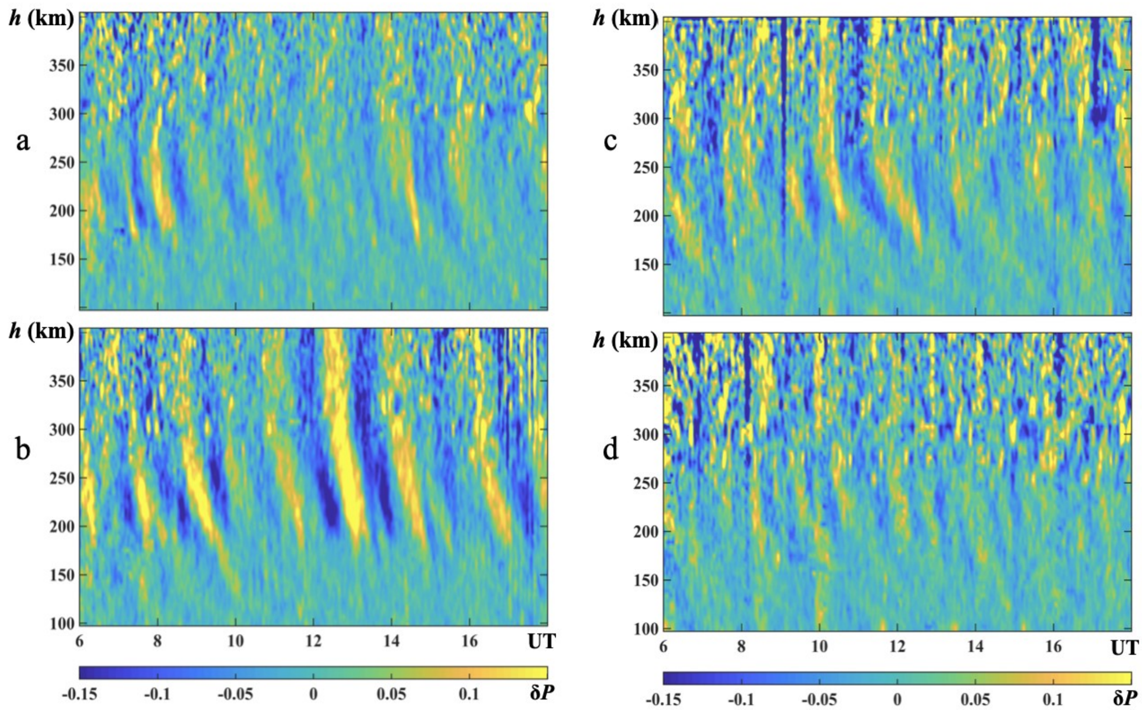

Figure 5.11. Altitude –time dependences of 5 – 125 min band-pass filtered relative variations in IS signal power for August 31 (a), September 1 (b), 2 (c) and 3 (d), 2016.

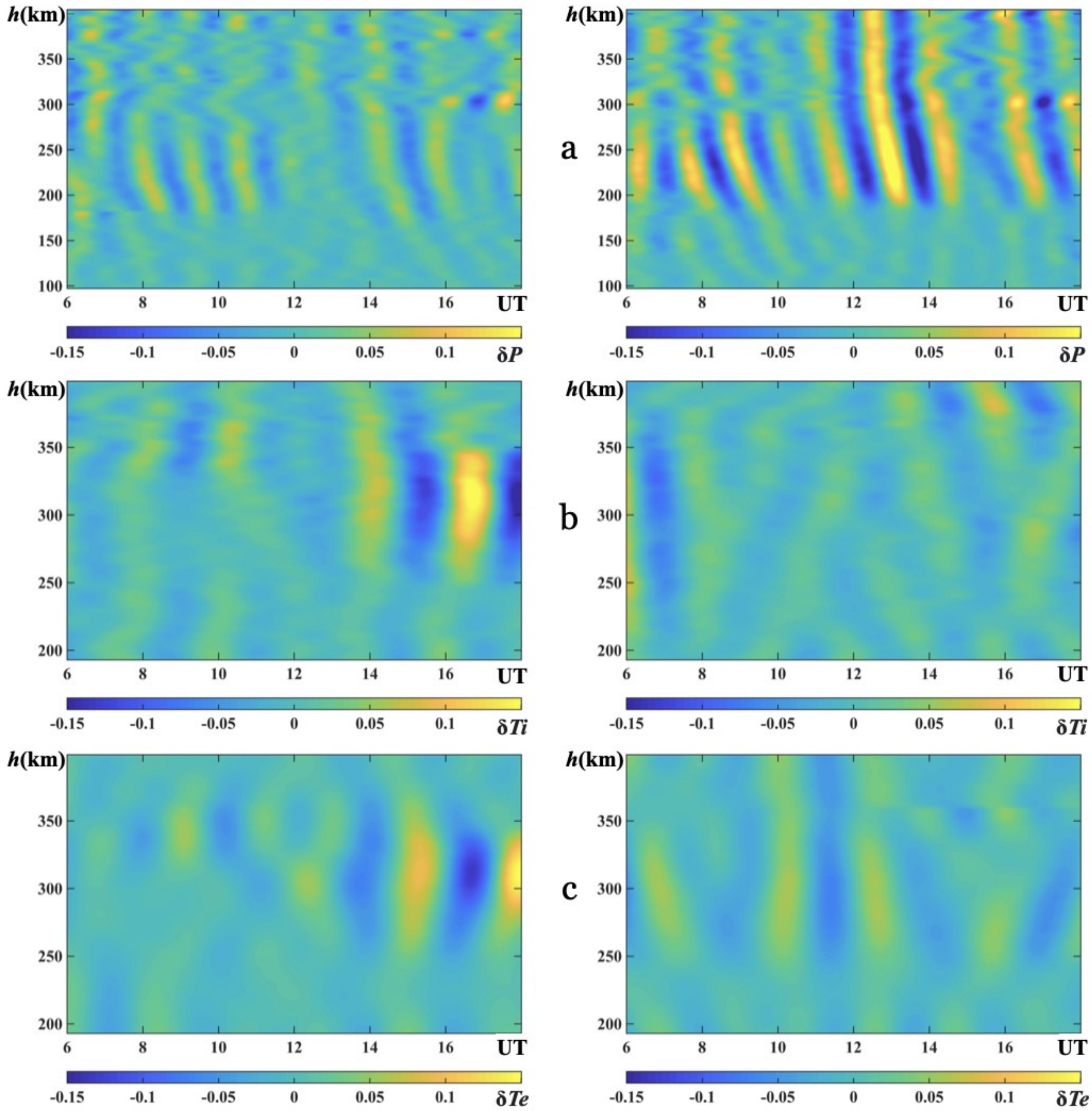

Figure 5.12. Altitude –time dependences of 60 – 105 min band-pass filtered relative variations in IS signal power (a), ion (b) and electron (c) temperatures for August 31 (left column) and September 1 (right column), 2016.

On September 1 and 2, an increase occurred in the maximum amplitudes of wave processes in the IS signal power by a factor of about 2. The relative amplitudes of TIDs in variations of plasma temperatures did not show pronounced variability from day to day, and were usually in the range of 0.03 – 0.12. The slope and curvature of the lines of the equal phase, which are better traced in the variations of δP due to the better altitude resolution, indicate that the oscillations occurred at lower altitudes, because the TID vertical phase velocity V_z had downward direction. Interestingly, the amplitudes of oscillations in IS signal power variations both exceeded and were smaller than the amplitudes of plasma temperatures on different days and for different TIDs.

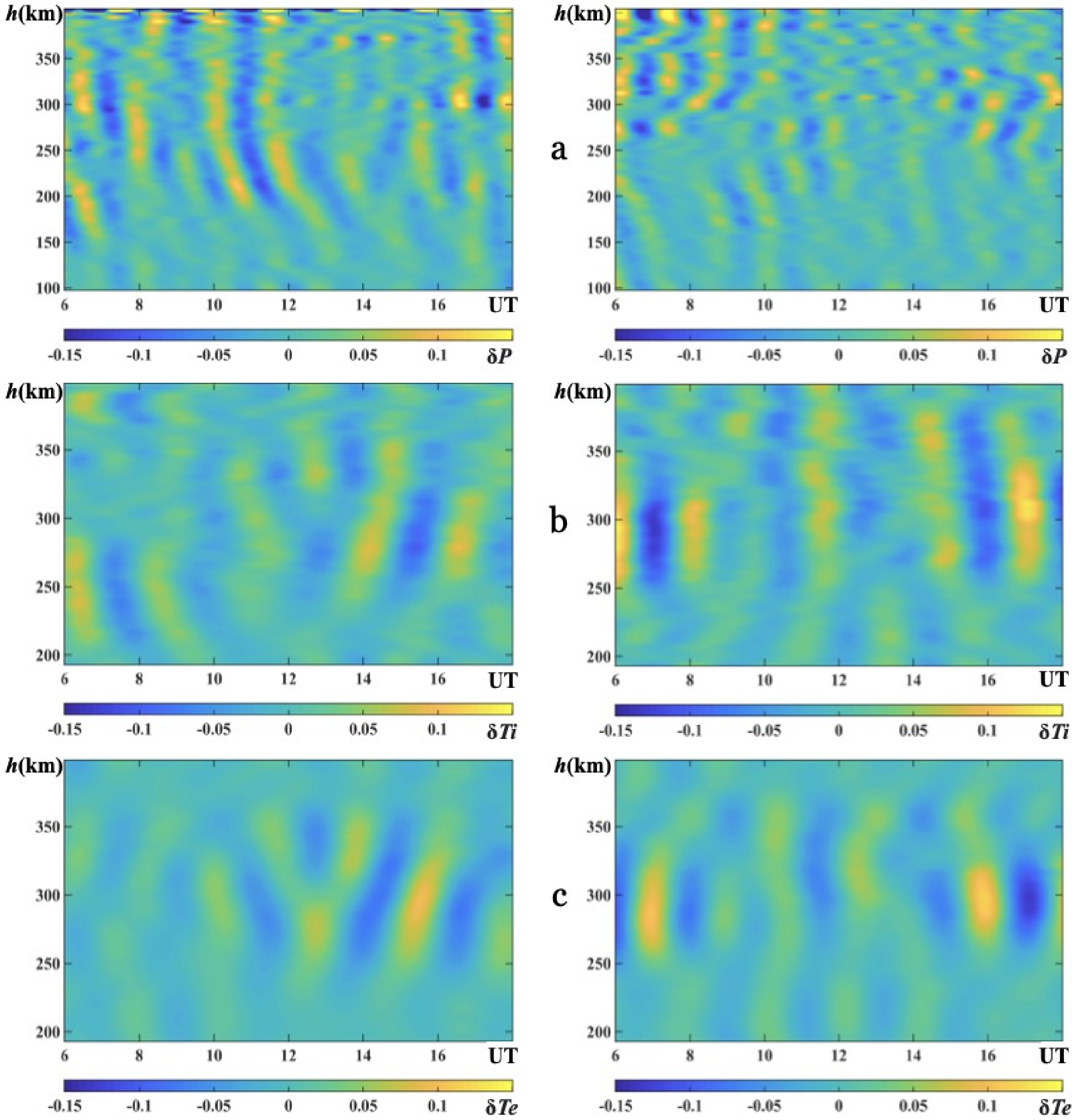

Figure 5.13. Same as Figure 5.12 but for September 2 (left column) and 3 (right column), 2016.

Fig. 5.14 shows the results of cross-correlation analysis for the relative variations in the IS signal power, as well as the amplitude of these oscillations. These results confirm the fact that the phase of all analyzed TIDs propagated upwards in the vertical direction. The values of the TID relative amplitudes in δP first increased, reached a maximum at altitudes of 150 – 300 km, and then decreased with increasing altitude. Altitude variations of δP_{max} were 0.02 – 0.2.

Table 5.3 shows the values obtained using cross-correlation analysis. This table shows that the value of $\delta P_{\max}$ was 0.07 on August 31 and September 3, 2016, while its values increased up to 0.14 – 0.18 and 0.11, respectively, on September 1 and 2, 2016. The values of V_z were in the range of 26 – 50 m/s, and

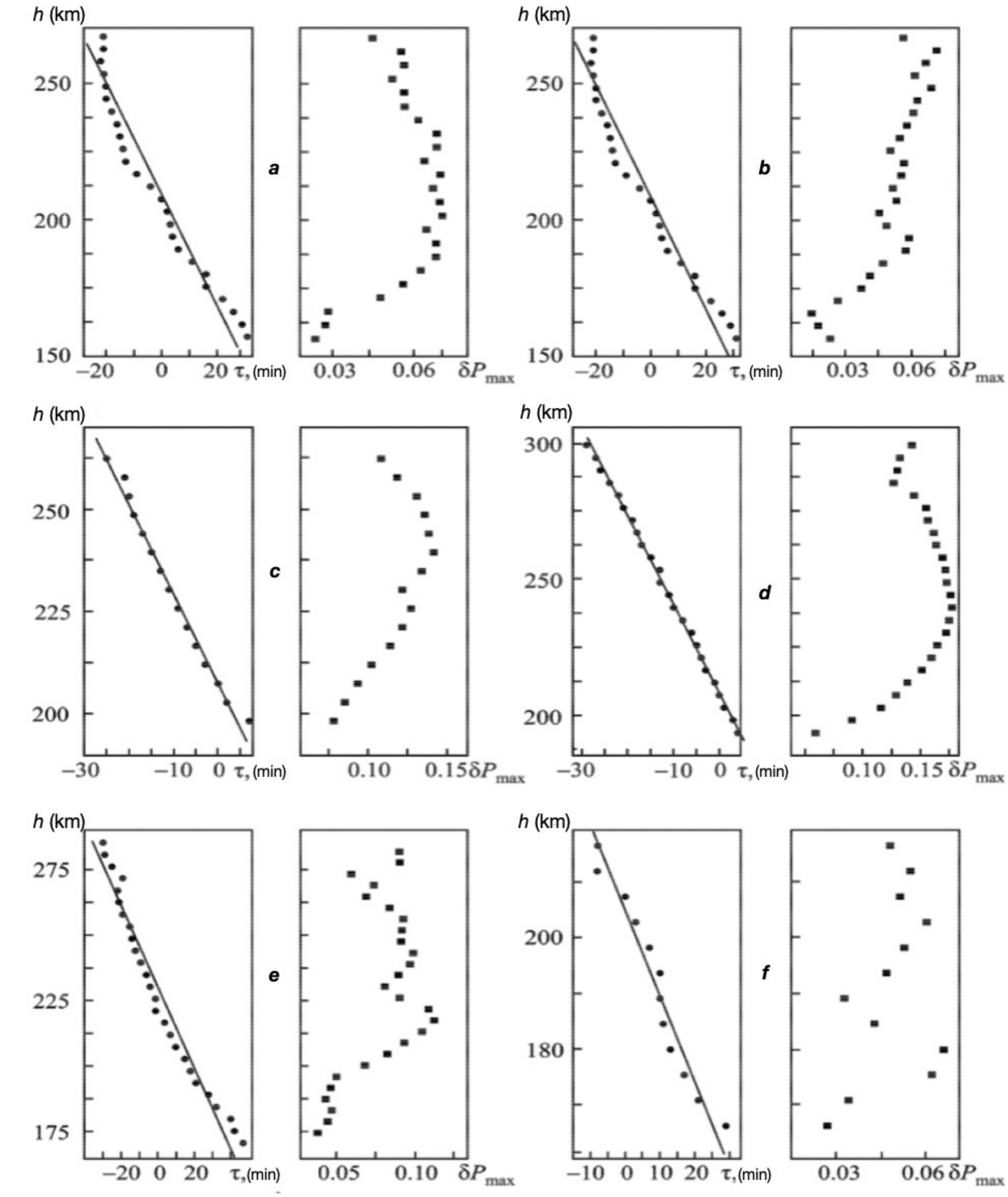

Figure 5.14. Altitude profiles of time delays or advances for oscillations δP relative to these oscillations at an altitude of 200 km together with their approximations by linear dependences, as well as the relative amplitudes $\delta P_{\max}$ of these TIDs, detected on August 31, 2016 from 07:00 to 12:00 UT (a) and from 13:00 to 17:00 UT (b); September 1, 2016 from 06:00 to 11:00 UT (c) and from 11:00 to 15:00 UT (d); September 2, 2016 from 09:00 to 14:00 UT (e); September 3, 2016 from 07:00 to 12:00 UT (f).

Table 5.3. Parameters of wave processes

Data	Time, UT	Height, km	T, min	h_{max}, km	δP_{max}	V_z, m/s	V_h, m/s	Λ_z, km	Λ_h, km
31.08.2016	07:00–12:00	170 – 280	75	210	0.07	50	360	220	1600
31.08.2016	13:00–17:00	150 – 270	85	260	0.07	30	270	170	1400
01.09.2016	06:00–11:00	190 – 270	80	240	0.14	40	270	180	1300
01.09.2016	11:00–15:00	185 – 310	90	240	0.18	50	450	290	2500
02.09.2016	09:00–14:00	160 – 290	85	215	0.11	30	212	130	1100
03.09.2016	07:00–12:00	160 – 220	80	180	0.07	30	224	120	1100

the values of V_h from 210 to 450 m/s, Λ_z varied in the range from 120 to 290 km, and Λ_h changed from 1100 to 2500 km.

The values of periods, horizontal phase velocities and wavelengths indicate that LSTIDs (Λ_h > 1000 km) occurred on the days of observations, which often propagate from the auroral region. Possible sources of such waves are Joule heating, Lorentz forcing and precipitation of energetic particles [Hocke & Schlegel, 1996]. These sources are known to have high-altitude localization in the auroral electrojet region (80 – 120 km). Since we studied TIDs in the mid-latitude ionosphere at altitudes of 150 – 400 km (see Figs. 5.11 – 5.13), which have an upward vertical group velocity, the position of the source region agrees well with the obtained results.

Magnetic field variations in the auroral region, in particular, AE index are known to be an indicator of variations in the auroral electrojet. Comparing the data of the AE index on the days of observations with the obtained experimental results showed that the predominant TIDs were detected during the intervals of significant increase in its values (up to 1500 nT) on September 1 – 3, 2016. However, on August 31, 2016, wave processes were also observed, albeit with less amplitudes than in the next two days, while the variations in the AE index were relatively small (maximum values did not exceed 200 nT). Thus, our results confirm that the increase in auroral electrojet intensity fluctuations, most likely, can only lead to an increase in the frequency of TIDs with fairly large amplitudes [Chernogor & Domnin, 2014].

For searching the relationship between the detected ionospheric disturbances and variations of the magnetic field at high latitudes, we performed a spectral analysis of the temporal dependences of the horizontal north-south component (H–component), registered in the geomagnetic observatory "St. Petersburg", whose longitude is closest to the longitude of the Kharkiv IS radar. The distance along the meridian between the observatory and the radar is about 1200 km. Magnetometric data were obtained from the SuperMAG database (http://supermag.jhuapl.edu/mag/).

Periodograms and energygrams of adaptive Fourier transform for magnetic field variations are presented in Fig. 5.15. The oscillations were localized during 11:00 – 15:00 UT and had periods of 40 – 80 mins on August 31.

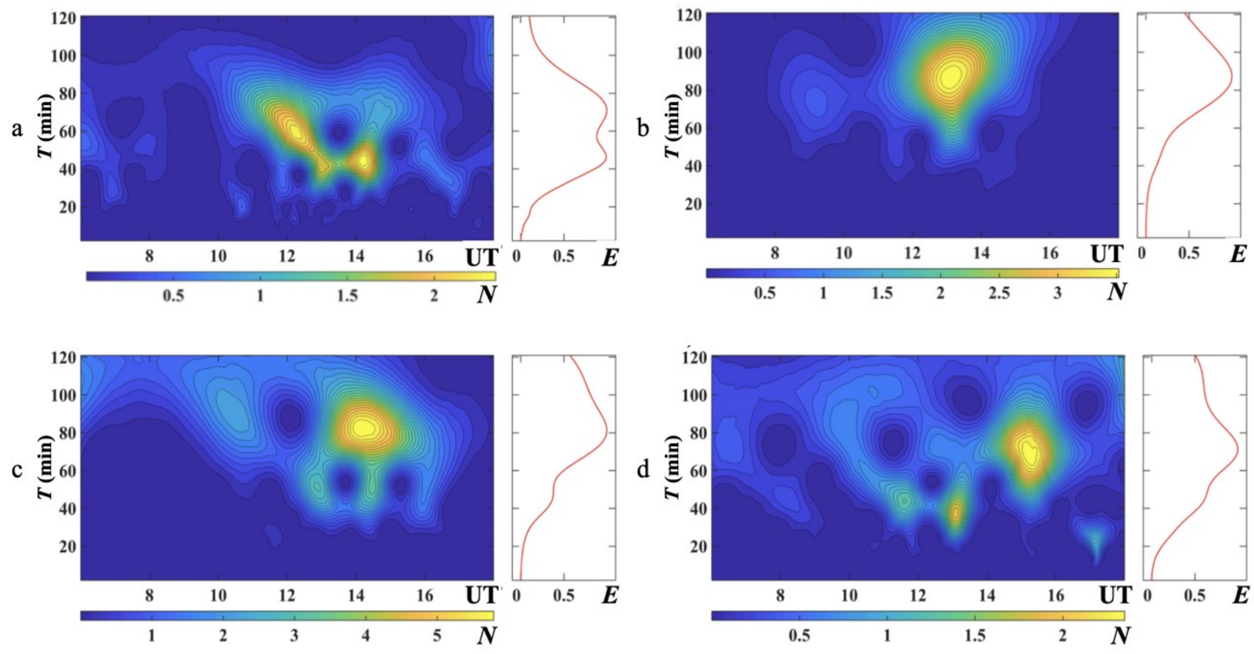

Figure 5.15. Results of spectral analysis performed for magnetometric data obtained by the Geomagnetic Observatory "St. Petersburg" (60.54° N, 29.72° E) for Augus1 31 (a), September 1 (b), 2 (c) 3 and (d), 2016.

Since the periods of TIDs on this day were large, and the disturbances themselves were observed both with advance and delay of 2 to 4 hours relative to the H-component oscillations, the wave processes over Kharkiv most likely had other sources of origin. However, during a geospace storm, the relationship between a number of TIDs and variations in the magnetic field can be traced quite clearly. Thus, on September 1, 2016, H-components fluctuated with $T \approx 90$ min near 13:00 UT, and TIDs with the same period were observed over Kharkiv with a delay of 0.5 – 1.5 h. In the afternoon of September 2 and 3, in the variations of the magnetic field, oscillations with $T \approx 80$ min near 14:00 UT and $T \approx 75$ min near 15:00 UT, respectively, were observed, which advanced the corresponding TIDs with similar periods by 1 – 2 h (see Fig. 5.4, 5.12, 5.14). Since the estimated values of V_h for these disturbances were 210 – 460 m/s (see Table 5.3), the time of arrival of waves from the auroral region (provided that they propagated strictly along the meridian) are in the range of 0.7 – 1.6 h, which is well consistent with the above values of disturbance delays.

5.4. Summary results of studies

Here we summarize the results of magnetic disturbances and storm effect observation.

Magnetic storm in November 2012.

1. Periods of predominant TIDs in variations of IS signal power were in the range from 60 to 120 minutes. The intensity of oscillations occurs in the morning

and evening, which indicates the solar terminator as the most likely additional source of their generation.

Magnetic storms in March and June 2016

2. In both periods of observations, the predominant TIDs are revealed near the solar terminator passages.

3. There is no obvious dependence of disturbance characteristics on global auroral indices of geomagnetic activity.

4. TIDs with the periods of 40 – 80 mins and 20 – 40 mins were detected. Relative amplitudes ranged from 0.03 to 0.15 for electron density and 0.03 to 0.10 for plasma temperatures over Kharkiv, and were equal to 0.08 – 0.35 for electron density and 0.03 – 0.15 for temperatures over Millstone Hill. Larger values of relative amplitudes are observed over Millstone Hill near the vernal equinox. Maximum amplitudes are registered at altitudes of 200 – 250 km. The duration of disturbances does not exceed 2 – 5 periods.

Magnetic storm in September 2016.

5. The periods of predominant oscillations were shown to be of 60 – 100 min. Their duration did not exceed two periods. No significant differences occurred in the values of these periods for the wave processes observed during the storm and in the previous magnetically quiet day.

6. It was demonstrated that the detected TIDs is a manifestation of AGWs in the ionosphere. The values of the relative amplitudes of the quasi-harmonic variations in the IS signal power on September 1 and 2, 2016 were approximately by a factor of 2 higher than the values on adjacent days. For different TIDs, they had both less and greater values of relative variation amplitudes for plasma temperatures. The vertical and horizontal components of the phase velocity and wavelength of LSTIDs were estimated. It is shown that V_z = 30 – 50 m/s, V_h = 210 – 450 m/s and Λ_z = 120 – 290 km, Λ_h = 1100 – 2500 km.

7. The relationship of a number of TIDs with variations in the magnetic field at high latitudes is established.

CHAPTER 6

NATURALLY AND ARTIFICIALLY INDUCED TRAVELING IONOSPHERIC DISTURBANCES

This chapter aims at reporting the results of TID observations during a presence of high energy natural and artificial sources. We describe the analysis and characterization of TIDs originated by total solar eclipse on March 20, 2015. The downward phase progression indicates that TIDs were induced by atmospheric gravity waves generated at lower altitudes. The detected TID parameters of periods, relative amplitudes, altitude range and TID horizontal propagation direction generally correspond to the results of other studies. We detected the TIDs over Kharkiv during and after the operation of the EISCAT heater facility.

6.1. Solar eclipse induced disturbances

Solar eclipses are considered to be one of the most important sources of ionospheric perturbations [Stankov et al., 2017]. They affect the atmospheric and ionospheric processes during the fast sunlight-umbra transitions and vice versa, over a wide altitude range (from the Earth's surface to the topside ionosphere). The identification of TIDs generated by the moving lunar umbra and penumbra is complex. This is due to the fact that solar eclipses, especially total, are relatively infrequent events in any specific region. In addition, it is often difficult to separate TIDs induced by solar eclipse from those caused by continuously existing other natural sources. The authors [Chimonas & Hines, 1970] were likely the first who have pointed to the possibility of AGWs generated during solar eclipses. Subsequently, some authors confirmed the occurrence of AGWs and TIDs [Bertin et al., 1977; Chernogor & Garmash, 2017; Coster et al., 2017], while other scientists did not reveal clear wave-like responses to such events [Jakowski et al., 2008]. The authors [Fritts and Luo, 1993] have described a possible mechanism for AGW generation by solar eclipses due to a decrease in the ozone density. Other authors [Liu et al., 1998; Altadill et al., 2001] have studied the AGW structure and estimated the values of vertical phase and group velocities of AGWs driven by a solar eclipse.

6.1.1. General information about solar eclipse

The total solar eclipse of 20 March 2015 began at 08:30 UT in Northwestern Europe and moved northeastwards, staying in Northern Europe (http://eclipse.gsfc.nasa.gov/SEanimate/SEanimate2001/SE2015Mar20T.GIF).
It was most visible from the North Atlantic and Arctic Oceans, Greenland, Iceland, Ireland, the United Kingdom, Faroe Islands and northern Norway. The umbra (total Moon shadow) began its pass off the south coast of Greenland. It then

moved to the northeast, passing between Iceland and the United Kingdom before moving over the Faroe Islands and the Svalbard archipelago of Norway. The eclipse was visible in varying degrees all over Europe. The longest duration of totality was 2 min and 47 s off the coast of the Faroe Islands. The specific feature of this solar eclipse was its occurrence during the recovery phase of a geomagnetic storm that began on March 17, 2015 (St. Patrick storm) and was accompanied by a negative ionospheric storm during March 20, 2015. Reduced electron densities could favor a detection of wave signatures in the ionosphere during the solar eclipse period.

The effects of the solar eclipse occurring on 20 March 2015 are reported in a number of papers (e.g., [Chernogor, 2016; Uryadov et al., 2016; Verhulst et al., 2016; Marlton et al., 2016; Stankov et al., 2017]). The eclipse-induced meteorological changes over the United Kingdom are presented in a special issue [Hanna et al., 2016]. The authors [Stankov et al., 2017] conducted multi-instrumental observations of solar eclipse effects. The author [Chernogor, 2016] have analyzed the quasi-periodic disturbances in electron density using data of the European ionosonde network. Summarizing, the complex nature of disturbances accompanying this solar eclipse caused an intense interest to study this event. Our results give new insight into propagation features of TIDs over Europe and may contribute to progress in understanding the whole chain of coupled processes triggered by eclipses.

6.1.2. Disturbance detection and characterization

Fig. 6.1 demonstrates a good localization of spectral peaks between 08:30 and 11:00 UT on 20 March both over Kharkiv and Tromsø. The observed variations in IS power over both sites have similar periods as well as event durations (of about 2 – 3 periods). The power spectra exhibit the oscillation energy peaks to be concentrated near the periods T = 50 – 60 min. The starts, main phases and ends of the local partial solar eclipse are marked in these graphs by the vertical lines. It is shown that TIDs were amplified before the start of the local eclipse at high latitudes (Fig. 6.1,a), whereas an enhancement in their amplitudes at middle latitudes occurred near the main phase of the local eclipse (Fig. 6.1,b).

Fig. 6.2 demonstrates TIDs observed in IS power during the solar eclipse and around the same time on the previous day, both in Tromsø and Kharkiv. At the time of the passing Moon penumbra, at both locations TIDs are present with amplitudes at least 3 times larger than the fluctuations seen on the previous day at the same time. The TID amplification was observed at altitude ranges of 180 – 250 km and 150 – 300 km for Tromsø and Kharkiv, respectively. The lines of constant phase progress forward in time with decreasing altitude. This is the typical signature of TIDs induced by AGWs generated at lower altitudes, as shown in a theoretical analysis [Hines, 1960]: while the energy in the waves is transported obliquely upward, the phase fronts propagate obliquely downward.

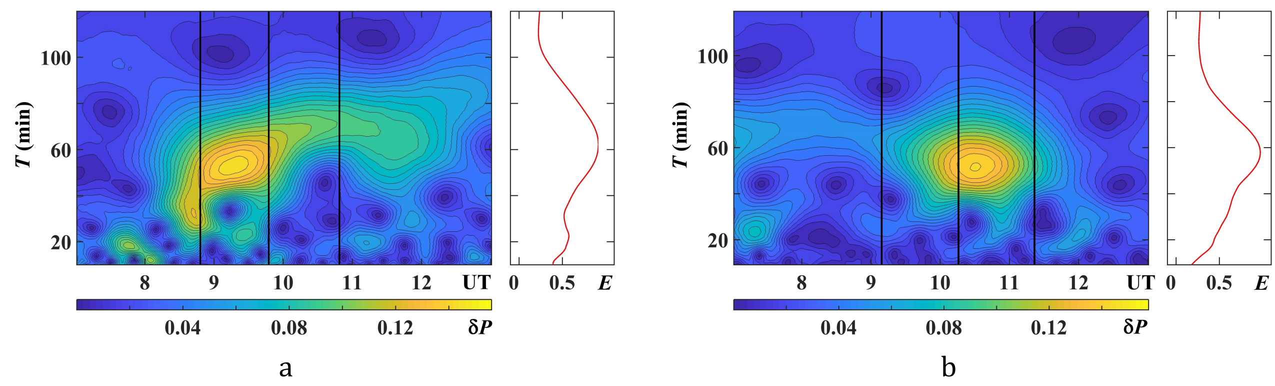

Figure 6.1. Results of spectral analysis using the adaptive Fourier transform performed for relative variations of IS power at the height of 200 km over (a) Tromsø, (b) Kharkiv. The vertical lines indicate the start, main phase and end of the solar eclipse in both locations.

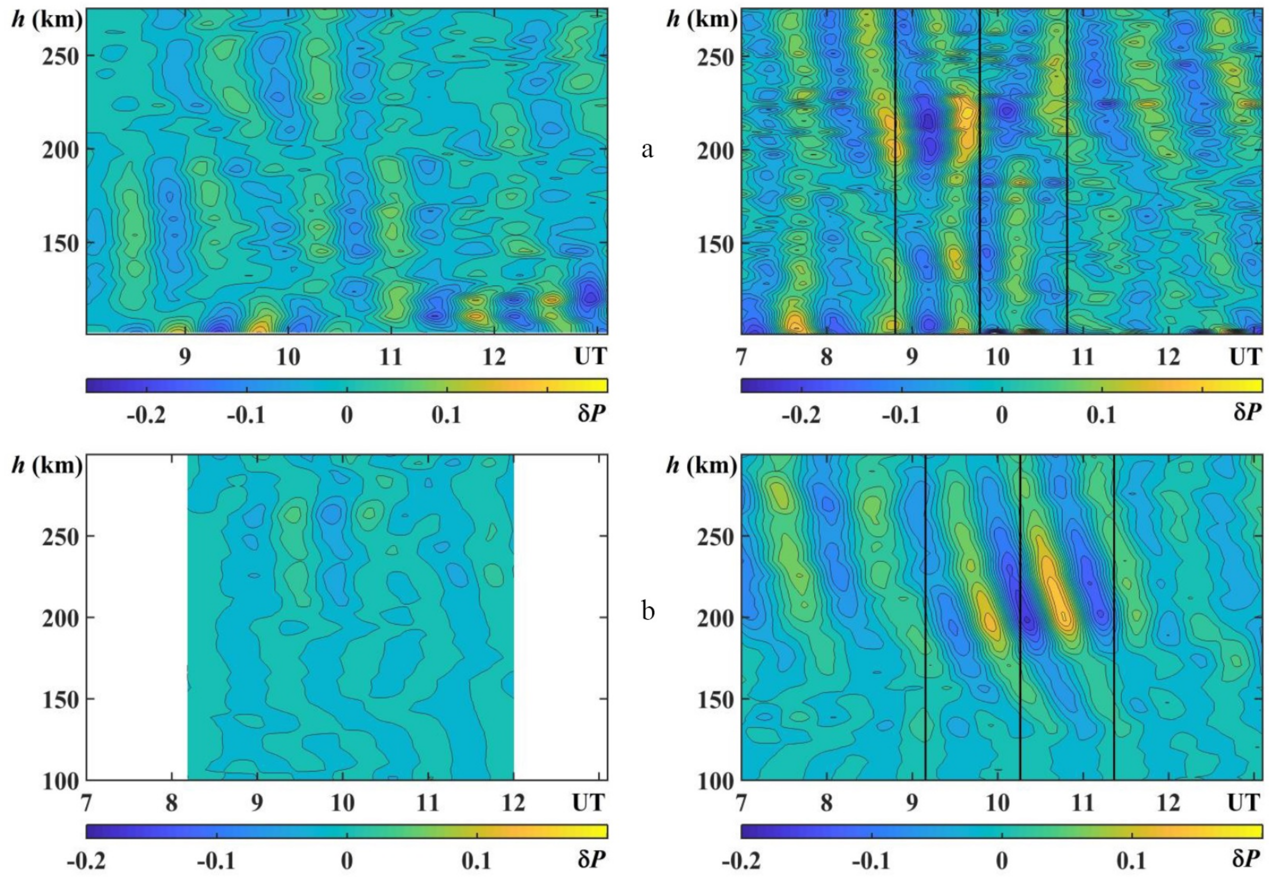

Figure 6.2. Altitude-time maps of 40–80 min band-pass filtered IS power relative variations observed during March 19 (left) and 20 (right), 2015 over (a) Tromsø, (b) Kharkiv.

The resulting downward phase propagation of AGWs/TIDs observed in vertical profiles has already been confirmed in many experiments (see, e.g., [Hocke et al., 1996; Vlasov et al., 2011]).

The results of estimation of TID vertical propagation characteristics are illustrated in Fig. 6.3. The dots in Fig. 6.3,a show the time lags resulting from the cross-correlation analysis mentioned in the previous section, performed at different altitudes in the detected main horizontal direction of propagation. The altitude dependence of time lags over Tromsø appears to be best-fitted with a first-order polynom (linear regression), whereas that over Kharkiv is better approximated by square-law function (see Fig. 6.3,a). The altitude dependencies of relative amplitudes exhibit a similar behavior over both observation sites. When altitude increases, the relative amplitude values rise, reach a maximum of 0.22 (22%) at the height of 220 km over Tromsø and of 0.17 (17%) at the height of 200 km over Kharkiv, followed by their gradual decrease (see Fig. 6.3,b). Due to the linear fit, the estimated vertical phase velocity V_Z over Tromsø had a constant value of about 57 m/s. V_Z over Kharkiv increased from 25 to 170 m/s with the altitude in the range of 120–310 km (Fig. 7c).

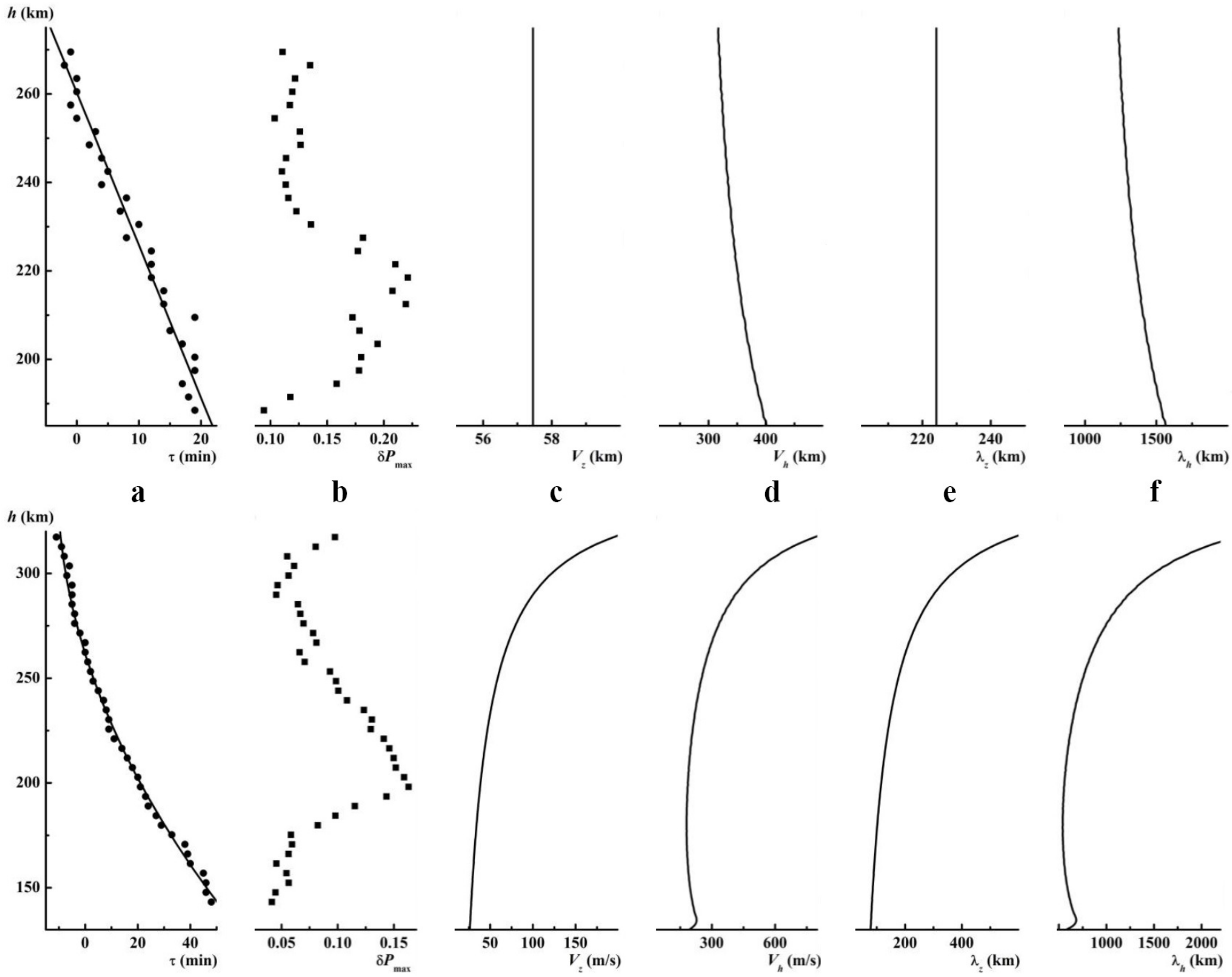

Figure 6.3. Altitude profiles of (a) time lags and advances of wave process arrival relative to that at 260 km, (b) relative amplitudes in IS power as well as estimated (c) vertical phase velocity, (d) horizontal phase velocity, (e) vertical wavelength and (f) horizontal wavelength on 20 March 2015 over Tromsø (top) and Kharkiv (bottom).

As shown in Fig. 6.3, the V_h values estimated from (3.15) varied from 300 to 350 m/s and from 180 to 800 m/s over Tromsø and Kharkiv, respectively (see Fig. 6.3,d). Finally, Fig. 6.3,e and Fig. 6.3,f present the altitude profiles of λ_z and λ_h. Like the vertical phase velocity, λ_z was estimated to be constant with altitude and equal to about 225 km over Tromsø. As for λ_h, it slightly changed between 1200 and 1400 km. Such values of λ_h are usually attributed to LSTIDs [Hocke & Schlegel, 1996]. The altitude dependencies of λ_z and λ_h over Kharkiv demonstrated their significant variations in the range of 80 – 800 km and 500 – 2000 km for vertical and horizontal phase velocity, respectively. The value of λ_h over Kharkiv was less than 1000 km at altitudes below about 280 km.

The main wave period of the TIDs is identified to be of 50 – 60 min (see Fig. 6.1). The same periodicity was also detected by the authors [Mošna et al., 2018] in the ionosphere and [Marlton et al., 2016] in variations of the surface temperature and pressure, although the last authors could not unambiguously associate it with the effect of this solar eclipse. It is important to note that TIDs with similar period values were found during other solar eclipses [Altadill et al., 2001], but also at other times, caused by sources such as geomagnetic storms [Borries et al., 2009], or the solar terminator passage [Nygrén et al., 2015; Panasenko et al., 2018].

The IS results show the clear downward phase progression (see Fig. 6.2) which indicates the AGW/TID sources being located at lower heights. The region responsible for AGW generation is located in the stratosphere and mesosphere (20 – 80 km) and encompasses the ozone layer [Chimonas & Hines, 1970; Fritts & Luo, 1993]. The AGWs, generated continuously due to the ozone cooling and the temperature gradient, propagate to ionospheric heights, resulting in TIDs. While such a mechanism can explain the observation of MSTIDs, it does not explain LSTIDs, which have a horizontal phase velocity more than that of sound in the lower and middle atmosphere. So, the LSTIDs can be generated in the lower thermosphere and in the ionosphere due to changes in atmospheric constituents [Müller-Wodarg et al., 1998], chemical and dynamical processes [Liu et al., 1998] as well as turbulence in the transition area between F1 and F2 regions [Altadill et al., 2001]. Furthermore, the dissipation of AGWs propagating from below occurs in the lower thermosphere. Secondary gravity waves are often generated by thermospheric body forces and may induce both LSTIDs and MSTIDs (see, e.g., [Vadas & Fritts, 2006]).

The detection of only the LSTIDs over Tromsø can be due to the beam scanning which led to averaging of medium-scale structures. The data acquired over Kharkiv substantially show MSTIDs at least up to the altitude of 280 km (see Fig. 6.3). The sharp increase in V_h at higher altitudes is likely caused by aliasing of the time lag detection of wave fronts on this piece of altitudinal dependence. However, it can also result from wave dissipation leading to vertical wavelength increase [Vadas & Fritts, 2006] or point to LSTID patterns. A neglect of U_h and its altitudinal gradient in (3.14) may also result in biases for V_h and λ_h values.

The effects on the atmosphere and ionosphere of each solar eclipse are unique and diverse. They strongly depend on factors as the time of day, season, level of magnetic activity, eclipse magnitude, and the path of Moon umbra and penumbra. Moreover, they can also either be amplified or suppressed by superimposed perturbations caused by other origins. Thus, a thorough investigation of eclipse-produced changes in the state of the atmosphere, including generation of waves, is of great importance for better understanding and improving the modeling of coupled processes occurring during such events.

6.2. EISCAT Heater operation induced disturbances

The ionospheric modification by high power HF radio waves is a kind of the active experiment conducted regularly after putting in use the ionospheric heating facilities in USA, Norway and Russia (former USSR). Powerful radio waves result in significant perturbations involving an increase in electron temperature, a change in electron density, low-frequency radiation of ionospheric current systems, generation of ionospheric irregularities with a wide range of scales, pump-induced artificial optical emissions, etc., in the irradiated ionospheric region [Fejer et al., 1985; Migulin & Gurevich, 1985; Stubbe et al., 1985]. Some recent results of such experimental studies have been published in the papers [Frolov et al., 2010; Vierinen et al., 2013].

Large scale disturbances during heating experiments have been detected at the distances of the order of 1000 km, along with local ones. They appear in the F-region as traveling ionospheric disturbances (TIDs) related to generation and propagation of acoustic-gravity waves (AGWs) in the upper atmosphere. Such disturbances were determined to be strongly depending on space weather conditions, the time of day, season of the year, the mode of the heating facility operation, etc (see, e.g., [Garmash & Chernogor, 1998]). Furthermore, since the parameters of these artificial disturbances appear to be close to the parameters of natural perturbations originating constantly in the ionosphere, it is often difficult to separate these two types of events. Nevertheless, the efforts to detect the disturbances occurring far from the heated plasma volume have been continuing [Domnin et al., 2012; Kunitsyn et al., 2012; Mishin et al., 2012]. The authors [Domnin et al., 2012] found wave disturbances in the ionosphere over Kharkiv, Ukraine during the operation of “Sura” facility. The authors [Kunitsyn et al., 2012] reported about wavelike disturbances coming out from the ionospheric region over the “Sura” heater. The authors [Mishin et al., 2012] observed AGWs induced by HAARP HF heating. Other authors [Pradipta & Lee, 2013] indicated the origin of AGWs from the edge of the HAARP facility heated region.

6.2.1. EISCAT Heater facility

A high-latitude heater is used to study the effect of powerful radio waves on the ionosphere [Vierinen et al., 2013].

Currently, 12 transmitters operate. They can continuously transmit a power of 100 kW in the frequency range from 2.7 to 8.0 MHz. However, existing transmitting antennas allow the use of frequencies only in the range of 3.85 – 8 MHz. In recent years, the transmitters have been operating at a peak power of 80 kW only. Each transmitter uses a vacuum lamp (tetrode) as the main amplifier. The amplifier is excited by a broadband preamplifier, which is made on transistors. Both devices are water cooled. Each transmitter has its own high voltage power supply, which provides up to 12 kV voltage and is connected directly to the supply network.

The generator has the ability to modulate the carrier frequency by rapidly changing its phase, as well as the amplitude and oscillation frequency using signals from the radar controller, based on the values loaded into its built-in memory. The generator consists of seven boards, each of which has two DDS devices based on the AD9953 chip. This chip includes a 14-bit digital-to-analog converter. Each generator board receives an input signal with a reference frequency of 10 MHz, which is derived from the GPS-synchronized rubidium frequency standard (Stanford Research Systems PRS10). For both DDS units, there is 16 kB of memory on the excitation board, designed to support rapid changes in the characteristics of one or more amplitudes, frequencies or phase shifts. The frequencies can be set using a 32-bit word that specifies an internal clock frequency of 200 MHz with a frequency resolution of 46.6 MHz. Frequency settings and control words are loaded into the AD9953 via the serial I/O port.

Although generators can set the absolute amplitudes and relative phases between DDS devices fairly accurately, it is still necessary to perform the traditional phasing procedure at some point in time. During this procedure, the power is gradually increased during the phase adjustment of the generator to give the specified values at the outputs of the transmitters for the specified frequency, polarization, beam direction, and transmitter combination. This is due to the fact that indefinite phase changes on the transmitter and strong electrical connections between the antennas make theoretically set settings impractical. However, after performing the correction procedure, the final values obtained for each transmitter are retained and can be reloaded into the generator memory if desired. This downloaded data, which determines continuous radiation with a given power, polarization, and direction, is the basis for modulating any of these parameters. The modulation of the RF radio wave amplitude is carried out by stepwise change of the amplitude values between 1 and 0, where 1 corresponds to the maximum, pre-loaded value.

6.2.2. Data sets

In 2012 a coordinated experimental campaign was conducted. The facilities employed included the EISCAT Heater, Dynasonde and incoherent scatter (IS) radar, located near Tromsø, Norway as well as IS radar and ionosonde, located near Kharkiv, Ukraine. The experiments were done at the morning hours on November 22 – 24.

The ionospheric heater transmitted pump waves with O-mode polarization having a frequency from 4.04 to 7.10 MHz. On November 22, 2012, it was operated during 05:33 – 09:00 UT period in 15-min cycles (9 min on, 6 min off), after which the pump modulation of 15 min on, 15 min off was alternated with 2 min square wave modulation during 15-min period, 15 min off. On November 23, 2012, the heater operation with 15-min cycles was from 05:03 until 09:00 UT followed by such pump modulation as in previous day. On November 24, 2012, the HF pump cycles were different. A sporadic-E layer appeared during the observations, so this experiment was excluded from the study. The effective radiated power increased from 140 to 850 MW being dependent on pump frequency and antenna array. The antenna beam was directed to the magnetic zenith which is 12° south of zenith.

The diagnostics of ionospheric plasma was performed by the Kharkiv IS radar being at the distance of about 2400 km. The time variations in incoherent scatter power, electron density and electron and ion temperatures being observed at different altitudes have been analyzed.

6.2.3. Observation results

Figure 6.4 presents temporal variations of pump frequency as well as F2-region critical frequency f_oF2 over EISCAT heater site. As seen in this figure, the heating was in underdense conditions from the experiment start to about 08:00 UT both on November 22 and November 23, followed by overdense conditions. After about 08:00 UT, the pump frequency increased stepwise to be slightly less than f_oF2 (see Fig. 6.4). The F2-region critical frequency over Kharkiv during these experiments was greater and fell within the range of 5.0 to 10.6 MHz and 5.4 to 10.0 MHz on November 22 and 23, respectively.

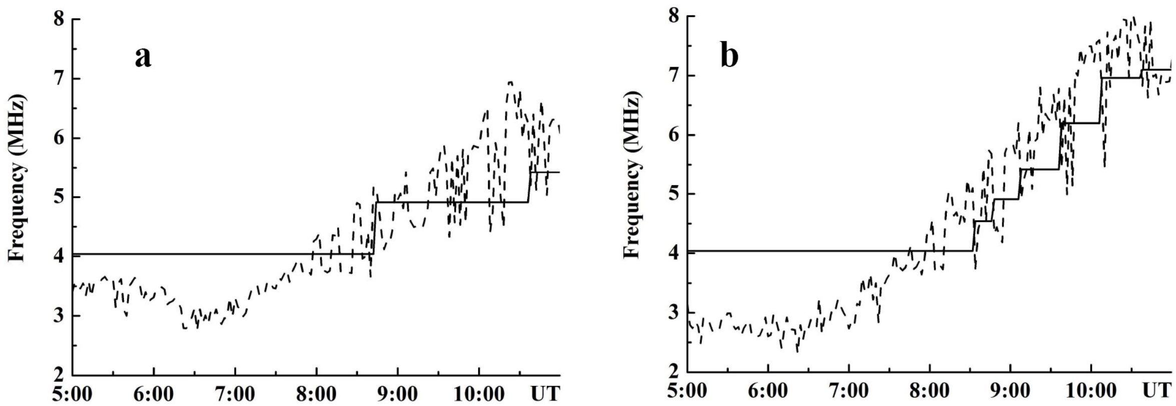

Figure 6.4. Pump frequency (solid line) and F2-region critical frequency measured by the Dynasonde (dashed line) during the EISCAT heating experiments conducted on (a) November 22 and (b) November 23, 2012

The temporal variations of the main ionospheric parameters over Kharkiv obtained from the IS radar data are indicated in Figs 6.5 and 6.6. These data covering the height range of 200 – 325 km have been filtered to detect the oscillations initiated by AGWs. The analysis shows that the fluctuations with the largest relative amplitudes were in the range of 40 – 80 min.

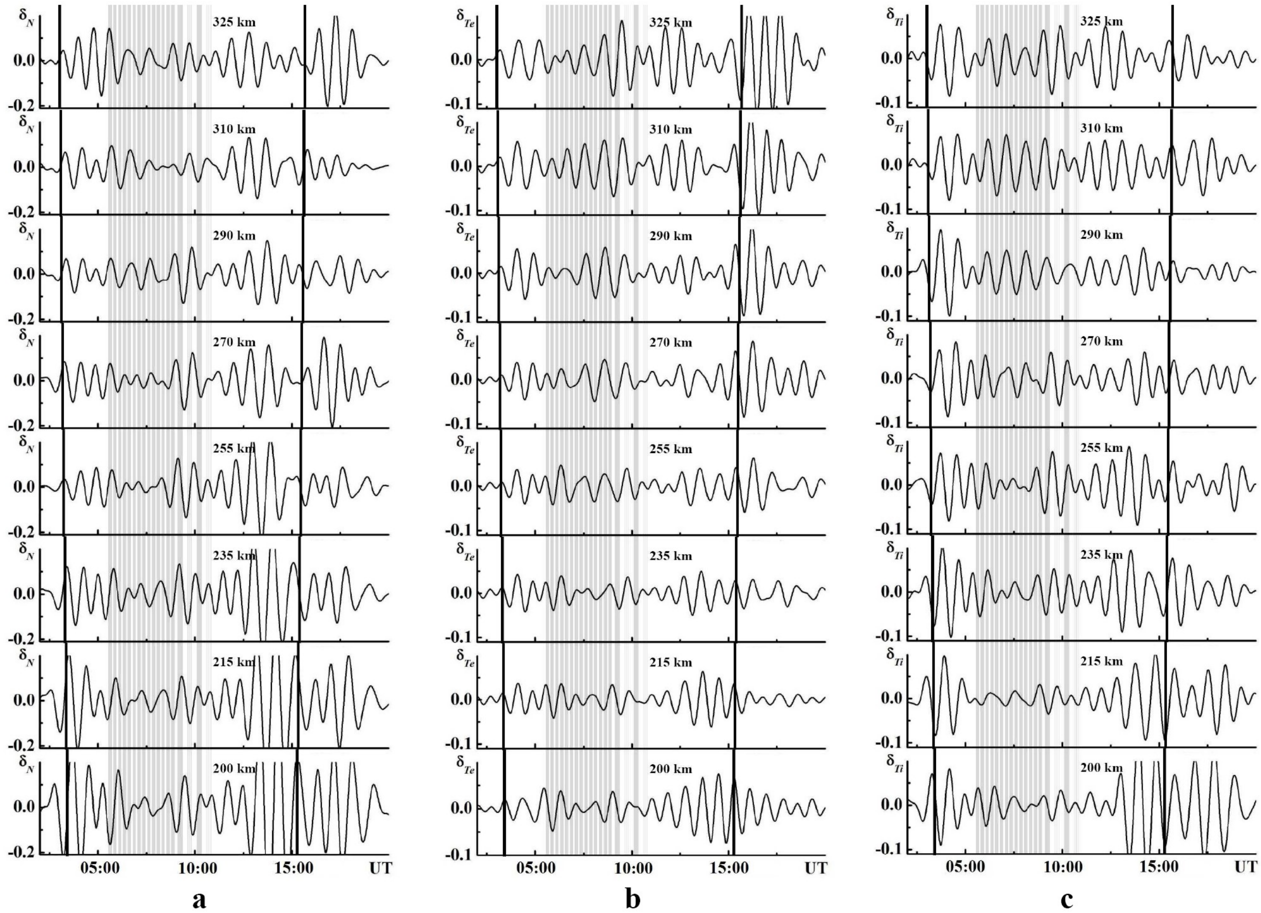

Figure 6.5. Relative fluctuations of (a) electron density, (b) electron temperature and (c) ion temperature filtered in 40 – 80 min band, at different altitudes on November 22, 2012. The shadow strips indicate heater-on times. The solid lines mark the times of sunrise and sunset terminator moving in the atmosphere above the Kharkiv incoherent scatter radar location.

The main criterion for TIDs selection was the occurrence of fluctuations with close dominant periods in the electron density, the electron temperature and the ion temperature simultaneously during almost the same time interval. Moreover, these fluctuations must cover a height range more than 50 km.

The strong variations in all ionospheric parameters being analysed occured between 04:00 – 07:00 UT and again 12:00 – 17:00 UT on November 22, 2012. Their relative amplitude values reached 0.05 – 0.2 for different parameters depending on the height (see Fig. 6.5). On November 23, 2012, such fluctuations with similar relative amplitudes were observed during 04:30 – 07:30 UT and 14:00

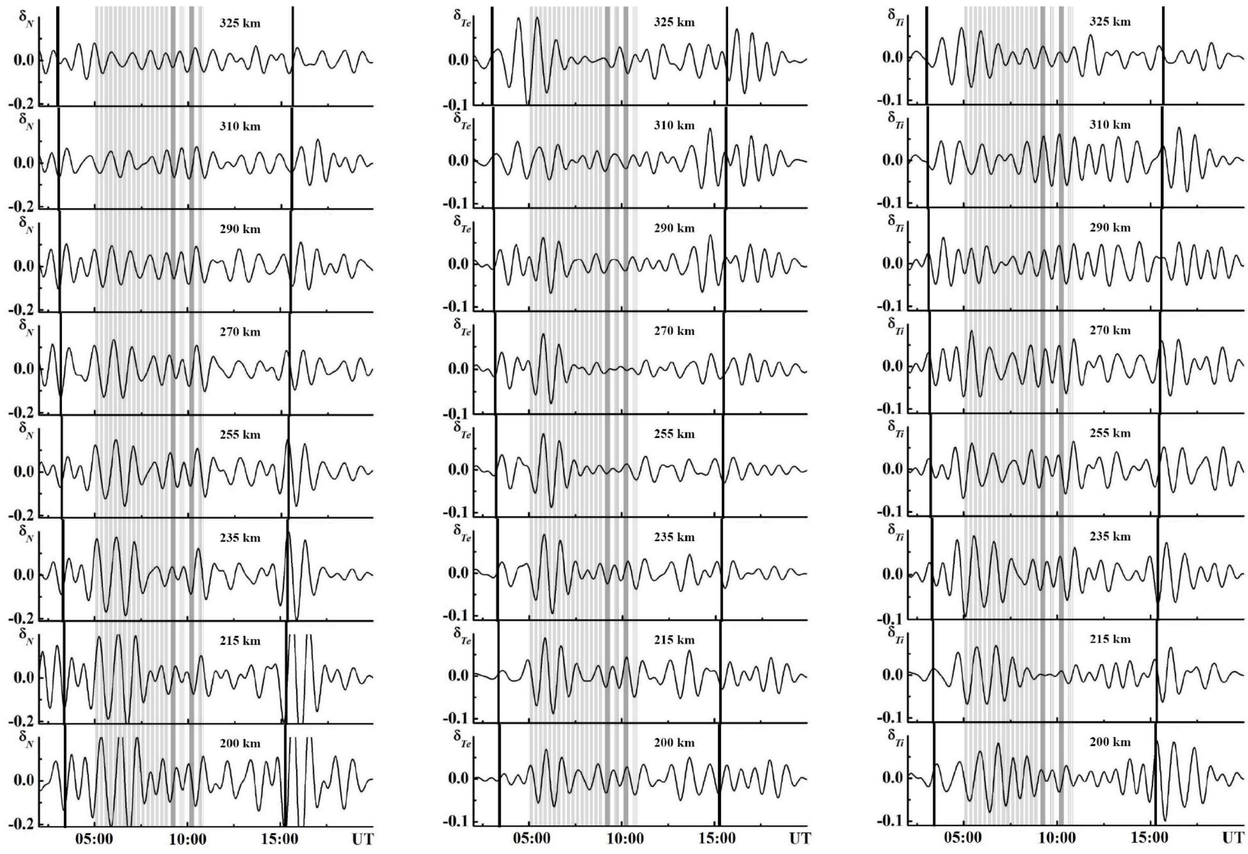

Figure 6.6. Same as Fig.6.5. but for relative fluctuations on November 23, 2012.

– 17:00 time intervals (see Fig. 6.6). These TIDs arose before the start or after the end of heating experiments. They are likely to be caused by the passage of solar terminators over Kharkiv IS radar site.

A pronounced TID was observed during the time interval from about 09:00 to 10:30 UT on November 22, 2012. As illustrated in Figure 6.5, the fluctuations with the dominant period of about 60 min were primarily observed at heights of 200 – 290 km. The values of the relative amplitude ranged from 0.05 to 0.15 for the electron density and 0.02 – 0.05 for the electron and ion temperatures. The duration of oscillations was usually about 2 periods. The TID was also detected during the heating experiment conducted on November 23, 2012. Its parameters were similar to that described above, but the time interval with oscillations was from about 10:00 to 12:00 UT (see Fig. 6.6).

As is well known (see, e. g., [Gurevich, 1976]), the strong effects of high power HF radio wave on the F2 region are produced when the pump frequency is equal to the upper hybrid resonance (UHR) frequency near the F2-peak. This became possible only after a change in the heating conditions from underdense to overdense, i.e after about 08:00 UT. Thus, if the TID observed after 09:00 UT on November 22 and after 10:00 UT on November 23, 2012 originated in the heated ionospheric region, their apparent horizontal velocity are not less than

330 – 660 m/s taking into account a transit time of 1 – 2 hours and the distance of about 2400 km. Such apparent horizontal velocities are associated with AGWs. However, since the exact time of wave disturbance onset is unknown, we cannot exclude the propagation of waves of another type, e. g. magnetohydrodynamic in nature.

Possible mechanisms for AGW generation in the heated region have been proposed in [Mishin et al., 2012; Chernogor, 2013; Pradipta & Lee, 2013]. The authors of [Pradipta & Lee, 2013] indicated the heater-induced wave disturbances to be generated at the edge of the heated region by sharp thermal gradients. The authors [Mishin et al., 2012; Chernogor, 2013] concluded that such disturbances can be produced by periodic heating of neutral gases. Moreover, other mechanisms may involve the modulation of ionospheric currents in the dynamo region, UHR region and in the ionospheric F-region by the propagating radio wave [Chernogor, 2013]. The detailed estimations made in [Chernogor, 2013] showed the most effective mechanism of TIDs generation during the ionospheric heating is modulation of the effective electron collision frequency in the UHR region.

The main problem we met is that we have no possibility to obtain the arrival direction of TIDs. Therefore, based only on the results of these measurements we cannot assert that the observed TIDs arrived from the heated region. However, even in the case of finding the arrival detection, the origin of the observed TIDs is not obvious. The AGWs producing the TIDs are known to be omnipresent in the atmosphere due to a large number of their natural and man-made sources. In particular, the detected TIDs could be generated in the polar region, although the experiments have been conducted during magnetically very quiet conditions when the planetary A_p and K_p indexes not exceed 7 and 1, respectively. Thus, long-term, regular measurements are needed to detect and identify high-power radio wave-induced TIDs as well as estimate their parameters during different space weather conditions.

Summarizing the above, we can conclude that TIDs in electron density, electron and ion temperatures have been detected in the ionospheric F2-region with Kharkiv IS radar during the operation of the EISCAT heating facility. An increase in relative amplitudes of wave disturbances with periods of 40 – 80 min in the height range from 200 to 290 km has been observed. Such disturbances are likely caused by AGW propagation generated by periodic HF modification of the ionosphere, although they can be generated by many other natural or man-made origins of AGWs and TIDs. The possible mechanisms for AGW generation in the modified region are the modulation of ionospheric currents in the UHR region or in the dynamo region by high power radio waves, the periodic heating of neutral gas and sharp thermal gradients at the edge of the heated region.

REFERENCES

Adeniyi, J. O. (1986). Magnetic storm effects on the morphology of the equatorial F2-layer. Journal of atmospheric and terrestrial physics, 48(8), 695.

Afraimovich, E. L., Ashkaliev, Y. F., Aushev, V. M., Beletsky, A. B., Vodyannikov, V. V., Leonovich, L. A., ... & Yakovets, A. F. (2002). Simultaneous radio and optical observations of the mid-latitude atmospheric response to a major geomagnetic storm of 6–8 April 2000. Journal of Atmospheric and Solar-Terrestrial Physics, 64(18), 1943.

Afraimovich, E. L. (2008). First GPS-TEC evidence for the wave structure excited by the solar terminator. Earth, planets and space, 60(8), 895.

Afraimovich, E. L., Edemskiy, I. K., Voeykov, S. V., Yasyukevich, Y. V., & Zhivetiev, I. V. (2009). Spatio-temporal structure of the wave packets generated by the solar terminator. Advances in space research, 44(7), 824.

Afraimovich, E. L., Edemskiy, I. K., Voeykov, S. V., Yasyukevich, Y. V., & Zhivetiev, I. V. (2010a). Travelling wave packets generated by the solar terminator in the upper atmosphere. Atmospheric and Oceanic Optics, 23(1), 21.

Afraimovich, E. L., Edemsky, I. K., Voeykov, S. V., Yasukevich, Y. V., & Zhivetiev, I. V. (2010b). MHD nature of ionospheric wave packets generated by the solar terminator. Geomagnetism and Aeronomy, 50(1), 79.

Altadill, D., Sole, J. G., & Apostolov, E. M. (2001). Vertical structure of a gravity wave like oscillation in the ionosphere generated by the solar eclipse of August 11, 1999. Journal of geophysical research: Space physics, 106(A10), 21419.

Anderson, T. W., & Finn, J. D. (2012). The new statistical analysis of data. Springer Science & Business Media.

Barabash, V. V., Panasenko, S. V., Aksonova, K. D., & Lisachenko, V. N. (2017). Characteristics of traveling ionospheric disturbances over Ukraine and West Antarctica during the strong geospace storm according to data of vertical sounding and incoherent scattering. Ukrainian Antarctic journal, (16), 113. (In Ukrainian)

Bertin, F., Hughes, K. A., & Kersley, L. (1977). Atmospheric waves induced by the solar eclipse of 30 June 1973. Journal of Atmospheric and Terrestrial Physics, 39(4), 457.

Bilitza, D. (2005). 35 years of International Reference Ionosphere–Karl Rawer's legacy. Advances in Radio Science, 2(G. 2), 283.

Bogomaz, O, Kotov, D, Panasenko, S, Emelyanov, L. (2017) Advances in software for analysis of Kharkiv incoherent scatter radar data. In: 2017 International Conference on Information and Telecommunication Technologies and Radio Electronics (UkrMiCo).

Borchevkina, O. P., Karpov, I. V., & Karpov, A. I. (2017). Observations of acoustic gravity waves during the solar eclipse on March 20, 2015 in Kaliningrad. Chemical physics, 36(12), 51. (In Russian)

Borisova, T. D., Blagoveshchenskaya, N. F., Kornienko, V. A., & Rietveld, M. T. (2007). Determining the ionospheric irregularity velocity vector based on doppler measurements in the artificially modified F2 region of the polar ionosphere. Geomagnetism and Aeronomy, 47(1), 76.

Borries, C., Jakowski, N., & Wilken, V. (2009). Storm induced large scale TIDs observed in GPS derived TEC. Annales Geophysicae, 27(4), 1605.

Borries, C., Jakowski, N., Kauristie, K., Amm, O., Mielich, J., & Kouba, D. (2017). On the dynamics of large-scale traveling ionospheric disturbances over Europe on 20 November 2003. Journal of Geophysical Research: Space Physics, 122(1), 1199.

Brace, L. H. (1998). Langmuir probe measurements in the ionosphere. Geophysical Monograph-American Geophysical Union, 102, 23.

Broom, S. M. (1984). A new ionosonde for Argentine Islands ionospheric observatory, Faraday Station. British Antarctic Survey Bulletin, 62, 1.

Bryunelli B. Ye., & Namgaladze A. A. (1988). Ionosphere Physics. Moscow, Nauka, 528 p. (In Russian)

Buonsanto, M. J. (1999). Ionospheric storms—A review. Space Science Reviews, 88(3), 563.

Burmaka, V. P., Taran, V. I., & Chernogor, L. F. (2005). Results of study of wave disturbances in the ionosphere using incoherent scatter technique. Advances in modern radio electronics, (3), 4. (In Russian)

Burmaka, V. P., & Chernogor, L. F. (2012). Wave disturbances in the ionosphere during a lasting solar activity minimum. Geomagnetism and Aeronomy, 52(2), 183.

Chekalin, S. V., & Shatrov, Ya. T. (1991). Influence of launches of transport space systems on the Earth's atmosphere. Moscow, Knowledge, (7), 1991. (In Russian)

Chernigovskaya, M. A., Shpynev, B. G., Habituev, D. S., Ratovsky, K. G., Belinskaya, A. Yu., Stepanov, A. E., Bychkov V. V., Grigoryeva S. A., Panchenko V. A., Kouba D. & Melich, Y. (2019). Longitudinal variations of ionospheric and geomagnetic parameters in the northern hemisphere during strong magnetic storms in 2015. Modern problems of remote sensing of the Earth from space, 16(5), 336. (In Russian)

Chernogor, L. F. (2008). Advanced methods of spectral analysis of quasiperiodic wave-like processes in the ionosphere: Specific features and experimental results. Geomagnetism and Aeronomy, 48(5), 652.

Chernogor, L. F. (2009). Remote radio sounding of the atmosphere and geospace. Kharkiv, V. N. Karazin Kharkiv national university. (In Russian)

Chernogor, L. F. (2011). The Earth–atmosphere–geospace system: main properties and processes. International journal of remote sensing, 32(11), 3199.

Chernogor, L. F. (2012). Geomagnetic pulsations accompanied the solar terminator moving through magnetoconjugate region. Radio Physics and Radio Astronomy, 17(1), 57. (In Russian)

Chernogor, L. F. (2013). Mechanisms for generating oscillations in the infrasound frequency range in the upper atmosphere by periodic high-power radio transmissions. Radio physics and radio astronomy, 17(3), 240. (In Russian)

Chenogor, L. F., & Domnin, I. F. (2014). Physics of geospace storms. Kharkiv, V. N. Karazin Kharkiv national university. (In Russian)

Chernogor, L. F., Panasenko, S. V., Frolov, V. L., & Domnin, I. F. (2015). Observations of the ionospheric wave disturbances using the Kharkov incoherent scatter radar upon RF heating of the near-earth plasma. Radiophysics and Quantum Electronics, 58(2), 79.

Chernogor, L. F. (2016). Wave processes in the ionosphere over Europe that accompanied the solar eclipse of March 20, 2015. Kinematics and Physics of Celestial Bodies, 32(4), 196.

Chernogor, L. F., & Garmash, K. P. (2017). Magneto-ionospheric effects of the solar eclipse of March 20, 2015, over Kharkov. Geomagnetism and Aeronomy, 57(1), 72.

Chernogor L. F., Domnin I. F., Emelyanov L. Ya., Lyashenko M. V. (2019). Physical processes in the ionosphere during the solar eclipse on March 20, 2015 over Kharkiv, Ukraine (49.6° N, 36.3° E). Journal of Atmospheric and Solar-Terrestrial Physics, 182.

Chimonas, G., & Hines, C. O. (1970). Atmospheric gravity waves induced by a solar eclipse. Journal of Geophysical Research, 75(4), 875.

Chisham, G., Lester, M., Milan, S. E., Freeman, M. P., Bristow, W. A., Grocott, A., ... & Walker, A. D. M. (2007). A decade of the Super Dual Auroral Radar Network (SuperDARN): Scientific achievements, new techniques and future directions. Surveys in geophysics, 28(1), 33.

Coster, A. J., Goncharenko, L., Zhang, S. R., Erickson, P. J., Rideout, W., & Vierinen, J. (2017). GNSS observations of ionospheric variations during the 21 August 2017 solar eclipse. Geophysical Research Letters, 44(24), 12041.

Danilkin, N. P. (2008). Radio sounding of the ionosphere by satellite and ground-based ionosondes. Proceedings of the Institute of Applied Geophysics, (87), 209. (in Russian)

Danilov, A. D., Kazimirovsky, E. S., Vergasov, G. V., & Hachikyan, G. Ya. (1987). Meteorological effects in the ionosphere. Gidrometeoizdat. (In Russian)

Danilov, A. D. (2013). Response of the F region to geomagnetic disturbances (review). Heliogeophysical research, (5), 1. (In Russian)

Davies, K. (1990). Ionospheric Radio. London, Peter Pergrinus.

Domnin, I. F., Panasenko, S. V., Uryadov, V. P., & Chernogor, L. F. (2012). Results of Radiophysical Study of Wave Disturbances in the Ionospheric Plasma During Its Heating by High-Power HF Radio Transmission of “Sura” facility. Radiophysics and Quantum Electronics, 55, 253.

Domnin, I. F, Chepurnyy, Y. M, Emelyanov, L. Y, Chernyaev, S. V, Kononenko, A. F, Kotov, D. V, Bogomaz, O. V, Iskra, D. A. (2014) Kharkiv incoherent scatter facility. Bulletin of the National Technical University “Kharkiv Polytechnic Institute". Series “Radiophysics and ionosphere", 47(1089), 28.

Dougherty, J. P., & Farley Jr, D. T. (1963). A theory of incoherent scattering of radio waves by a plasma: 3. Scattering in a partly ionized gas. Journal of Geophysical Research, 68(19), 5473.

Edemsky, I. K., Voeykov, S. V., & Yasukevich, Yu. V. (2011). Seasonal and latitudinal variations in the parameters of MHD wave disturbances generated by the solar terminator. Modern problems of remote sensing of the Earth from space, 8(4), 107. (In Russian)

Evans, J. V. (1969). Theory and practice of ionosphere study by Thomson scatter radar. Proceedings of the IEEE, 57(4).

Fejer, J. A., Gonzales, C. A., Ierkic, H. M., Sulzer, M. P., Tepley, C. A., Duncan, L. M., ... & Gordon, W. E. (1985). Ionospheric modification experiments with the Arecibo heating facility. Journal of atmospheric and terrestrial physics, 47(12).

Förster, M., & Jakowski, N. (2000). Geomagnetic storm effects on the topside ionosphere and plasmasphere: a compact tutorial and new results. Surveys in Geophysics, 21(1), 47.

Frissell, N. A., Baker, J. B. H., Ruohoniemi, J. M., Gerrard, A. J., Miller, E. S., Marini, J. P., ... & Bristow, W. A. (2014). Climatology of medium-scale traveling ionospheric disturbances observed by the midlatitude Blackstone SuperDARN radar. Journal of geophysical research: space physics, 119(9), 7679.

Fritts, D. C., & Luo, Z. (1993). Gravity wave forcing in the middle atmosphere due to reduced ozone heating during a solar eclipse. Journal of Geophysical Research: Atmospheres, 98(D2), 3011.

Fritts, D. C., & Alexander, M. J. (2003). Gravity wave dynamics and effects in the middle atmosphere. Reviews of geophysics, 41(1).

Frolov, V. L., Komrakov, G. P., Kunitsyn, V. E., Padokhin, A. M., Vasiliev, A. E., & Kurbatov, G. A. (2010). Sounding of the ionosphere disturbed by the “Sura” heating facility radiation using signals of the GPS satellites. Radiophysics and Quantum Electronics, 53(7), 379.

Fukao, S., Sato, T., Tsuda, T., Kato, S., Wakasugi, K., & Makihira, T. (1985a). The MU radar with an active phased array system: 1. Antenna and power amplifiers. Radio Science, 20(6), 1155.

Fukao, S., Tsuda, T., Sato, T., Kato, S., Wakasugi, K., & Makihira, T. (1985b). The MU radar with an active phased array system: 2. In-house equipment. Radio Science, 20(6), 1169.

Galushko, V. G., Paznukhov, V. V., Sopin, A. A., & Yampolski, Y. M. (2016). Statistics of ionospheric disturbances over the Antarctic Peninsula as derived from TEC measurements. Journal of Geophysical Research: Space Physics, 121(4), 3395.

Gardner, F. F., & Pawsey, J. L. (1953). Study of the ionospheric D-region using partial reflections. Journal of Atmospheric and Terrestrial Physics, 3(6), 321.

Garmash, K. P., & Chernogor, L. F. (1998). Elegtromagnetic and geophysical effects in the near-Earth plasma, stimulated by high power high frequency radio waves. Electromagnetic phenomena, 1(1), 90. (In Russian)

Garmash, K. P., Rozumenko, V. T., Tyrnov, O. F., Tsymbal, A. M., & Chernogor, L. F. (1999). Radiophysical studies of processes in near-Earth plasma disturbed by high-energy sources. Foreign radio electronics. Advances in modern radio electronics, (7), 3. (In Russian)

Georges, T. M. (1973). Infrasound from convective storms: Examining the evidence. Reviews of Geophysics, 11(3), 571.

Gershman, B. N. (1974). Dynamics of the ionospheric plasma. Moscow, Science.

Gossard, E. E., & Hooke, W. H. (1975). Waves in the atmosphere: Atmospheric infrasound and gravity waves. Their generation and propagation. Amsterdam, Elsevier Scientific Publishing Co.

Gurevich, A. V. (1976). Nonlinear phenomena in the ionosphere. Radiophysics and Quantum Electronics, 19(6), 595.

Hanna, E., Penman, J., Jónsson, T., Bigg, G. R., Björnsson, H., Sjúrðarson, S., ... & Bryant, R. G. (2016). Meteorological effects of the solar eclipse of 20 March 2015: analysis of UK Met Office automatic weather station data and comparison with automatic weather station data from the Faroes and Iceland. Philosophical Transactions of the Royal Society A: Mathematical, Physical and Engineering Sciences, 374(2077).

Hapgood, M. (2017). Satellite navigation—Amazing technology but insidious risk: Why everyone needs to understand space weather. Space Weather, 15(4), 545.

Harris, M. J., Arnold, N. F., & Aylward, A. D. (2002). A study into the effect of the diurnal tide on the structure of the background mesosphere and thermosphere using the new coupled middle atmosphere and thermosphere (CMAT) general circulation model. Annales Geophysicae, 20(2), 225.

Hassenpflug, G., Yamamoto, M., Luce, H., & Fukao, S. (2008). Description and demonstration of the new Middle and Upper atmosphere Radar imaging system:

1-D, 2-D, and 3-D imaging of troposphere and stratosphere. Radio Science, 43(02).

Heaviside, O. (1902). The theory of electric telegraphy. Encyclopaedia Britannica, 33, 215.

Heelis, R. A., & Hanson, W. B. (1998). Measurements of thermal ion drift velocity and temperature using planar sensors. Geophysical Monograph. American Geophysical Union, 102, 61.

Hernández-Pajares, M., Juan, J. M., Sanz, J., & Aragón-Àngel, A. (2012). Propagation of medium scale traveling ionospheric disturbances at different latitudes and solar cycle conditions. Radio Science, 47(6).

Hines, C. O. (1960). Internal atmospheric gravity waves at ionospheric heights. Canadian Journal of Physics, 38(11), 1441.

Hocke, K., & Schlegel, K. (1996). A review of atmospheric gravity waves and travelling ionospheric disturbances: 1982–1995. Annales Geophysicae, 14(9), 917.

Hocke, K., Schlegel, K., & Kirchengast, G. (1996). Phases and amplitudes of TIDs in the high latitude F-region observed by EISCAT. Journal of Atmospheric and Terrestrial Physics, 58(1-4), 245.

Hocking, W. K. (1997). Strengths and limitations of MST radar measurements of middle-atmosphere winds. Annales Geophysicae, 15(9), 1111.

Holdsworth, D. A., Vincent, R. A., & Reid, I. M. (2001). Mesospheric turbulent velocity estimation using the Buckland Park MF radar. Annales Geophysicae, 19(8), 1007.

Holt, J. M., Zhang, S. R., & Buonsanto, M. J. (2002). Regional and local ionospheric models based on Millstone Hill incoherent scatter radar data. Geophysical research letters, 29(8), 48.

Hooke, W. H. (1968). Ionospheric irregularities produced by internal atmospheric gravity waves. Journal of Atmospheric and Terrestrial Physics, 30(5), 795.

Hunsucker, R. D. (1982). Atmospheric gravity waves generated in the high-latitude ionosphere: A review. Reviews of Geophysics, 20(2), 293.

Jacobi, C., Portnyagin, Y. I., Solovjova, T. V., Hoffmann, P., Singer, W., Fahrutdinova, A. N., Ishmuratov, R. A., Beard, A. G., Mitchell, N. J., Muller, H. G., Schminder, R., Kürschner, D., Manson, A. H., & Meek, C. E. (1999). Climatology of the semidiurnal tide at 52–56 N from ground-based radar wind measurements 1985–1995. Journal of Atmospheric and Solar-Terrestrial Physics, 61(13), 975.

Jacobi, C., Gavrilov, N. M., Kürschner, D., & Fröhlich, K. (2006). Gravity wave climatology and trends in the mesosphere/lower thermosphere region deduced from low-frequency drift measurements 1984–2003 (52.1 N, 13.2 E). Journal of atmospheric and solar-terrestrial physics, 68(17), 1913.

Jakowski, N., Stankov, S. M., Wilken, V., Borries, C., Altadill, D., Chum, J., ... & Cander, L. R. (2008). Ionospheric behavior over Europe during the solar eclipse of 3 October 2005. Journal of Atmospheric and Solar-Terrestrial Physics, 70(6), 836.

Karpov, I. V., & Bessarab, F. S. (2008). Model studying the effect of the solar terminator on the thermospheric parameters. Geomagnetism and Aeronomy, 48(2), 209.

Karpov, I. V., Kshevetsky, S. P., Borchevkina, O. P., Radievsky, A. V., & Karpov, A. I. (2016). Disturbances of the upper atmosphere and ionosphere initiated by sources of acoustic-gravity waves in the lower atmosphere. Chemical physics, 35(1), 59. (In Russian)

Kasahara, Y., Kasaba, Y., Kojima, H., Yagitani, S., Ishisaka, K., Kumamoto, A., ... & Shinohara, I. (2018). The plasma wave experiment (PWE) on board the Arase (ERG) satellite. Earth, Planets and Space, 70(1).

Kamide, Y., & Chian, A. C. L. (Eds.). (2007). Handbook of the solar-terrestrial environment. Springer Science & Business Media.

Kazimirovsky, E. S., & Kokourov, V. D. (1979). Motions in the ionosphere. Novosibirsk, Nauka, 344 p. (In Russian)

Kennelly, A. E. (1902). On the elevation of the electrically-conducting strata of the Earth's atmosphere. Electrical world and engineer, 39(11), 473.

Kirchengast, G., Hocke, K., & Schlegel, K. (1995). Gravity waves determined by modeling of traveling ionospheric disturbances in incoherent-scatter radar measurements. Radio science, 30(5), 1551.

Knudsen, D. J., Burchill, J. K., Buchert, S. C., Eriksson, A. I., Gill, R., Wahlund, J. E., ... & Moffat, B. (2017). Thermal ion imagers and Langmuir probes in the Swarm electric field instruments. Journal of Geophysical Research: Space Physics, 122(2), 2655.

Kotake, N., Otsuka, Y., Ogawa, T., Tsugawa, T., & Saito, A. (2007). Statistical study of medium-scale traveling ionospheric disturbances observed with the GPS networks in Southern California. Earth, planets and space, 59(2), 95.

Koval, A., Chen, Y., Stanislavsky, A., Kashcheyev, A., & Zhang, Q. H. (2018). Simulation of Focusing Effect of Traveling Ionospheric Disturbances on Meter-Decameter Solar Dynamic Spectra. Journal of Geophysical Research: Space Physics, 123(11), 8940.

Kozak, L. V., & Pylypenko, S. G. (2011). Temperature changes of the Earth upper atmosphere over storms from satellite measurements. Astronomical School's Report, 7(1), 42.

Kozlovsky, A., Turunen, T., & Ulich, T. (2013). Rapid-run ionosonde observations of traveling ionospheric disturbances in the auroral ionosphere. Journal of Geophysical Research: Space Physics, 118(8), 5265.

Kumamoto, A., Tsuchiya, F., Kasahara, Y., Kasaba, Y., Kojima, H., Yagitani, S., ... & Obara, T. (2018). High frequency analyzer (HFA) of plasma wave experiment (PWE) onboard the Arase spacecraft. Earth, Planets and Space, 70(1).

Kunitsyn, V. E., Andreeva, E. S., Frolov, V. L., Komrakov, G. P., Nazarenko, M. O., & Padokhin, A. M. (2012). Sounding of HF heating-induced artificial ionospheric disturbances by navigational satellite radio transmissions. Radio Science, 47(4).

Kunitsyn, V. E., Krysanov, B. Yu., & Vorontsov, A. M. (2015). Generation of acoustic-gravity waves by various sources on the Earth's surface. Moscow University Bulletin. Series 3. Physics. Astronomy, (6). (in Russian)

Kurdyaeva, Y. A., Kshevetskii, S. P., Gavrilov, N. M., & Kulichkov, S. N. (2018). Correct boundary conditions for the high-resolution model of nonlinear acoustic-gravity waves forced by atmospheric pressure variations. Pure and Applied Geophysics, 175(10), 3639.

Kutelev, K. A., & Berngardt, O. I. (2014). Medium-scale wave disturbances in the F-layer of the ionosphere during two hours after the fall of the Chelyabinsk meteorite from observations of the ESW radar. Meteorite Chelyabinsk-year on Earth, 171. (In Russian)

Leonovich, L. A., Romanova, E. B., Tatshilin, A. V., & Kovtunenko, V. G. (2005). Modeling of ionospheric effect of solar flare on September, 23, 1998. Solar-terrestrial physics, (8), 135. (In Russian)

Liu, J. Y., Hsiao, C. C., Tsai, L. C., Liu, C. H., Kuo, F. S., Lue, H. Y., & Huang, C. M. (1998). Vertical phase and group velocities of internal gravity waves derived from ionograms during the solareclipse of 24 October 1995. Journal of Atmospheric and Solar-Terrestrial Physics, 60(17), 1679.

Lizunov, G. V., & Fedorenko, A. K. (2013). Atmospheric gravity waves generation by solar terminator according to “Atmosphere Explorer-E” satellite data. Radio Physics and Radio Astronomy, 11(1), 49. (In Russian)

Lomidze, L., Knudsen, D. J., Burchill, J., Kouznetsov, A., & Buchert, S. C. (2018). Calibration and validation of Swarm plasma densities and electron temperatures using ground-based radars and satellite radio occultation measurements. Radio Science, 53(1), 15.

MacDougall, J. W., & Jayachandran, P. T. (2011). Solar terminator and auroral sources for traveling ionospheric disturbances in the midlatitude F region. Journal of atmospheric and solar-terrestrial physics, 73(17-18), 2437.

Mannucci, A. J., Wilson, B. D., Yuan, D. N., Ho, C. H., Lindqwister, U. J., & Runge, T. F. (1998). A global mapping technique for GPS-derived ionospheric total electron content measurements. Radio science, 33(3), 565.

Mannucci, A. J., Iijima, B. A., Lindqwister, U. J., Pi, X., Sparks, L., & Wilson, B. D. (1999). GPS and ionosphere: review of radio science 1996–1999.

Manson, A., Meek, C., Hagan, M., Hall, C., Hocking, W., MacDougall, J., Franke, S., Riggin, D., Fritts, D., Vincent, R., & Burrage, M. (1999). Seasonal variations of the semi-diurnal and diurnal tides in the MLT: Multi-year MF radar observations from 2 to 70 N, and the GSWM tidal model. Journal of Atmospheric and Solar-Terrestrial Physics, 61(11), 809.

Manson, A. H., Meek, C. E., Koshyk, J., Franke, S., Fritts, D. C., Riggin, D., Hall, C., M., Hocking, W. K., MacDougall, J., Igarashi, K., & Vincent, R. A. (2002). Gravity wave activity and dynamical effects in the middle atmosphere (60–90km): observations from an MF/MLT radar network, and results from the Canadian Middle Atmosphere Model (CMAM). Journal of atmospheric and solar-terrestrial physics, 64(1), 65.

Marlton, G. J., Williams, P. D., & Nicoll, K. A. (2016). On the detection and attribution of gravity waves generated by the 20 March 2015 solar eclipse. Philosophical Transactions of the Royal Society A: Mathematical, Physical and Engineering Sciences, 374(2077).

Marple Jr, S. L., & Carey, W. M. (1989). Digital spectral analysis with applications. Prentice-Hall, New York.

Matsuoka, A., Teramoto, M., Nomura, R., Nosé, M., Fujimoto, A., Tanaka, Y., ... & Shinohara, I. (2018). The ARASE (ERG) magnetic field investigation. Earth, Planets and Space, 70(1).

Medvedev, A. V., Ratovsky, K. G., Tolstikov, M. V., Oinats, A. V., Alsatkin, S. S., & Zherebtsov, G. A. (2017). Relation of internal gravity wave anisotropy with neutral wind characteristics in the upper atmosphere. Journal of Geophysical Research: Space Physics, 122(7), 7567.

Merzlyakov, E. G., & Portnyagin, Yu. I. (1999). Long-term changes in the parameters of the wind regime of the lower thermosphere in temperate latitudes (90 – 100 km). Physics of atmosphere and ocean, 35(4), 531. (In Russian)

Middleton, H. R., Mitchell, N. J., & Muller, H. G. (2002). Mean winds of the mesosphere and lower thermosphere at 52 N in the period 1988–2000. Annales Geophysicae, 20(1), 81.

Migulin, V. V., & Gurevich, A. V. (1985). Investigation in the USSR of non-linear phenomena in the ionosphere. Journal of atmospheric and terrestrial physics, 47(12), 1181.

Mishin, E., Sutton, E., Milikh, G., Galkin, I., Roth, C., & Förster, M. (2012). F2-region atmospheric gravity waves due to high-power HF heating and subauroral polarization streams. Geophysical research letters, 39(11).

Miyoshi, Y., Shinohara, I., Takashima, T., Asamura, K., Higashio, N., Mitani, T., ... & Seki, K. (2018). Geospace exploration project ERG. Earth, Planets and Space, 70(1).

Mošna, Z., Boška, J., Knížová, P. K., Šindelářová, T., Kouba, D., Chum, J., Rejfek L., Potužníková K., Arikan F. & Toker, C. (2018). Observation of the solar eclipse of

20 March 2015 at the Pruhonice station. Journal of Atmospheric and Solar-Terrestrial Physics, 171, 277.

Müller-Wodarg, I. C. F., Aylward, A. D., & Lockwood, M. (1998). Effects of a mid-latitude solar eclipse on the thermosphere and ionosphere-A modelling study. Geophysical Research Letters, 25(20), 3787.

Namboothiri, S. P., Manson, A. H., & Meek, C. E. (1993). Variations of mean winds and tides in the upper middle atmosphere over a solar cycle, Saskatoon, Canada, 52 N, 107 W. Journal of atmospheric and terrestrial physics, 55(10), 1325.

Namboothiri, S. P., Meek, C. E., & Manson, A. H. (1994). Variations of mean winds and solar tides in the mesosphere and lower thermosphere over time scales ranging from 6 months to 11 yr: Saskatoon, 52 N, 107 W. Journal of Atmospheric and Terrestrial Physics, 56(10), 1313.

Nerushev, A. F. (2014). Jet streams in the Earth's atmosphere. Earth and Universe, (6), 16. (in Russian)

Nishioka, M., Saito, A., & Tsugawa, T. (2009). Super-medium-scale traveling ionospheric disturbance observed at midlatitude during the geomagnetic storm on 10 November 2004. Journal of Geophysical Research: Space Physics, 114(A7).

Nygrén, T., Aikio, A. T., Voiculescu, M., & Cai, L. (2015). Radar observations of simultaneous traveling ionospheric disturbances and atmospheric gravity waves. Journal of Geophysical Research: Space Physics, 120(5), 3949.

Otsuka, Y., Shiokawa, K., Ogawa, T., & Wilkinson, P. (2002). Geomagnetic conjugate observations of equatorial airglow depletions. Geophysical Research Letters, 29(15), 43.

Otsuka, Y., Shiokawa, K., Ogawa, T., & Wilkinson, P. (2004). Geomagnetic conjugate observations of medium-scale traveling ionospheric disturbances at midlatitude using all-sky airglow imagers. Geophysical research letters, 31(15).

Otsuka, Y., Suzuki, K., Nakagawa, S., Nishioka, M., Shiokawa, K., & Tsugawa, A. (2013). GPS observations of medium-scale traveling ionospheric disturbances over Europe. Annales Geophysicae, 31(2), 163.

Oynats, A. V., Kurkin, V. I., & Chernigovskaya, M. A. (2012). Meteorological effects in the ionosphere according to the SuperDARN Hokkaido decameter radar. Modern problems of remote sensing of the Earth from space, 9(4), 113. (In Russian)

Panasenko, S. V. (2011). Filtration of temporal variations in the power of an incoherently scattered signal in the presence of irregular interference and equipment failures. Bulletin of the National Technical University “Kharkiv Polytechnic Institute". Series “Radiophysics and ionosphere", 44, 40. (In Russian)

Panasenko, S. V., Goncharenko, L. P., Erickson, P. J., Aksonova, K. D., & Domnin, I. F. (2018). Traveling ionospheric disturbances observed by Kharkiv and Millstone Hill incoherent scatter radars near vernal equinox and summer solstice. Journal of Atmospheric and Solar-Terrestrial Physics, 172, 10.

Panasenko, S. V., Otsuka, Y., van de Kamp, M., Chernogor, L. F., Shinbori, A., Tsugawa, T., & Nishioka, M. (2019). Observation and characterization of traveling ionospheric disturbances induced by solar eclipse of 20 March 2015 using incoherent scatter radars and GPS networks. Journal of Atmospheric and Solar-Terrestrial Physics, 191.

Pancheva, D., Mitchell, N., Middleton, H., & Muller, H. (2003). Variability of the semidiurnal tide due to fluctuations in solar activity and total ozone. Journal of Atmospheric and Solar-Terrestrial Physics, 65(1), 1.

Pedersen, T., Gustavsson, B., Mishin, E., MacKenzie, E., Carlson, H. C., Starks, M., & Mills, T. (2009). Optical ring formation and ionization production in high-power HF heating experiments at HAARP. Geophysical research letters, 36(18).

Picone, J. M., Hedin, A. E., Drob, D. P., & Aikin, A. C. (2002). NRLMSISE-00 empirical model of the atmosphere: Statistical comparisons and scientific issues. Journal of Geophysical Research: Space Physics, 107(A12), 15.

Piggott, W. R., & Rawer, K. (1972). URSI handbook of ionogram interpretation and reduction.

Portnyagin, Yu. I., & Shpringer, K. (Eds.). (1978). Measurement of wind at altitudes of 90 – 100 km with ground-based techniques. Gidrometeoizdat. (In Russian)

Portnyagin, Yu. I., & Solovjova, T. V. (2000). Global empirical wind model for the upper mesosphere/lower thermosphere. I. Prevailing wind. Annales Geophysicae, 18 (3), 300.

Portnyagin, Y. I., Merzlyakov, E. G., Solovjova, T. V., Jacobi, C., Kürschner, D., Manson, A., & Meek, C. (2006). Long-term trends and year-to-year variability of mid-latitude mesosphere/lower thermosphere winds. Journal of atmospheric and solar-terrestrial physics, 68(17), 1890.

Pradipta, R., & Lee, M. C. (2013). Investigation of acoustic gravity waves created by anomalous heat sources: experiments and theoretical analysis. Physica Scripta, 2013(T155).

Pulyaev, V. A., Dzubanov, D. A., & Domnin I. F. (2011). Determination of the parameters of the ionosphere using the technique of incoherent scattering of radio waves. Kharkiv, Textbook. (in Russian)

Radicella, S. M. (2009). The NeQuick model genesis, uses and evolution. Annals of geophysics, 52(3-4), 417.

Reinisch, B. W., Haines, D. M., & Kuklinski, W. S. (1992). The new portable Digisonde for vertical and oblique sounding. Proceedings of the AGARD EPP 50th Symposium, London, England, 11.

Reinisch, B. W., Galkin, I. A., Khmyrov, G. M., Kozlov, A. V., Lisysyan, I. A., Bibl, K., ... & Hamel, R. (2008). Advancing digisonde technology: The DPS-4D. American Institute of Physics. AIP Conference Proceedings, 974(1), 127.

Reinisch, B. W., & Galkin, I. A. (2011). Global ionospheric radio observatory (GIRO). Earth, planets and space, 63(4), 377.

Rich, F. J. (1994). Users Guide for the Topside Ionospheric Plasma Monitor (SSIES, SSIES-2 and SSIES-3) on Spacecraft of the Defense Meteorological Satellite Program, Volume 1: Technical Description.

Rietveld, M. T., Wright, J. W., Zabotin, N., & Pitteway, M. L. V. (2008). The tromsø dynasonde. Polar Science, 2(1), 55.

Rishbeth, H., & Williams, P. J. S. (1985). The EISCAT ionospheric radar-The system and its early results. Quarterly Journal of the Royal Astronomical Society, 26, 478.

Roble, R. G., & Ridley, E. C. (1994). A thermosphere – ionosphere – mesosphere – electrodynamics general circulation model (TIME-GCM): Equinox solar cycle minimum simulations (30 – 500 km). Geophysical Research Letters, 21(6), 417.

Schunk, R., & Nagy, A. (2009). Ionospheres: physics, plasma physics, and chemistry. Cambridge university press.

Shindin, A. V., Grach, S. M., Klimenko, V. V., Nasyrov, I. A., Sergeev, E. N., Beletski, A. B., ... & Gumerov, R. I. (2015). The 630 nm and 557.7 nm airglow during HF ionosphere pumping by the SURA facility radiation for pump frequencies near the fourth electron gyroharmonic. Radiophysics and Quantum Electronics, 57(11), 759.

Shiokawa, K., Katoh, Y., Satoh, M., Ejiri, M. K., Ogawa, T., Nakamura, T., ... & Wiens, R. H. (1999). Development of optical mesosphere thermosphere imagers (OMTI). Earth, planets and space, 51(7), 887.

Shpynev, B. G., Pancheva, D., Muhtarov, P., Kurkin, V. I., Ratovsky, K. G., Chernigovskaya, M. A., Belinskaya A. Yu., & Stepanov, A. E. (2014). Aeronomic effects of sudden stratospheric warming in January 2009 and their influence on the ionosphere. Study of the Earth from space, (3), 3. (In Russian)

Singer, W., Bremer, J., Hoffmann, P., Manson, A. H., Meek, C. E., Schminder, R., Kürschner D., Portnyagin Yu. I., Makarov N. A., Muller H. G., Kazimirovsky E. S., & Clark, R. R. (1994). Geomagnetic influences upon tides – winds from MLT radars. Journal of Atmospheric and Terrestrial Physics, 56(10), 1301.

Smertin, V., & Namgaladze, A. (1978). Comparison of the day and night effects of internal gravity waves in the F2 region of the mid-latitude ionosphere. Geomagnetism and Aeronomy, 18, 90. (In Russian)

Sokolov, S. N. (2011). Magnetic storms and their effects in the lower ionosphere: Differences in storms of various types. Geomagnetism and Aeronomy, 51(6), 741.

Solov'ev, I. A. (2000). Satellite navigation systems. Eco-Trends. (in Russian)

Somsikov, V. M. (2011). Solar terminator and dynamic phenomena in the atmosphere: A review. Geomagnetism and Aeronomy, 51(6), 707.

Song, Q., Ding, F., Wan, W., Ning, B., Liu, L., Zhao, B., Li, Q, & Zhang, R. (2013). Statistical study of large-scale traveling ionospheric disturbances generated by the solar terminator over China. Journal of Geophysical Research: Space Physics, 118(7), 4583.

Spilker, J. J., & Parkinson, B. W. (1996). Overview of GPS operation and design. Global Positioning System: Theory and applications., 1, 29.

Stankov, S. M., Bergeot, N., Berghmans, D., Bolsée, D., Bruyninx, C., Chevalier, J. M., ... & West, M. J. (2017). Multi-instrument observations of the solar eclipse on 20 March 2015 and its effects on the ionosphere over Belgium and Europe. Journal of Space Weather and Space Climate, 7, A19.

Stepanov, A. E., Philippov, L. D., & Ratovsky, K. G. (2014). Traveling ionospheric disturbances according to the data of vertical sounding of the ionosphere in northeastern Russia. Natural resources of the Arctic and Subarctic, 1 (73).

Stubbe, P., Kopka, H., Rietveld, M. T., Frey, A., Høeg, P., Nielsen, E., ... & Holt, O. (1985). Ionospheric modification experiments with the Tromsø heating facility. Journal of atmospheric and terrestrial physics, 47(12), 1151.

Suslov, A. I., Yerohin, N. S., Mikhailovskaya, L. A., Arteha, S. N., & Gusev, A. A. (2017). Modeling the passage of large-scale IGWs from the troposphere to the ionosphere. Modern problems of remote sensing of the Earth from space, 14(5), 19. (In Russian)

Themens, D. R., Jayachandran, P. T., Langley, R. B., MacDougall, J. W., & Nicolls, M. J. (2013). Determining receiver biases in GPS-derived total electron content in the auroral oval and polar cap region using ionosonde measurements. GPS solutions, 17(3), 357.

Tsugawa, T., Saito, A., & Otsuka, Y. (2004). A statistical study of large-scale traveling ionospheric disturbances using the GPS network in Japan. Journal of Geophysical Research: Space Physics, 109(A6).

Tsugawa, T., Otsuka, Y., Coster, A. J., & Saito, A. (2007). Medium-scale traveling ionospheric disturbances detected with dense and wide TEC maps over North America. Geophysical Research Letters, 34(22).

Tumanova, Yu. S., Andreeva, E. S., & Nesterov, I. A. (2016). Observations of the ionospheric trough over Europe at different levels of geomagnetic disturbance according to radio tomography data. Scientific Notes of the Physics Faculty of Moscow University, (3), 163906.

Uryadov, V. P., Kolchev, A. A., Vybornov, F. I., Shumaev, V. V., Egoshin, A. I., & Chernov, A. G. (2016). Ionospheric effects of a solar eclipse of March 20, 2015 on oblique sounding paths in the Eurasian longitudinal sector. Radiophysics and Quantum Electronics, 59(6), 431.

Vadas, S. L., & Fritts, D. C. (2005). Thermospheric responses to gravity waves: Influences of increasing viscosity and thermal diffusivity. Journal of Geophysical Research: Atmospheres, 110(D15).

Vadas, S. L., & Fritts, D. C. (2006). Influence of solar variability on gravity wave structure and dissipation in the thermosphere from tropospheric convection. Journal of Geophysical Research: Space Physics, 111(A10).

Vadas, S. L. (2007). Horizontal and vertical propagation and dissipation of gravity waves in the thermosphere from lower atmospheric and thermospheric sources. Journal of Geophysical Research: Space Physics, 112(A6).

Vadas, S. L., & Liu, H. L. (2009). Generation of large-scale gravity waves and neutral winds in the thermosphere from the dissipation of convectively generated gravity waves. Journal of Geophysical Research: Space Physics, 114(A10).

Vadas, S. L., & Nicolls, M. J. (2009). Temporal evolution of neutral, thermospheric winds and plasma response using PFISR measurements of gravity waves. Journal of Atmospheric and Solar-Terrestrial Physics, 71(6-7), 744.

Verhulst, T. G., Sapundjiev, D., & Stankov, S. M. (2016). High-resolution ionospheric observations and modeling over Belgium during the solar eclipse of 20 March 2015 including first results of ionospheric tilt and plasma drift measurements. Advances in Space Research, 57(11), 2407.

Vierinen, J., Kero, A., & Rietveld, M. T. (2013). High latitude artificial periodic irregularity observations with the upgraded EISCAT heating facility. Journal of Atmospheric and Solar-Terrestrial Physics, 105, 253.

Vlasov, A., Kauristie, K., Kamp, M., Luntama, J. P., & Pogoreltsev, A. (2011). A study of traveling ionospheric disturbances and atmospheric gravity waves using EISCAT Svalbard Radar IPY-data. Annales Geophysicae, 29(11), 2101.

Wilson, B. D., Mannucci, A. J., & Edwards, C. D. (1995). Subdaily northern hemisphere ionospheric maps using an extensive network of GPS receivers. Radio Science, 30(3), 639.

Wu, Y. W., Liu, R. Y., Zhang, B. C., Wu, Z. S., Hu, H. Q., Zhang, S. R., Zhang, Q. H., Liu J. M., & Honary, F. (2013). Multi-instrument observations of plasma features in the Arctic ionosphere during the main phase of a geomagnetic storm in December 2006. Journal of Atmospheric and Solar-Terrestrial Physics, 105, 358.

Xu, G. (2007). GPS: Theory, Algorithms and Applications. Berlin, Springer.

Yasyukevich, Y. V., Zakharov, V. I., Kunitsyn, V. E., & Voeikov, S. V. (2015). The response of the ionosphere to the earthquake in Japan on March 11, 2011 as estimated by different GPS-based methods. Geomagnetism and aeronomy, 55(1), 108.

Yerohin, N. S., Mikhailovskaya, L. A., & Shalimov, S. L. (2007). Passage of large-scale internal gravity waves to ionospheric heights through wind structures in the lower and middle atmosphere. Geophysical research, (7), 53. (in Russian)

Yiğit, E., & Medvedev, A. S. (2009). Heating and cooling of the thermosphere by internal gravity waves. Geophysical Research Letters, 36(14).

Zalizovski, A. V., Kashcheiev, A. S., Kashcheiev, S. B., Koloskov, A. V., Lisachenko, V. N., Paznukhov, V. V., ... & Yampolski, Y. M. (2018). A prototype of a portable coherent ionosonde. Space Science and Technology, 24(3).

Zhang, S. P., Goncharenko, L. P., Salah, J. E., Roble, R. G., & Shepherd, G. G. (2003). Climatology of neutral winds in the lower thermosphere over Millstone Hill (42.6 N) observed from ground and from space. Journal of Geophysical Research: Space Physics, 108(A1).

Zhang, S. D., Yi, F., & Hu, X. (2004). MF radar observation of mean wind and tides of winter mesopause (80 – 98km) region over Wuhan (30° N, 114° E). Journal of atmospheric and solar-terrestrial physics, 66(1), 15.

SCIENTIFIC EDITION

S. V. Panasenko, K. D. Aksonova, D. V. Kotov

CHARACTERISTICS OF TRAVELING IONOSPHERIC DISTURBANCES FROM INCOHERENT SCATTER DATA

MONOGRAPH

English

The authors of publications are responsible for the accuracy of facts, dates, names, surnames, digital data, spelling, punctuation and stylistic design

Published (PDF): 20.06.2021. Signed for printing: 25.06.2021.
Format 60×84/16. Offset Paper. Digital printing.
The headset is Cambria. Conventionally printed sheets 8,61.
Circulation: 150 copies. Order № 22708.

Printed from the finished original layout.

Compilers:

Institute of Ionosphere of NAS and MES of Ukraine
61001, Ukraine, Kharkiv, Kyrpychova str., 16
E- mail: iion@khpi.kharkov.ua | URL: http://iion.org.ua/en/about/

NGO European Scientific Platform
21037, Ukraine, Vinnytsia, Zodchykh str. 18/81
Tel.: +38 098 1948380; +38 098 1956755
E-mail: info@ukrlogos.in.ua | URL: www.ukrlogos.in.ua

Publisher [ISBN]: Primedia E-launch LLC.
TX 75001, United States, Texas, Dallas.
E-mail: info@primediaelaunch.com | URL: www.primediaelaunch.com

Publisher [printed copies]: Sole proprietorship - Gulyaeva V.M.
08700, Ukraine, Obuhiv, Malyshka str. 5. E-mail: 5894939@gmail.com
Certificate of the subject of the publishing business: ДК No 6205 of 30.05.2018 р.